



HAL
open science

Optics and structure of metal clusters at the atomic scale

Alfredo Campos Otero

► **To cite this version:**

Alfredo Campos Otero. Optics and structure of metal clusters at the atomic scale. Condensed Matter [cond-mat]. Université Paris Saclay (COmUE), 2018. English. NNT : 2018SACLS401 . tel-02342598

HAL Id: tel-02342598

<https://theses.hal.science/tel-02342598v1>

Submitted on 1 Nov 2019

HAL is a multi-disciplinary open access archive for the deposit and dissemination of scientific research documents, whether they are published or not. The documents may come from teaching and research institutions in France or abroad, or from public or private research centers.

L'archive ouverte pluridisciplinaire **HAL**, est destinée au dépôt et à la diffusion de documents scientifiques de niveau recherche, publiés ou non, émanant des établissements d'enseignement et de recherche français ou étrangers, des laboratoires publics ou privés.

Optics and Structure of Metal Clusters at the Atomic Scale

Thèse de doctorat de l'Université Paris-Saclay
préparée à l'Université Paris Sud

École doctorale n°572 Ondes et Matière (EDOM)
Spécialité de doctorat: Nanophysique

Thèse présentée et soutenue à Orsay, le 31/10/2018, par

Alfredo Campos Otero

Composition du Jury:

Maria Tchernycheva Directeur de recherche, CNRS-Université Paris-Sud (– C2N)	Présidente
Natalia Del Fatti Professeur, Université Claude Bernard Lyon 1 (– ILM)	Rapporteuse
Caroline Bonafos Directeur de recherche, CNRS-Université de Toulouse (– CEMES)	Rapporteuse
Bernd von Issendorff Professeur, University of Freiburg (– FMF)	Examineur
Mathieu Kociak Directeur de recherche, CNRS-Université Paris-Sud (– LPS)	Directeur de thèse
Matthias Hillenkamp Chargé de recherche, CNRS- Université Claude Bernard Lyon 1 (– ILM)	Invité
Eleicer Ching Professeur, Universidad Tecnológica de Panamá (– PMC)	Invité

Synthèse

Il est bien connu que les propriétés optiques de nanoparticules de métaux nobles, en particulier or et argent, s'écartent fortement de celles de matériaux macroscopiques. Pour des tailles comprises entre une dizaine et quelques centaines de nanomètres, elles sont dominées par les plasmons de surface (SPs). Ceux-ci sont très bien décrits par des modèles purement classiques. D'un autre côté, des agrégats de quelques dizaines d'atomes se comportent comme des systèmes essentiellement quantiques, présentant de nouveaux effets (débordement de la densité électronique, polarisabilité réduite, effets non-locaux, transitions moléculaires/atômiques discrètes). La transition entre le régime purement classique et le régime quantique est un domaine pratiquement vierge. Il est cependant clair que de la structure atomique exacte de l'agrégat ainsi que de son environnement immédiat (substrat, matrice, oxydation) dépendent les propriétés électroniques et optiques. Les études expérimentales se sont longtemps heurtées à cette double contrainte d'obtenir la structure exacte des agrégats dans un environnement donné en parallèle à leurs propriétés optiques. Des mesures d'absorption optique ont été faites depuis longtemps. Cependant, de telles mesures sont effectuées sur un ensemble de particules, ce qui entraîne un élargissement inhomogène de la réponse plasmonique, rendant ardue l'observation des effets quantiques. Dans ce travail de thèse j'ai abordé ce problème par une méthode originale de microscopie (Scanning Transmission Electron Microscopy (STEM)) et spectroscopie électronique (Electron Energy Loss Spectroscopy (EELS)) permettant de mesurer en parallèle les propriétés optiques et structurales d'agrégats individuels à l'échelle atomique. En raison de la petite taille des agrégats qu'il fallait étudier pour explorer le régime quantique, un effort tout particulier a été porté sur l'optimisation des paramètres d'acquisition afin d'améliorer le rapport signal sur bruit et la résolution énergétique des spectres EELS. Afin d'évaluer la pertinence de mes mesures EELS, nous les avons avec nos collaborateurs systématiquement comparées à des mesures d'absorption optique sur le même type d'échantillons qui ont été préparés par de techniques physiques.

Les mesures d'absorption optique sur des agrégats d'argent en silice ont montré que l'énergie du plasmon ne dépend pas de la taille. Ce comportement a été rigoureusement vérifié par des calculs prenant en compte des effets classiques et quantiques ainsi que des effets d'environnement. Ces calculs montrent qu'avoir une matrice diélectrique peut contrecarrer les effets quantiques et résulter en l'absence de décalage énergétique du plasmon. Dans la caractérisation STEM-EELS le scénario est différent. Les mesures effectuées sur des agrégats individuelles ont montré dans un premier temps que l'apparition du plasmon dépend de la dose électronique. Avec l'augmentation de la dose une couche de porosité locale autour de la particule est créée ce qui promouvait un décalage énergétique du plasmon vers le bleu. Ce décalage était plus important pour les petits agrégats (diamètre < 5 nm) mettant en évidence des effets quantiques liés à la taille. La comparaison de nos manipulations STEM-EELS et optiques, ainsi que l'obtention d'une théorie prenant une description quantique qui considère l'environnement locale, nous a permis de trouver une compatibilité entre les deux techniques et de comprendre les controverses existant dans la littérature.

En parallèle, je me suis intéressé à la région purement classique au travers de structures lithographiées de quelques centaines de nanomètres. Bien que les cavités plasmoniques triangulaires aient été largement étudiées dans la littérature, une classification en termes de modes plasmoniques de respiration et de côté manquait. Dans cette étude, les résultats expérimentaux STEM-EELS, de modèles analytiques ainsi que de simulations nous ont permis de décrire la nature des différents modes.

Remerciements

Je voudrais tout d'abord remercier tous les membres du groupe STEM du laboratoire LPS pour m'avoir accueilli pendant tout ce temps et m'avoir traité comme faisant partie de la famille. La forte ambiance de collaboration m'a permis de travailler très efficacement et d'être très productif. En premier lieu, je tiens à remercier mon directeur de thèse Mathieu Kociak pour m'avoir donné la possibilité de travailler avec lui et pour l'envie de faire de la recherche qu'il m'a inspirée. Mathieu m'a toujours surpris par sa vaste connaissance en théorie et en expérimentation. Pour moi, il est un exemple à suivre en particulier pour ses qualités humaines. L'humeur de certaines réunions m'a relaxé en période de stress. Dans les moments de blocage dans les manips ou l'analyse de données, Mathieu avait toujours des solutions géniales. C'était vraiment merveilleux de travailler avec un grand scientifique comme Mathieu. Je remercie ensuite affectueusement Odile Stéphan qui m'a permis de travailler dans le groupe STEM et pour tout le soutien tout au long de ma formation dans la recherche. Je remercie également Luiz Tizei, Jean-Denis Blazit, Marcel Tencé, Alexandre Gloter et Xiaoyan Li pour leurs soutiens pour les explications sur le fonctionnement des microscopes comme pour toute l'aide patiente dans les manips qu'ils m'ont apportée.

Je voudrais remercier aussi Laura Bocher, Christian Colliex, Nathalie Brun, Mike Walls, Marta De Frutos et Alberto Zobelli qui ont apporté une atmosphère conviviale. Je serai toujours content de me rappeler de bons moments passés avec eux. Je remercie aussi Michele Amato, avec qui j'ai partagé mon bureau, pour toutes les conversations hors recherche et surtout en foot.

Un grand merci aux thésards et postdocs du groupe STEM: Adrien Teurtrie, Sophie Meuret, Xuan Zhang, Pabitra Das, Steffi Woo et particulièrement à Hugo Lourenço qui avait toujours le temps pour échanger des idées et de répondre à toutes mes questions avant de passer voir Mathieu.

Je tiens à remercier mon jury de thèse, et en particulier mes rapportrices Caroline Bonafos et Natalia Del Fatti, qui a pris de son temps pour lire mon manuscrit, assister à ma soutenance et donner des commentaires et opinions constructives à l'heure de la soutenance.

D'une manière générale, je tiens à remercier tous les collaborateurs de l'ILM à Lyon en commençant par Matthias Hillenkamp qui était comme mon deuxième directeur de thèse. Il a été un guide pour me permettre de finir ce travail de thèse. Il a toujours été au courant de mes manips et de l'interprétation des résultats. Cela a été un plaisir de travailler avec une personne comme Matthias, qui va jusqu'au bout en détails avec une rigueur scientifique formidable. Ensuite, je voudrais remercier Nicolas Troc qui a initié ce travail au cours de sa thèse. De plus, je remercie Jean Lermé pour son modèle théorique sans lequel ma thèse serait incomplète.

Je remercie Hans-Christian Weissker de l'Université d'Aix Marseille qui est le chef du projet ANR dans lequel cette thèse a été financée. Je le remercie de m'avoir accordé sa confiance. Les longues discussions dans les réunions m'ont aidé à avoir un esprit plus critique dans la recherche.

Je remercie nos collaborateurs Jérôme Martin et Davy Gérard de l'Université de Technologie de Troyes et Arnaud Arbouet de l'Université de Toulouse pour les discussions qui m'ont aidé à finir une partie de ce travail.

Je tiens également à remercier Eleicer Ching de l'Universidad Tecnológica de Panamá qui faisait partie du Jury et qui a fait un long voyage pour venir en France et voir ma soutenance de thèse. Il a suivi mon chemin scientifique depuis ma licence et il a été un guide important dans mes projets professionnels.

Je remercie Yueyuan, Majid, Giulio, Raphael, José et Mostafa pour m'avoir simplifié la vie à Orsay. Ces dernières années ont été formidables.

Je remercie également ma famille qui a toujours cru en moi et m'a toujours soutenu. Tout particulièrement ma mère Marina Otero et mon père Alfredo Campos, qui m'ont apporté un soutien sans faille tout au long de mes études et de ma vie. Ce travail leur est dédié. Je n'oublie pas mes deux frères, Henry et Marylin.

Enfin, je remercie de tout mon cœur Albania, qui a fait preuve d'une grande patience tout au long de mon Master et de ma thèse, et qui m'a toujours soutenu, surtout dans les moments difficiles.

Contents

Synthèse	i
Remerciements	iii
Chapter 1: Introduction	1
1.1. Characterization techniques for plasmonics	2
1.2. Statement of the problem.....	2
1.2.1. Plasmonics in the quantum regime	2
1.2.2. Plasmonics in the classical regime	4
1.3. Methodology.....	4
1.4. Outline of this thesis	5
Chapter 2: Theoretical fundamentals	7
2.1. Introduction	7
2.2. Maxwell equations.....	7
2.2.1. Constitutive relations	8
2.2.2. Helmholtz equations	9
2.3. Permittivity of a bulk metal	10
2.3.1. Drude-Sommerfeld model	10
2.3.2. Lorentz-Drude model (Interband transitions).....	12
2.4. Surface plasmons (SPs) in the classical regime.....	13
2.4.1. Surface plasmons polaritons (SPPs).....	13
2.4.2. Localized Surface Plasmons (LSPs).....	17
2.4.3. Fast electron excitation	19
2.4.4. Link between optics and EELS in a sphere	25
2.4.5. Link between optics and EELS for any geometry.....	27
2.5. Surface plasmons (SPs) in the quantum regime	29
2.5.1. Classical/quantal model of sub-10 nm particles	29
2.5.2. Jellium model	30
2.5.3. Density functional theory (DFT)	31
2.5.4. Time dependent local density approximation (TDLDA)	33
2.5.5. Link between optics and EELS in a quantum framework.....	35
2.6. Conclusion	37
Chapter 3: Instrumentation and data analysis	39
3.1. Introduction	39
3.2. Optical Absorption Spectroscopy	40
3.3. Scanning transmission electron microscope (STEM)	41
3.3.1. Elastic and inelastic electron-matter interaction.....	44

3.3.2. HAADF image.....	45
3.3.3. Electron Energy Loss Spectroscopy (EELS).....	46
3.3.4. EELS data acquisition (spectrum-image).....	49
3.3.5. Data Analysis of a spectrum-image.....	50
3.4. Sample fabrication of silver clusters	54
3.5. Conclusion	57
Chapter 4: Optimization of EELS data acquisition	59
4.1. Introduction	59
4.2. EELS-CCD camera.....	60
4.3. EEL spectrometer optimization	63
4.3.1. Aberrations	63
4.3.2. Energy dispersion and beam current	65
4.3.3. Dynamic range.....	67
4.4. Calibration of the EEL spectrum.....	68
4.5. Improving signal-to-noise ratio (combining pixels in the spectrum-image)	69
4.6. Role of the impact parameter	70
4.7. Electron dose effects.....	72
4.7.1. Afterglows	72
4.7.2. Electron dose damage.....	72
4.7.3. Contamination	74
4.8. Stack of spectrum-images.....	75
4.9. Deconvolution of weak signals.....	76
4.10. Fitting noise data and background subtraction.....	79
4.11. Conclusion.....	81
Chapter 5: Optical and EELS results in silver clusters	83
5.1. Introduction	83
5.2. Optical absorption results of silver nanoparticles.....	85
5.2.1. Optical absorption results and classical/quantal calculations.....	87
5.3. EELS results of silver nanoparticles.....	90
5.3.1. Surface signal	90
5.3.2. Electron dose study.....	91
5.3.3. STEM-EELS results and classical/quantal calculations.....	95
5.4. Comparison of EELS, Optical, and classical/quantal calculation results.....	96
5.5. Conclusion.....	98
Chapter 6: Volume plasmon.....	99
6.1. Introduction	99
6.2. Volume plasmon in sub-10 nm metal nanoparticles in literature.....	100

6.3. Volume plasmon results	101
6.3.1. Electron dose evolution	102
6.3.2. Size evolution	104
6.4. Conclusion	107
Chapter 7: Surface plasmons in triangular nanocavities	109
7.1. Introduction	109
7.2. Sample preparation and methods.....	110
7.3. STEM-EELS results of Al nanotriangles	111
7.4. Fabry-Pérot analytical models	113
7.4.1. One-dimensional cavity	113
7.4.2. 2D-triangular cavity.....	115
7.5. EELS Green Dyadic Method (GDM-Simulations)	120
7.5.1. Comparison of simulations with EELS results and analytical model	121
7.6. Dispersion relations	123
7.7. Conclusion	124
Chapter 8: Conclusions and perspectives.....	125
8.1. General conclusions.....	125
8.2. Perspectives	127
8.2.1. Chromatem preliminary result in a gold nanoparticle	127
Appendices	129
A. EELS probability of a sphere embedded in an absorbing medium.....	129
B. Estimation of the interband transition (<i>ib</i>) permittivity	133
C. Two-body Coulomb interaction in presence of a dielectric media.....	135
D. Electrostatic potential in two nested spherical interfaces	137
E. ZLP in different substrates and vacuum	139
F. Simulation of the plasmonic response of oxidized core-shell Ag/Ag _x O/SiO ₂ nanoparticles	141
G. Supplementary STEM-EELS experiments on silver clusters	143
Bibliography.....	145
Résumé:	154
Abstract:	154

Chapter 1: Introduction

The optical properties of metallic nanoparticles deviate strongly from those of macroscopic materials. In metallic nanoparticles they are dominated by the localized surface plasmons (LSPs) which correspond to collective free electrons oscillations. The LSPs properties depend on the type of metal, geometry, immediate environment (substrate, matrix and oxidation) and eventually on the size of the nanoparticles.

In nanoparticles with diameters larger than ~ 10 nm, the LSPs are very well described by purely classical models. On the other hand, clusters of a few nanometers behave essentially like quantum systems, presenting new effects such as electron spill-out, ineffective ion-core polarizability, non-local effects or even discrete molecular/atomic transitions in the very small clusters. In this quantum regime, the LSPs energy can be shifted to higher or lower energies depending on a trade-off between quantum effects. Figure 1 shows a scheme of the classical and quantum regimes of the LSPs in silver nanoparticles.

In the classical regime, the LSPs can be described by classical electrodynamics theory using the bulk classical permittivity. When the size of the particles is much smaller than the exciting wavelength (quasistatic approximation), the LSPs properties are depending on the geometry and aspect ratio rather than the nanoparticle absolute size. In nanoparticles larger than ~ 50 nm a red shift of the LSPs with the increase of size is obtained (see figure 1) which is an extrinsic size effect governed by the dimension of the nanoparticle compared to the exciting wavelength (retardation effects).

In the quantum regime (nanoparticles smaller than 10 nm), the permittivity is size-dependent and it must be treated in the frame of more complex models taking account quantum effects. In this case the quasistatic approximation is valid and therefore, for a sphere, any LSP energy shift is an intrinsic effect related to a balance between several quantum effects.

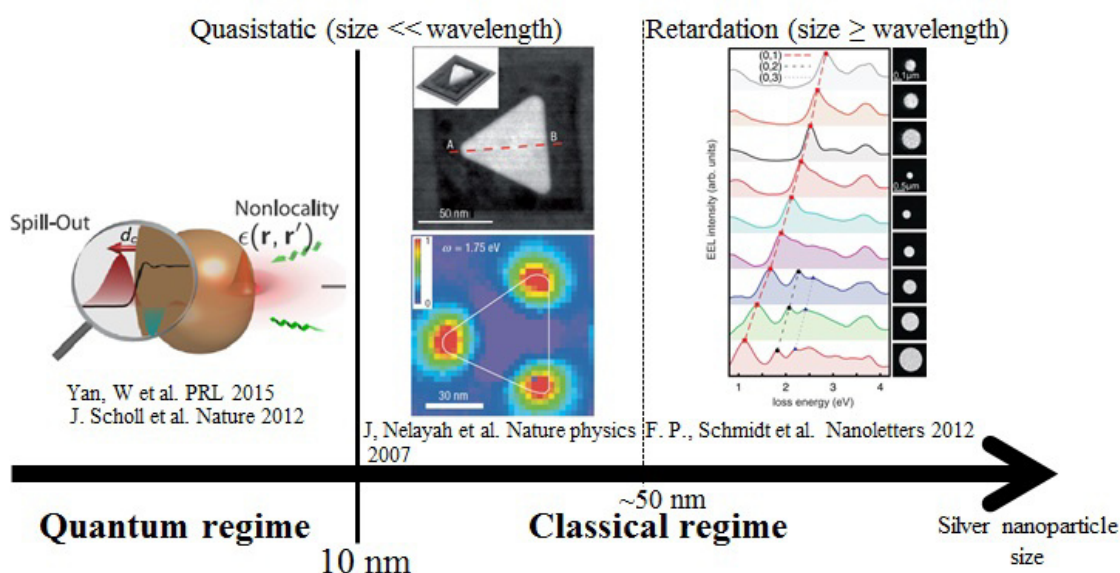


Figure 1.1: Scheme of the LSPs regimes in silver nanoparticles. In particles smaller than 10 nm, quantum effects must be considered and in particles larger than 10 nm, classical theories describe the plasmon resonances. In the classical regime for particles larger than ~ 50 nm, retardation effects must be considered.

The improvement of fabrication techniques has enabled a high control of the particle size and geometry, leading to developments of technological applications such as: solar cells [1], [2], biological sensing [3], surface-enhanced Raman scattering (SERS) [4], cancer therapy [5], catalysis [6], among others applications.

1.1. Characterization techniques for plasmonics

Optical techniques such as optical extinction spectroscopies have been used for a long time to study the LSPs on ensembles of particles. In recent years, near field techniques (such as SNOM [7], SMS [8], [9], EELS [10], Cathodoluminescence [11]) enabled to reveal spectrally and map LSPs in individual nanoparticles. Among the single nanoparticle techniques, a particularly powerful is the Electron Energy Loss Spectroscopy (EELS) in a Scanning Transmission Electron Microscope (STEM). The STEM-EELS enables to map spatial and spectral variations of LSPs with a sub-10 nm spatial resolution [10], [12]–[14] and it has been proven to be a perfect nanoscale counterpart of optical spectroscopies for nanoparticles in the classical regime [15], [16]. Due to the weak plasmon signal of sub-10 nm particles, the STEM-EELS studies have been limited only to large nanoparticles (larger than 10 nm). However, recently, with the improvement of the sensitivity of the EELS detection systems and the energy resolution, the STEM-EELS studies pushed the accessible nanoparticle size range down to <10 nm [17]–[19]. This has opened the possibility to compare STEM-EELS with optical extinction spectroscopy in very small nanoparticles in the quantum regime.

1.2. Statement of the problem

In my thesis I studied the size-dependent LSPs in silver clusters in the quantum regime and as a secondary study I focused on the classification of plasmon modes in triangular cavities in the classical regime.

1.2.1. Plasmonics in the quantum regime

As mentioned previously, the LSPs in the classical regime can be described by the optical constants of the classical bulk metal. In this case, the electronic structure of the metal is characterized by continuous band structures (see figure 1.2). When the size of a metallic particle decreases, the band structures become discrete energy levels and the plasmon response fragments into discrete transitions [20]. In the transition from the bulk to molecular states, the LSPs properties are modified by quantum effects. Which and how quantum effects modify the plasmon response has been of huge interest from a fundamental point. However, the experimental results show blue, red or absence of energy plasmon shift with decreasing particle size which does not facilitate the interpretation of the influence of the quantum effects. Not only the energy position of the LSP is modified, but also the linewidth which suffers changes by the quantum effects [21]. The discrepancy and contradiction of some results require a deeper study in the plasmon resonance in the quantum regime [22].

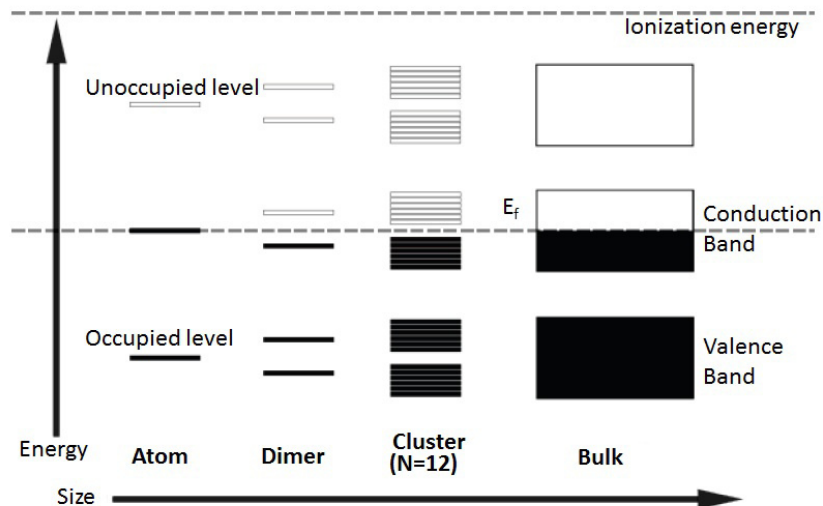


Figure 1.2: Simplified diagram showing the transition from discrete energy levels for the atom to conduction and valence bands for massive metal solids [23]. E_f denotes the Fermi energy.

The electronic structure of a silver atom ($[\text{Kr}] 4d^{10}5s^1$) shows that there is only one electron in the s orbital. With a large number of silver atoms to form a nanoparticle, the s-electrons create the conduction band and the d-electrons create the d-band. Under electromagnetic excitation the oscillation of the conduction electrons (free electrons) creates a plasmon peak. The border of the d-band is at $\sim 4\text{eV}$ below the Fermi level. Then, the threshold of the d-electron transitions towards the conduction band is at $\sim 4\text{eV}$. For a spherical silver particle in vacuum, the energy of the LSPs is $\leq 3.5\text{eV}$ (classical quasistatic regime) that is lower than the d-electron transitions threshold and, therefore, the plasmon resonances can be clearly identifiable. This is not the case of gold where there exist an overlapping of the d-electron transitions threshold and the energy of the LSPs that makes it difficult to observe plasmon resonances in very small gold nanoparticles. For this reason, silver is a good metal to do plasmonic studies in the quantum regime. However, this metal can be easily oxidized. It is therefore extremely important to protect silver clusters against oxidation by *in situ* experiments in vacuum (or in rare gas) or by a matrix protection in supported clusters (as it is the case of this thesis).

Since several decades the LSPs of metal clusters have been studied by optical absorption (extinction) technique in ensembles of particles. In this technique, an inhomogeneous line broadening is reported due to the average response of the ensemble of particles. This makes difficult to observe the quantum effects and a high control on the size distribution of particles is needed. On the other hand, the STEM-EELS technique gives precise information of the size, geometry and local environment of an individual particle during spectra acquisition and therefore some of the problems presented in optical absorption (extinction) technique are circumvented. However, the detection of plasmon signal in an individual sub-10 nm particle requires a high optimization of the EELS detection systems due to the weak signal in these particles.

In the literature on the quantum regime, the results obtained by optical absorption in the old works and STEM-EELS techniques in the recent years are controversial. Indeed, the

STEM-EELS studies in silver clusters [17]–[19] have found a large blue shift of the LSPs with decreasing size for particles deposited onto a substrate and prepared by wet chemical methods. These works presented a contradiction with older optical literature [24]–[27] which was not discussed at all. Another recent STEM-EELS work [28] was performed in silver nanoparticles prepared by a physical method and embedded in a matrix which showed, in the largest particles, a constant energy value of the plasmon resonance in agreement with optical results in embedded particles. However, in the smallest particles an abrupt and strong blue shift is observed which has never reported in optical results of embedded particles [26], [27].

From the theoretical point of view, different models exist which take into account the non-locality of the plasmonic response [18], [19]. However, most of them do not take into account fundamental aspects such as spill-out (that is a non-vanishing electron density outside the metal), the surface layer of ineffective ion-core polarizability (ineffective interband transitions from the d-band to conduction band close to the surface of the metal) or the influence of the local environment. More details of the quantum effects will be presented later in chapter 2.

This thesis is an attempt to do single-particle STEM-EELS and ensemble optical absorption characterization on samples prepared by the same conditions and to use a classical/quantal theoretical model, which takes all the relevant quantum effects, in order to explain both results and solve contradictions.

1.2.2. Plasmonics in the classical regime

In the classical regime, the plasmonic properties are well described by classical electrodynamic theory using the optical constant of the classical bulk material.

Since the last decades, the plasmon resonances in flat nanostructures have been widely studied theoretically and experimentally by near field techniques such as the STEM-EELS. From theoretical studies a direct link between optical and electron excitation has been reported [15] and different numerical calculation methods has been implemented to plasmonic studies (BEM [29], DDA [30], FDTD [31], GDM [32]). The STEM-EELS performed in these flat nanostructures revealed, spatially and spectrally, a rich variety of plasmon modes. In Ref. [33], these modes were classified as edge modes and radial breathing modes. The edge modes are located along the periphery (well known in the literature) and the radial breathing modes (RBMs) are concentrated inside the nanostructures [33]. Unlike the edge modes, the RBMs present a zero net dipole moment and due to this symmetry they cannot be excited by light in the quasistatic limit, but it is possible by electrons. The RBMs have been reported for different structures such as nanotriangles [10], [34]–[36], nanosquares [37], nanodisks [33], [38]. However, the complete description of edge modes and RBMs has only been done for the case of the nanodisks [33], [38]. Different studies have only given a partial comprehension of the mode structure in nanotriangles (Nelayah et al. [10], [36], Keast et al. [34], Hao et al. [35], Kumar et al. [39], Fung et al. [40], Das et al. [41], and Koh et al. [42]).

In this thesis we focused in the complete description of edge and RBMs in nanotriangular structures and the understanding of their nature by analytical models and classical GDM simulations.

1.3. Methodology

Silver clusters embedded in silica matrix were prepared by Nicolas Troc and Matthias Hillenkamp in the Institut Lumière Matière in Lyon, and in order to evaluate the

relevance of the STEM-EELS measurements, optical absorption measurements were performed by collaborators from the Institut Lumière Matière in Lyon (M. Hillenkamp and N. Troc) on samples prepared by the same conditions. The results were compared and interpreted in the framework of a classical/quantal theoretical model [43], [44] (developed by Jean Lermé from the Institut Lumière Matière in Lyon) taking into account all relevant classical and quantum effects of both the electronic density in the nanoparticle and its environment, as well as of the electric field excitation on a self-consistent level.

For triangular nanostructures (prepared by Jérôme Martin and Davy Gérard in the Université Technologique de Troyes, France), Fabry-Pérot analytical models and EELS-GDM simulations [32] (performed by Arnaud Arbouet from the Université de Toulouse, France) were used in order to indexing all the plasmon modes and interpret their nature. All the EELS experiments and related analysis were performed in the Laboratoire de Physique des Solides in Orsay.

1.4. Outline of this thesis

The following chapters of this manuscript contain:

Chapter 2: The theoretical fundamentals necessary to describe the plasmon resonances. Firstly, the plasmon resonances will be described in a classical approach by the excitation of light and electrons. Second, the plasmon resonances will be described by a classical/quantal approach. A direct relationship between optical and electron excitations, in classical and quantum regimes, is demonstrated.

Chapter 3: The experimental principles for plasmonic experiments by optical absorption and STEM-EELS techniques are presented. The data analysis strategies to extract plasmonic information from EELS raw data are given in details. The sample preparation of silver clusters is commented.

Chapter 4: Here the STEM-EELS optimization to detect weak plasmon signals is detailed. The spectrometer aberration, the source of noise and the effect of the electron irradiation on the samples are presented as well as the strategies to avoid or reduce all these problems.

Chapter 5: The STEM-EELS and optical absorption results of surface plasmons in silver clusters are presented together with classical/quantal calculations in order to interpret the results. An exhaustive comparison with literature is done solving contradictions.

Chapter 6: The excitation of volume plasmons is described by an electron beam excitation. STEM-EELS results in sub-10 nm silver nanoparticles are presented and discussed.

Chapter 7: In this chapter the STEM-EELS results of aluminum nanotriangles are presented and the indexing and interpretation of the plasmon modes is done by classical Fabry-Pérot analytical models and classical simulations.

Chapter 8: In this chapter the general conclusions are presented and some preliminary results obtained with a new microscope (Chromatem microscope) are shown.

Chapter 2:

Theoretical fundamentals

2.1. Introduction

Since ancient times, humanity has used metallic particles to manipulate light. In ancient Rome, the artists fabricated a cup (Lycurgus cup) using embedded gold/silver alloy particles, which under illumination present a red color on the transmitted light and a green color on the scattered light [45]. In medieval times, the cathedrals were decorated by stained glasses which incorporated particles in their compositions responsible of some of the colors [46]. However, the physical origin of these colors was not understood. In the middle of the 19th century, great progress was made when the understanding of electric and magnetic phenomena were combined by a set of equations developed by James Clerk Maxwell [47]. It was discovered that the nature of light was an electromagnetic wave. At the beginning of the 20th century, Gustav Mie published a paper [48] on the interaction of light with colloidal metal particles which explained very well the color with the particle sizes. Although Mie's results were known since the beginning of the 20th century, it was not until the advance of new fabrication and characterization techniques that the nanoscaled objects became accessible and manipulated, which has led to nanoscale light engineering with fascinating properties. Nowadays, the interaction of light with metallic nanoparticles is one of the most attractive and fascinating subjects of research from fundamental studies to applications in engineering.

In this chapter we will present the fundamental of electromagnetic theory and a classical model of the dielectric function of bulk metals. Then, the optical properties of metallic nanostructures and metal-dielectric interfaces are described considering a classical approach of the dielectric function. On the other hand, in order to describe the optical properties of very small metallic nanoparticles (smaller than 10 nm in diameter where quantum effects are expected), a classical/quantal model of the electronic properties of nanoparticles is presented.

The excitation of the nanoparticles is made by light or electrons and we proved a direct relation between both excitations in a classical and quantum regime. We use SI units throughout this chapter.

2.2. Maxwell equations

The Maxwell equations were developed at the macroscopic scale where the charges and their associated currents are considered as charge densities ρ and current densities \mathbf{j} . These quantities are considered continuous functions of space. In their differential form, the Maxwell equations are [49]

$$\nabla \times \mathbf{E}(\mathbf{r}, t) = -\frac{\partial \mathbf{B}(\mathbf{r}, t)}{\partial t} \quad (2.2.1)$$

$$\nabla \times \mathbf{H}(\mathbf{r}, t) = \frac{\partial \mathbf{D}(\mathbf{r}, t)}{\partial t} + \mathbf{j}(\mathbf{r}, t) \quad (2.2.2)$$

$$\nabla \cdot \mathbf{D}(\mathbf{r}, t) = \rho(\mathbf{r}, t) \quad (2.2.3)$$

$$\nabla \cdot \mathbf{B}(\mathbf{r}, t) = 0 \quad (2.2.4)$$

Where \mathbf{E} is the electric field, \mathbf{D} the electric displacement, \mathbf{H} the magnetic field and \mathbf{B} the magnetic induction. These macroscopic fields are the average of all the microscopic fields created at the microscopic scale.

Maxwell equations must hold on the boundaries of a material. Considering a small rectangular path along the boundary (this rectangle cross from medium 1 to medium 2), the Maxwell equations lead to [49]

$$\mathbf{n} \times (\mathbf{E}_1 - \mathbf{E}_2) = 0 \quad (2.2.5)$$

$$\mathbf{n} \times (\mathbf{H}_1 - \mathbf{H}_2) = \mathbf{K} \quad (2.2.6)$$

$$\mathbf{n} \cdot (\mathbf{D}_1 - \mathbf{D}_2) = \sigma \quad (2.2.7)$$

$$\mathbf{n} \cdot (\mathbf{B}_1 - \mathbf{B}_2) = 0 \quad (2.2.8)$$

Where \mathbf{K} is a surface current density, σ is a surface charge density and \mathbf{n} is the unit normal vector on the boundary. In a source-free material $\mathbf{K} = 0$ and $\sigma = 0$.

To describe the electromagnetic properties of a medium we have to introduce the macroscopic polarization \mathbf{P} and magnetization \mathbf{M} [49]

$$\mathbf{D}(\mathbf{r}, t) = \varepsilon_0 \mathbf{E}(\mathbf{r}, t) + \mathbf{P}(\mathbf{r}, t) \quad (2.2.9)$$

$$\mathbf{H}(\mathbf{r}, t) = \mu_0^{-1} \mathbf{B}(\mathbf{r}, t) - \mathbf{M}(\mathbf{r}, t) \quad (2.2.10)$$

Where ε_0 and μ_0 are the permittivity and the permeability in vacuum, respectively.

2.2.1. Constitutive relations

The Maxwell equations do not describe how the charge currents are generated in matter. Thus, for electromagnetic fields in a material it is necessary to introduce supplementary relations. In a linear and isotropic material, the relation between \mathbf{D} and \mathbf{E} and between \mathbf{B} and \mathbf{H} are

$$\mathbf{D}(\mathbf{r}, t) = \varepsilon_0 \int d\mathbf{r}' \int dt' \varepsilon(\mathbf{r} - \mathbf{r}', t - t') \mathbf{E}(\mathbf{r}', t') \quad (2.2.11)$$

$$\mathbf{B}(\mathbf{r}, t) = \mu_0 \int d\mathbf{r}' \int dt' \mu(\mathbf{r} - \mathbf{r}', t - t') \mathbf{H}(\mathbf{r}', t') \quad (2.2.12)$$

ε and μ being the relative permittivity and permeability in the material. In an anisotropic medium ε and μ must be replaced using tensorial forms. We note that in this thesis we only consider isotropic materials.

We can observe in equation 2.2.11 that \mathbf{D} at the instant t depends on the field \mathbf{E} at all times t' (temporal dispersion). Additionally, \mathbf{D} at a point \mathbf{r} depends on \mathbf{E} at all points \mathbf{r}' (spatial dispersion). The same is observed in the relation between \mathbf{B} and \mathbf{H} in equation 2.2.12. A dispersive material in space is called a non-local material. Non-local effects

are observed at small separations between two media or in small metallic particles of sizes comparable to the mean-free path of electrons (~ 10 nm) [17], [19], [50]–[52]. In the Fourier space the convolution in space and time of the constitutive relations 2.2.11 and 2.2.12 becomes a simple product

$$\mathbf{D}(\mathbf{k}, \omega) = \varepsilon_0 \varepsilon(\mathbf{k}, \omega) \mathbf{E}(\mathbf{k}, \omega) \quad (2.2.13)$$

$$\mathbf{B}(\mathbf{k}, \omega) = \mu_0 \mu(\mathbf{k}, \omega) \mathbf{H}(\mathbf{k}, \omega) \quad (2.2.14)$$

Additional constitutive relations are [49]

$$\mathbf{P}(\mathbf{k}, \omega) = \varepsilon_0 \chi_e(\mathbf{k}, \omega) \mathbf{E}(\mathbf{k}, \omega) \quad (2.2.15)$$

$$\mathbf{M}(\mathbf{k}, \omega) = \chi_m(\mathbf{k}, \omega) \mathbf{H}(\mathbf{k}, \omega) \quad (2.2.16)$$

Being χ_e and χ_m the electric and magnetic susceptibility.

In the case where it is possible to neglect the spatial dispersion (for example in large particles > 10 nm diameter), we can impose a so-called local response where

$$\varepsilon(\mathbf{r} - \mathbf{r}', t - t') = \delta(\mathbf{r} - \mathbf{r}') \varepsilon(t - t') \quad (2.2.17)$$

Then, the equation 2.2.11 in Fourier space becomes

$$\boxed{\mathbf{D}(\mathbf{k}, \omega) = \varepsilon_0 \varepsilon(\omega) \mathbf{E}(\mathbf{k}, \omega)} \quad (2.2.18)$$

This last equation is called the local approximation where the relative permittivity just considers frequency dependence.

2.2.2. Helmholtz equations

By combining the Maxwell equations 2.2.1 and 2.2.2, the constitutive relations and transforming to frequency space we obtain the Helmholtz equations

$$\nabla \times \nabla \times \mathbf{E}(\mathbf{r}, \omega) - k^2 \mathbf{E}(\mathbf{r}, \omega) = i\omega \mu_0 \mu(\omega) \mathbf{j}(\mathbf{r}, \omega) \quad (2.2.19)$$

$$\nabla \times \nabla \times \mathbf{H}(\mathbf{r}, \omega) - k^2 \mathbf{H}(\mathbf{r}, \omega) = \nabla \times \mathbf{j}(\mathbf{r}, \omega) \quad (2.2.20)$$

Where $k = (\omega/c) \sqrt{\mu \varepsilon} = k_0 \sqrt{\mu \varepsilon}$, being $k_0 = (\omega/c)$ and c the vacuum speed of light (3×10^8 m/s) which is related to the permittivity and permeability in vacuum by $c = 1/\sqrt{\mu_0 \varepsilon_0}$.

Considering a free-source material and the identity $\nabla \times \nabla \times = -\nabla^2 + \nabla \nabla \cdot$, the Helmholtz equations are simplified

$$\nabla^2 \mathbf{E}(\mathbf{r}, \omega) + k^2 \mathbf{E}(\mathbf{r}, \omega) = 0 \quad (2.2.21)$$

$$\nabla^2 \mathbf{H}(\mathbf{r}, \omega) + k^2 \mathbf{H}(\mathbf{r}, \omega) = 0 \quad (2.2.22)$$

2.3. Permittivity of a bulk metal

To model the optical response of nanostructures it is necessary the knowledge of the relative permittivity. In a classical regime (the case of large nanoparticles) it is possible to use the experimental bulk permittivity of the metal or the classical analytical models of the bulk permittivity of the metal as obtained by the Drude-Sommerfeld model [49] or the Lorentz-Drude model [53]. These classical models describe the optical response of free electrons inside a bulk metal in a local approximation (the \mathbf{k} dependency of the relative permittivity is not considered). On the other hand, in a quantum regime (case of very small nanoparticles), the electrons must be treated in a quantum framework taking into account quantum effects (details of a classical/quantal model taking account quantum effects will be presented in section 2.5).

In the following of this section, we will describe the classical analytical models of the bulk permittivity of a metal. These models will be used to describe the optical properties of metallic nanostructures and metal-dielectric interfaces in a classical regime in section 2.4.

2.3.1. Drude-Sommerfeld model

In the Drude-Sommerfeld model the conduction electrons are considered as delocalized and quasi-free. These electrons do not interact with each other. Let's assume a time-dependent external electric field $\mathbf{E}(t) = \mathbf{E}_0 e^{-i\omega t}$ acting on an electron of effective mass m_e and charge $-e$ (where $e = 1.6 \cdot 10^{-19}$ C is the elementary charge). This interaction induces a movement of the electron described by the Newton equation [49]

$$m_e \frac{\partial^2 \mathbf{r}}{\partial t^2} + m_e \gamma \frac{\partial \mathbf{r}}{\partial t} = -e E_0 e^{-i\omega t} \quad (2.3.1)$$

Where \mathbf{r} is the position of the electron and γ is the mean collision rate. γ is related to the mean-free path l by $\gamma = v_f/l$ where v_f is the Fermi velocity.

Assuming a solution $\mathbf{r} = \mathbf{r}_0 e^{-i\omega t}$, from 2.3.1 we obtain

$$\mathbf{r}_0 = \frac{e}{m_e \omega^2 + i\omega m_e \gamma} \mathbf{E}_0 \quad (2.3.2)$$

The displacement of the electron presents a dipolar moment given by $-e\mathbf{r}$. The collective effect of all individual dipolar moments results in a polarization of the material given by $\mathbf{P} = -n e \mathbf{r}$, where n is the electron density. We can then write

$$\mathbf{P} = \frac{-ne^2}{m_e \omega^2 + i\omega m_e \gamma} \mathbf{E} \quad (2.3.3)$$

From the constitutive relation (equation 2.2.15), the polarization can be expressed as $\mathbf{P}(\omega) = \varepsilon_0 \chi_e(\omega) \mathbf{E}(\omega)$ where χ_e is related to the relative permittivity of the material by $\chi_e(\omega) = 1 - \varepsilon(\omega)$. Comparing these relations with equation 2.3.3 we obtain the Drude permittivity ε_D

$$\varepsilon_D(\omega) = 1 - \frac{\omega_p^2}{\omega(\omega + i\Upsilon)} \quad (2.3.4)$$

Where ω_p is the bulk plasma frequency or volume plasmon frequency defined by

$$\omega_p = \sqrt{\frac{ne^2}{\varepsilon_0 m_e}} \quad (2.3.5)$$

The volume plasmon corresponds to compressional electron oscillations of the free electrons inside a metal [54]. These oscillations present longitudinal symmetry as in acoustic waves. Due to the longitudinal symmetry of the volume plasmon it is not possible to excite it by traditional optical experiments [54]. However, it is possible to excite it by an electron beam as it will be shown theoretically in section 2.4.3 and experimentally in chapter 6.

In an electron excitation experiment (EELS experiment), the electron loses energy during the interaction. The cross-section of the interaction is proportional to the loss function $\text{Im}[-1/\varepsilon]$ (see sections 2.4.3 and 3.3.3 for details). With the Drude permittivity the loss function presents a maximum at the volume plasmon frequency ($\varepsilon(\omega_p) \sim 0$). At this condition the real part of the relative permittivity has to be close to zero ($\text{Re}[\varepsilon] \sim 0$) and at the same time coinciding with a weak value of the imaginary part of the relative permittivity ($\text{Im}[\varepsilon] \sim 0$). Figure 2.1 illustrates the real and imaginary part of the Drude permittivity and the loss function for the case of silver ($\omega_p = 8.28$ eV and $\Upsilon = 0.045$ eV, values extracted from Ref. [53] for silver).

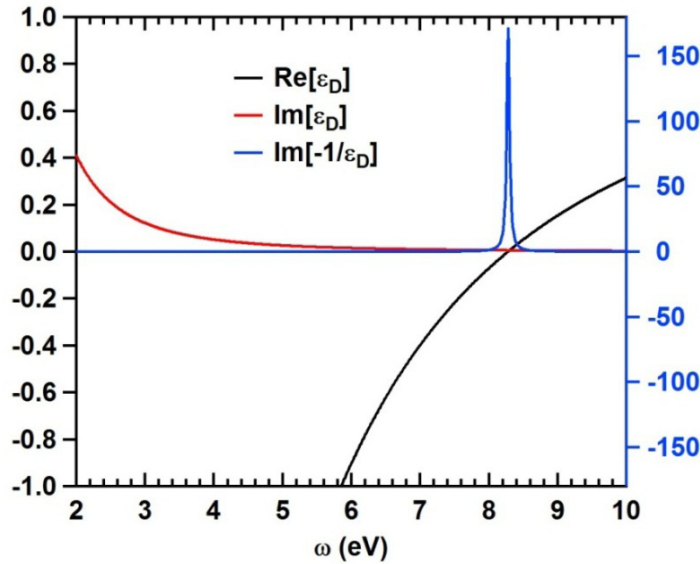


Figure 2.1: Real and imaginary part of the Drude permittivity with $\omega_p = 8.28$ eV and $\Upsilon = 0.045$ eV (values extracted from Ref. [53] for silver). The loss function $\text{Im}[-1/\varepsilon_D]$ presents a maximum value at the volume plasmon frequency. This coincides when $\text{Re}[\varepsilon_D] \sim 0$ and $\text{Im}[\varepsilon_D] \sim 0$.

2.3.2. Lorentz-Drude model (Interband transitions)

In noble metals there exist interband transitions (*ib*) from the d-valence electron band to the conduction band. Taking into account the *ib*, the relative permittivity is then written as

$$\varepsilon(\omega) = \varepsilon_{ib} + \varepsilon_D(\omega) - 1 = \varepsilon_{ib} - \frac{\omega_p^2}{\omega(\omega + iY)} \quad (2.3.6)$$

Where ε_{ib} takes into account the interband transitions. In a Lorentz-Drude oscillator model (LD model) [53], the interband transitions are modeled as oscillators described by a simple semi-quantal model

$$\varepsilon_{ib}(\omega) = 1 + \sum_{j=1}^s \frac{f_j \omega_p^2}{(\omega_j^2 - \omega^2) + iY_j} \quad (2.3.7)$$

Where s is the number of oscillators with frequency ω_j , strength f_j , and collision rate Y_j . The value parameters can be obtained by fitting the model to experimental data. In Ref. [53] the parameters values are tabulated for several metals.

In figure 2.2 the loss function ($\text{Im}[-1/\varepsilon]$) is plotted using the relative permittivity of equation 2.3.6 in the case of silver. The maximum of the loss function is now at ~ 3.8 eV which is red shifted with respect to the case of the loss function considering the Drude permittivity (see figure 2.1). This shift is related to the interband transitions.

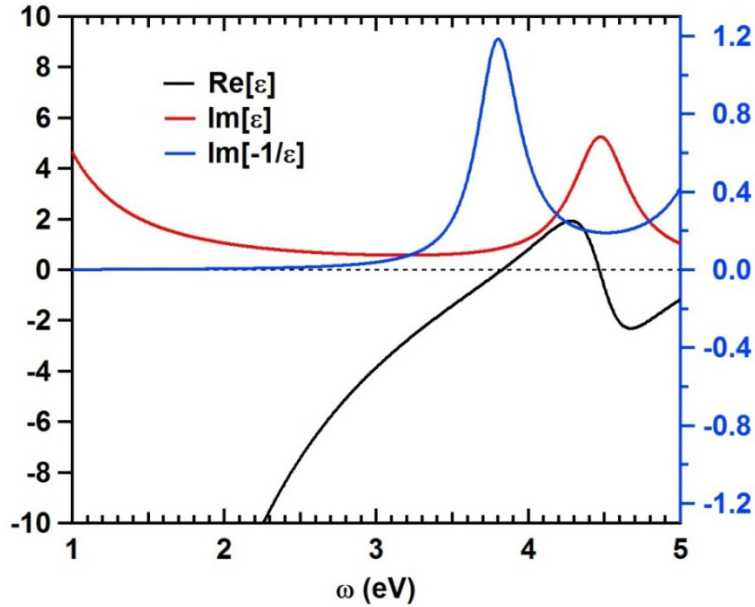


Figure 2.2: Real and imaginary part of the relative permittivity defined by equation 2.3.6 with $\omega_p = 8.28$ eV, $Y = 0.045$ eV and $\varepsilon_{ib}(\omega)$ parameters taken from Ref. [53] for silver. The loss function $\text{Im}[-1/\varepsilon]$ shows its maximum at ~ 3.8 eV, which shifts strongly with respect to the maximum of the loss function considering the Drude permittivity (maximum at 8.28 eV). This red shift is due to the interband transitions term. The maximum of the loss function coincides with $\text{Re}[\varepsilon] \sim 0$ and $\text{Im}[\varepsilon] \sim 0$. The peak of the imaginary part of the relative permittivity comes from the interband transitions.

In real systems, the real and imaginary parts of the relativity permittivity are deduced from the experimental loss function by the Kramers-Kronig analysis.

2.4. Surface plasmons (SPs) in the classical regime

The optical properties of metallic nanostructures and metal-dielectric interfaces are dominated by plasmon resonances which are collective oscillations of free electrons. Beside the volume plasmon, which is described inside the metal as compressive electron oscillations (see previous section), another kind of plasmons appears due to the surface. These are the surface plasmons (SPs) that correspond to electron oscillations creating an accumulation of charges on the surface. In the case of metal-dielectric interfaces, the surface plasmons are described by propagating electron oscillations along the interface which are called surface plasmon polaritons (SPPs) [55]. In the case of metallic nanostructures, smaller than the wavelength of excitation, the electrons oscillations are non-propagating but rather confined by the closed surface of the nanostructures and therefore they are called localized surface plasmons (LSPs) [55].

2.4.1. Surface plasmons polaritons (SPPs)

Here, we will present the SPPs in a planar metal-dielectric interface, a thin film and a multilayer system. Additionally, their dispersion relations (Energy vs wavenumber) are presented. The SPPs will be used later in chapter 7 to interpret experimental results in aluminum nanotriangles.

Considering an incident wave on a metal-dielectric interface projected in the plane x-z, as presented in figure 2.3a, the linearity of the free-source Helmholtz equations allows to divide the situation in two parts [56]: For the electric field perpendicular to the plane (s-polarised wave) and for a magnetic field perpendicular to the plane (p-polarised wave). The s-polarised wave gives the conditions $(H_x, H_z, E_y \neq 0)$ and $(H_y, E_x, E_z = 0)$. The p-polarised wave gives the conditions $(H_x, H_z, E_y = 0)$ and $(H_y, E_x, E_z \neq 0)$.

We can write the electric and magnetic fields as [56]

$$\mathbf{E}(\mathbf{r}) = \mathbf{E}(x, z) = \mathbf{E}(z)e^{ik_x x} \quad (2.4.1)$$

$$\mathbf{H}(\mathbf{r}) = \mathbf{H}(x, z) = \mathbf{H}(z)e^{ik_x x} \quad (2.4.2)$$

Being k_x the propagation constant (wavenumber) in the x direction.

With these electric and magnetic fields, the source-free Helmholtz equations can be simplified to

$$\frac{\partial^2 \mathbf{E}(z)}{\partial z^2} - \gamma_z^2 \mathbf{E}(z) = 0 \quad (2.4.3)$$

$$\frac{\partial^2 \mathbf{H}(z)}{\partial z^2} - \gamma_z^2 \mathbf{H}(z) = 0 \quad (2.4.4)$$

Where

$$\gamma_z^2 = k_x^2 - \epsilon k_0^2 \quad (2.4.5)$$

In the following of this section and in order to illustrate the dispersion relation of different systems we will consider aluminum as metal ($\omega_p = 15 \text{ eV}$), which approximates to the Drude permittivity without losses ($\gamma = 0$), $\epsilon_D(\omega) = 1 - (\omega_p/\omega)^2$. It is possible to prove that the s-polarised waves only exist if the magnetic permeability of the metal (or dielectric) is negative (see Ref. [56]). This is only possible in metamaterials which are not taken into account in this thesis work. In the following of this section we just consider the p-polarised waves.

Planar Interface between two half-spaces

In the interface between two medias (see figure 2.3a) we propose a solution of equation 2.4.4 as

$$\mathbf{H}(z) = \begin{cases} H_1 e^{-\gamma_1 z} \hat{y} & z > 0 \\ H_2 e^{\gamma_2 z} \hat{y} & z < 0 \end{cases} \quad (2.4.6)$$

γ_1 and γ_2 being positives due to the evanescence of the waves.

The continuity of the perpendicular field \mathbf{D} and the continuity of the parallel electric field \mathbf{E} lead to

$$\frac{\gamma_1}{\epsilon_1} = -\frac{\gamma_2}{\epsilon_2} \quad (2.4.7)$$

As γ_1 and γ_2 are positives, the only way to satisfy this condition is that one of the materials has a negative relative permittivity, which is the case of metallic materials. Then, the p-polarised waves exist in metal-dielectric interfaces. These waves are the surface plasmon polaritons (SPPs).

Using the equations 2.4.5 and 2.4.7 we obtain the dispersion relation

$$\boxed{k_x^2 = k_0^2 \frac{\epsilon_1 \epsilon_2}{\epsilon_1 + \epsilon_2}} \quad (2.4.8)$$

To illustrate the dispersion relation, a half-space aluminum and a half-space vacuum as dielectric ($\epsilon_2 = 1$) are considered. The dispersion relation is plotted in figure 2.3b. Two branches are observed in this figure: The high energy branch, known as Brewster mode, corresponds to radiative modes and not to an evanescent wave. The low energy branch corresponds to the SPPs.

The dispersion relation of the SPPs follows the dispersion relation of light at low wavenumbers while at high wavenumbers ($k_x \rightarrow \infty$) the dispersion relation presents an asymptotic limit. The asymptotic value is achieved at the condition $\epsilon_1 + \epsilon_2 = 0$. The corresponding frequency, in the Drude-Sommerfeld model, is therefore $\omega_{SP} = \omega_p / \sqrt{1 + \epsilon_2}$. This asymptotic limit is known as the surface plasmon (SP) in a metal-dielectric interface in the quasistatic limit. In a quasistatic limit all points of an object respond simultaneously to an excitation field. This means that retardation is neglected.

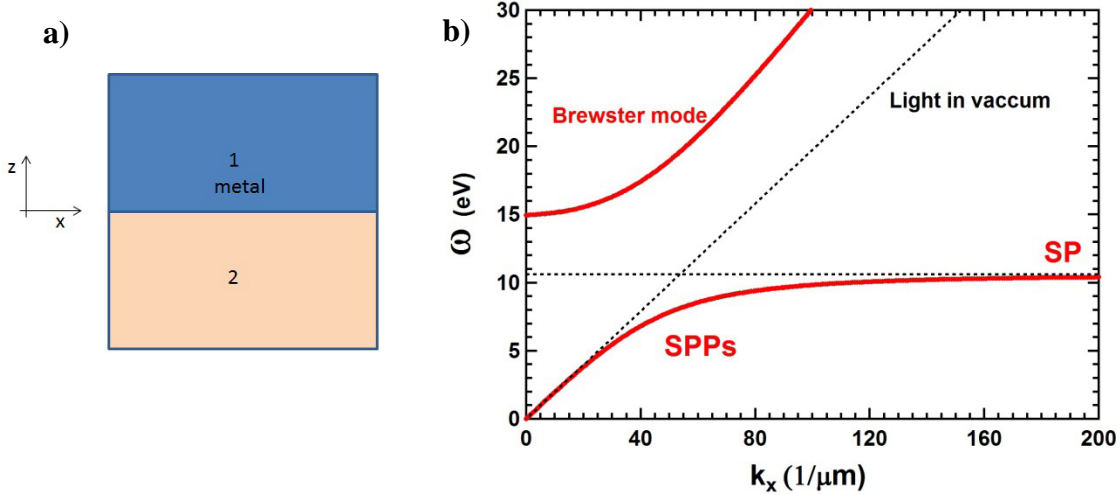


Figure 2.3: (a) Scheme of a metal-dielectric interface. (b) Dispersion relation of the SPPs in an aluminum-vacuum interface. The high energy branch corresponds to the Brewster mode, which does not correspond to an evanescent wave. The low energetic branch corresponds to the SPPs and it presents an asymptotic limit at high wavenumbers ($k_x \rightarrow \infty$), which is the surface plasmon (SP) in a quasistatic limit. At low wavenumbers the SPPs approach the light dispersion in vacuum.

Thin film

A metallic thin film (medium 2) between two half-space media (1 and 3) is shown in figure 2.4a. This configuration is known as IMI (Insulator-Metal-Insulator). For this system we propose the following solution of the Helmholtz equation 2.4.4

$$\mathbf{H}(z) = \begin{cases} H_1 e^{-\gamma_1 z} \hat{y} & z > \frac{a}{2} \\ H_2^- e^{-\gamma_2 z} \hat{y} + H_2^+ e^{\gamma_2 z} \hat{y} & \frac{a}{2} > z > -\frac{a}{2} \\ H_3 e^{\gamma_3 z} \hat{y} & -\frac{a}{2} > z \end{cases} \quad (2.4.9)$$

In thin films, the electromagnetic fields can couple between both interfaces. The coupling creates a symmetric and an antisymmetric charge distribution. The antisymmetric mode is known as Long Range Surface Plasmon Polaritons (LRSPPs) and the symmetric mode is known as Short Range Surface Plasmon Polaritons (SRSPPs).

Applying the boundary conditions and introducing the notation $B_i = \gamma_i / \epsilon_i$ we obtain

$$\begin{pmatrix} e^{\gamma_2 a} (B_1 + B_2) & B_1 - B_2 \\ B_3 - B_2 & e^{\gamma_2 a} (B_2 + B_3) \end{pmatrix} \begin{pmatrix} H_2^+ \\ H_2^- \end{pmatrix} = \begin{pmatrix} 0 \\ 0 \end{pmatrix} \quad (2.4.10)$$

The solution of this equation gives the dispersion relation and it is obtained when the determinant of the matrix is zero. The solution is then

$$\boxed{e^{2\gamma_2 a} = \frac{B_1 - B_2}{B_1 + B_2} \frac{B_3 - B_2}{B_3 + B_2}} \quad (2.4.11)$$

The thin film system has two solutions corresponding to the antisymmetric (LRSPPs) and the symmetric (SRSPPs) mode (see figure 2.4b). We note that both solutions converge (at $k_x \rightarrow \infty$) to the surface plasmon (SP) of a metal-dielectric interface.

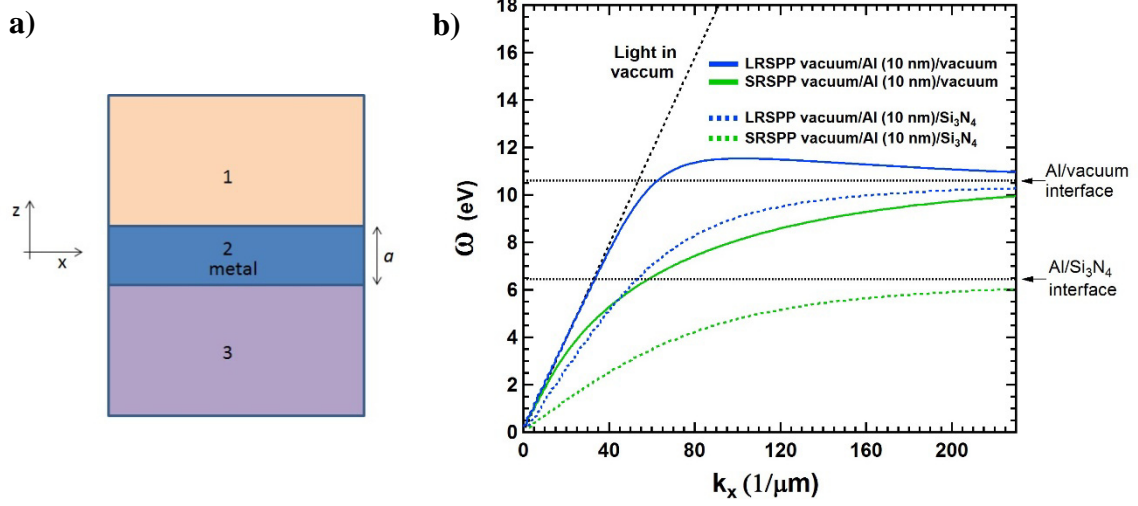


Figure 2.4: (a) Scheme of a thin metal film (medium 2) which is between two dielectric half-space media (medium 1 and 3). (b) Dispersion relation of LRSPPs and SRSPPs for an aluminum thin film of 10 nm thickness with vacuum in both sides. We also present the dispersion relation of LRSPPs and SRSPPs for the same thin film with vacuum in one side and silicon nitride ($\epsilon=4.41$) in the other side.

Multilayer system

A multilayer system will be used later in chapter 7 in order to describe the dispersion relation in an aluminum thin film supported on a thin substrate.

In this configuration we consider a metallic thin film (medium m) which is between a half-space dielectric (medium 4) and a dielectric thin film (medium 2). The other interface of medium 2 is in contact with a half-space dielectric (medium 1). The configuration is illustrated in figure 2.5 which is known as IIMI (insulator-insulator-metal-insulator).

The proposed solution of the Helmholtz equation 2.4.4 is

$$H_y = e^{ik_x x} \begin{cases} A_1 e^{-\gamma_1 z} & a + b < z \\ A_2^- e^{-\gamma_2 z} + A_2^+ e^{\gamma_2 z} & a < z < a + b \\ A_m^- e^{-\gamma_m z} + A_m^+ e^{\gamma_m z} & 0 < z < a \\ A_4 e^{\gamma_4 z} & z < 0 \end{cases} \quad (2.4.12)$$

Applying the boundary conditions and using the notation $B_i = \gamma_i / \epsilon_i$ we obtain the equation

$$C \begin{pmatrix} A_2^- \\ A_2^+ \\ A_m^- \\ A_m^+ \end{pmatrix} = \begin{pmatrix} 0 \\ 0 \\ 0 \\ 0 \end{pmatrix} \quad (2.4.13)$$

Where C is

$$C = \begin{pmatrix} B_1 e^{-\gamma_2(a+b)} - B_2 e^{-\gamma_2(a+b)} & B_1 e^{\gamma_2(a+b)} + B_2 e^{\gamma_2(a+b)} & 0 & 0 \\ 0 & 0 & B_4 + B_m & B_4 - B_m \\ e^{-\gamma_2 a} & e^{\gamma_2 a} & -e^{-\gamma_m a} & -e^{\gamma_m a} \\ B_2 e^{-\gamma_2 a} & -B_2 e^{\gamma_2 a} & -B_m e^{-\gamma_m a} & B_m e^{\gamma_m a} \end{pmatrix} \quad (2.4.14)$$

Then the dispersion relation is obtained when the determinant of C is zero ($|C| = 0$). Figure 2.5b displays the dispersion of LRSPPs and SRSPPs for an IIMI system. We note that both solutions converge (at $k_x \rightarrow \infty$) to the surface plasmon (SP) of a metal-dielectric interface.

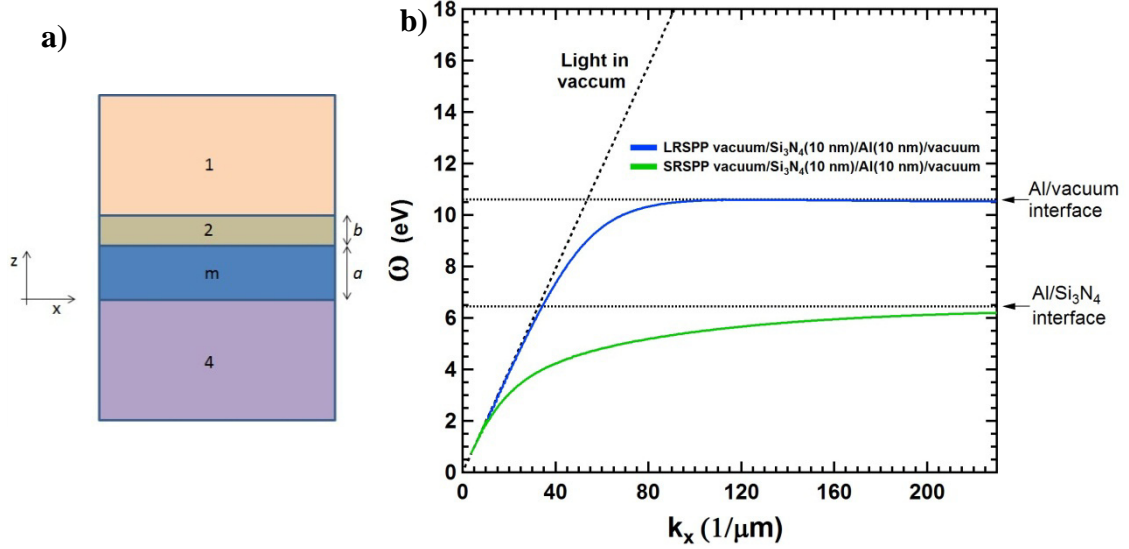


Figure 2.5: (a) Scheme of an IIMI (Insulator-Insulator-Metal-Insulator). A metallic thin film (medium m) is between a half-space dielectric (medium 4) and a dielectric thin film (medium 2). The other interface of medium 2 is in contact with a half-space dielectric (medium 1). (b) LRSPPs and SRSPs in an IIMI configuration considering an aluminum thin film (10 nm), a silicon nitride ($\epsilon=4.41$) thin film (10 nm) and medium 1 and 4 as vacuum.

2.4.2. Localized Surface Plasmons (LSPs)

In a nanostructure smaller than the wavelength of an exciting field, the interaction of light with the nanostructure is characterized by non-propagating waves [55] which are the localized surface plasmons (LSPs). In the quasistatic classical regime, i.e the regime where retardation is not relevant, the optical properties of the nanostructure do not depend on its size, but on its relative dimension.

LSPs in a sphere in a quasistatic classical regime

To find the response of a metallic spherical particle to an electromagnetic field, we consider a metallic sphere of radius R filled by a relative permittivity $\epsilon(\omega)$ embedded in a non-absorbing medium of relative permittivity $\epsilon_m(\omega)$. An external field $\mathbf{E}_{op} = \mathbf{E}_0 e^{i(\mathbf{k}\cdot\mathbf{r} - \omega t)}$ excites the particle and polarizes it. We assume a particle diameter very small compared to the wavelength (λ) of the field ($2R \ll \lambda$). This is the quasistatic approximation [57]. Due to this approximation we can neglect the spatial variation of the field (see figure 2.6).

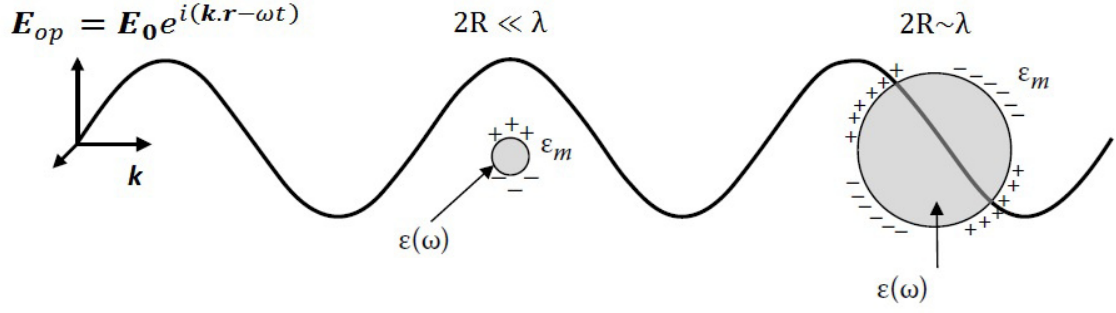


Figure 2.6: Metallic sphere exposed to an electromagnetic wave. If the particle diameter is smaller than the wavelength of the wave it is possible to neglect the spatial variation of the wave. This is the quasistatic approximation [57]. Under this condition a dipolar distribution of charge is created. However, if the particle diameter is comparable to the wavelength of the wave, a complex distribution of charge is created.

Neglecting the spatial variation of the exciting wave, we can assume an external linearly-polarized field $\mathbf{E}_{op}(t)$ as

$$\mathbf{E}_{op}(t) = \frac{1}{2\pi} \int_{-\infty}^{\infty} d\omega (E^z(\omega)\hat{\mathbf{z}} + E^x(\omega)\hat{\mathbf{x}}) e^{-i\omega t} \quad (2.4.15)$$

The potential associated to this field in frequency space and spherical coordinate is

$$V_{op}(\mathbf{r}, \omega) = \sum_{M=0}^1 A_{L=1,M}^{op}(\omega) r P_{L=1,M}(\cos(\theta)) \cos(M\varphi) \quad (2.4.16)$$

With $A_{L=1,0}^{op}(\omega) = -E^z(\omega)$, $A_{L=1,1}^{op}(\omega) = -E^x(\omega)$ and where $P_{L,M}$ are the associated Legendre polynomials. The induced potential inside and outside the particle is obtained by solving the Laplace equation $\nabla^2 V_{ind} = 0$ with the boundary conditions at the interfaces and the continuity of the total potential and the normal component of the displacement electric field. Outside the particle, the induced potential is

$$V_{ind,out}(\mathbf{r}, \omega) = - \sum_{M=0}^1 R^3 \frac{\epsilon - \epsilon_m}{\epsilon + 2\epsilon_m} \frac{A_{L=1,M}^{op}(\omega)}{r^2} P_{L=1,M}(\cos(\theta)) \cos(M\varphi) \quad (2.4.17)$$

Writing $V_{op}(\mathbf{r}, \omega)$ and $V_{ind,out}(\mathbf{r}, \omega)$ in the form

$$V_i(\mathbf{r}, \omega) = \sum_{M=0}^1 r P_{L=1,M}(\cos(\theta)) \cos(M\varphi) v_{i,L=1,M} \quad (2.4.18)$$

with $i = op$ or ind, out one can define the optical dipolar polarizability by the ratio of the induced potential with the exciting potential at $r = R$

$$\alpha(\omega) = -4\pi\epsilon_0\epsilon_m R^3 \left. \frac{v_{ind,out,L=1,M}}{v_{op,L=1,M}} \right|_{r=R} \quad (2.4.19)$$

Therefore

$$\alpha(\omega) = 4\pi\epsilon_0\epsilon_m R^3 \frac{\epsilon - \epsilon_m}{\epsilon + 2\epsilon_m} \quad (2.4.20)$$

A nanoobject under electromagnetic illumination can absorb and scatter radiation. The sum of the absorption σ_{abs} and scattering σ_{scatt} cross-sections is known as the extinction cross-section $\sigma_{ext} = \sigma_{abs} + \sigma_{scatt}$. In small nanoparticles, with diameters below 20-40 nm, the scattering cross-section is negligible [57] and the extinction cross-section is identical to the absorption cross-section $\sigma_{ext} = \sigma_{abs}$.

The absorption cross-section is the ratio between the power dissipated by a dipole and the intensity of the electromagnetic exciting wave. The power dissipated is determined by $P_{abs} = (\omega/2)\text{Im}[\mathbf{p} \cdot \mathbf{E}_{op}^*]$, where $\mathbf{p} = \alpha\mathbf{E}_{op}$. The intensity of the exciting wave is $I_0 = (1/2)c\epsilon_0\sqrt{\epsilon_m}E_0^2$. Then the absorption cross-section (identical to the extinction cross-section) is

$$\sigma_{ext} = \sigma_{abs} = \frac{\omega}{c\epsilon_0\sqrt{\epsilon_m}} \text{Im}[\alpha(\omega)] \quad (2.4.21)$$

The imaginary part of the relative permittivity of silver is relatively small in the UV-visible. Then the function $\text{Im}[\alpha(\omega)]$ is enhanced when $\text{Re}[\epsilon] + 2\epsilon_m = 0$. At this condition a dipolar LSP is excited.

2.4.3. Fast electron excitation

The advance of STEM-EELS technique in the recent years has achieved electron beam probes of the order of $\leq 1\text{\AA}$. Such electron probe diameters enable to explore matter spectrally at the atomic resolution. In this part we will describe the volume plasmon in a bulk material and the LSPs in a sphere by an electron beam excitation.

Retarded and non-retarded approximations

As noted in Ref. [58], the validity of a retarded or non-retarded approximations in EELS relies on several aspects. If one considers the particle itself, the finiteness of the speed of light c is important when the propagation time of an electromagnetic wave through the characteristic wavelength (d) of the electron cloud oscillation is comparable to its period of oscillation. This condition is obtained when $\omega(d/c) > 1$. In a sphere of radius R , the characteristic wavelength is $d \sim R/L$, where L is the mode order. Therefore, the retardation becomes significant when $\omega(R/c) > L$. The silver clusters diameters studied by EELS in this thesis are between 9 to 1.7 nm and their LSP energies between ~ 2.7 to ~ 3.6 eV, respectively. Therefore, $\omega R/c$ is ≤ 0.06153 , which is less than 6.5 % of $L = 1$ (dipolar mode) and even smaller for $L = 2, L = 3, L = 4$. This result allows neglecting retardation effects due to the small size of the clusters. On the other hand, in the aluminum nanotriangles studied in this work (from 125 to 700 nm side length and 40 nm thick), the retardation effect has to be considered due to the large size of nanoparticles. In this last case a red shift of LSPs with the increase of size is presented

due to retardation.

Another retardation effect concerns the Lorentz contraction. It can be neglected if $\gamma = 1/\sqrt{1 - (v/c)^2} \sim 1$ [58]. In EELS experiments with silver clusters and aluminum nanotriangles, the incoming electrons were accelerated at 60 kV ($\sim 0.45 c$) and 100 kV ($\sim 0.5 c$), respectively. Therefore $\gamma = 1.12$ and $\gamma = 1.15$, respectively. While small, the effect is not completely negligible. However the Lorentz contraction factor intervenes only in the electron probe position dependent function [59]. Otherwise speaking, it renormalizes the electron impact parameter (distance between the electron and the center of the nanoparticle in the plane of the nanoparticle), here by $\sim 12\%$ and $\sim 15\%$, therefore changing the absolute intensity of the simulated EEL spectra. As in the present work we do not consider the absolute intensity of the spectra, this effect is irrelevant for our discussion.

Electron energy loss inside a material

As mentioned in section 2.3, the volume plasmon can be excited by a moving electron inside the material. To study the electron energy loss inside a material, we assume an electron that propagates with a constant velocity \mathbf{v} in the z axis ($\mathbf{v} = v \hat{\mathbf{z}}$). The length of the material is noted L (this is the length along the direction of the electron propagation). Additionally, we consider a non-retarded approximation.

Using the Poisson equation, we can calculate the potential inside the material in presence of the electron. The electric field associated to this potential is

$$\mathbf{E}(\mathbf{r}, t) = \frac{ie}{(2\pi)^3} \int_{-\infty}^{\infty} d\mathbf{k} \int_{-\infty}^{\infty} d\omega \frac{\mathbf{k} \delta(\omega - \mathbf{k} \cdot \mathbf{v}) e^{-i(\omega t - \mathbf{k} \cdot \mathbf{r})}}{k^2 \varepsilon_0 \varepsilon(\mathbf{k}, \omega)} \quad (2.4.22)$$

The electron loses energy as it passes through the material due to the electric field inside the material acting back on it. The electron energy loss expressed in terms of external electron density and the electric field is

$$\Delta E = - \int_{-\infty}^{\infty} dt \int_{-\infty}^{\infty} d\mathbf{r} \rho^{ext}(\mathbf{r}, t) \mathbf{v} \cdot \mathbf{E}(\mathbf{r}, t) \quad (2.4.23)$$

The external electron density associated to the movement of the electron can be written as

$$\rho^{ext}(\mathbf{r}, t) = -e \delta(\mathbf{r} - \mathbf{v}t) \quad (2.4.24)$$

Introducing the expressions of the electric field inside the material (equation 2.4.22) and the electron density (2.4.24) in the equation 2.4.23 we obtain

$$\Delta E = \frac{e^2}{2\pi^2 \varepsilon_0 v} \int_{-\infty}^{\infty} dt \int_{\omega/v}^{\infty} \frac{dq}{q} \int_0^{\infty} \omega d\omega \text{Im} \left[-\frac{1}{\varepsilon(\mathbf{q}, \omega)} \right] \quad (2.4.25)$$

The term $\text{Im}[-1/\varepsilon(\mathbf{q}, \omega)]$ is known as the loss function where \mathbf{q} is the transferred momentum by the electron. With transferred momentums below a cutoff value (q_c), the \mathbf{q} -dependence of the relative permittivity is neglected (local approximation) and the loss function becomes $\text{Im}[-1/\varepsilon(\omega)]$. The cutoff value of the transferred momentum in a STEM-EELS experiment is determined by an EELS aperture collection angle at the

entrance of the EEL spectrometer (more details in chapter 3).

The electron energy loss is related to the electron energy loss probability per unit of frequency $\Gamma(\omega)$ by [15]

$$\Delta E = \int_0^{\infty} \hbar\omega d\omega \Gamma(\omega) \quad (2.4.26)$$

Comparing equation 2.4.25 and 2.4.26 and using $dz = v dt$ we get

$$\Gamma(\omega) = \frac{e^2 L}{2\pi^2 \varepsilon_0 \hbar v^2} \ln\left(\frac{q_c v}{\omega}\right) \text{Im}\left[-\frac{1}{\varepsilon(\omega)}\right] \quad (2.4.27)$$

In the Drude-Sommerfeld model, the loss function has a maximum at the volume plasmon frequency ω_p . However, in practice due to interband transitions, the volume plasmon measured by EELS can appear shifted (~ 3.8 eV for silver as presented in figure 2.2).

In nanoparticles, two effects appear due to the boundaries. The first one is the emergence of LSPs and the second one is the Begrenzung effect [60]. This last effect has the same functional form as that of the loss function but with opposite sign and a position-dependent pre-factor which increases close to the boundaries. In very small particles the Begrenzung effect can screen the volume plasmon signal.

The Begrenzung effect is not restricted to plasmons, but affects the measurement of all kinds of excitations present in the bulk [60].

In the case of a retarded approximation, the equation 2.4.27 is modified and includes the Cherenkov radiation. This radiation is emitted when the electron pass through a material with a speed higher than the phase velocity of light in the medium [61]. In the EELS experiments of this thesis there is no evidence of this radiation.

Electron energy loss near a sphere

Here, we describe the excitations of LSPs by a moving electron. An electron passing near a sphere can induce an electric field which reacts back on the electron. We consider a non-retarded approximation. This part compiles results from Refs. [15], [58], [59], [62], [63]. We define a sphere of radius R embedded in a non-absorbing medium and a point electron moving at a constant velocity $\mathbf{v} = v \hat{\mathbf{z}}$ along the trajectory $\mathbf{r}_e(t) = (x_0, 0, z(t))$, where x_0 is the electron impact parameter and $z = vt$. In order to facilitate calculations, we will work in a spherical system with the center placed in the center of the sphere (see figure 2.7).

The coordinates of the electron will be expressed in the referential of the sphere. In this spherical system $r_e = (x_0^2 + z^2)^{1/2}$ and $\cos(\theta_e) = z/r_e = vt/r_e$. The potential of the electron at a position \mathbf{r} where $r_e > r$ is [62], [63]

$$V_e(\mathbf{r}, t) = -\frac{e}{4\pi\varepsilon_0\varepsilon_m|\mathbf{r} - \mathbf{r}_e|} \quad (2.4.28)$$

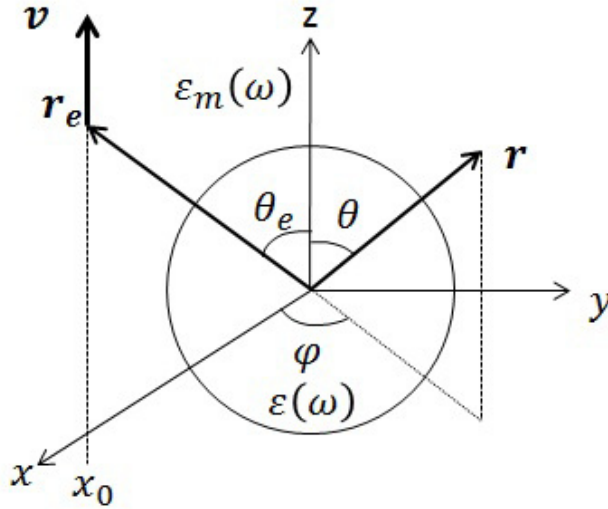


Figure 2.7: Schematics of a sphere embedded in a medium and excited by a fast electron.

Expressing equation 2.4.28 in a multipole expansion and applying a Fourier transform

$$V_e(\mathbf{r}, \omega) = \sum_{L=0}^{\infty} \sum_{M=0}^L A_{LM}^e r^L P_{LM}(\cos(\theta)) \cos(M\varphi) \quad (2.4.29)$$

Being $A_{LM}^e = -\frac{e}{4\pi\epsilon_0\epsilon_m} N_{LM} I_{LM}$, where N_{LM} and I_{LM} are defined as

$$N_{LM} = \frac{(2 - \delta_{0M})(L - M)!}{(L + M)!} \quad (2.4.30)$$

And

$$I_{LM}(\omega, x_0) = \int_{-\infty}^{\infty} dt r_e^{-(L+1)} P_{LM}(\cos(\theta_e)) e^{i\omega t} = \frac{2i^{L-M} |\omega/v|^L K_M(|\omega x_0/v|) (\omega/|\omega|)^{L-M}}{v^{(L-M)!}} \quad (2.4.31)$$

P_{LM} are the associated Legendre polynomials. δ_{0M} is unity if $m=0$ and is zero otherwise. K_M is the modified Bessel function of second kind.

The induced potential inside and outside the particle is obtained by solving the Laplace equation $\nabla^2 V_{ind} = 0$ with the boundary conditions at the interfaces and the continuity of the total potential and the normal component of the displacement electric field. Outside the particle the induced potential is

$$V_{ind,out}(\mathbf{r}, \omega) = -\sum_{L=1}^{\infty} \sum_{M=0}^L A_{LM}^e \frac{R^{2L+1}}{r^{L+1}} P_{LM}(\cos(\theta)) \cos(M\varphi) \frac{L(\epsilon - \epsilon_m)}{(L\epsilon + (L+1)\epsilon_m)} \quad (2.4.32)$$

The term $L = 0$ does not contribute to the induced potential. Writing $V_e(\mathbf{r}, \omega)$ and $V_{ind,out}(\mathbf{r}, \omega)$ in the form

$$V_i(\mathbf{r}, \omega) = \sum_{L=1}^{\infty} \sum_{M=0}^L r^L P_{LM}(\cos(\theta)) \cos(M\varphi) v_{i,LM} \quad (2.4.33)$$

with $i = e$ or ind, out one can define the multipolar polarizability of order (L, M) as

$$\alpha_{LM}(\omega) = -4\pi\epsilon_0\epsilon_m R^{2L+1} \left. \frac{v_{ind,out,LM}}{v_{e,LM}} \right|_{r=R} \quad (2.4.34)$$

We assume a sphere filled by a relative permittivity $\epsilon(\omega)$ and embedded in a non-absorbing medium of relative permittivity $\epsilon_m(\omega)$. Then the multipolar polarizability is

$$\alpha_{LM}(\omega) = 4\pi\epsilon_0\epsilon_m R^{2L+1} \frac{L(\epsilon - \epsilon_m)}{L\epsilon + (L+1)\epsilon_m} \quad (2.4.35)$$

We note that in the classical limit the multipolar polarizability only depends on L and we can simplify the notation to $\alpha_L(\omega)$. This equation is similar to equation 32 in Ref. [59] except for a pre-factor due to a slight difference in the definition of the polarizability.

The energy loss by a fast electron passing near a sample with constant velocity \mathbf{v} along a straight line $\mathbf{r}_e(t)$ can be related to the force exerted by the induced electric field \mathbf{E}_{ind} acting back on the electron [15]

$$\Delta E = e \int_{-\infty}^{\infty} dt \mathbf{v} \cdot \mathbf{E}_{ind}(\mathbf{r}_e(t), t) \quad (2.4.36)$$

The energy loss can be expressed in term of the electron energy loss probability per unit of frequency $\Gamma(\omega)$ by the equation 2.4.26 ($\Delta E = \int_0^{\infty} \hbar\omega d\omega \Gamma(\omega)$). Using $\mathbf{E}_{ind} = -\nabla V_{ind,out}$ we can write

$$\Gamma(\omega) = -\frac{e}{\pi\hbar\omega} \int_{-\infty}^{\infty} dt \operatorname{Re}\{\mathbf{v} \cdot \nabla V_{ind,out}(\mathbf{r}_e, \omega) e^{-i\omega t}\} \quad (2.4.37)$$

Solving the product $\mathbf{v} \cdot \nabla V_{ind,out}(\mathbf{r}, \omega)$ evaluated at $\mathbf{r} = \mathbf{r}_e$ and introducing it in equation 2.4.37 we get

$$\Gamma(\omega) = \frac{e^2}{4\pi^3 \hbar v^2 (\epsilon_0 \epsilon_m)^2} \sum_{L=1}^{\infty} \sum_{M=0}^L M_{LM} \left[K_M \left(\frac{\omega x_0}{v} \right) \right]^2 \left(\frac{\omega}{v} \right)^{2L} \operatorname{Im}[\alpha_L(\omega)] \quad (2.4.38)$$

Being K_M the modified Bessel function of second kind and $M_{LM} = (2 - \delta_{0M}) / [(L - M)! (L + M)!]$. Same expression is presented in Refs. [59], [62] but in different unit system.

Equation (2.4.38) is valid in the dielectric continuum approximation (polarizability in term of the dielectric constants of bulk material). However, provided α_L is replaced by α_{LM} and defined as per equation (2.4.34), it can be extended to any other approximation. The EELS probability of a sphere embedded in an absorbing medium is also developed

and presented in the appendix A.

If the quantum nature of incoming electrons is considered, the energy loss probability must include information about their wave nature [59]. However, in a conventional STEM-EELS experiment (see chapter 3), a large number of scattered inelastic electrons are collected and the electron wave interferences information is lost [64]. It leads to the classical equation 2.4.38. Therefore, in the case of this thesis we can neglect the quantum nature of the electron beam.

In non-conventional electron microscope experiments it has been possible to make use of the quantum nature of the electron beam, see Ref. [65].

Higher order modes: In expression 2.4.38, the term $[K_M(x)]^2$ for $x \ll 1$ (which is true in the EELS experiments of small silver clusters) diverges as (except for $M = 0$)

$$K_M^2(x) \sim [2^{M-1}(M-1)!x^{-M}]^2 \quad (2.4.39)$$

The term $M=L$ dominates all the other M terms ($M < L$) and expression 2.4.38 at $M=L$ approximates to

$$\Gamma_L(\omega) \approx \frac{Re^2}{4\pi^2\hbar v^2\varepsilon_0\varepsilon_m} \sum_{L=1}^{\infty} n_L \left(\frac{R}{x_0}\right)^{2L} \text{Im} \left[\frac{L(\varepsilon - \varepsilon_m)}{L\varepsilon + (L+1)\varepsilon_m} \right] \quad (2.4.40)$$

Where $n_L = 2^{2L+1}[(L-1)!]^2/(2L)!$

Considering a constant particle radius and x_0 variable, the LSP modes scales as $\sim 1/x_0^{2L}$. It means that at impact parameters far from the surface only the dipolar mode is efficiently excited and the electric field felt by the particle is similar to a plane wave like in optical experiments, as already discussed in the literature [66].

In the case $x_0 \rightarrow R$, the expression 2.4.40 depends only linearly in radius

$$\boxed{\Gamma_L(\omega) \approx \frac{Re^2}{4\pi^2\hbar v^2\varepsilon_0\varepsilon_m} \sum_{L=1}^{\infty} n_L \text{Im} \left[\frac{L(\varepsilon - \varepsilon_m)}{L\varepsilon + (L+1)\varepsilon_m} \right]} \quad (2.4.41)$$

This is an important result that proves the feasibility to study small nanoparticles in EELS experiments at $x_0 \rightarrow R$ without losing too much signal with the decrease of particle size. Another interesting study is the ratio of the EELS probability of higher order modes with respect to the dipolar mode.

Introducing $\alpha_L^{EELS} = L(\varepsilon - \varepsilon_m)/(L\varepsilon + (L+1)\varepsilon_m)$ in equation 2.4.41

$$\Gamma_L(\omega) \approx \frac{Re^2}{4\pi^2\hbar v^2\varepsilon_0\varepsilon_m} \sum_{L=1}^{\infty} n_L \text{Im}[\alpha_L^{EELS}] \quad (2.4.42)$$

Considering the Lorentz-Drude model of Ref. [53] for silver we obtain $\text{Im}[\alpha_{L=2}^{EELS}]/\text{Im}[\alpha_{L=1}^{EELS}] \sim 0.86$ and $\text{Im}[\alpha_{L=3}^{EELS}]/\text{Im}[\alpha_{L=1}^{EELS}] \sim 0.81$ at the resonance conditions. We also obtain $n_{L=2}/n_{L=1} = 0.33$ and $n_{L=3}/n_{L=1} = 0.17$. Therefore $\Gamma_{L=2}/\Gamma_{L=1} \approx 0.28$ and $\Gamma_{L=3}/\Gamma_{L=1} \approx 0.14$. Because the ratio $\Gamma_{L>1}/\Gamma_{L=1}$ is equal or smaller than 0.28, the dipolar mode has the more important contribution in an EEL

spectrum when $x_0 \rightarrow R$.

2.4.4. Link between optics and EELS in a sphere

From equation 2.4.35 evaluating the dipolar term $L = 1$ we obtain

$$\alpha_{L=1}(\omega) = 4\pi\epsilon_0\epsilon_m R^3 \frac{\epsilon - \epsilon_m}{\epsilon + 2\epsilon_m} = \alpha(\omega) \quad (2.4.43)$$

The dipolar EELS polarizability $\alpha_{L=1}(\omega)$ and the dipolar optical polarizability $\alpha(\omega)$ (equation 2.4.20) are therefore equal. In fact, the EELS response of a sphere is essentially dipolar when either the impact parameter is large with respect to the sphere radius and/or the particle diameter is small compared to the free space wavelength of the plasmon. From the dipolar term of equation 2.4.38 and using the expression of the extinction cross-section (equation 2.4.21) we get

$$\Gamma_{L=1}(\omega) = \frac{ce^2\omega}{4\pi^3\hbar v^4\epsilon_0\epsilon_m^{3/2}} \sigma_{ext}(\omega) \left[\left[K_0 \left(\frac{\omega x_0}{v} \right) \right]^2 + \left[K_1 \left(\frac{\omega x_0}{v} \right) \right]^2 \right] \quad (2.4.44)$$

This equation can in principle also be derived from equation 34 in Ref. [59]. If one only considers the dipolar EELS response of a spherical particle in a non-absorbing medium, it is directly proportional to the extinction cross-section (see figure 2.8). The energy dependence of EELS and optical extinction cross-section are therefore almost identical close to the resonance (except for a ω prefactor).

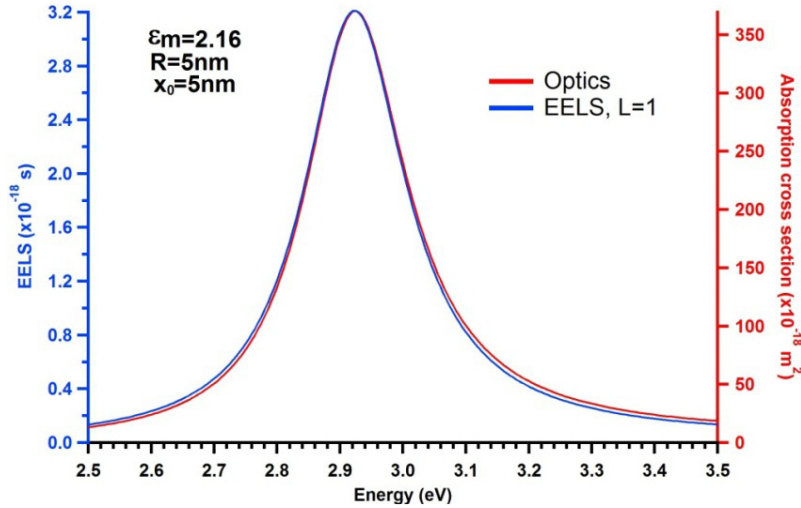


Figure 2.8: Comparison between the optical extinction cross-section from equation 2.4.21 and the EELS dipolar response (from equation 2.4.38) for $x_0=5$ nm for a 5 nm radius particle. The relative permittivity of the medium is assumed constant ($\epsilon_m = 2.16$) and the relative permittivity of silver is modeled from the Lorentz-Drude model of Ref. [53].

In practical experiments, one does not keep x_0 constant, but rather try to locate the electron probe as close as possible to the surface of the particle. At small impact parameters and low frequencies (which is the case of small silver nanoparticles

embedded in a matrix) $[K_1(\omega x_0/v)]^2 \gg [K_0(\omega x_0/v)]^2$. With this approximation we obtain

$$\Gamma_{L=1}(\omega) \approx \frac{ce^2}{4\pi^3 \hbar v^2 \varepsilon_0 \varepsilon_m^{3/2}} \frac{\sigma_{ext}(\omega)}{\omega x_0^2} \quad (2.4.45)$$

Therefore, in practical EELS experiments where we set the impact parameter very close to the surface of the particle $x_0 \rightarrow R$ we get

$$\boxed{\Gamma_{L=1}(\omega) \approx \frac{ce^2}{4\pi^3 \hbar v^2 \varepsilon_0 \varepsilon_m^{3/2}} \frac{\sigma_{ext}(\omega)}{\omega R^2}} \quad (2.4.46)$$

Because the optical extinction cross-section scales as R^3 , the EELS probability depends linearly on the radius. This result proves the feasibility to study small nanoparticles in EELS experiments without losing too much signal with respect to optical experiments.

Multilayer spherical system

In this part we will prove that the proportionality EELS-optics can be extended for any spherical systems consisting of an arbitrary number of concentric homogeneous linear media (dielectric or metallic). The radius of the last concentric sphere is noted R_{max} . This result was obtained with the collaboration of Jean Lermé from the Institut Lumière Matière at the Université de Lyon 1, France.

The dipolar component of the potential created by the incident electron in the radial region $x_0 \geq r$ (x_0 is the impact parameter) can be obtained from equation 2.4.29

$$V_e^{L=1}(\mathbf{r}, \omega) = \sum_{M=0}^1 A_{L=1,M}^e(\omega) r P_{L=1,M}(\cos(\theta)) \cos(M\varphi) \quad (2.4.47)$$

Now comparing this last equation with the equation 2.4.16 of an optical excitation [$V_{op}(\mathbf{r}, \omega) = \sum_{M=0}^1 A_{L=1,M}^{op}(\omega) r P_{L=1,M}(\cos(\theta)) \cos(M\varphi)$], we can observe that both equations have an identical form. The tight relationship between EELS and optics is clear at least for the dipolar term, since the response of any system subject to a given applied potential will not depend on the nature of the source of excitation. Each Fourier component of the induced potential, $V_{ind,in/out}(\mathbf{r}, \omega)$, inside and outside the system, will be the same in both contexts (EELS and optics), except for a mere multiplicative factor (linear response), that is, $A_{L=1,M}^e(\omega)$ (EELS) or $A_{L=1,M}^{op}(\omega)$ (optics). In particular, outside the system (in the radial region $r > R_{max}$), each Fourier component of the induced potential satisfies the homogeneous Laplace equation $\nabla^2 V_{ind}(\mathbf{r}, \omega) = 0$, whatever the complexity of the system and the theoretical approach are (note that in a classical dielectric description $\nabla^2 V_{ind}(\mathbf{r}, \omega) = 0$ holds also in the radial region $r < R_{max}$). Outside the system each Fourier component $V_{ind}(\mathbf{r}, \omega)$ expresses thus as

$$V_{ind,out}^{L=1,M}(\mathbf{r}, \omega) = -\frac{1}{4\pi \varepsilon_0 \varepsilon_m} \sum_{M=0}^1 \frac{D_{L=1,M}(\omega)}{r^2} P_{L=1,M}(\cos(\theta)) \cos(M\varphi) \quad (2.4.48)$$

With $D_{L=1,M}(\omega) = D'_{L=1,M}(\omega)A_{L=1,M}^e(\omega)$ for EELS or $D_{L=1,M}(\omega) = D'_{L=1,M}(\omega)A_{L=1,M}^{op}(\omega)$ for Optics. The coefficient $D'_{L=1,M}(\omega)$ depends only on the system, but not on the physical context. In fact $D'_{L=1,M}(\omega)$ is the polarizability of the system where the relative permittivities of all the concentric layers are considered.

Using the induced potential of equation 2.4.48 in the electron energy loss probability (equation 2.4.37) for the dipolar term we get

$$\Gamma_{L=1}(\omega) = \frac{e^2\omega^2}{4\pi^3\hbar v^4(\epsilon_0\epsilon_m)^2} \text{Im}[D'_{L=1,M}(\omega)] \left[\left[K_0 \left(\frac{\omega x_0}{v} \right) \right]^2 + \left[K_1 \left(\frac{\omega x_0}{v} \right) \right]^2 \right] \quad (2.4.49)$$

Using the induced potential of equation 2.4.48 and using the formalism of section 2.4.2 for the calculation of the optical extinction (or absorption) cross-section we obtain

$$\sigma_{ext} = \sigma_{abs} = \frac{\omega}{c\epsilon_0\sqrt{\epsilon_m}} \text{Im}[D'_{L=1,M}(\omega)] \quad (2.4.50)$$

Because equation 2.4.49 and 2.450 are proportional to $\text{Im}[D'_{L=1,M}(\omega)]$, then the proportionality of the dipolar EELS with the optical extinction cross-section (equation 2.4.44) is quite general, suitable for any spherically multilayer symmetric system, provided that $x_0 > R_{max}$.

2.4.5. Link between optics and EELS for any geometry

Considering a simple situation of a non-dispersive and non-absorbing material inserted in a cavity of arbitrary geometry (size smaller than the exciting wavelength), a set of discrete photonic eigenmodes exists and their eigenvectors $\mathbf{E}_m(\mathbf{r})$ and eigenfrequencies ω_m are solutions of the Helmholtz equation [67]

$$\nabla^2 \mathbf{E}_m(\mathbf{r}) + \epsilon(\mathbf{r}) \frac{\omega_m^2}{c^2} \mathbf{E}_m(\mathbf{r}) = 0 \quad (2.4.51)$$

In this situation we can define a density of states (DOS) which counts the number of eigenmodes per unit volume and unit frequency [67]

$$\eta(\omega) = \frac{1}{V} \sum_m \delta(\omega - \omega_m) \quad (2.4.52)$$

The DOS characterizes the total number of eigenmodes per unit volume and unit frequency of the material on the whole. This means that the DOS is a global quantity. Another DOS can be introduced as a local quantity (LDOS) which can be obtained by the weighted summation of the eigenmode amplitudes at a position \mathbf{r} [67]

$$\eta(\mathbf{r}, \omega) = \frac{1}{V} \sum_m |\mathbf{E}_m(\mathbf{r})|^2 \delta(\omega - \omega_m) \quad (2.4.53)$$

$\eta(\mathbf{r}, \omega)$ corresponds to the total number of eigenmodes per unit volume and unit frequency in a given position \mathbf{r} . This quantity is similar to the local density of states presented in solid-state physics, which provides the number of states accessible to

electrons per volume unit and energy unit at a given position.

In terms of the electric Green's tensor $\vec{\mathbf{G}}^E$, the LDOS can be written as [49]

$$\eta(\mathbf{r}, \omega) = \frac{2\omega}{\pi c^2} \text{Im}\{Tr[\vec{\mathbf{G}}^E(\mathbf{r}, \mathbf{r}, \omega)]\} \quad (2.4.54)$$

Where Tr denotes the trace of the electric Green's tensor. In a general case of an absorbing material, described by a complex frequency-dependent relative permittivity $\varepsilon(\mathbf{r}, \omega)$, the electric Green's tensor is defined as the solution of [49]

$$\nabla \times \nabla \times \vec{\mathbf{G}}^E(\mathbf{r}, \mathbf{r}', \omega) - \varepsilon(\mathbf{r}, \omega) \frac{\omega^2}{c^2} \vec{\mathbf{G}}^E(\mathbf{r}, \mathbf{r}', \omega) = \vec{\mathbf{I}} \delta(\mathbf{r} - \mathbf{r}') \quad (2.4.55)$$

$\vec{\mathbf{I}}$ being the unit dyad (unit tensor). Because the electromagnetic response of a material is contained in the electric Green's tensor, the expression 2.4.54 takes into account retardation effects.

We can define a projected local density of states $\eta_{\hat{\mathbf{n}}}$ (nLDOS) along the axis $\hat{\mathbf{n}}$ as [49]

$$\eta_{\hat{\mathbf{n}}}(\mathbf{r}, \omega) = \frac{6\omega}{\pi c^2} \text{Im}\{\hat{\mathbf{n}} \cdot \vec{\mathbf{G}}^E(\mathbf{r}, \mathbf{r}, \omega) \cdot \hat{\mathbf{n}}\} \quad (2.4.56)$$

$\eta_{\hat{\mathbf{n}}}$ has a much greater interest than η because it is related with the well-known formula for spontaneous decays of two-level quantum system in an arbitrary reference system. The nLDOS can be measured by SNOM techniques.

Due to the relevance of the nLDOS in nanooptics, it is important to prove a relation between EELS and the nLDOS. For this purpose we are going to develop the EELS probability in the Green formalism based in the work of J. García de Abajo and M. Kociak of Ref. [15].

The electron energy loss probability is [15]

$$\Gamma(\omega) = \frac{e}{\pi \hbar \omega} \int_{-\infty}^{\infty} dt \text{Re}\{\mathbf{v} \cdot \mathbf{E}_{ind}(\mathbf{r}_e, \omega) e^{-i\omega t}\} \quad (2.4.57)$$

The induced electric field in frequency space can be expressed in terms of the electric Green tensor $\vec{\mathbf{G}}^E(\mathbf{r}, \mathbf{r}', \omega)$ and by an external current density $\mathbf{j}^{ext}(\mathbf{r}', \omega)$ as [49]

$$\mathbf{E}_{ind}(\mathbf{r}_e, \omega) = i\omega\mu\mu_0 \int_{-\infty}^{\infty} d\mathbf{r}' \vec{\mathbf{G}}^E(\mathbf{r}_e, \mathbf{r}', \omega) \cdot \mathbf{j}^{ext}(\mathbf{r}', \omega) \quad (2.4.58)$$

After some calculations we find

$$\Gamma(\omega) = \frac{e^2 \mu \mu_0}{\pi \hbar} \text{Im}\{G_{zz}^E(\mathbf{R}_0, \mathbf{R}_0, q, -q, \omega)\} \quad (2.4.59)$$

Where $q = \omega/v$ and $G_{zz}^E(\mathbf{r}_e, \mathbf{r}', \omega) = \hat{\mathbf{z}} \cdot \vec{\mathbf{G}}^E(\mathbf{r}_e, \mathbf{r}', \omega) \cdot \hat{\mathbf{z}}$

The nLDOS of equation 2.4.56 and the EELS probability Γ of equation 2.4.59 are not exactly identical. Now we can introduce a projected local density of states $\tilde{\eta}_{\hat{z}}$ expressed in combination of real space in the x-y plane and in Fourier space along the z direction

$$\tilde{\eta}_{\hat{z}}(\mathbf{R}_0, q, \omega) = \frac{6\omega}{\pi c^2} \text{Im}\{G_{zz}^E(\mathbf{R}_0, \mathbf{R}_0, q, -q, \omega)\} \quad (2.4.60)$$

Using equations 2.4.60 and 2.4.59 we obtain the relation

$$\Gamma(\omega) = \frac{e^2 \mu \mu_0 c^2}{6\hbar \omega} \tilde{\eta}_{\hat{z}}(\mathbf{R}_0, q, \omega) \quad (2.4.61)$$

We note that $\tilde{\eta}_{\hat{z}}$ is a partial Fourier transform of $\eta_{\hat{z}}$. Then the EELS probability is directly proportional to the partial Fourier transform of the zLDOS.

Finally, we can conclude that the EELS probability is related to the zLDOS, in the real space of the x-y plane and in the Fourier space along the z direction. The different behavior along the z-axis can be inferred from the fact that the electrons are only affected by the z component of the electric field, parallel to its propagation [67]. This means that a special care should be taken into account to interpret the relation between both quantities. It has been proved that at the vicinity of the particles (small z values) the EELS probability and the zLDOS can differ so strongly [68].

Recently it has been experimentally demonstrated a tomographic approach for reconstructing the three-dimensional photonic local density of states in plasmonic nanoparticles in STEM-EELS experiments [16].

2.5. Surface plasmons (SPs) in the quantum regime

In this section we will present the properties of small silver nanoparticles (< 10 nm) by a classical/quantal point of view in order to describe the size-dependent optical response.

2.5.1. Classical/quantal model of sub-10 nm particles

In order to take into account the size effects in the optical response of metal clusters, it is necessary to introduce quantum mechanics. *Ab initio* calculations can be used in the case of clusters of few atoms but in larger clusters the time of calculation is too large to be feasible. For this reason fully *ab initio* methods cannot be carried out for large clusters, and nowadays *first-principles* approaches are restricted to small sizes (roughly a few tens or one hundred atoms at the maximum) and/or low-Z elements [69]–[72]. For sizes involving up to a few hundred atoms, a discrete lattice geometry, non-optimized, could be retained, but only in the framework of approximate schemes for computing the electronic structure. This can be achieved in combining linear-response theory with a tight-binding electronic description, much less time-consuming, as in the case of covalent elements [73], [74], or under simplifying assumptions for calculating the electronic structure (spherical average of the electron-background interaction or jellium-calculation for instance [75], or cylindrical average of the electron density [76]). The optical response calculated within such formalisms, which take into account the discrete ionic lattice in some approximate computational scheme, however, corresponds to a specific -often arbitrarily- ionic geometry.

A mixed classical/quantal jellium-type model involving spherical concentric nested dielectric background media has been used in this work. This model was developed by Jean Lermé [43], [44] (from the Institute Lumière Matière at the Université de Lyon 1, France) and extended to EELS formalism within this thesis work.

The calculations are based on (i) the density functional theory (DFT) for computing the ground-state and (ii) the time-dependent local-density-approximation formalism (TDLDA) for computing the optical response. As compared to pioneering formalisms, that are suitable for free alkali jellium spheres [77], the present model includes phenomenologically (but self-consistently) the absorption/screening properties of the ionic core background (effects related to the bulk interband-transitions contribution) and the screening properties of the surrounding non-absorbing matrix [43], [44]. In particular, the model describes self-consistently the mutual interplay between the optical excitations and induced fields in the various media. This model was successfully applied in previous works to alumina-embedded noble metals nanoclusters, allowing the observed size evolutions for Ag, Au and Cu to be rationalized in a common theoretical framework [27], [78], [79].

The model includes all the important contributions:

- (1) the surface layer of ineffective ion-core polarizability d (see later in section 2.5.2);
- (2) the surrounding dielectric matrix, including a possible local porosity d_m ;
- (3) the electronic spill-out, i.e. the extension of electron density beyond the particle radius in a non- infinite potential well;
- (4) all the relevant finite-size quantum effects, in particular the non-locality of the electronic response.

2.5.2. Jellium model

The geometry used in the classical/quantal model is presented in figure 2.9.

In the metallic particle, the conduction electrons corresponding to the bulk s-p band, responsible for the collective surface plasmon excitation and underlying most of the (quantum) finite-size effects, are quantum mechanically treated, whereas the ionic background is phenomenologically described by both: (i) a step-walled homogeneous spherical positively-charged distribution (*jellium*) of radius $R = r_s N^{1/3}$ (r_s is the Wigner-Seitz (WS) radius per conduction electron in the bulk ($r_s = 1.6 \text{ \AA}$ for silver) and N the number of atoms), and, (ii) a homogeneous polarizable/absorbing dielectric medium [frequency-dependent relative complex dielectric function $\varepsilon_{ib}(\omega)$ (dimensionless input data of the model), corresponding to the interband transitions, assumed to be bulk-like] extending up to $R_1 = R - d$ where d is the skin thickness of ineffective ion polarizability. Appendix B describes how $\varepsilon_{ib}(\omega)$ is estimated.

The parameter d , which is of main importance for explaining the finite-size effects in noble metal clusters, as compared to alkali elements, deserves to be commented. This skin of vanishing polarizability was introduced by Liebsch [80] in the context of electron energy loss at metal surfaces, and applied early to rare-gas matrix-embedded Ag_N -clusters within a classical approach involving concentric nested dielectric media [81]. This surface property, subsequently discussed by several authors [78], [82], [83], is thought to be related to both the spatial localization of the d-electron wavefunctions relative to the Wigner-Seitz radius [82] and the change of the effective polarizability of the ionic-cores depending on the embedding medium or local environment [83]. Strictly speaking the thickness d has to be considered as a free phenomenological parameter. In view of the approximation consisting in replacing the discrete ionic structure by

homogeneous step-walled jellium and dielectric medium, a rigorous prescription for setting its value cannot be defined. In this work the value has been set in order to reproduce the experimental finite-size effects observed in free Ag_N^+ clusters [24], [78]. The comparison of experimental data and the classical/quantal model (see section 5.2.1) led to the value of $d \approx 3.5$ bohr (1.85 \AA), on the order of the WS radius per conduction electron in bulk silver. This value was systematically used in previous works framework [27], [78], [79].

Another important parameter is the local porosity of the matrix at the interface particle/matrix. The local porosity layer, d_m , extends the radius of the system beyond the particle radius $R_2 = R + d_m$. The local porosity d_m is modeled with a vacuum layer as used in theoretical models [43], [44]. The layer of local porosity can be very small ($\sim 1 \text{ \AA}$ or even neglected) depending on the fabrication conditions. Later in chapter 5 it will be shown that in EELS experiments the electron dose can increase this local porosity layer.

The mixed classical/quantal model involves thus three nested spherical interfaces, figure 2.9, located at $r = R_1 = R - d$, $r = R$ and $r = R_2 = R + d_m$, but two background dielectric interfaces separating three homogeneous background media ($\epsilon_b(\omega) = \epsilon_{ib}(\omega)$ for $r < R_1$, $\epsilon_b(\omega) = 1$ for $R_1 < r < R_2$ and $\epsilon_b(\omega) = \epsilon_m(\omega)$ for $r > R_2$). In the following the parameters d and d_m will be given in bohr units a_0 ($a_0 = 0.529 \text{ \AA}$).

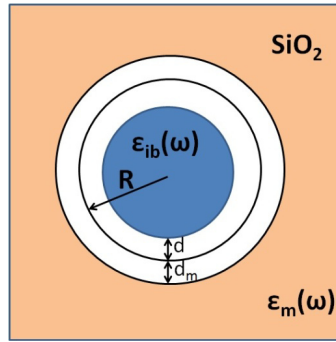


Figure 2.9: Geometrical system used in the classical/quantal model which involves a spherical particle of radius R with the skin thickness of ineffective ion polarizability d , the local porosity d_m and the matrix environment.

2.5.3. Density functional theory (DFT)

The first step in the calculation of the optical response consists in determining the ground state of the system, namely in solving iteratively the Kohn-Sham (KS) equations

$$\left\{ -\frac{\hbar^2}{2m} \nabla^2 + V_{eff}(\rho, \mathbf{r}) \right\} \varphi_i(\mathbf{r}) = \epsilon_i \varphi_i(\mathbf{r}) \quad (2.5.1)$$

The single-electron effective KS potential $V_{eff}(\rho, \mathbf{r})$ is a functional of the electron density $\rho(\mathbf{r})$. It gathers the interactions with the homogeneous charge distribution $\rho_+(\mathbf{r})$ of the jellium sphere ($\rho_+(\mathbf{r}) = e\rho_{0+}H(R - r)$) where $\rho_{0+} = 3/(4\pi r_s^3)$, $H(x)$ the Heaviside step-function and e the elementary charge) and with the conduction electron charge density $-\rho(\mathbf{r})$ (the so-called classical Coulomb term), as well as the exchange-correlation contribution $V_{xc}(\rho(\mathbf{r}))$. It writes

$$V_{eff}(\rho, \mathbf{r}) = V_{e-jel}(\mathbf{r}) + V_{e-e}(\rho, \mathbf{r}) + V_{xc}(\rho(\mathbf{r})) \quad (2.5.2)$$

with

$$V_{e-e}(\rho, \mathbf{r}) + V_{e-jel}(\mathbf{r}) = \frac{e^2}{4\pi\epsilon_0} \int V_c(\mathbf{r}, \mathbf{r}') (\rho(\mathbf{r}') - \rho_+(\mathbf{r}')) d^3r' \quad (2.5.3)$$

And

$$V_{xc}(\rho(\mathbf{r})) = \frac{\delta E_{xc}(\rho)}{\delta \rho(\mathbf{r})} \quad (2.5.4)$$

In equation 2.5.3, $(e^2/(4\pi\epsilon_0))V_c(\mathbf{r}, \mathbf{r}')$ is the effective Coulomb interaction between two free elementary charges located at \mathbf{r} and \mathbf{r}' , in the presence of the polarizable background-dielectric media. $V_c(\mathbf{r}, \mathbf{r}')$ depends on the parameter set $\{R_1, R_2, \epsilon_{ib}, \epsilon_m\}$ ($V_c(\mathbf{r}, \mathbf{r}', \omega) = 1/|\mathbf{r} - \mathbf{r}'|$ in the absence of underlying dielectric media). Different $V_c(\mathbf{r}, \mathbf{r}')$ -expressions prevail, depending on the values of r and r' relative to the dielectric interface radii R_i . The analytical formulas for one and two concentric dielectric interfaces can be found in Ref. [79] (see appendix C).

As in previous studies, in particular Ref. [43], [44], the local Gunnarsson-Lundqvist exchange-correlation energy functional $E_{xc}(\rho)$ [84] of widespread use in the cluster physics literature [77], [85], has been assumed throughout this work.

Typical results of the DFT calculations are shown in Figure 2.10. This Figure displays the normalized ground-state electron density $\rho_{gs}(r)/\rho_{0+}$ and the effective KS potential $V_{eff}(\rho_{gs}, r)$ for the parameter set [$N = 832$ ($R \approx 1.5 \text{ nm} = 28 a_0$), $d = 3.5 a_0$ and $d_m = 2 a_0$], which exhibit the diffuse surface profiles of the electron density and of the confining finite-depth potential. It is observed the extension of electron density beyond the particle radius (spill-out effect).

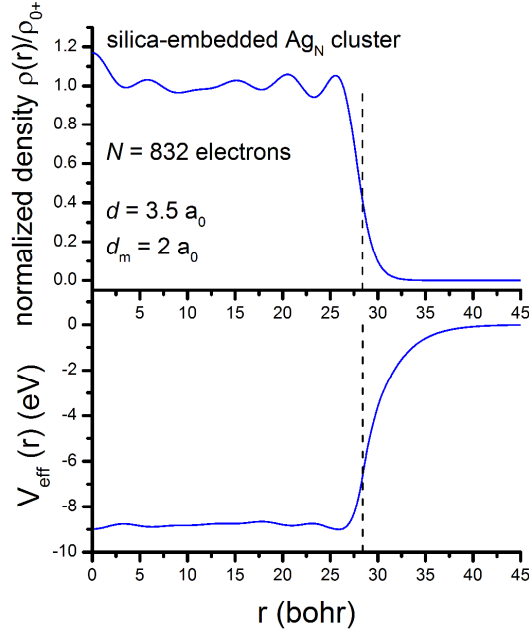


Figure 2.10: Results of ground-state calculation for silica-embedded Ag832 cluster (size $N = 832$; $R \approx 1.5 \text{ nm} = 28 \text{ bohr}$), with $d = 3.5 a_0$ and $d_m = 2 a_0$, computed within the Kohn-Sham DFT formalism. Upper panel: Self-consistent ground-state electron density normalized to the jellium density $\rho_{0+} = 3/(4\pi r_s^3)$. Lower panel: Kohn-Sham confining potential.

2.5.4. Time dependent local density approximation (TDLDA)

The second step in the optical response calculation consists in computing the optical response within the TDLDA formalism. In this step we consider an optical excitation.

In response to an applied monochromatic field of frequency ω , $\mathbf{E}_0(t) = E_0 e^{-i\omega t} \hat{\mathbf{z}}$, the “matrix-embedded particle” is polarized, giving rise to a total dipole $\mathbf{p}(t) = \alpha(\omega) \mathbf{E}_0(t)$, and -in particular- a time-varying electronic density $\delta\rho(\mathbf{r}, \omega) e^{-i\omega t}$ is induced inside the metal sphere (conduction electron density). The electron density is thus $\rho(\mathbf{r}, t) = \rho_{gs}(\mathbf{r}) + \delta\rho(\mathbf{r}, \omega) e^{-i\omega t}$. The above terminology “matrix-embedded particle” is intentionally used to keep in mind that the metal particle (the conduction electrons and the polarizable ionic cores) and the matrix underlie the induced dipolar field. To this applied external field corresponds, in the non-retarded quasistatic limit, the electron potential energy $V_{ext}^{bare}(\mathbf{r}, \omega) e^{-i\omega t}$, with $V_{ext}^{bare}(\mathbf{r}, \omega) = ezE_0$ (usually referred to as the “external, or applied, potential energy” in the standard TDLDA formalism). The absorption (identical to extinction for small nanoparticles) cross-section is related to the imaginary component of the overall complex dynamical polarizability $\alpha(\omega)$ via the equation $\sigma_{ext}(\omega) = \sigma_{abs}(\omega) = \omega/c\epsilon_0\sqrt{\epsilon_m(\omega)} \text{Im}[\alpha(\omega)]$ (equation 2.4.21).

Due to the linearity of Maxwell’s equations in the presence of dielectric media, the polarizability of the “matrix-embedded particle” is the sum of two contributions, that is $\alpha(\omega) = \alpha_c(\omega) + \alpha_e(\omega)$, corresponding respectively to the two “time-varying free charge sources” involved in the electromagnetic problem. The first one, $\alpha_c(\omega)$, is associated with the (implicit) free charge source giving rise to the applied field $\mathbf{E}_0(t)$. $\alpha_c(\omega)$, which results from the surface polarization charge densities on the dielectric interfaces, that are *directly* induced by $\mathbf{E}_0(t)$, is nothing else but the dynamical polarizability of the classical problem (quasistatic limit) in the absence of the conduction electron gas. Its expression is straightforwardly obtained in solving the Poisson equation taking into account the boundary equations at both dielectric interfaces R_i (continuity of the electrostatic potential and of the normal component of the electric displacement field) and at large distance ($\mathbf{E}(\mathbf{r}, t) \rightarrow \mathbf{E}_0(t)$ for $r \rightarrow \infty$). The (rather involved) $\alpha_c(\omega)$ -expression depends on the input model parameters $\{R_1, R_2, \epsilon_{ib}(\omega), \epsilon_m(\omega)\}$. To this classical problem corresponds the electrostatic potential $\phi_c(\mathbf{r}, \omega)$ (different expressions prevail in each nested concentric dielectric medium, see appendix D for the case of two nested spherical interfaces).

The second contribution, $\alpha_e(\omega)$, is associated with the induced time-varying free charge density $\delta\rho(\mathbf{r}, \omega)$. The corresponding dipolar field is sustained by both $\delta\rho(\mathbf{r}, \omega)$ and the directly $\delta\rho$ -induced polarization charges inside the backgrounds and at the dielectric interfaces. In the presence of dielectric media, the potential energy associated with the classical electromagnetic problem [i.e. $V_{ext}(\mathbf{r}, \omega) = -e\phi_c(\mathbf{r}, \omega)$] plays the role of the effective external potential energy for the electron gas [43], [44]. $V_{ext}(\mathbf{r}, \omega)$ has therefore to be substituted for the applied external potential energy $V_{ext}^{bare}(\mathbf{r}, \omega) = ezE_0$ in the standard TDLDA equations (established in the absence of underlying background dielectric media) which relate the induced electron density $\delta\rho(\mathbf{r}, \omega)$ and the polarizability $\alpha_e(\omega)$ to the external potential. One has therefore

$$\delta\rho(\mathbf{r}, \omega) = \int \chi(\mathbf{r}, \mathbf{r}', \omega) V_{ext}(\mathbf{r}', \omega) d\mathbf{r}' \quad (2.5.5)$$

And

$$\begin{aligned}
\alpha_e(\omega) &= -\frac{1}{E_0^2} \int \delta\rho(\mathbf{r}, \omega) V_{ext}(\mathbf{r}, \omega) d\mathbf{r} \\
&= -\frac{1}{E_0^2} \int \int \chi(\mathbf{r}, \mathbf{r}', \omega) V_{ext}(\mathbf{r}, \omega) V_{ext}(\mathbf{r}', \omega) d\mathbf{r} d\mathbf{r}'
\end{aligned} \tag{2.5.6}$$

Where $\chi(\mathbf{r}, \mathbf{r}', \omega)$ is the non-local many-body correlation function. Note that the spatial non-locality is an intrinsic feature of the TDLDA formalism since the induced electron density change at \mathbf{r} depends on the excitation applied at any other point \mathbf{r}' of the system. Within the TDLDA it is assumed that the response of the interacting electronic system can be calculated as in the independent-particle case with the condition that the induced variation of the ground-state KS potential energy $V_{eff}(\rho_{gs}, \mathbf{r})$, that is

$$\delta V_{eff}(\mathbf{r}, \omega) = \int \left[\frac{\partial V_{eff}(\rho_{gs}, \mathbf{r}')}{\partial \rho(\mathbf{r}')} \right]_{\rho_s} \delta \rho(\mathbf{r}', \omega) \tag{2.5.7}$$

$$\delta V_{eff}(\mathbf{r}, \omega) = \frac{e^2}{4\pi\epsilon_0} \int V_c(\mathbf{r}, \mathbf{r}') \delta \rho(\mathbf{r}') + \left. \frac{\partial V_{xc}(\rho(\mathbf{r}))}{\partial \rho} \right|_{gs} \delta \rho(\mathbf{r}) \tag{2.5.8}$$

is added to the external one $V_{ext}(\mathbf{r}, \omega)$ in equation 2.5.5. The induced electron density $\delta\rho(\mathbf{r}, \omega)$ is thus solution of an implicit equation, from which is derived the integral equation relating $\chi(\mathbf{r}, \mathbf{r}', \omega)$ to the independent-electron correlation function $\chi^0(\mathbf{r}, \mathbf{r}', \omega)$, namely

$$\chi(\mathbf{r}, \mathbf{r}', \omega) = \chi^0(\mathbf{r}, \mathbf{r}', \omega) + \iint \chi^0(\mathbf{r}, \mathbf{r}_1, \omega) K(\mathbf{r}_1, \mathbf{r}_2, \omega) \chi(\mathbf{r}_2, \mathbf{r}', \omega) d\mathbf{r}_1 d\mathbf{r}_2 \tag{2.5.9}$$

where the kernel $K(\mathbf{r}_1, \mathbf{r}_2, \omega)$ writes as

$$K(\mathbf{r}_1, \mathbf{r}_2) = \frac{e^2}{4\pi\epsilon_0} V_c(\mathbf{r}_1, \mathbf{r}_2) + \left. \frac{\partial V_{xc}[\rho(\mathbf{r})]}{\partial \rho(\mathbf{r})} \right|_{gs} \delta(\mathbf{r}_1 - \mathbf{r}_2) \tag{2.5.10}$$

Finally $\chi^0(\mathbf{r}, \mathbf{r}', \omega)$ can be expressed in terms of the occupied KS orbitals and of the retarded single-particle Green's functions $G(\mathbf{r}, \mathbf{r}', \omega)$ of the ground-state KS-Hamiltonian, namely

$$\begin{aligned}
\chi^0(\mathbf{r}, \mathbf{r}', \omega) &= \sum_i \varphi_i^*(\mathbf{r}) \varphi_i(\mathbf{r}') G(\mathbf{r}, \mathbf{r}', \varepsilon_i + \hbar\omega) \\
&+ \varphi_i(\mathbf{r}) \varphi_i^*(\mathbf{r}') G^*(\mathbf{r}, \mathbf{r}', \varepsilon_i - \hbar\omega)
\end{aligned} \tag{2.5.11}$$

with

$$G(\mathbf{r}, \mathbf{r}', E) = \langle \mathbf{r} | [E + i\hbar\delta - H]^{-1} | \mathbf{r}' \rangle \tag{2.5.12}$$

where H is the single-particle KS ground-state Hamiltonian and δ is an infinitesimal positive real parameter. In equation 2.5.11 the index i runs over the occupied ground-state KS-orbitals φ_i of energies ε_i (a $T = 0$ K temperature is assumed). The parameter δ in equation 2.5.12 acts as an *effective* numerical smoothing parameter. In the absence of Landau damping, the minimum plasmon band width is equal to $2\hbar\delta$. In order to reduce

the computational time, the size evolutions determined for each (d, d_m) -parameter set have been extracted from TDLDA spectra computed with $\hbar\delta = 60 \text{ meV}$.

Figure 2.11 displays typical absorption spectra, in using two strongly different δ -parameters [$\hbar\delta = 5 \text{ meV}$ (black curve) and $\hbar\delta = 60 \text{ meV}$ (blue curve)]. In the frame of self-consistent quantum-mechanical models, the decay of the coherent plasmon excitation was ascribed for a long time to its coupling, via the particle surface, with one-electron excitations (single particle-hole ($p-h$) transitions), mechanism referred to as “Landau damping mechanism (LDM)” in cluster physics [77], [85]. This mechanism is indeed the main dissipative decay mechanism in the small size range.

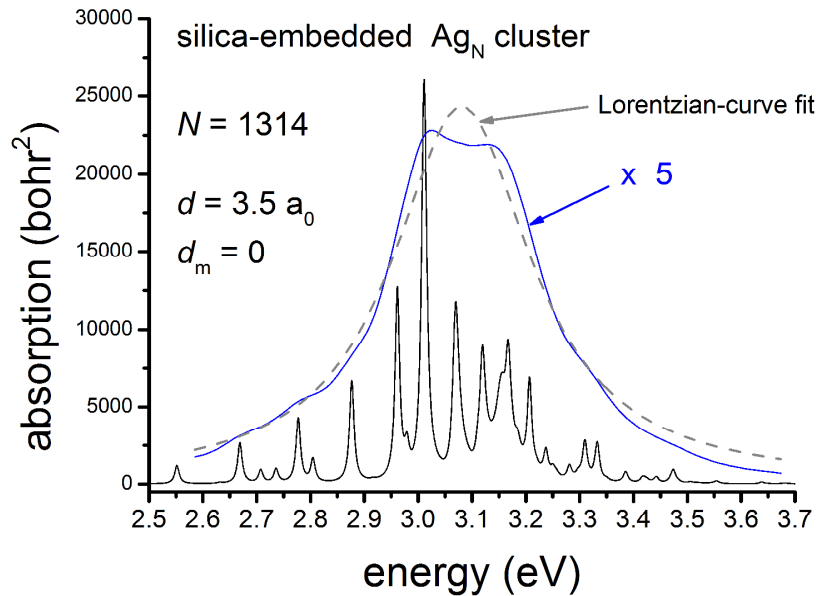


Figure 2.11: Absorption cross-section of silica-embedded Ag_{1314} cluster, for $d = 3.5 a_0$ and $d_m = 0$, computed in using two different δ -values in the Green’s functions [$\hbar\delta = 5 \text{ meV}$ (black curve) and $\hbar\delta = 60 \text{ meV}$ (blue curve)]. The blue curve is multiplied by a factor of 5 for easier comparison and the grey dashed curve is a Lorentzian-shaped curve fit of the blue-curve.

The size evolution of the LSP frequency is ruled by the competition between opposite size trends, namely the red-shift and blue-shift trends induced by, respectively, (i) the spill-out effect, and (ii) the surface layer of ineffective ion-core polarizability as well as the local porosity at the metal/matrix interface. This classical/quantal model will be used later in chapter 5 to interpret the plasmon resonance in very small silver nanoparticles.

2.5.5. Link between optics and EELS in a quantum framework

Now we have to prove that the proportionality between the EELS probability and the optical extinction cross-section is also valid in the frame of more complex models or/and theoretical approaches, for instance in which the conduction electrons in the metallic media are described through explicit charge distributions and their responses computed eventually in the frame of a quantum formalism, as the classical/quantal DFT-TDLDA calculations.

Considering the Jellium-model (figure 2.9) the maximum radius of the system is

$R_{max} = \max(R + d_m, R + \delta_{spill})$, where R is the radius of the spherical particle, δ_{spill} is the thickness of the electron spill-out tail in the ground state (on the order of 2-3 bohr radius) and d_m is the local porosity layer.

The non-locality of the optical response only affects the spatial region where the electronic charge distribution is extended ($r < R + \delta_{spill}$). The non-local many-body correlation function $\chi(\mathbf{r}, \mathbf{r}', \omega)$ vanish if r' (or r) $> R + \delta_{spill}$. However, with the introduction of a local porosity (considering $d_m > \delta_{spill}$), the non-locality affect the global system until the interface $R + d_m$.

Then, in a region where $r > R_{max}$ and considering an applied electric field $E_0 e^{-i\omega t} \hat{\mathbf{z}}$, the induced total potential can be written as

$$\phi_{ind,out}(\mathbf{r}, r > R_{max}) = \frac{1}{4\pi\epsilon_0\epsilon_m} \frac{(\alpha_c(\omega) + \alpha_e(\omega))E_0}{r^2} \cos(\theta) \quad (2.5.13)$$

Where $\alpha_c(\omega)$ and $\alpha_e(\omega)$ are calculated in a classical and quantum framework respectively. The sum $\alpha_c(\omega) + \alpha_e(\omega)$ corresponds to the total polarizability $\alpha(\omega)$. Then the induced total potential is

$$\phi_{ind,out}(\mathbf{r}, r > R_{max}) = \frac{1}{4\pi\epsilon_0\epsilon_m} \frac{\alpha(\omega)E_0}{r^2} \cos(\theta) \quad (2.5.14)$$

Using equation 2.4.47 in the optical form with an applied electric field $E_0 e^{-i\omega t} \hat{\mathbf{z}}$ we get

$$V_{ind,out}^{L=1,M}(\mathbf{r}, \omega) = \frac{1}{4\pi\epsilon_0\epsilon_m} \frac{D'_{L=1,M=0}(\omega)E_0}{r^2} \cos(\theta) \quad (2.5.15)$$

Comparing equation 2.5.15 with 2.5.14 we get

$$D'_{L=1,M=0} = \alpha(\omega) \quad (2.5.16)$$

As discussed in section 2.4.4, the term $D'_{L=1,M}$ depends only on the system and it is independent of the physical context (EELS or optics). Therefore we can conclude that the polarizability $\alpha(\omega) = \alpha_c(\omega) + \alpha_e(\omega)$ only depends on the system and not on the way the sample is excited (EELS or optics). Then the proportionality EELS-extinction cross-section (equation 2.4.44) is also valid in a quantum context, provided that $x_0 > R_{max}$.

In EELS experiments, the impact parameter x_0 of the electron beam can be very close to the particle surface. Then, the electron beam can pass through the region $R \leq x_0 \leq R_{max}$. We observed experimentally that the EEL signal for impact parameters passing this region presented the plasmon resonance at the same energy as for larger impact parameters away from the particle $x_0 > R_{max}$. It means that the contribution to the electron energy loss of the electrons passing through $R \leq x_0 \leq R_{max}$ can be neglected. The reason is that the force acting back on the electron is essentially perpendicular to the electron velocity when the electron is close to the x-y plane (see figure 2.12) and therefore this force do not do a work on the electron ($e\mathbf{v} \cdot \nabla V_{ind}^{L=1,M}(\mathbf{r}_e, \omega) \approx 0$). In consequence the EEL spectrum does not depend critically on the exact value of the impact parameter beyond the particle radius R .

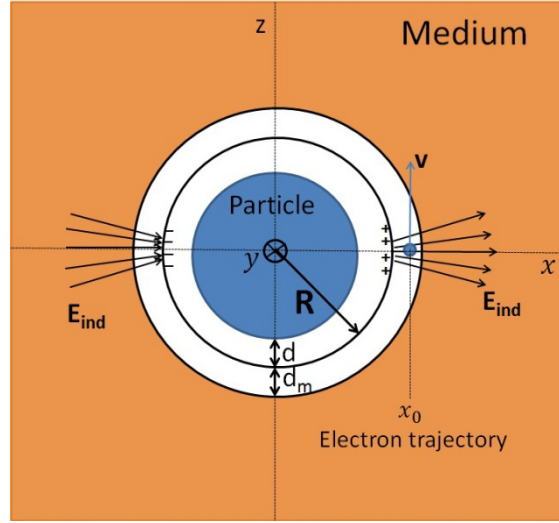


Figure 2.12: Scheme of an electron passing inside the porosity layer d_m . When the electron is inside the porosity layer it is close to the plane x - y of the particle (small z values). In this situation, the induced electric field acting back on the electron is essentially perpendicular to the electron velocity, therefore, the work of the force acting back on the electron is negligible $e\mathbf{v} \cdot \nabla V_{ind}^{L=1,M}(\mathbf{r}_e, \omega) \approx 0$. It means that an electron passing inside the porosity layer does not contribute significantly to the electron energy loss.

2.6. Conclusion

In this chapter the fundamentals of the electromagnetic theory were introduced and the dielectric function of a bulk metal was obtained by classical models. Plasmon resonances were studied such as the volume plasmon in a bulk metal, the surface plasmon polaritons (SPPs) in metal-dielectric interfaces and localized surface plasmons (LSPs) in nanostructures. The LSPs in metallic nanoparticles were studied in a classical regime by light and electron excitations. We proved that there is a direct relation between optical and electron excitation. Furthermore, placing the electron impact parameter very close to the particle surface showed a linear dependency of the EELS signal with the particle radius. This shows the feasibility to get EEL signal in very small particles without a drastic decrease in intensity.

Finally, a classical/quantal model which takes into account quantum effects was developed in order to describe the surface plasmon resonance in small nanoparticles. The proportionality between the light and electron excitation was also demonstrated in the case of a quantum framework.

Chapter 3:

Instrumentation and data analysis

3.1. Introduction

The use of light has enabled humanity to explore the properties of matter since our early years. In daily life we employ the light to characterize objects that are around us. For example, the color of the light emitted by a heated material gives us information about the temperature of the material [86]. With more sophisticated techniques we can access to more quantitative information such as the concentration of a solution according to the light that it absorbs or the thickness of a thin film by the interferences of light that is trapped by the interfaces. The advance of science and the understanding of nature are intrinsically related to the optical properties of matter. Some examples are [86]: the study of the blackbody radiation that has led to the formulation of quantum physics, the optical emission from atoms and molecules that revealed the quantization of energetic levels, the development of the laser which provided a huge advance in spectroscopy techniques, fiber optics for communication among other examples. The development of instrumental tools to produce electromagnetic waves at different wavelengths and the control on the preparation methods of materials has enabled us to explore physical and chemical properties of matter at the nanometric scale. Nowadays, different instrumental techniques enable the study of the light-matter interactions at different conditions of temperature, environment, pressure, etc.

In this thesis, the optical properties of metallic nanoparticles are studied by optical absorption spectroscopy and/or electron energy loss spectroscopy (EELS). Both techniques are complementary and measure the same quantity (the polarizability, see chapter 2). Through this chapter we will see the instrumental part of both techniques and the post-processing analysis that have been performed in the EELS raw data to extract plasmonic information. Figure 1 shows a scheme of optical and electron excitation techniques performed in this thesis in samples prepared under the same conditions. Additionally, the sample preparation of silver clusters is described.

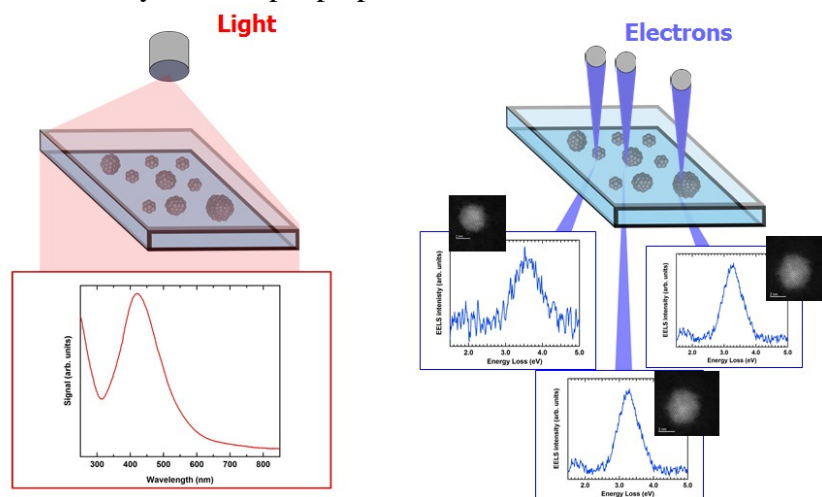


Figure 3.1: Optical absorption and EELS experiments performed on samples prepared by the same conditions. While in optical experiments the measurements are made in a set of particles, in EELS experiments the individual particles are measured. In parallel with the EELS experiment an image of the particle can be acquired.

3.2. Optical Absorption Spectroscopy

The optical absorption characterization of silver clusters embedded in silica matrix in this thesis was carried out in the Institut Lumière Matière in Lyon by collaborators (M. Hillenkamp and N. Troc).

The absorption of radiation by a sample can be studied by a transmitted light beam. The transmission consists in measuring how much of a known light intensity that shines on a sample pass through it, as a function of the wavelength of the light. The transmission can be described by the Beer Lambert law

$$T = I/I_0 = e^{-AK_{abs}} \quad (3.2.1)$$

Where I_0 is the incident signal intensity, I the transmitted intensity, K_{abs} the absorption coefficient, and A the path length. The product AK_{abs} is known as absorbance and it is often called the optical density of the object. The absorption cross-section can be expressed as

$$\sigma_{abs} = K_{abs}/N \quad (3.2.2)$$

Where N is the atomic number density.

In this work the optical measurements were performed on an ensemble of silver particles. These measurements were carried out in a Lambda 900 UV/Visible Spectrometer Perkin Elmer that has a spectral range from 185 to 900 nm. This spectrometer can be used in reflection or transmission configuration but only transmission experiments were performed because the scattering can be neglected in very small nanoparticles as it was discussed in section 2.4.2.

In order to remove the signal coming from the substrate, a reference signal (on the substrate covered by matrix) is taken and divided by the signal of the whole system. Thus the absorption coefficient of the reference is removed from the absorption coefficient of the whole system

$$I_{ref}/I = e^{A(K-K_{ref})} \quad (3.2.3)$$

Another data acquisition strategy was the use of incident polarized light beam (p-polarised) in order to avoid Fabry-Pérot interferences between the two interfaces of the matrix (which is of the order of several wavelengths) and the tilting of the sample in the Brewster angle in which the p-polarised light is totally transmitted (see figure 3.2).

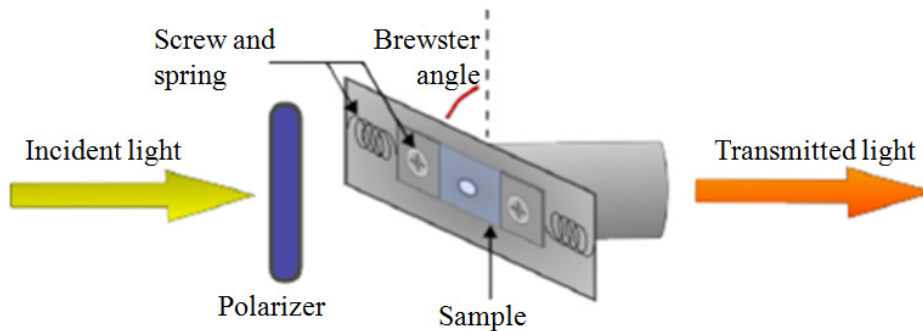


Figure 3.2: Scheme of the sample holder and the optical measurements of a set of silver particles. Adapted from Ref. [87].

3.3. Scanning transmission electron microscope (STEM)

The scanning transmission electron microscope (STEM) was invented by Manfred von Ardenne in Germany in the 1937-1938, just after the invention of the transmission electron microscope TEM in 1932 by Knoll and Ruska [88]. The lack of electronics, high vacuum and bright of electron sources made this instrument not practical. It was not until the 1960s and 1970s when the STEM was re-invented by Crewe and coworkers with new implementations such as: bright cold field emission source, electronic readout, ultra-high vacuum and an electron energy loss spectrometer (EELS). Nowadays with the invention of aberration correctors and monochromators for the STEM-EELS system, it has been possible to access to the atomic resolution with a high spectral resolution opening a window for a variety of experiments previously out-of-reach.

Figure 3.3 presents a schematic of a STEM system fitted with different detectors. A basic operating principle of a STEM microscope can be described as follows:

An electron gun produces electrons which are accelerated towards a sample. The electron beam is focused and scanned on the sample by electromagnetic lenses. The electrons transmitted throughout the sample are collected by detectors. Furthermore, the radiation emitted by the sample during the interaction with the electrons can also be collected.

In a typical plasmonic experiment three detectors can be used:

- * The High Angle Annular Dark Field (HAADF) detector, which collects elastic electrons scattered at high angles, is used to obtain an image of the sample.
- * The Electron Energy Loss Spectrometer (EELS), which collects elastic and inelastic scattered electrons, is used to obtain a spectrum.
- * A Cathodoluminescence (CL) spectrometer can be used in order to study the light emitted by the sample.

It is important to notice that the HAADF detector and the EELS (or CL) spectrometer work at the same time.

Other acronyms presented in figure 3.3 are:

CCD: Charge Coupled Device

EDS: Energy Dispersive x-ray spectroscopy

SPIM: Spectrum image (spectrum acquired in each point of the electron scan). The SPIM electronic box in figure 3.3 refers to the electronics necessary for scan the electron beam and acquires data with synchronization.

In the following the main parts of a STEM microscope and detectors will be presented in more details.

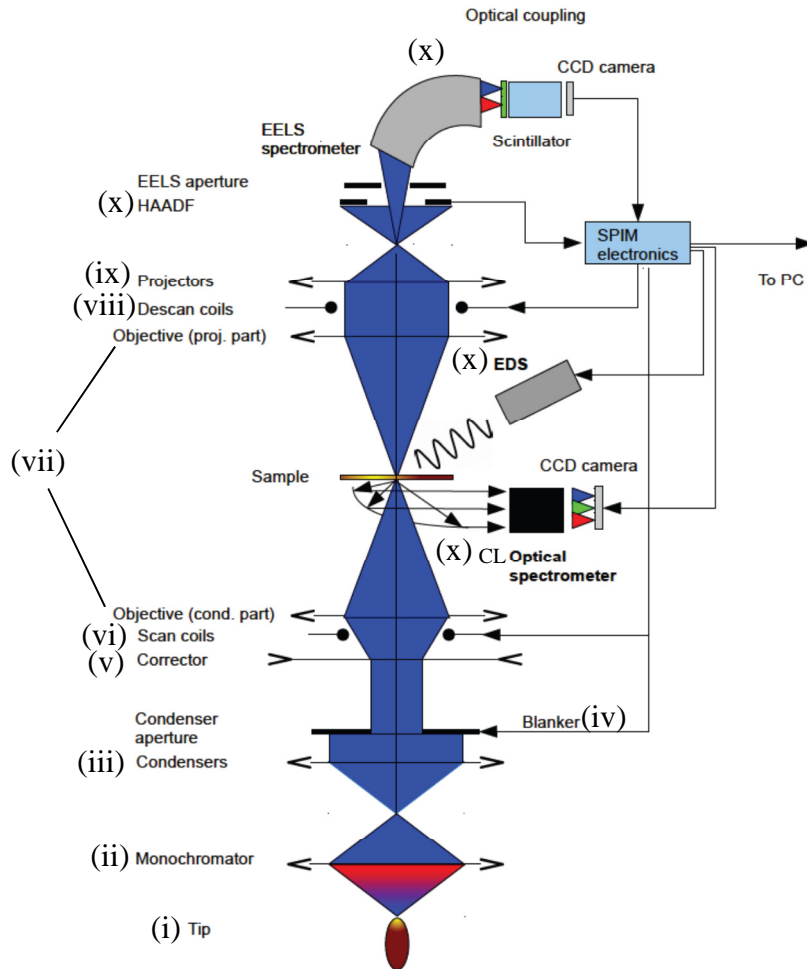


Figure 3.3: Basic scheme of a typical STEM microscope. Adapted from Ref. [60].

From the bottom to the top on figure 3.3 the STEM microscope consists in a collection of several elements:

- (i) Electron gun (tip): This element produces the electrons that are guided towards the sample. Different electron gun technologies are used such as thermionic emission source, Schottky field emission source and the cold field emission gun (cFEG). The last one has the highest brightness with good emission stability. The brightness is defined as the intensity divided by the area and by the solid angle. It is one of the most important parameters because it ensures a good probe current density. Among all the technologies of electron guns, the cFEG has the lowest energy spread and enables the better energy resolution. This is indispensable for plasmonic experiments.
- (ii) Monochromator (optional): This device decreases the energy spread of the electron beam leading to the improvement of the spectral resolution. A decrease in the number of electrons reaching the sample is expected.
- (iii) Condenser lenses: These lenses are used to place the electron beam along the optical axis of the microscope and to determine the probe size, the angle of convergence and the beam current. It is possible to tune these parameters independently by the combination of the condensers. To reduce aberrations, condenser apertures can be used.
- (iv) Blanker: A blanker is used to avoid a long exposition and saturation of signal on the EELS detector.
- (v) Corrector (optional): This device reduces the spherical aberrations leading to very

small electron probe size formation and relatively high currents in small probes [89].

(vi) Scan coils: These coils make possible the scanning of the electron beam on the sample. The blanker is synchronized with the scan coils.

(vii) Objective lens: The objective lens is one of the most critical parts in a STEM microscope. This lens is the stronger one on the system with a short focus depth (few millimeters). This enables the collection of electrons in a large angular range in order to form a very sharp probe on the sample.

(viii) Descan coils: These coils (synchronized with the scan coils) are used to center the electron beam in the EEL spectrometer entrance.

(ix) Projector lenses: These elements control the angular range of transmitted electrons impinging on different detectors [89].

(x) Detectors: Different detectors can be used according to the type of study that the experimentalist wants to do. HAADF, EELS and Cathodoluminescence (CL) detectors are the most useful for plasmonics studies. The HAADF and EELS detectors were used in this thesis and more details will be explained in this chapter. The Cathodoluminescence detector is not used in this thesis and no more details will be given.

The microscope used in this work is an UltraSTEM200 from NION Company. This microscope is a Cs-corrected dedicated microscope fitted with a cFEG electron gun and a homemade EELS detection system. It can operate at incident electron energy of 60 keV where the probe size can reach $\sim 1.2 \text{ \AA}$. It is also possible to work at 100 keV and 200 keV reaching smaller probe sizes ($<1 \text{ \AA}$). A scheme of the UltraSTEM200 is presented in figure 3.4a. The electron gun is placed at the bottom of the microscope and from the bottom to the top the column is composed by two gun lenses, three condenser lenses (CL1, CL2, CL3), a C3/C5 corrector, an objective lens and sample chamber, a set of Projector lens (PL1 to PL4) and the different detectors BF/ABF/MAADF/HAADF/EELS. The acronyms BF, ABF and MAADF refer to bright field, annular bright field and medium-angle annular dark field respectively. These detectors are used to form images. We did not use these detectors in this thesis work. The SPIM electronics box of the UltraSTEM200 is homemade, developed by Marcel Tencé in the Laboratoire de Physique des Solides in Orsay.

The aberration corrector counts with octupoles and quadrupoles lenses which allow to correct third and fifth order geometric aberrations in order to obtain atomic resolution images. For more details on the aberration correction the reader is referred to [90], [91]. A retractable CCD camera is used before the EELS spectrometer in order to get an image (Ronchigram) of the sample which facilitates the alignment of the microscope and the correction of aberrations. In this retractable CCD camera, the electron beam current is measured.

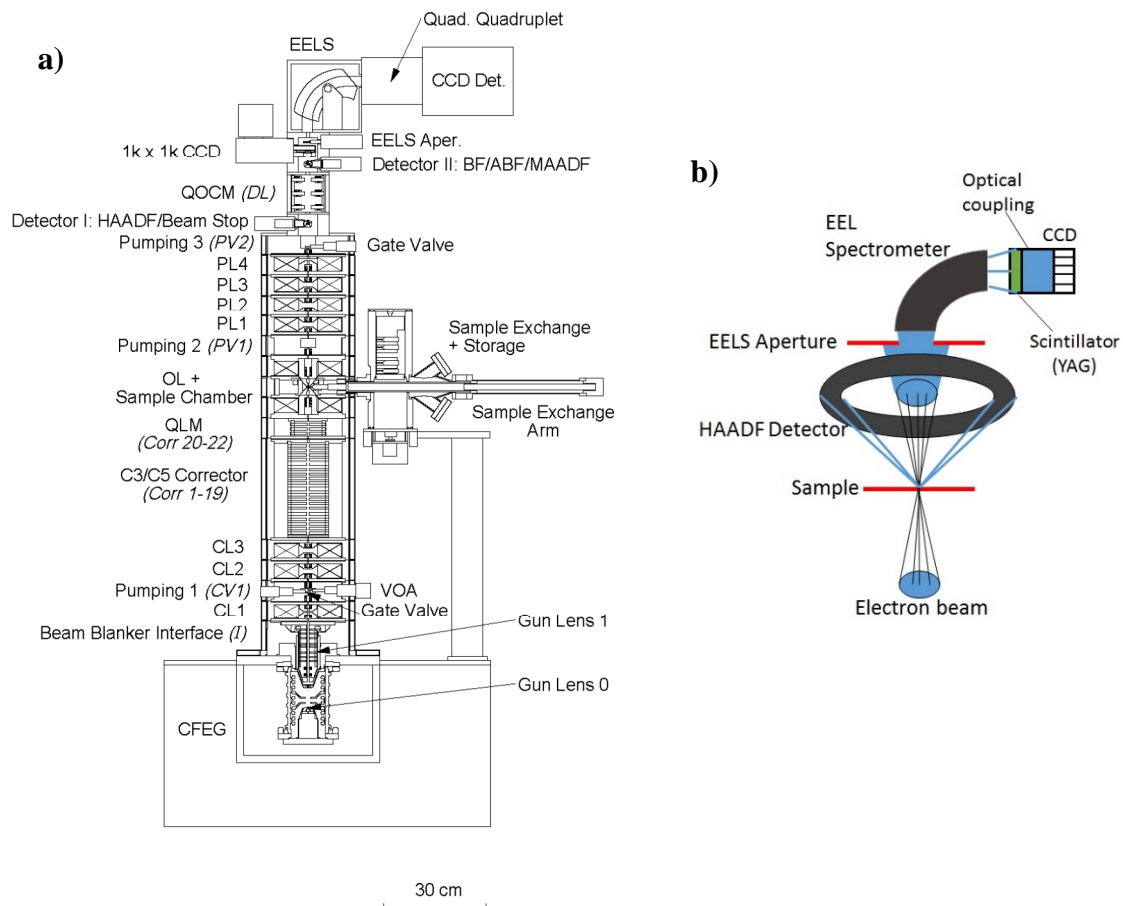


Figure 3.4: (a) Schematic cross-section of the UltraSTEM200 column [91]. (b) Basic scheme of the HAADF and EELS detectors.

3.3.1. Elastic and inelastic electron-matter interaction

The electrons passing through a material can interact with the atoms by electrostatic Coulomb forces, leading to transmitted elastic and inelastic electron scattering.

Elastic scattering

The elastic scattering is the result of the deflection of the incoming electron after having interacted with a nucleus. The incoming electrons interacting very close to the immediate vicinity of a nucleus are scattered at high angles and the distribution is similar to the Rutherford scattering of alpha particles [92]. However most of the incoming electrons pass further from an atom. In this situation the interaction is weaker and they are scattered at low angles, typically between 10-100 mrad for a 100 keV incident electron energy [92].

In crystalline materials the elastic scattered electrons can interfere and the continuous distribution of the scattering becomes peaked where the angles corresponds to the atomic position of atoms in the crystal. These electrons are referred to as diffracted electrons.

Inelastic scattering

In an inelastic interaction, the incoming electron can loss energy due to different process.

The main mechanisms of energy loss are:

(i) The interaction of an incoming electron with an inner-shell electron in an atom.

In this interaction the inner-shell electron can make a transition to unoccupied electron states absorbing similar or greater energy than its binding energy. In this case the incoming electrons scatter typically at ~ 10 mrad for a 100 keV incident electron energy [92]. After the interaction with the incoming electron, the atom is left in an excited state and it loses energy by the transition of outer-shell electrons to the vacant. This produces x-rays radiation or Auger electron emission.

(ii) The interaction of an incoming electron with outer-shell electrons.

In insulators or semiconductors, a valence electron can make interband transition through the energy gap. In this case the incoming electron is scattered typically between 1 or 2 mrad for a 100 keV incident electron energy [92]. In the de-excitation process of the sample there is emission in the visible region (Cathodoluminescence) or the energy is dissipated in the form of heat.

(iii) The interaction of an incoming electron with an electron cloud coming from a band of delocalized states in a solid (this means that atomic core levels do not participate).

In this case the incoming electron excites a collective oscillation of electrons which is known as plasmon. This oscillation takes the form of longitudinal waves inside the solid. The energy of this oscillation is between 5-30 eV for the majority of solids [92].

In thin samples or small particles, the incoming electron can also excite localized surface plasmons as studied in section 2.4.3.

(iv) The interaction of an incoming electron with the array of atoms (this interaction can excite phonons in the material). The excitation of phonons reduces a small fraction of the incoming electron energy. In the past, these electrons cannot be resolved due to the small fraction of energy loss. With the recent advances in the improvement of energy resolution in STEM-EELS system, the phonons have been spectrally resolved [93], [94].

3.3.2. HAADF image

The High-angle annular dark field (HAADF) signal corresponds to the elastic electrons scattered through high angles, typically greater than 80 mrad. These electrons must pass not further than 0.3 Å from the atomic nucleus. At this condition the electrons are largely incoherent. The dark field term comes from the fact that a hole appears dark in an HAADF image because not scattering of electrons.

The HAADF detector has a form of ring (see figure 3.4b) which collects the elastic electrons scattered at high angles and let pass electrons scattered at low angles that can be collected by other detectors as the EEL spectrometer. In a HAADF detector the count of electrons is made by a scintillator-photomultiplier tubes system.

The intensity detected by the HAADF detector depends on the composition and thickness of a sample through the equation $I_{HAADF} = kI_0NtZ^{4/3}$, where I_{HAADF} is the detected intensity, k is a constant depending on the electron velocity, I_0 is the incident electron beam intensity, N the number of atoms per unit volume, t the sample thickness and Z the atomic number. For a homogenous sample of one material, the HAADF signal gives a contrast proportional to the thickness of the sample and for a sample composed of different materials, the HAADF signal gives chemical contrast information. Figure 3.5 shows an example of a HAADF image with the atomic resolution of a silver nanoparticle as studied in this thesis. It is possible to recognize the atomic columns.

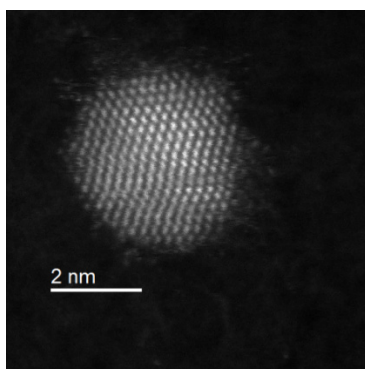


Figure 3.5: HAADF image of a silver nanoparticle supported on carbon substrate.

3.3.3. Electron Energy Loss Spectroscopy (EELS)

The EEL spectrometer collects transmitted electrons and separates them by their energy loss after the interaction with matter (see figure 3.4b). The spectrometer we used is essentially made up of a magnetic prism that disperses the electron trajectories along one direction as a function of energy [60]. At the entrance of the EEL spectrometer an aperture (EELS aperture) can be used, which reduces the angle of collection of scattered electrons in order to reduce aberrations (see figure 3.6a, more details on the aberration correction for EELS experiments will be presented in chapter 4). Due to the scanning of the beam on the sample, the transmitted electron beam can shift at the spectrometer entrance axis during the scanning. To avoid this problem, descan coils (synchronized with the scan coils) are used in order to center the electron beam in the spectrometer entrance axis (see figure 3.3). In the EEL spectrometer, combined quadrupoles-sextupoles lenses allow correcting third-order aberrations. A scheme of the EEL spectrometer with the quadrupoles (FocusX, FocusY, Q1, Q2, Q3, Q4) and sextupoles (SX, SY) lenses is shown in figure 3.6b.

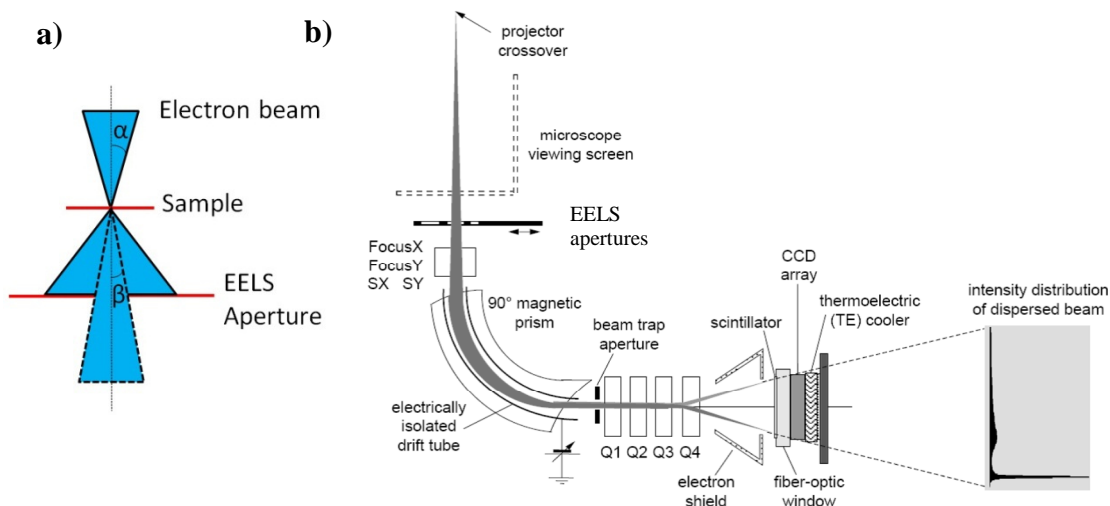


Figure 3.6: (a) Scheme of the convergence semi-angle α and collection semi-angle β . The collection semi-angle β is determined by the EELS aperture diameter. (b) Scheme of an Electron Energy Loss Spectrometer with quadrupoles and sextupoles lenses (FocusX, FocusY, Q1, Q2, Q3, Q4 to index quadrupoles and SX, SY to index sextupoles) (image taken from [95]). The electrons are dispersed according to their energy lost and arrive to a scintillator-CCD system.

A scheme of the interaction of an incident electron with a sample is presented in figure 3.7. The angular and energy dependence of the inelastic scattering inside the material is represented by a double-differential cross-section [92]

$$\frac{d^2\sigma}{d\Omega dE} \propto \left(\frac{1}{\theta^2 + \theta_E^2} \right) \text{Im} \left[-\frac{1}{\varepsilon(\mathbf{q}, E)} \right] \quad (3.3.1)$$

Where $\theta_E = (c/v)^2 E / (E_0 + m_0 c^2)$ is a characteristic angle, E_0 is the incident electron energy, E is the energy loss and θ is the scattered angle of the electron. This equation is valid in the approximation of small angles $\theta \ll 1 \text{ rad}$ and $E \ll E_0$.

In equation 3.3.1 we can identify the loss function $\text{Im}[-1/\varepsilon(\mathbf{q}, E)]$ that we obtained in section 2.4.3 for the EELS probability inside a material. The transferred momentum in the direction of the incoming electron is $q_{\parallel} = k_0 \theta_E$, where k_0 is the momentum of the incoming electron. In the small angle approximation, the total transferred momentum is therefore $q^2 \approx k_0^2 (\theta^2 + \theta_E^2)$.

The double differential cross-section at low scattering angles is dominated by the Lorentzian factor $(\theta^2 + \theta_E^2)^{-1}$ where the angle θ_E represents the half-width at half maximum (FWHM) of the Lorentzian. The maximum of the signal comes from the electrons that scatter at $\theta = 0$ (maximum of the Lorentzian). In a typical EELS experiment at 100 keV we have $k_0 = 169 \text{ rad}/\text{\AA}$ and with an energy loss of 10 eV we have $\theta_E \sim 0.1 \text{ mrad}$. Considering just the electrons scattered at $\theta = 0$ we obtain $q = 0.017 \text{ \AA}^{-1}$ which is much smaller than the Fermi wavenumber $q_f \sim 1 \text{ \AA}^{-1}$. Then the transferred momentum can be neglected. For electrons scattered only in few mrad, the component perpendicular of the transferred momentum is most important than the parallel but still smaller than the Fermi wavenumber and additionally their contribution to the inelastic signal is weak. All this means that in a standard STEM-EELS experiment the non-locality (\mathbf{q} dependency of the response) is not induced by a transfer of momentum and therefore an STEM-EELS experiment is equivalent to an optical experiment in the bulk of a material.

In the case of the electron beam passing near a sample surface, the relation EELS-Optics is evident (see section 2.4.3 for the case of a spherical particle).

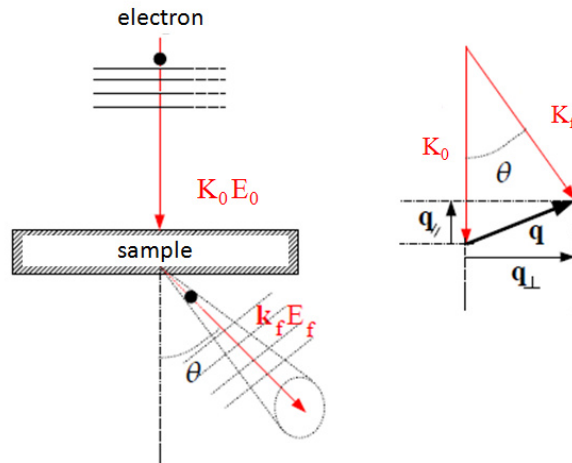


Figure 3.7: Scheme of an EELS experiment. The incident electron of energy E_0 and momentum \mathbf{k}_0 is inelastic scattered with energy loss $E = E_0 - E_f$, momentum \mathbf{k}_f and angle θ . A momentum \mathbf{q} is transferred to the sample.

EEL spectrum

An EEL spectrum is formed by the inelastic transmitted electrons dispersed along the CCD camera. An illustration of an EEL spectrum is presented in figure 3.8. At low energy losses (<100 eV) the region is called Low-Loss and at high losses (>100eV) the region is called Core-Loss. The Low-Loss region studies phenomena from the infrared, passing through the visible, to the ultraviolet range. It is an adapted region to obtain optical information of the sample. On the other hand, the Core-Loss region is in the X-Rays range that gives chemical information of the sample. This very huge range of energies studied by EEL spectroscopy made it one of the most powerful techniques.

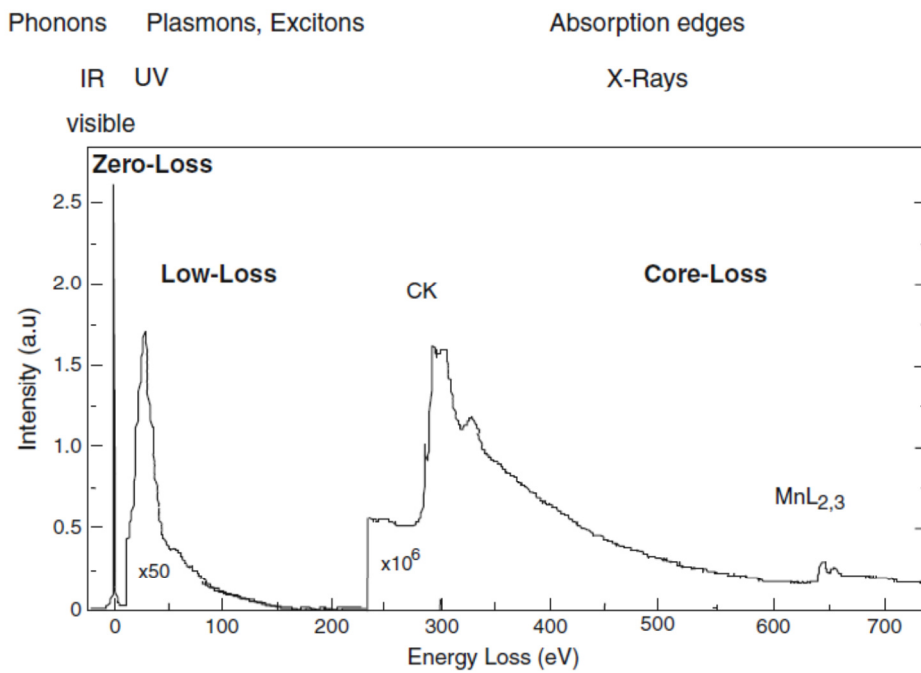


Figure 3.8: A typical EEL spectrum [60]. The Low-Loss region contains an intense peak at zero energy (the ZLP) and peaks corresponding to individual and collective excitations such as: interband transitions, excitons, plasmons and phonons. The Core-Loss region contains peaks related to the chemical composition of the sample.

Low-Loss region

The Low-Loss region (losses < 100 eV) is related to the excitation of phonons, excitons, interband transitions or collective oscillations such as volume plasmon or surface plasmons. At zero energy, an intense peak is observed which corresponds to the electrons that do not loss energy during the interaction. This peak is called the zero loss peak (ZLP) and its full width at half maximum (FWHM) define the energy resolution of the spectrometer. In the study of signals at very low energies the ZLP tail can mask the peaks and deconvolution techniques or monochromation solutions have to be employed. Writing the permittivity of a material as $\epsilon(\omega) = \epsilon'(\omega) + i\epsilon''(\omega)$, the excitation of the volume plasmon corresponds to the zeros of ϵ' coinciding with weak values of ϵ'' . On the other hand, the interband transitions correspond to the maxima of ϵ'' . In the case of surface plasmons in nanostructures in a non-retarded classical regime, the resonance condition depends on the geometry of the particle and the surrounding medium. For the

case of a sphere a dipolar surface plasmon is obtained at $\varepsilon' + 2\varepsilon_m = 0$ (being ε_m the relative permittivity of the surrounding medium) as discussed in section 2.4.2.

Core-Loss region

The Core-Loss region (losses > 100 eV) is related to the individual excitation of inner-shell electron transitions to unoccupied electron states. In this region the loss function can be approximate to $\text{Im}[-1/\varepsilon(\omega)] = \varepsilon''(\omega)/(\varepsilon'^2(\omega) + \varepsilon''^2(\omega)) \approx \varepsilon''(\omega)$ due to the fact that $\varepsilon'(\omega) \rightarrow 1$ and $\varepsilon''(\omega) \rightarrow 0$. This corresponds to an absorption process. Additionally, in this region it is possible to obtain information about the fine structure related to the nature of chemical bonds. An example of Core Loss spectrum is presented in figure 3.9.

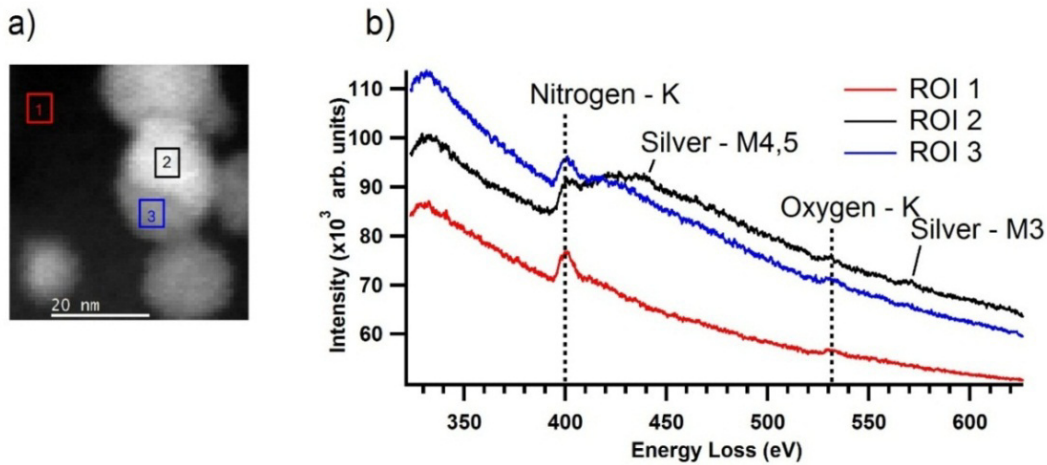


Figure 3.9: (a) HAADF image of a set of silver particles. (b) EEL spectra in different regions of interest. The signature of silver is presented.

3.3.4. EELS data acquisition (spectrum-image)

In a STEM microscope with an EEL spectrometer, it is possible to acquire a HAADF signal and an EEL spectrum in each electron position while scanning. This mode of acquisition is known as spectral-image mode. Once the electrons pass through the sample, they are collected by the HAADF detector and the EEL spectrometer which work at the same time. At the end of the scan, both a HAADF image and a spectrum-image (EEL spectrum in each pixel of the scan) are generated which can be compared pixel by pixel.

The spectrum-image (spim) is represented by a cube (the datacube) in which the x and y axes correspond to the coordinates of the electron beam scanning on the sample and the z axis corresponds to the EEL spectra recorded in each point of the scan. Figure 3.10 shows the operation principle of a STEM-EELS system to generate a HAADF image and a spectrum-image.

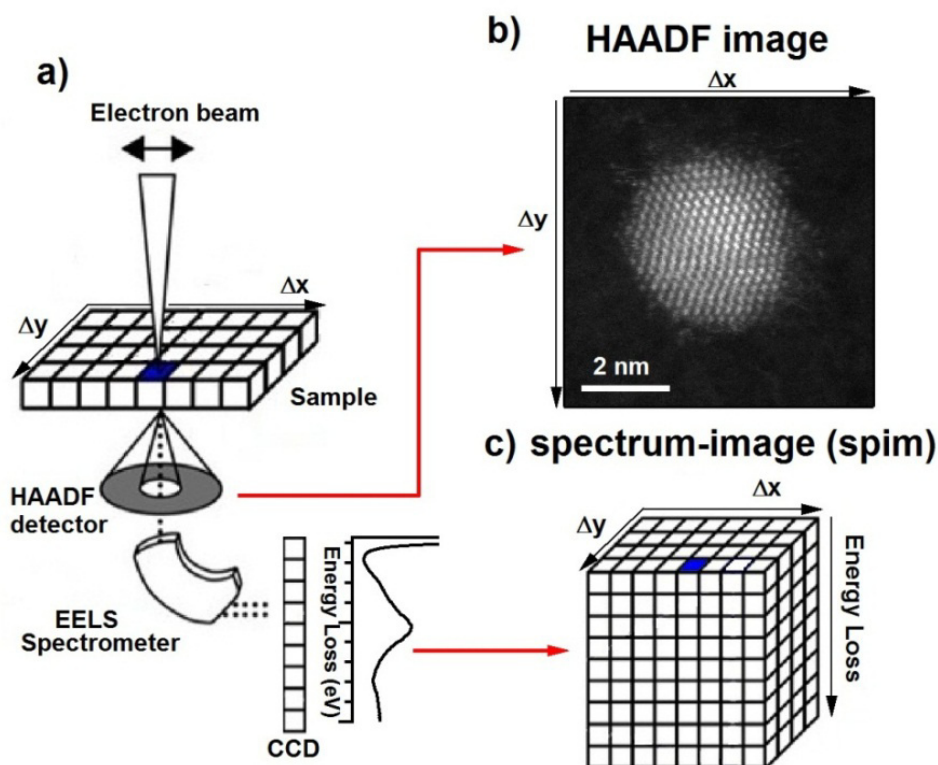


Figure 3.10: Scheme of the operating principle of a STEM microscope with an EEL spectrometer. (a) Scanning of a sample point by point with a focused electron beam. (b) HAADF image of the sample obtained at the end of the scan. (c) Spectrum-image (spim) obtained at the end of the scan in which the x - y axes represent the spatial coordinates of the electron beam scan and the z axis corresponds to the EEL spectra recorded at each point of the scan. Parts of this image were extracted from <http://www.gatan.com>.

3.3.5. Data Analysis of a spectrum-image

The raw spectrum-image has to be treated in order to extract correct graphs and be able to do a coherent interpretation of the results. In the following, the main steps for data treatment of plasmonic STEM-EELS experiments will be presented.

Alignment of the EEL spectra

Due to the instabilities of the high voltage, the EEL spectra can shift on the CCD camera over time. This is reflected in a shift of the ZLP position from one pixel (x_1, y_1) to another (x_2, y_2) in a spectrum-image. In order to correct the ZLP shift a procedure of alignment is applied which places the ZLP maximum at the same energy position (0 eV) for all the pixels (x, y) of the spectrum-image. This procedure of alignment was performed automatically by the free software Hyperspy [96]. Figure 3.11 shows the evolution of the ZLP over time. Without any alignment, the ZLP moves ~ 67 meV during 73 ms. This increases the linewidth of the ZLP of the sum of all the spectra and, therefore, causes resolution loss. After the alignment procedure, the ZLP only moves ~ 22 meV during the same period, i.e. one pixel of the CCD detector.

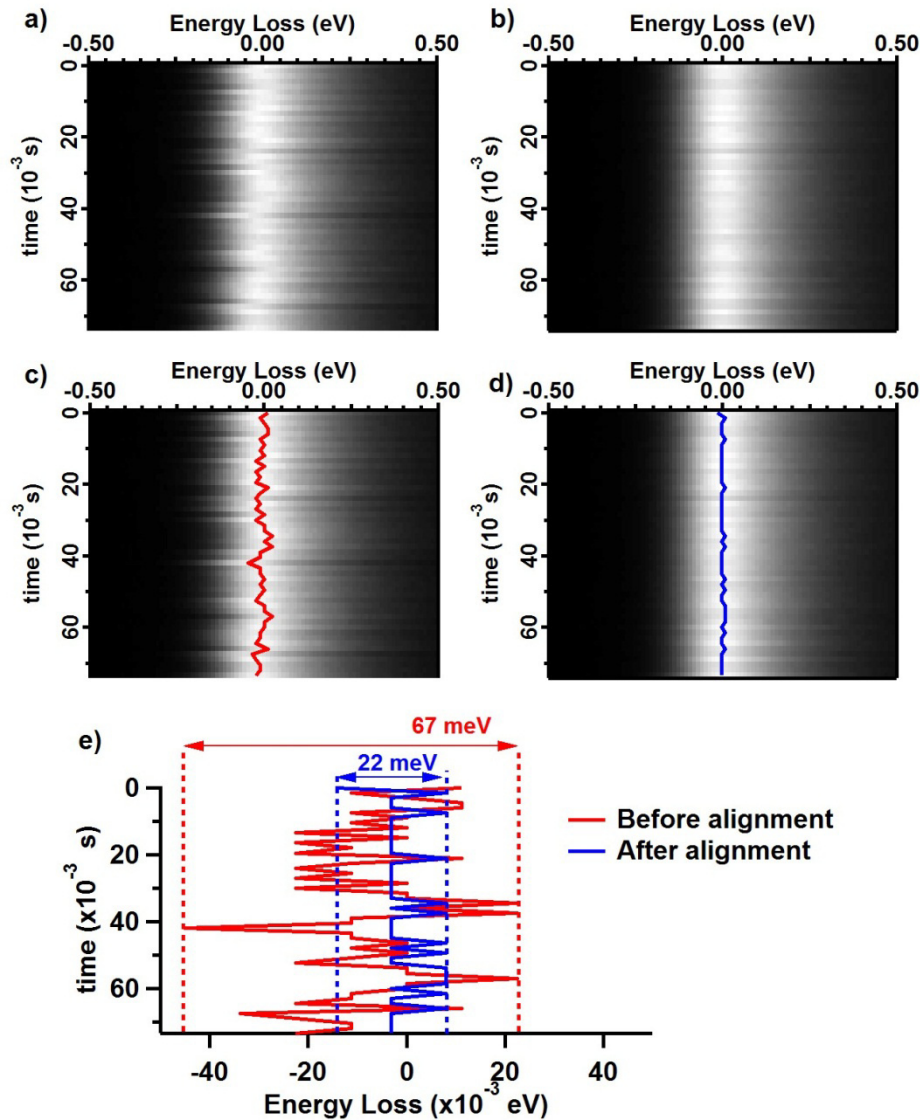


Figure 3.11: EEL spectra showing the ZLP position over time. (a) Before alignment. (b) After alignment. (c) The maximum position of the ZLP is plotted before alignment. (d) The maximum position of the ZLP is plotted after alignment. (e) Comparison of the ZLP maximum position during 73 ms before and after alignment. The ZLP moves ~ 67 meV for the case without alignment and only ~ 22 meV after alignment.

Deconvolution

When the plasmon resonances are at very low energies, the peaks can be hidden by the tail of the ZLP. In this case, a mathematical deconvolution technique is used to reduce the ZLP width and resolve the plasmon peaks.

The Richardson-Lucy (RL) deconvolution technique has been widely used in astronomy for the reconstruction of images affected by optical defects. This technique has been adapted to EEL spectra to improve the spectral resolution [10], [97].

The aberrations of the spectrometer, the beam spreading in the detector, and the finite energy width of the electron source cause cross channeling. Instead of getting a point representing a specific energy, a spread over multiple channels is obtained forming a

blurred point [98].

Mathematically the degradation of the energy resolution is expressed by the following convolution product

$$I(i) = P(i) \otimes O(i) \quad (3.3.2)$$

Where $I(i)$ is the measured signal (blurred signal), $O(i)$ represents the original signal and $P(i)$ is the instrumental response (point spread function (PSF)). The original signal $O(i)$ can be extracted from equation 3.3.2 by a deconvolution. The instrumental function $P(i)$ is obtained with an EEL spectrum (containing the ZLP) taken in vacuum or on the substrate.

The Richardson-Lucy algorithm consists in finding the function $O(i)$ by the following iterative process

$$O_j^{s+1} = O_j^s \left(\frac{\sum_i \frac{P_{i,j} I_i}{\sum_l P_{i,l} O_l^s}}{\sum_i P_{i,j}} \right) \quad (3.3.3)$$

Where s is the number of iterations, O_j^{s+1} is an estimator after s iterations.

The RL deconvolution can introduce artifacts in the Low-Loss region which forces to reduce the number of iterations. Different criteria of the optimum number of iterations exist (see Ref. [98]). The free software Hyperspy [96] was used to perform the RL deconvolution in this thesis.

Figure 3.12 shows an EEL spectrum extracted from the sum of pixels along the edge of an aluminum nanotriangle (40 nm thickness). In this region, surface plasmons are excited but are not clearly distinguished in the spectrum due to the influence of the ZLP tail. If one applies the RL deconvolution with different number of iterations, it is possible to resolve the plasmon peaks.

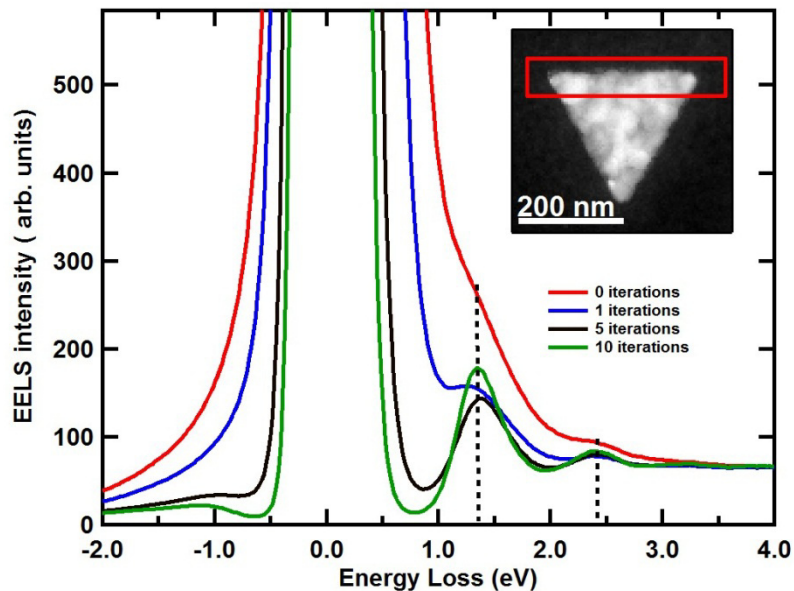


Figure 3.12: EEL spectrum (red curve) taken from the sum of pixels along the edge of an aluminum nanotriangle studied in this thesis (red box in the HAADF image of the inset). Different number of iterations are applied leading to the reduction of the ZLP width and, therefore, to enhance the observation of the plasmon peaks.

In the study of very small nanoparticles (as the case of silver clusters in this thesis), the EEL signal is very noisy and the RL deconvolution can present some difficulties in the interpretation. In chapter 4 it will be studied the RL deconvolution technique for weak signals.

Filtered maps

With a spectrum-image it is possible to create filtered maps. A filtered map is generated by plotting the EEL signal intensity of each pixel x-y in a chosen energy range. An illustrative way to understand the formation of a filtered map is presented in figure 3.13. In this example, two energy intervals are chosen and their corresponding filtered maps are generated.

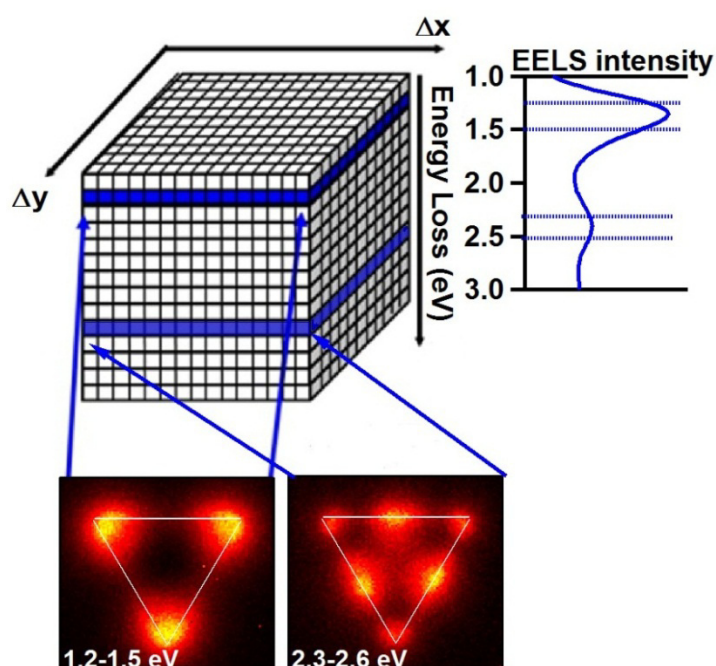


Figure 3.13: Illustrative example of the formation of filtered maps. The maps are generated by the EELS intensity in each pixel x-y in a specific energy range. If the energy ranges correspond to plasmon resonance energies, then the maps reveal the spatial symmetry of the plasmon resonances. More specifically the filtered maps can be linked to the projection onto the electron beam trajectory of the local density of states (z LDOS).

Multipeak fitting and fitted maps

With a spectrum-image it is also possible to create fitted maps. Fitted maps are generated by fitting the EEL spectrum of each pixel x-y with a model and by plotting the fitting parameter values at each pixel x-y. In order to carry out this procedure, first an EEL spectrum coming from a pixel x-y (or the sum of pixels x-y) of an interested area is fitted by a model (see figure 3.14a). Then, the parameter values obtained by this fit are used as initial parameter values to start the fitting procedure (fit of the EEL spectrum of each pixel x-y with the model). In the model it is also possible to include a

background if necessary.

Unlike the filtered maps, the fitted maps can resolve overlapped peaks and study the evolution of the energy position and FWHM of the plasmon peaks throughout different regions of the sample. The multidimensional fitting procedure was carried out by the free software Hyperspy [96]. Figure 3.14b shows the fitted maps of the intensity of the two Gaussians used in the fitting procedure and their corresponding sigma values ($FWHM/2\sqrt{2\ln(2)}$).

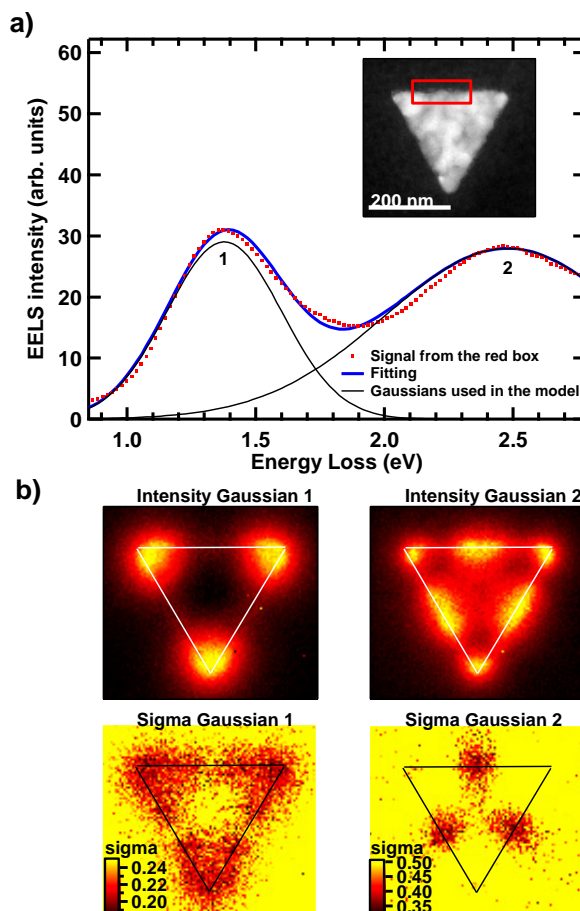


Figure 3.14: (a) A model containing two Gaussians is used to fit an EEL spectrum coming from the sum of pixels in the red box of the HAADF image. Then, the parameters values of this fit are used to start the fitting procedure (fit of the EEL spectrum of each pixel x - y with the model). (b) The intensity and the sigma ($FWHM/2\sqrt{2\ln(2)}$) parameters of each Gaussian are plotted for each pixel x - y . The energy positions of the Gaussians were fixed in the fitting procedure.

3.4. Sample fabrication of silver clusters

The silver cluster samples were prepared by physical methods (Energy Cluster Beam Deposition (LECBD) [99] and magnetron sputtering [100]) by our collaborators Matthias Hillenkamp and Nicolas Troc in the Institut Lumière Matière, Université de Lyon 1, France. In these methods, the silver clusters are produced in a gas phase from a silver target of high purity. The clusters are guided towards a substrate (which has been previously covered by a silica layer) and deposited at the same time with silica (co-deposition), see figure 3.15. At the end we obtained encapsulate clusters. The choice of

silica matrix is because it is transparent to the visible light and does not present EEL signal at low energies.

The nanoparticle concentration is adjusted by the relative fluxes of the silica matrix and the metal particles. Special care was taken into account on the concentration in order to get well separated clusters to avoid coalescence and to avoid optical signal coming from the coupling of particles.

The clusters were deposited at low energy by the process of soft-landing [101], in which the clusters were decelerated before the impact on the substrate (typically < 0.5 eV/atom). The soft-landing avoids the fragmentation of the clusters. A time-of-flight mass spectrometer (TOF-MS) was employed to study the size distribution of the clusters before deposition.

The substrate used for optical characterization was of fused silica and for STEM-EELS characterization was of carbon (3 nm thickness).

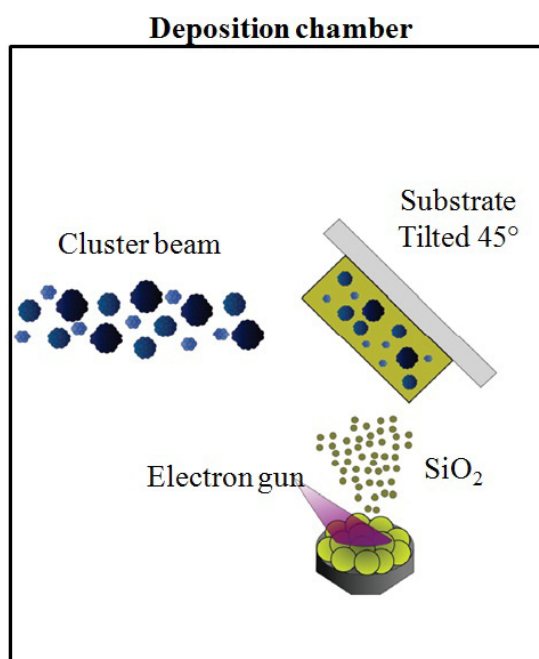


Figure 3.15: *Simplified schema of the cluster-matrix co-deposition. Adapted from Ref. [87].*

In the samples prepared for EELS characterization which studies individual particles, a large size distribution of particles and a low concentration of particles are convenient. However, in the case of optical characterization on ensemble of particles, a narrow size distribution is strictly needed. Because the optical response depends on the volume of the particles (see equation 2.4.21), the optical signal could be dominated by the largest particles even if the size distribution is centered in the small particles. One example is illustrated in figure 3.16 where the size distribution is centered at particles of ~ 50 atoms but due to the extended tail of the size distribution towards large particles, the optical density (proportional to the volume of the particles) is centered to particles of ~ 75 atoms.

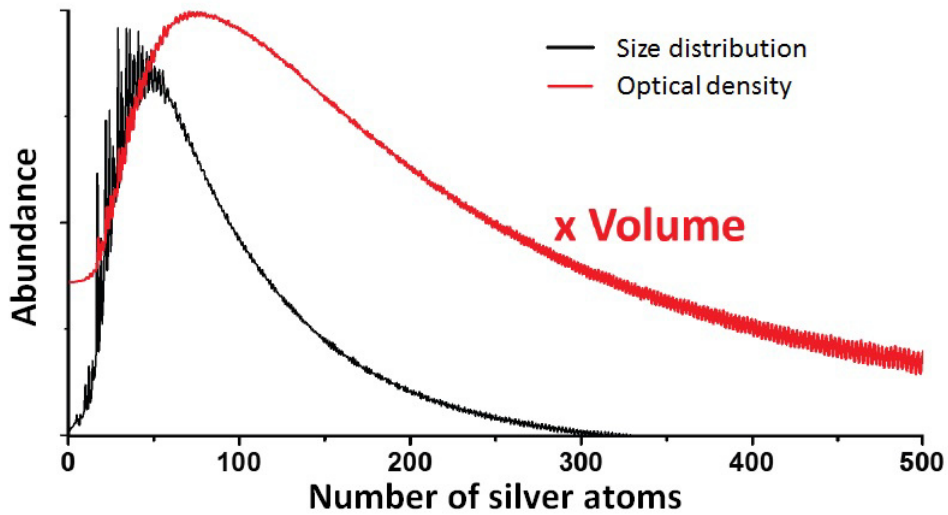


Figure 3.16: Time-of-flight mass spectrum of silver clusters whose distribution is centered around 50 atoms ($d \approx 1.2$ nm). The optical density associated with each cluster size was also calculated. For large sizes, the masses are no longer resolved and the signal corresponds to amplified noise. Taken from Ref. [87].

In order to crop the tail of the size distribution and get a narrow distribution, a quadrupolar mass spectrometer (QMS) was used to remove small and large cluster ions from the beam prior to deposition, see figure 3.17. The position and width of the transmission window can be tuned via the parameters of the QMS.

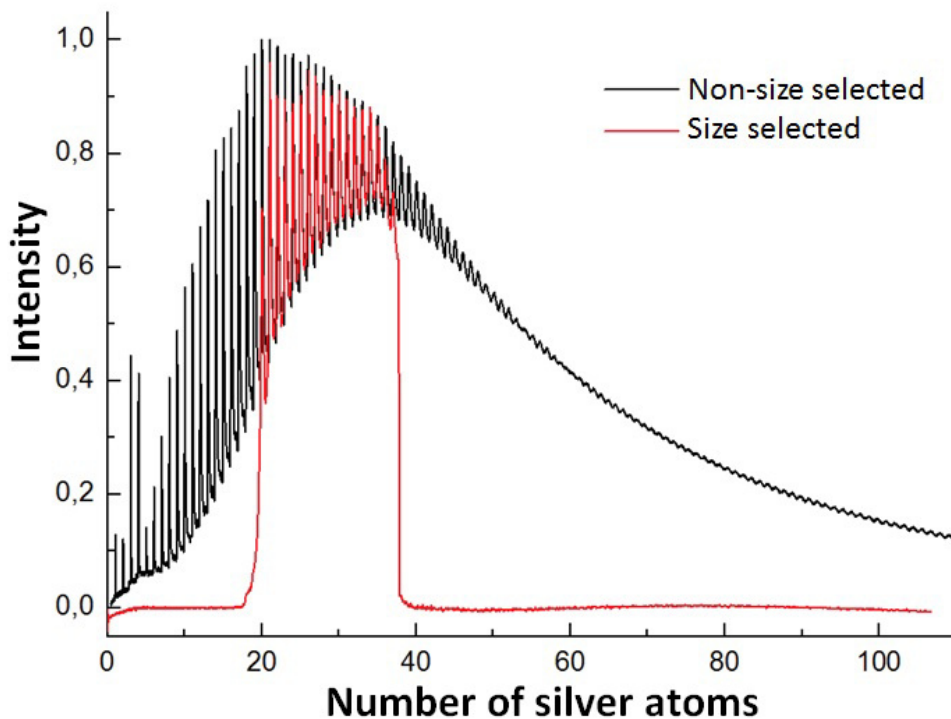


Figure 3.17: The black curve represents an unfiltered mass spectrum. The red curve represents the distribution filtered by the QMS. Taken from Ref. [87].

In samples prepared for optical characterization, a high optical density of particles is needed in order to get a reasonable level of signal and, at the same time, the particles must be well separated to avoid signal coming from the coupling of particles. To obtain these conditions, the samples for optical characterization were prepared with thickness of $\sim 1\ \mu\text{m}$ and concentrations of $<1\ \text{at.}\%$. On the other hand, the STEM-EELS characterization requires thin samples and for this characterization the samples were prepared with thickness of 30-100 nm. The table 3.1 summarizes the samples prepared in this thesis

	Cluster samples for STEM-EELS characterization	Cluster samples for optical characterization
Source	Energy Cluster Beam Deposition (LECBD) or magnetron sputtering	Magnetron sputtering
Silica thickness	30-100 nm	1 μm
Narrow size distribution	Not necessary	Yes (by the QMS)
Particle Concentration	Low	Low
Soft-landing	Yes	Yes
Substrate	Carbon (3 nm thickness)	fused silica

Table 3.1: *Samples prepared for STEM-EELS and optical characterization.*

After the preparation, the samples were taken out of the preparation chamber and characterized by optical experiments or stored under argon atmosphere and sent to us for EELS characterization. The time between preparation and optical characterization is of several minutes and between preparation and STEM-EELS characterization is of several hours.

3.5. Conclusion

In this chapter the optical absorption characterization, the electron energy loss spectroscopy (EELS) technique and the sample preparation of silver clusters were described. The STEM-EELS system was detailed from an experimental point of view. The data analysis of raw EELS data was presented showing that deconvolution techniques can be a very efficient tool to resolve plasmon peaks in large nanostructures. All the data processing described in this chapter can be used for most of the plasmonic studies with a STEM-EELS system in particles of a few hundred nanometers. However, in very small nanoparticles the plasmon signals are weak and a more in-depth optimization of the STEM-EELS system must be considered. This will be described in the next chapter.

Chapter 4: Optimization of EELS data acquisition

4.1. Introduction

In the previous chapter it was shown that low energy plasmons, close to the ZLP, can be superimposed on the ZLP tail. These plasmon peaks can be resolved by the reduction of the ZLP width (improvement of the energy resolution). In very small nanoparticles the plasmon signals are weaker than in large nanoobjects and, therefore, the ZLP width is not the only parameter to be considered. The dynamic range, the signal-to-background and signal-to-noise ratios play also a crucial role in the observation of weak plasmon signals. The dynamic range (ability to detect at the same time the more intense and the weakest signals) is extremely important to acquire the ZLP and a weak plasmon signal in the same spectrum, see figure 4.1. On the other hand, the improvement of the signal-to-noise ratio cannot be done by acquiring data during long time due to electron dose effects. It is evidenced that in very small particles the electron dose can reduce the size of the particles or even destroy them. This double constraint of detecting weak signals with low electron doses requires bringing the EELS detection to high optimization.

In this chapter I will present the optimization of the EEL spectrometer setting and the CCD acquisition parameters in order to improve the energy resolution, the dynamic range and the signal-to-background and signal-to-noise ratios. The EELS-CCD detection system will be explained in more details and the sources of noise and the way to overcome them are also presented. The electron dose effects and the strategies to reduce them will be discussed. Additionally, the EELS data analysis methods to study weak plasmon peaks will be described.

The optimization of the EELS experiment and data analysis enabled the detection of plasmon signals in silver particles as small as 1.7 nm in diameter without electron dose damage. This has been one of my main contributions in this thesis.

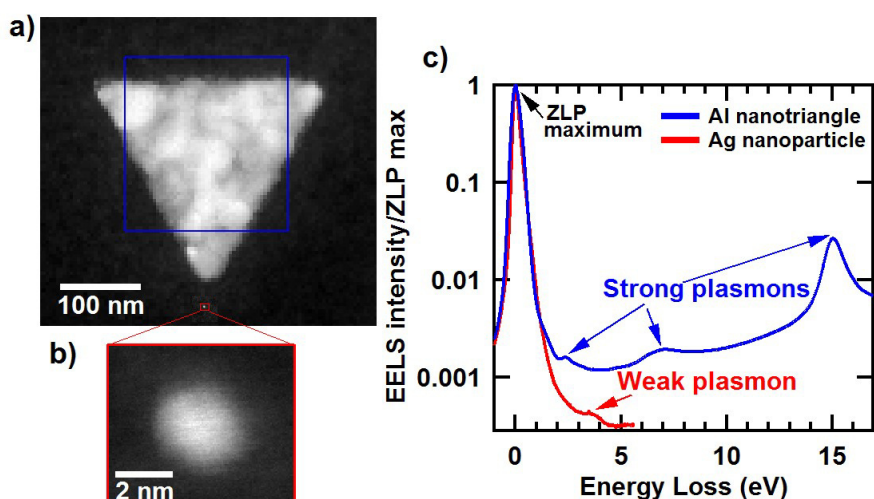


Figure 4.1: The two types of samples studied in this thesis: aluminum nanotriangles and silver particles. (a) Image showing an Al nanotriangle and an Ag particle with the same scale bar for comparison. (b) Zoom on the silver nanoparticle. (c) Comparison of the EELS plasmon signal extracted from both samples (blue and red boxes in the image) where a clear difference of the plasmon intensities is evidenced. The weak plasmon signal in the silver particle has required a high optimization in order to be detected.

4.2. EELS-CCD camera

The EEL spectrometer disperses the transmitted electrons in one direction according to their energy loss. Usually in EELS experiments a CCD camera is used as a detector in which the horizontal direction is the dispersive axis and the vertical direction is the non-dispersive axis. The transmitted electrons cannot be directly acquired by the CCD sensor and a scintillator has to be employed in order to convert the incident electrons into photons (see figure 4.2a). These photons arrive to the CCD sensor and are converted into electrons. In each pixel of the CCD camera the number of electrons produced is proportional to the number of photons that arrives. Each pixel can hold a maximum number of electrons. The charge in a pixel is read-out by changing the electrical bias of an adjacent pixel so the charge travels out the sensor (figure 4.2b). Then an analog to digital (A/D) electronic measures the voltage created by the packet of electrons and turns this into a digital number that can then be digitally transmitted to and saved by a computer. In the read-out process the signal can be amplified by a gain factor (g). Furthermore, in this read-out process a read-out noise is added.

The EEL spectrometer of the UltraSTEM200 works with a CCD camera (ProEM+:1600 EMCCD from Princeton Instrument) which has 1600 pixels along the dispersive axis and 200 pixels along the non-dispersive axis. This CCD camera is a 16-bit A/D system. It means that it can display $2^{16} = 65\,535$ ADU (analog to digital unit) in any given pixel. The scintillator is an Yttrium Aluminum Garnet (YAG). The optical coupling between the CCD sensor and the scintillator is a homemade optical lenses system. This system significantly reduces the sources of signal variations with respect to traditional optical coupling using optical fibers. The homemade optical lenses system was developed by Marcel Tencé in the Laboratoire de Physique des Solides in Orsay.

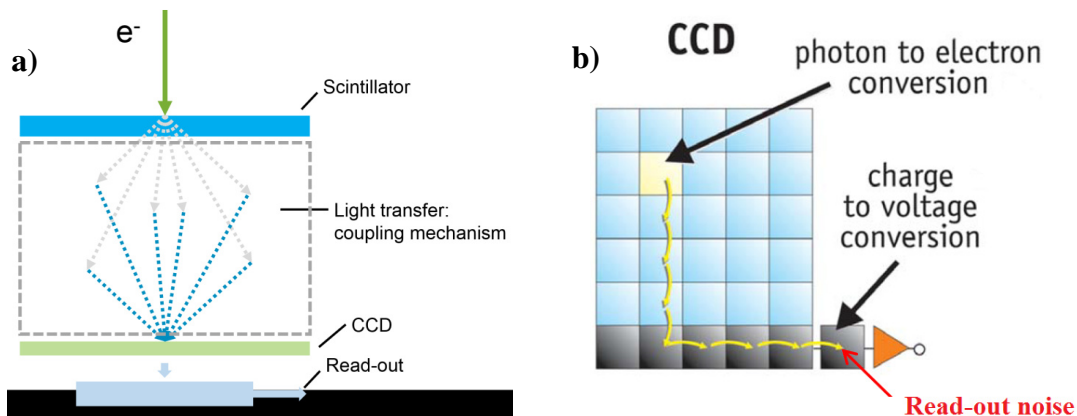


Figure 4.2: (a) Scheme of the scintillator-CCD sensor. (b) Illustration of a CCD camera as used for EELS experiments in this thesis. The electron charge travels out the sensor by changing the electrical bias of an adjacent pixel. At the end the charge is converted into an electronic number. A read-out noise is added to the signal in this process (read-out noise). The images were adapted from <http://www.gatan.com>.

Another important parameter of the CCD camera is the quantum efficiency (QE) which corresponds to the quantity of photons converted into electrons. It is an intrinsic property of the CCD and it depends on the wavelength of incident photons. For simplicity we will consider it constant and equal to unity ($QE=1$) which is close to the reality (see figure 4.3).

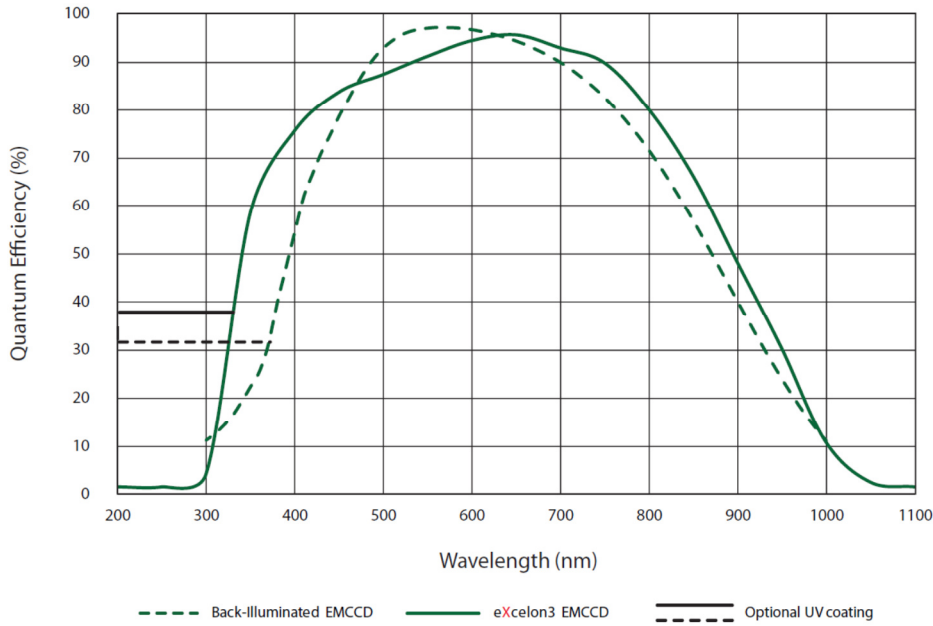


Figure 4.3: Quantum efficiency (QE) of the ProEM+:1600 EMCCD (used in the UltraSTEM200) measured at 25 °C (green dashed line). The QE is close to unity at 550 nm. Data taken from <https://www.princetoninstruments.com>. The scintillator (YAG) used in the UltraSTEM200 EEL spectrometer emits light at 550 nm which ensures the maximum QE of the CCD camera.

A CCD camera can be affected by different sources of noise:

Shot noise: the shot noise is a fundamental property of the stochastic nature of the electron gun emission, as well as the quantum nature of light and arises from the resulting statistical fluctuations in the number of photons emitted from the scintillator. This is an unavoidable source of noise which can be described by a Poisson statistic. If S is the signal, then the shoot noise is

$$N_S = g\sqrt{S} \quad (4.2.1)$$

Let's note that the amount of signal is a function of the acquisition time (t).

Dark current and its noise: The dark current (DC) is created by electrons generated thermally in the silicon substrate of the CCD camera. The dark current noise is given by the square root of the dark current signal. Since dark charges also go through the gain process the dark current noise is

$$N_{DC} = g\sqrt{DC} \quad (4.2.2)$$

The dark current is also a function of the acquisition time and it decreases drastically at low temperatures.

Read-out noise: This is the intrinsic noise of the electronic of the CCD camera associated to the transformation of charge carriers into voltage. The read-out noise is noted as the square root of the readout background R

$$N_R = \sqrt{R} \quad (4.2.3)$$

Gain variation: As the amplified signal is gS and from one pixel to another the gain can be different, we have to consider the gain variation

$$N_{g \text{ var}} = S(\delta g) \quad (4.2.4)$$

The total noise can be written as

$$N_t = \sqrt{N_S^2 + N_{DC}^2 + N_R^2 + N_{g \text{ var}}^2} \quad (4.2.5)$$

$$N_t = \sqrt{g^2S + g^2N_{DC} + R + S^2(\delta g)^2} \quad (4.2.6)$$

Then the signal to noise ratio (SNR) can be written

$$SNR = \frac{gS}{N_t} = \frac{gS}{\sqrt{g^2S + g^2N_{DC} + R + S^2(\delta g)^2}} \quad (4.2.7)$$

At low temperatures the dark current can be neglected (the CCD camera is cooled in the EELS experiments performed in this thesis and the dark current is negligible)

$$SNR = \frac{gS}{\sqrt{g^2S + R + S^2(\delta g)^2}} \quad (4.2.8)$$

Due to the fact that the CCD-scintillator optical coupling in the UltraSTEM200 is performed through optical lenses, the CCD sensor is not in direct contact with any element and it can be cooled at lower temperatures than the case of attached CCD-scintillator by optical fiber. In this way we reduce the dark current in a more significant way.

From equation 4.2.8 we can deduce that:

*At low dose (low signal) the SNR is limited by the read-out noise. In this case the increase of gain could help to increase the SNR.

*At high dose (high signal) the SNR is limited by the noises proportional to the signal like gain variation. It is an important observation since it shows that it is not possible to acquire data forever to increase the SNR.

In order to increase the signal-to-noise ratio a number of pixels in the non-dispersive axis can be combined (binning) creating a 'big pixel' which is then read and digitized. In this way the read-out noise is added once for the big pixel instead of a read-out noise for each individual pixel. With binning equation 4.2.8 becomes

$$SNR = \frac{MgS}{\sqrt{Mg^2S + R + MS^2(\delta g)^2}} \quad (4.2.9)$$

Where M is the number of binned pixels. A binning of 200 pixels in the non-dispersive axis was used in this thesis for EELS experiments.

4.3. EEL spectrometer optimization

At the beginning of my thesis, there were two main issues with the electron gun that affected the optimization of the compromise between energy resolution and current. The first was related to electronics noise in the electron gun tank, which was diagnosed, motivated this thesis experimental challenges, few months before my thesis start and fixed by the manufacturer by changing the electron gun driving electronics. The second issue related to the optimization of the electron gun optics, meaning an optimization of the focal length of the gun lens 0 in figure 3.4, which suffers from chromatic aberrations. With these changes we obtained high electron beam currents (necessary for plasmonic experiments in small particles) and at the same time a good energy resolution. We note that before these changes, the energy resolution (FWHM of the ZLP) was on the order of 400 meV and no plasmon signal could be detected in silver nanoparticles smaller than 5 nm. After the changes we obtained ZLP FWHM ≤ 300 meV with high electron beam currents (~ 60 pA), see figure 4.4. The experiments for the focal optimization were performed by K. March and M. Kociak in the Laboratoire de Physique des Solides in Orsay.

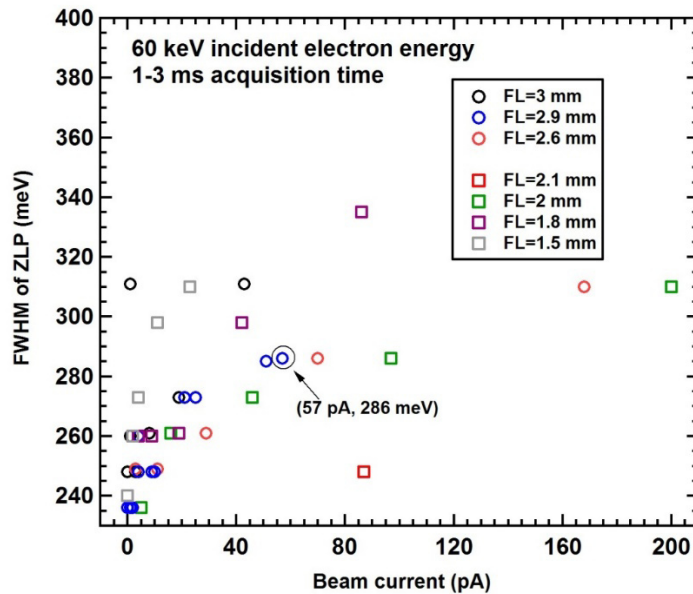


Figure 4.4: Full width at half maximum of the ZLP as a function of the electron beam current for different focal length. For FL=2.9 mm the ZLP FWHM was lower than 300 meV with high beam currents (~ 60 pA). The experiment was done without sample (in vacuum). “FL” is the focal length of the gun lens.

4.3.1. Aberrations

The full width at half maximum of the ZLP (energy resolution) strongly depends on the aberrations of the EEL spectrometer. In the Low-Loss region, the ZLP appears as a very intense spot (see figure 4.5) in the two dimensional CCD camera. The ZLP spot must be as sharp as possible along the disperse axis (x axis of the CCD) in order to get the lowest ZLP width. However, this spot can suffer from aberrations which deform the ZLP spot into different symmetries. Figure 4.5 shows the lower order aberrations that affect the ZLP spot symmetry. To correct these aberrations, combined quadrupoles (FocusX, FocusY, Q1, Q2, Q3, Q4) and sextupoles (SX, SY) lenses are used.

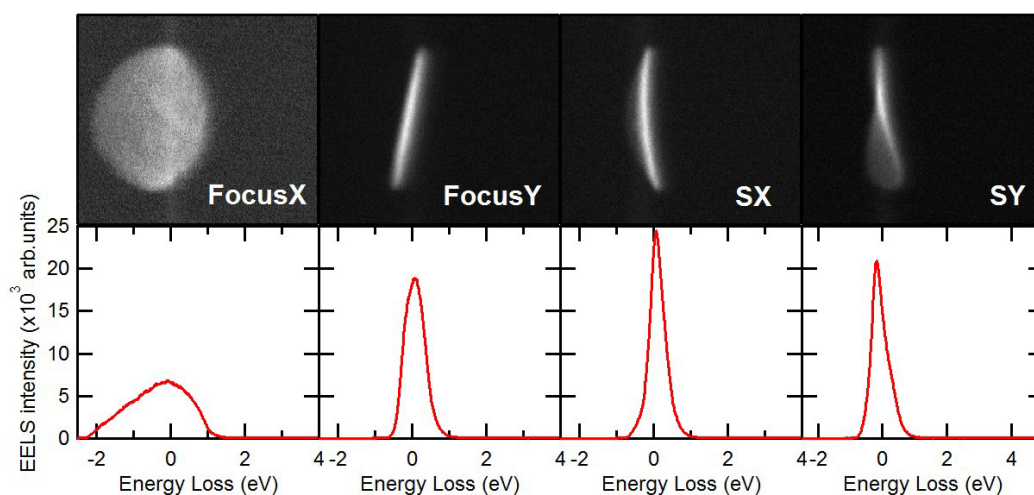


Figure 4.5: (Upper panel) Lower order aberrations that affect the ZLP spot symmetry and the quadrupole-sextupoles lenses needed to correct them. (Bottom panel) EEL spectra coming from a binning of 200 pixels in the non-dispersive axis (y axis) of the CCD camera in upper panel. The signals were taken on carbon substrate at similar electron beam currents and acquisition times.

After the correction of the aberrations by the quadrupoles/sextupoles lenses, the ZLP achieves the lowest width (figure 4.6). To decrease even more the ZLP width, EELS apertures are used, see section 3.3.3. This enables the reduction of the collection angles and, therefore, to avoid the electrons trajectories that contribute more to the aberrations. In the UltraSTEM200 microscope with EELS apertures of 2 and 1 mm, the collection semi-angle (β) is reduced from 30 mrad to around 17 mrad, respectively. Figure 4.6 shows the change of the ZLP spot with EELS apertures of 2 and 1 mm. The intensity of the ZLP is reduced with the 1 mm aperture due to the reduction of the number of electrons impinging on the CCD camera.

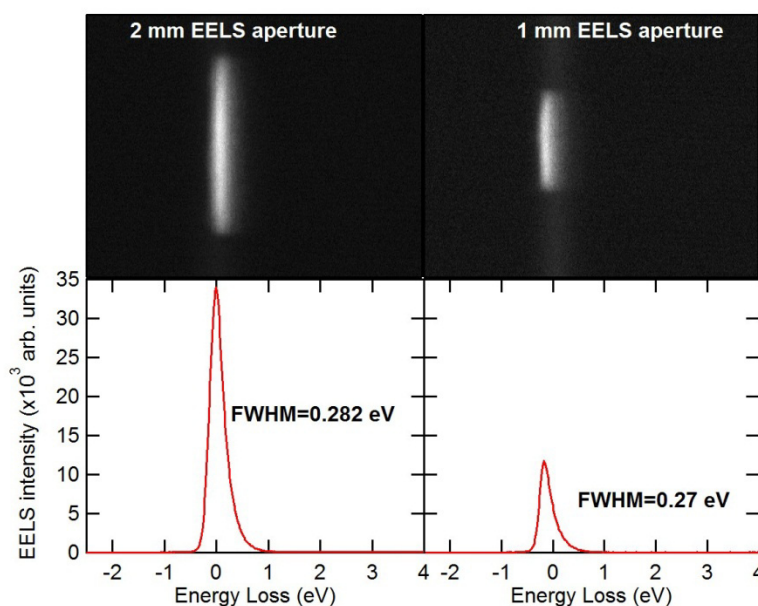


Figure 4.6: (Upper panel) ZLP spots with EELS apertures of 2 and 1 mm, respectively. (Bottom panel) EEL spectra obtained after binning of 200 pixels in the non-dispersive axis (y axis) of the CCD camera in upper panel.

The ratio of area under the curves of figure 4.6 (area defined as $area = Intensity_{max} * FWHM$) is ~ 3.3 , which means that there is ~ 3 times less electrons impinging on the CCD camera with the 1 mm EELS aperture.

The EEL spectra of figure 4.6 are normalized by the ZLP maximum and compared in figure 4.7. As observed the ZLP width is reduced with the smallest EELS aperture.

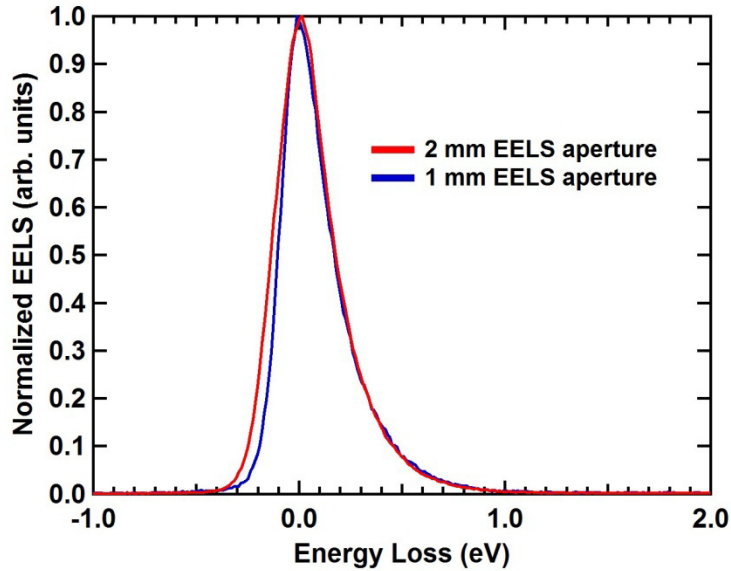


Figure 4.7: Comparison of the ZLP with EELS apertures of 2 and 1 mm. The ZLP FWHM decreases from 0.282 eV to 0.27 eV when passing from 2 to 1 mm EELS aperture, respectively.

The asymmetric form of the ZLP is characteristic of a field emission source where the energy profile is described by the Fowler-Nordheim (F-N) Distribution [102].

4.3.2. Energy dispersion and beam current

As discussed previously, the ZLP tail is crucial because it can mask weak plasmon peaks. The energy dispersion (energy per pixel in the CCD dispersive axis) can affect the extent of the ZLP tail and the ZLP FWHM as was reported in literature [103]. The smaller the ZLP FWHM, the easier it is to distinguish low loss signals (plasmons, phonons, excitons, interband transitions). However, the ZLP FWHM is not the only parameter to be considered since the low loss signal can be very weak and might be lost on the ZLP tail background. A good figure of merit is the Kimoto limit, which corresponds to the Full width at 1/1000 max [104]. In figure 4.8 it is observed that the lowest ZLP FWHM and the lowest ZLP tail intensity (touching the Kimoto limit) are found at the lowest energy dispersion (0.011 eV/pixel). Through this thesis we used this energy dispersion.

The increase of beam current promotes the appearance of the *Boersch effect* which corresponds to a broadening of the distribution of axial velocities due to statistical Coulomb interactions between the electron beam particles. This spreads the energy of the electrons and it is reflected in an increase of the ZLP width. As figure 4.9 shows, the lowest ZLP FWHM is found at lowest beam currents. However, in practice it is not

convenient to work at very low beam currents because the low signal on the EELS detector. We used a current beam between 40 to 140 pA in which there is a good compromise between energy resolution and an acceptable level of signal on the EELS detector.

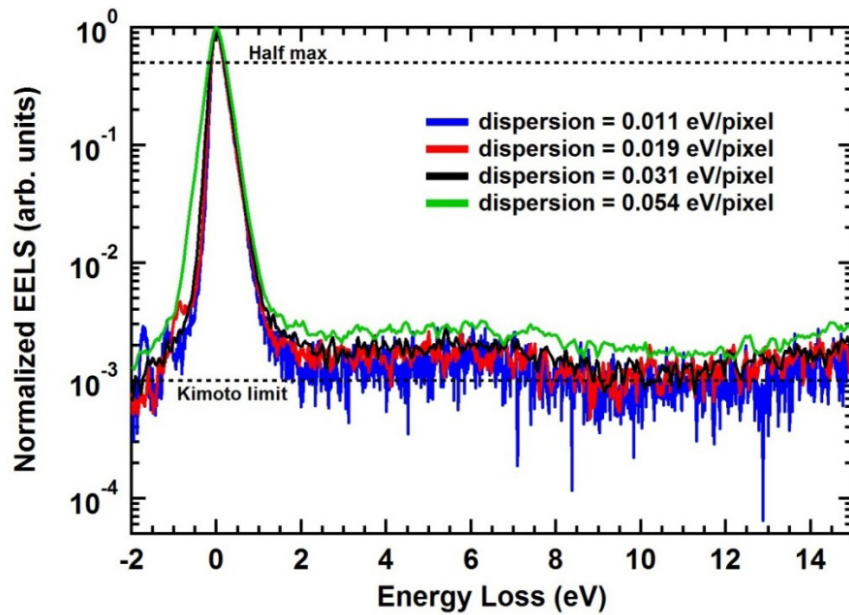


Figure 4.8: Width and tail intensity of the ZLP taken on carbon substrate for different energy dispersions. The lowest ZLP FWHM and ZLP tail intensity were obtained at the lowest energy dispersions. The ZLP FWHM was 0.43 eV, 0.31 eV, 0.29 eV and 0.27 eV for energy dispersions of 0.054 eV/pixel, 0.031 eV/pixel, 0.019 eV/pixel and 0.011 eV/pixel respectively. At low energy dispersion the intensity of the ZLP tail is close to the Kimoto limit at energies ≥ 2 eV and down to 10^{-3} at energies ≥ 7 eV.

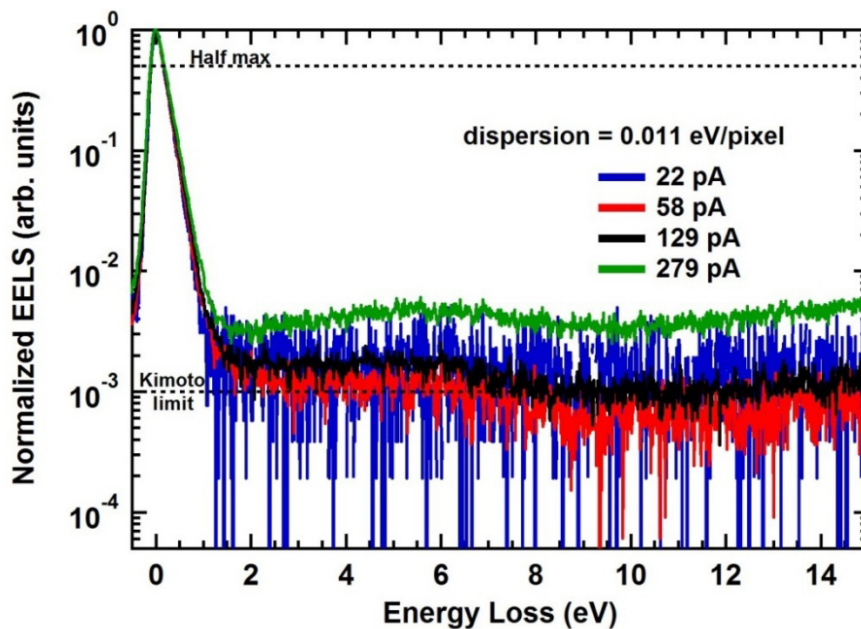


Figure 4.9: Decrease of the ZLP width with the decrease of electron beam currents. The best resolution is obtained at low electron beam currents. The ZLP FWHM was 0.29 eV, 0.27 eV, 0.27 eV and 0.26 eV for beam currents of 279 pA, 129 pA, 58 pA and 22 pA respectively. The spectra were taken on carbon substrate. For the lowest beam currents, the ZLP tail is close to the Kimoto limit at energies ≥ 2 eV and down to 10^{-3} at energies ≥ 7 eV.

The reason why we do not have ZLP tails below 10^{-3} ZLP maximum at low energies (1-4 eV) is most probably due to the carbon substrate. The carbon presents a peak shoulder at ~ 6 eV. In appendix E, EEL spectra acquired in different substrates and in vacuum are presented. We found that the ZLP tail goes down 10^{-3} ZLP maximum in silicon nitride substrate at energies ≥ 2 eV. However, in Si_3N_4 substrates it was easier to create damage by the electron beam irradiation. This caused the particles to move a lot and promoted mechanical instability. On the other hand, the carbon substrate presented better stability under the electron beam irradiation. Additionally, the thickness of the carbon substrate is only 3 nm, which allows getting more signal in the EELS detection system. For these reasons we decided to use carbon substrates.

4.3.3. Dynamic range

One of the difficulties of EELS experiments in sub-10 nm silver particles is the measurement of weak plasmon signals on top of the ZLP tail which, at the energy of the plasmon resonance, is of similar intensity (10^{-3} of the ZLP maximum), see figure 4.10. Dynamic range can be defined as the ratio between the maximum output signal level and the noise floor. Dynamic range represents the CCD camera's ability to display the more intense and weakest signals.

In EELS experiments on small silver nanoparticles a CCD camera with a large dynamic range was used in order to measure the intense ZLP (necessary for the energy calibration of the spectrum as will be described in the next section) and weak plasmon peaks in the same spectrum. A strategy for increasing the dynamic range is to take advantage of the maximum of counts available (A/D units) in a given pixel. It is achieved by adjusting the acquisition time in order to put the ZLP maximum close to the saturation ($\sim 60\,000$ counts).

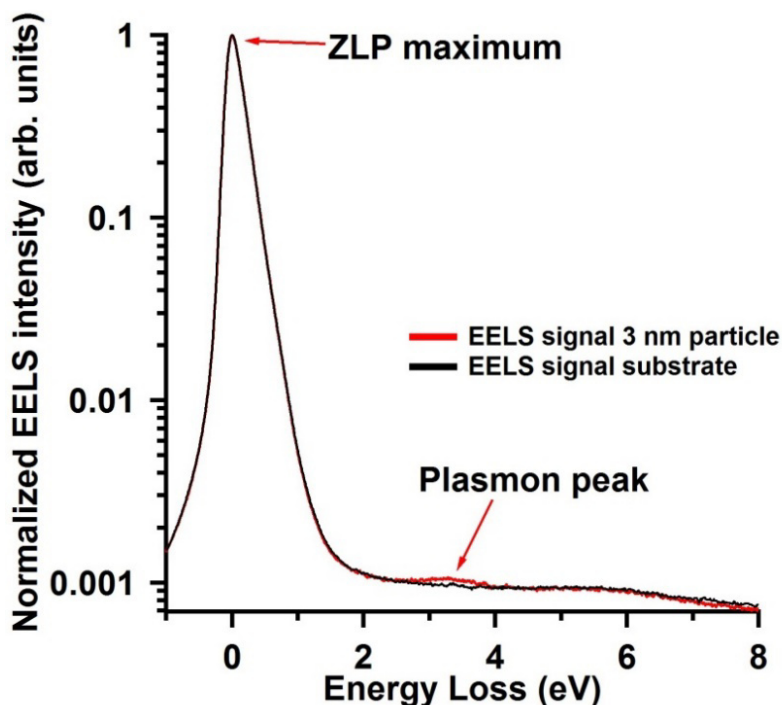


Figure 4.10: EEL signal from the surface of a 3 nm silver nanoparticle compared to the EEL signal from only the carbon substrate (covered by silica). Note the logarithmic scale for the EELS intensity. In the spectral region of interest, the ZLP tail intensity is of the order of 10^{-3} with respect to the ZLP maximum.

4.4. Calibration of the EEL spectrum

In order to detect any shift in the plasmon resonance of nanoparticles it is important to verify the calibration of the EEL spectra. Usually the energy calibration can be done if there are at least two peaks of known energies. However, in Low-Loss EELS experiments it is not always the case. Most of the time, the only peak we know very well is the ZLP.

In order to verify the calibration, a voltage is applied to a drift tube (see scheme of figure 3.6b) which shifts the EEL spectrum in the dispersive axis of the CCD camera. The shift of the EEL spectrum is measured by the ZLP shift and compared with the applied drift tube voltage. For example, with a drift tube voltage of 2 V, the ZLP should shift around 2 eV. If this is not the case the EEL spectra must be recalibrated.

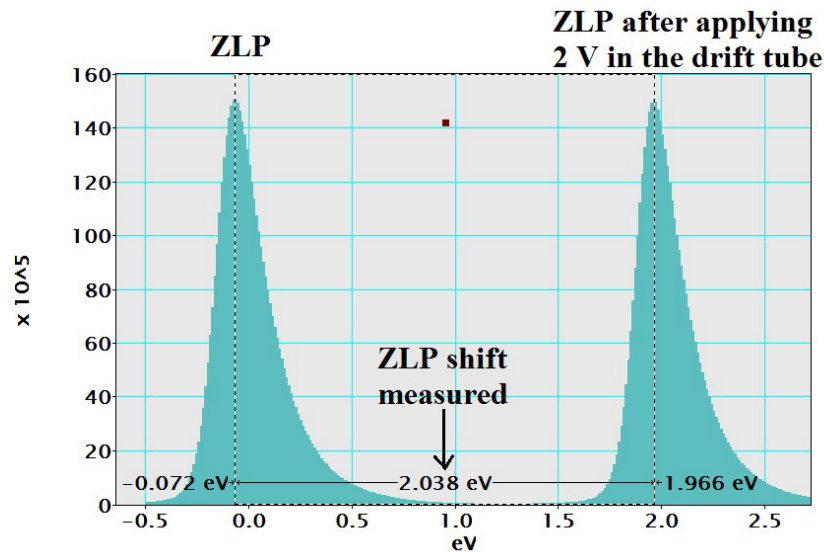


Figure 4.11: A drift tube voltage is applied which shifts the ZLP on the dispersive axis of the CCD camera. The ZLP shift is measured and compared with the drift tube voltage.

Table 4.1 shows the comparison between applied drift tube voltages and the ZLP shift measured in different days. A relative error is estimated at 1 %.

Date	Drift tube voltage	ZLP shift measured
09/08/2016	2 V	2.005 eV
23/01/2017	2 V	2.027 eV
16/03/2017	2 V	2.005 eV
	14 V	14.144 eV
10/02/2017	2 V	1.971 eV
11/02/2017	2 V	2.038 eV
14/02/2017	2 V	2.027 eV

Table 4.1: Drift tube voltages and the corresponding ZLP shift measured in the EEL spectrum in different days. The energy dispersion was set to 0.011 eV/pixel in all measurements.

4.5. Improving signal-to-noise ratio (combining pixels in the spectrum-image)

As discussed in section 4.2, the binning of the CCD in the non-dispersive axis helps to increase the signal to noise ratio. However, it is not enough to bring out a weak plasmon signal. In order to evidence a weak surface plasmon peak and increase the signal to noise ratio it is necessary to sum numerous spectra in a spectrum-image for beam positions close to the nanoparticle surface as shown in figure 4.12. In this figure the signal increases by three orders of magnitude, making the signal-to-noise ratio much larger than 30.

With the sum of m pixels in a spectrum-image equation 4.2.9 can be written as

$$SNR = \frac{mMgS}{\sqrt{mMg^2S + mR + mMS^2(\delta g)^2}} \quad (4.5.1)$$

For example, with a 16 bit CCD camera, the ZLP is put close to the saturation ($2^{16} \approx 60000$). Considering a weak plasmon peak of 10^{-4} ZLP (6 counts), a read-out background of ~ 20 counts, a gain of 1, binning of 1 and ignoring the gain variation for simplicity we obtain

$$SNR \approx \frac{mS}{\sqrt{mS + mR}} \quad (4.5.2)$$

For $m=1$

$$SNR \approx \frac{S}{\sqrt{S + R}} = \frac{6}{\sqrt{6 + 20}} \approx 1$$

It is impossible to detect this signal. However, summing 900 pixels we obtain

$$SNR \approx \frac{mS}{\sqrt{mS + mR}} = \frac{900 * 6}{\sqrt{900 * 6 + 900 * 20}} \approx 35$$

In this case the SNR is larger than 30 and the peak can be easily observed.

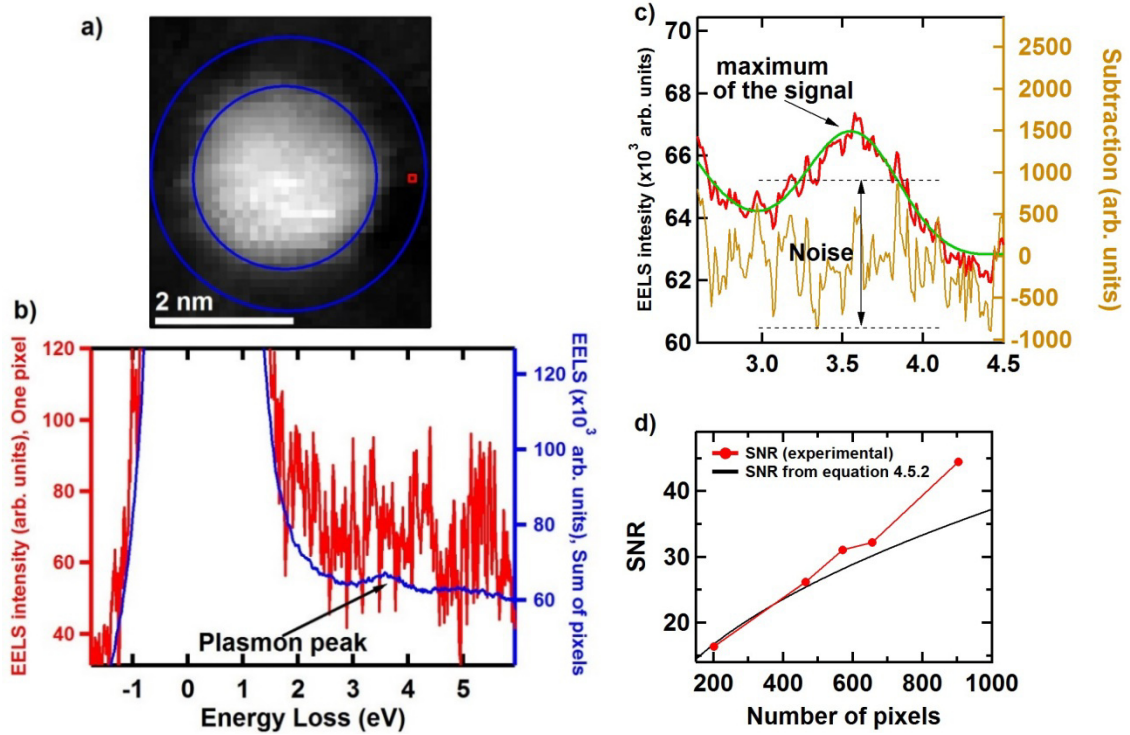


Figure 4.12: (a) Silver nanoparticle of 2.7 nm diameter embedded in silica matrix. (b) Comparison of spectra extracted from one pixel (red spectrum extracted from the red box in a) and the spectrum resulting from the sum of the spectra contained in numerous pixels (blue spectrum extracted from the pixels between the blue circles in a). The plasmon peak is observed only after summation (900 pixels were summed around the particle). (c) Fit of the plasmon peak. The subtraction of the plasmon peak with the fit gives the noise. (d) Signal-to-noise ratio (SNR) is calculated as the maximum of the plasmon peak divided by the noise in the spectral range 3-4 eV. We observe an increase of SNR with the increase of number of pixels.

4.6. Role of the impact parameter

One interesting parameter explored in this thesis is the electron impact parameter x_0 . In real experiments, one tries to locate the electron probe as close as possible to the surface of the nanoparticles ($x_0 \rightarrow R$), see section 2.4.3. At small impact parameters and low energies (which is the case of small silver nanoparticles embedded in silica matrix) we found that the dipolar mode in the EELS probability is proportional to the extinction (or absorption) cross-section (equation 2.4.46)

$$\Gamma_{L=1}(\omega) \propto \frac{\sigma_{ext}}{\varepsilon_m^{3/2} \omega R^2} = R \frac{4\pi}{c \varepsilon_m} \text{Im}[(\varepsilon - \varepsilon_m)/(\varepsilon + 2\varepsilon_m)] \quad (4.6.1)$$

Because the optical extinction (or absorption) cross-section scales as R^3 , the EELS probability depends linearly on the radius (see figure 4.13a). This is an important result that proves the feasibility to study small nanoparticles in EELS experiments without losing too much signal. In figure 4.13b and c, the calculated absorption cross-section (calculated from equation 2.4.21) and the EELS probability (calculated from equation 2.4.44 at $x_0 = R$) are plotted for different silver nanoparticles diameters embedded in silica matrix. The experimental EELS results (figure 4.13d) are also plotted for different

silver nanoparticles in silica, with similar electron doses, taken in a region around the nanoparticles surface (see inset of figure 4.13d). As it is observed for a 2 nm nanoparticle, the absorption cross-section is very weak with respect to a 10 nm nanoparticle. This is the reason why it is difficult to do optical experiments on a very small individual particle. On the other hand, the EELS probability of a 2 nm particle has a level of signal only 5 times smaller than a 10 nm particle. It means that in EELS experiments in particles as small as 2 nm there is no such drastic signal loss with respect to a 10 nm nanoparticle. The later was confirmed experimentally in figure 4.13d which proves the feasibility to do EELS experiments in very small silver clusters. Figure 4.13d also shows a LSP blue shift with the decrease of particle size that will be explained later in the frame of a classical/quantal calculation in chapter 5.

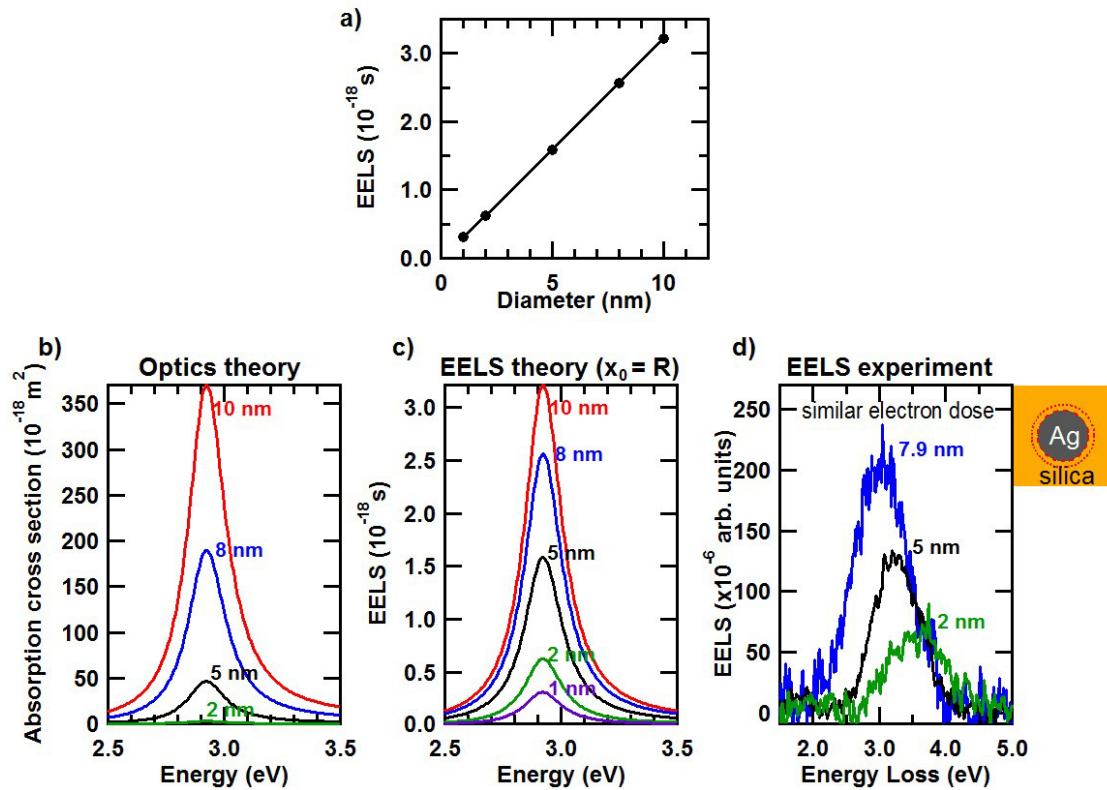


Figure 4.13: (a) Calculated EELS probability intensity at the dipolar surface plasmon resonance as a function of silver particle diameter from equation 2.4.44. (b) Calculated absorption cross-section spectra for silver nanoparticles of different diameters calculated from equation 2.4.21. (c) Calculated EEL spectra for silver nanoparticles of different diameters (from equation 2.4.44) and excited at $x_0 = R$. In a, b and c, the relative permittivity of the silica surrounding medium is assumed constant ($\epsilon_m = 2.16$) and the relative permittivity of silver is modeled from the Lorentz-Drude model of Ref. [53]. (d) Experimental EELS results for nanoparticles of different diameters and similar electron doses.

4.7. Electron dose effects

4.7.1. Afterglows

An afterglow is created when the EEL spectrum moves on the CCD camera and due to the high intensity of the ZLP, the scintillator-CCD system continues to detect signal where the ZLP was before moving (see figure 4.14). The reason why the scintillator-CCD system continues to detect signal is not well understood. The decrease of the intensity of an afterglow does not follow a linear behavior with time and it remains during long time. The best way to avoid an afterglow is to place the ZLP at zero energy position at the beginning of the experiment and always verify that the voltage instabilities do not shift it. An afterglow can create confusion if it is close to a real signal.

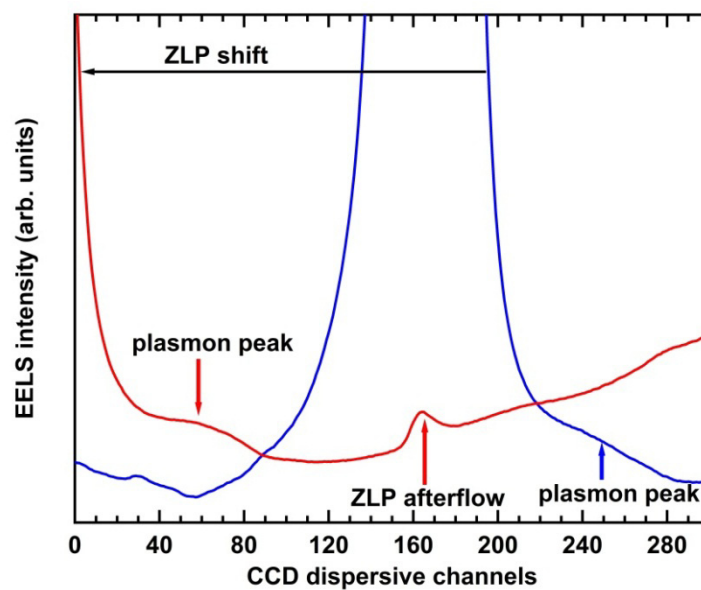


Figure 4.14: ZLP shifted intentionally to the left, out of the CCD camera. Before shift (blue spectrum) a small plasmon peak is observed. After the shift (red spectrum), the ZLP is out of the CCD camera and it enables the increase of the acquisition time without saturation of the CCD camera and the plasmon signal becomes more visible. However, we can observe an afterglow in the position where the ZLP was before shift, which could be misunderstood.

4.7.2. Electron dose damage

The energy of the electron beam can induce damages on the small particles and their environment. Special care has to be taken into account in order to avoid size reduction of the particles. For particles larger than 5 nm the electron beam damage is not evident during long exposition times. However, in sub-5 nm particles the reduction of size appears faster. Figure 4.15 shows the reduction of size of a sub-5nm silver nanoparticle submitted to long expositions to the electron beam.

Long exposition time (~ 1 hour)

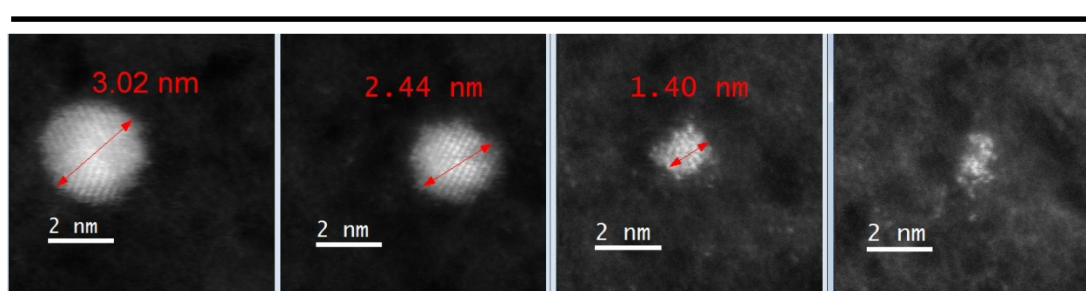


Figure 4.15: Size reduction of a silver nanoparticle exposed during ~1 hour to the electron beam scanning.

With low electron doses it is possible to avoid the size reduction of particles as it is shown in figure 4.16. The electron dose is the beam current multiplied by the acquisition time and divided by the area of the electron probe (more details in section 4.8).

Low electron dose ($0.9 \cdot 10^7$ electrons/ \AA^2)

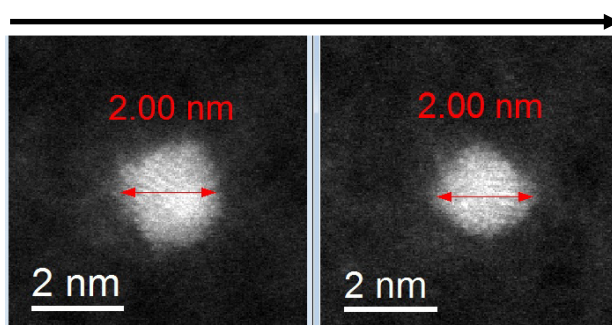


Figure 4.16: Avoiding size reduction of a silver particle exposed at low electron dose ($0.9 \cdot 10^7$ electrons/ \AA^2). The size of the particle remains the same but it is possible a particle rotation under the electron beam. We note that at this low dose it was possible to detect plasmon signals as will be presented in the results of chapter 5.

As already mentioned, the EEL signal coming from small nanoparticles is weak compared to larger nanoobjects (>50 nm). The constraint of using small doses in small nanoparticles makes the difference in signal intensities even more remarkable (see figure 4.17). However, with the large dynamic range of the CCD camera and the optimization of the EEL spectrometer and parameter acquisition, weak plasmon signals were detected at low electron dose without size reduction.

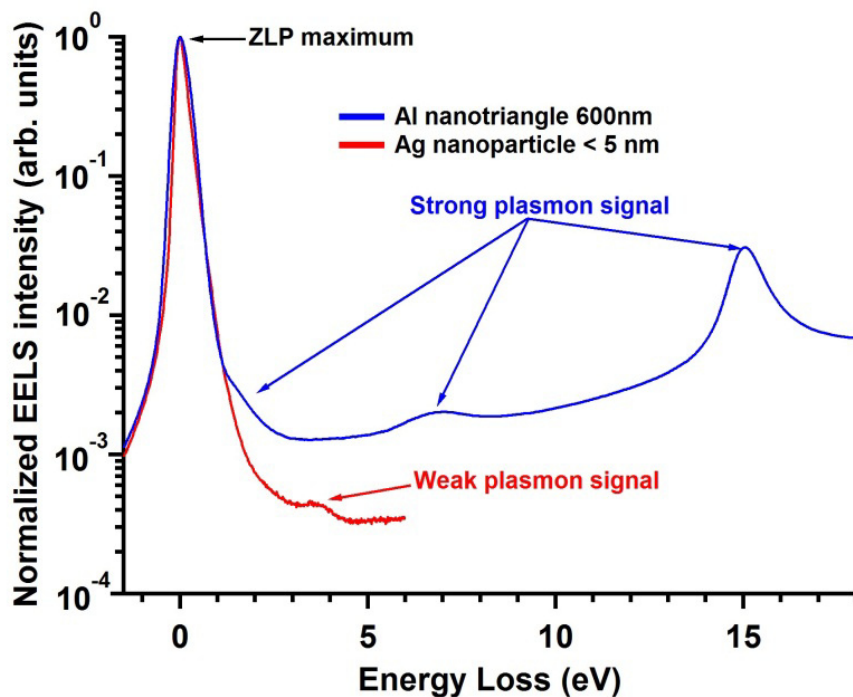


Figure 4.17: EEL signal of a sub-5 nm silver nanoparticle at low electron dose compared to the EEL signal coming from an aluminum nanotriangle of 600 nm side length. Both particles are deposited on Si_3N_4 substrates. It is clear the difference in the plasmon signal intensities of both nanoparticles.

4.7.3. Contamination

Another problem that can be present in STEM-EELS measurements is the contamination, which is the polymerization of hydrocarbon molecules on the surface of the sample induced by the incoming electron. This polymer has low surface mobility and a low vapor pressure [105]. Because the contamination increases the thickness of the sample it appears directly in HAADF images as a white spot (see figure 4.18a) and in the EEL spectra it appears as a peak at ~ 6 eV with a very high intensity (figure 4.18b). The intensity of the contamination peak increases with the increase of electron dose and the plasmon peaks can be hidden. The sources of contaminations in our experiments are not so clear but could be related to sample preparation or to the transfer through air to the storage boxes or even the microscope itself.

To avoid contamination problems we baked the samples in vacuum at ~ 100 °C before introducing them into the microscope. The heat promotes the desorption of hydrocarbons from the sample surface. If the contamination appeared during experiments, we changed of region on the sample or we applied an electron beam shower during few minutes. The beam shower consists in exposing a large sample area with the electron beam. With this process the surface hydrocarbons are fixed (polymerized) in a large area and prevent the diffusion towards a focus probe [105].

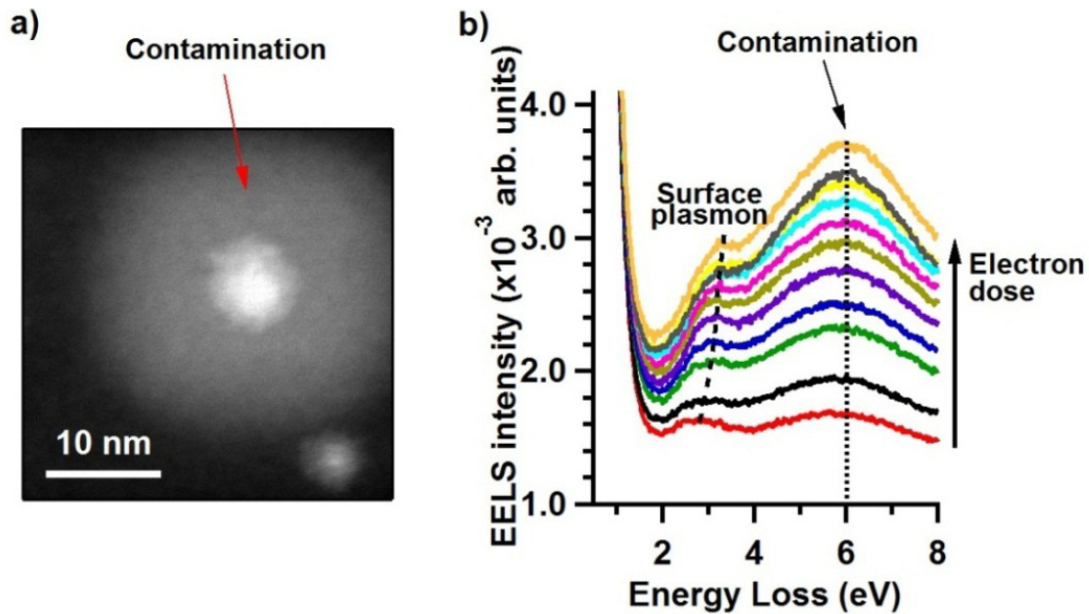


Figure 4.18: (a) HAADF image showing a big white spot of contamination around a silver nanoparticle after spectra acquisition. (b) EEL spectra from the surface of a silver nanoparticle showing a peak at around 6 eV that is attributed to the contamination. This peak increases with the increase of electron dose and the surface plasmon peaks can be hidden.

4.8. Stack of spectrum-images

In order to monitor the impact of the electron irradiation in small particles, another data acquisition strategy was used. Instead of taking a single spectrum-image, a stack of spectrum-images (each spectrum-image with a low number of pixels $\sim 50 \times 50$) was taken (typically 10 or 5 spectrum-images per stack were acquired). In that way the electron beam scans very fast on the sample several times. Together with the spectrum-images, their associated HAADF images are also acquired (see figure 4.19a). The stack acquisition allows studying the evolution of the particle morphology and the plasmon signal (see figure 4.19b) with the electron dose.

The electron dose for each spectrum-image is defined as

$$e \text{ dose} = It/A \quad (4.8.1)$$

Where I is the beam current, t is the acquisition time per pixel and A is the area of the electron probe. For EELS experiments in silver nanoparticles, the acquisition times were between 1-3 ms, the electron probe has $\sim 1.2 \text{ \AA}$ of diameter (typical value of the UltraStem200 microscope working at 60 kV) and the beam current between 40-140 pA. Additionally, before and after a stack acquisition, a high resolution HAADF image is taken in order to observe (with a better spatial resolution) any change on the particle morphology and environment.

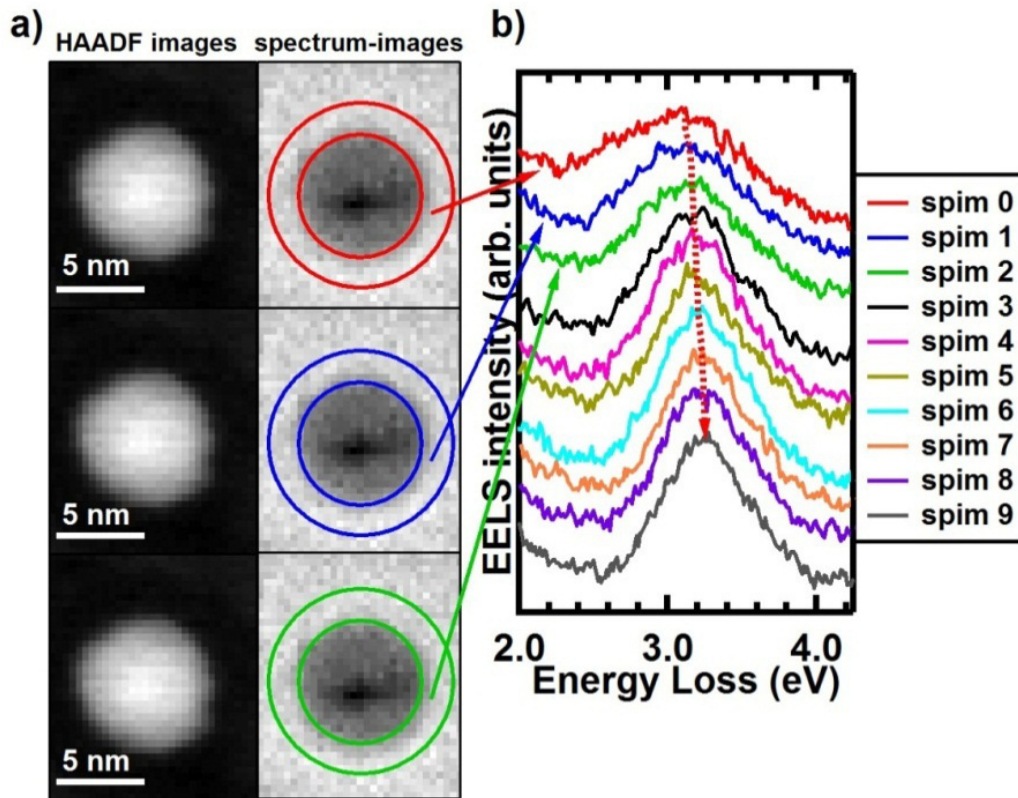


Figure 4.19: Scheme of an acquisition of a stack of spectrum-images. (a) The spectrum-images with their associated HAADF images are acquired. (b) From each spectrum-image the surface plasmon signal is extracted.

4.9. Deconvolution of weak signals

Richardson-Lucy (RL) deconvolution algorithm (presented in section 3.3.5) has been widely used to extract plasmon signals in the Low-Low region in large nanoobjects [10], [98]. Despite the extended use of RL deconvolution in EELS plasmonic studies, deconvolution techniques have not been widely explored in very weak and noisy plasmon signals. Bellido et al. [98] studied the impact of the deconvolution in simulated plasmon signals with intensities of 10^{-2} ZLP maximum. However, this intensity is high with respect to the signals detected in very small particles ($\sim 10^{-3}$ ZLP and 10^{-4} ZLP). In this section we test the performance of the Richardson-Lucy deconvolution (using the free software Hyperspy [96]) in simulated signals with intensities below 10^{-2} ZLP maximum.

In order to create simulated data, an experimental EEL spectrum (energy dispersion of 0.011 eV/pixel and ZLP FWHM of 0.27 eV) taken in a carbon substrate (covered by silica matrix) was normalized by the ZLP maximum and fitted with 11 Gaussians between -1.5 and 7 eV (see figure 4.20a).

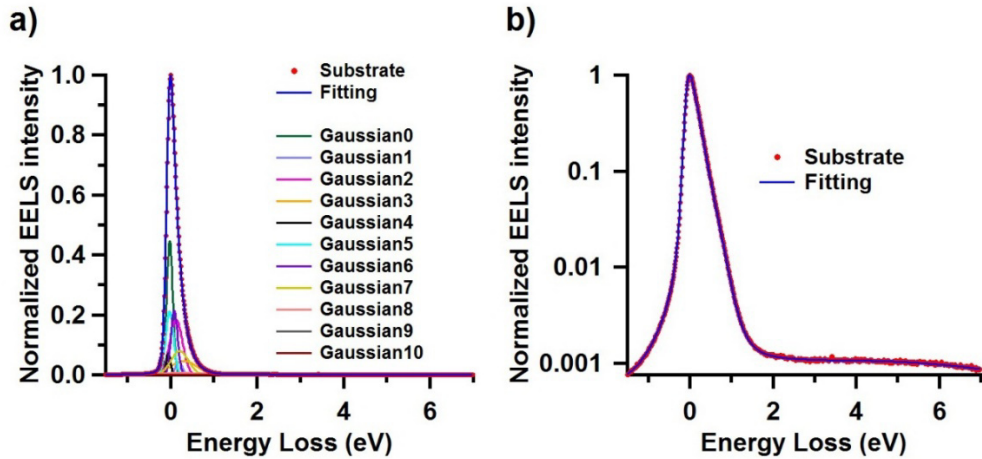


Figure 4.20: (a) Experimental EEL spectrum taken in a carbon substrate (covered by silica) normalized by the ZLP maximum and fitted with 11 Gaussians between -1.5 to 7 eV. (b) Logarithmic scale of the EEL spectrum taken on the substrate and the fitting curve. The ZLP tail intensity is close to $\sim 10^{-3}$ ZLP maximum at ≥ 2 eV.

As observed in figure 4.20b the fitting works very well. With the fitted EEL spectrum, a spectrum-image of 50x50 pixels was reconstructed (see figure 4.21a). Each pixel contains the fitted EEL spectrum (each spectrum presents the same experimental energy dispersion = 0.011 eV/pixel). Additionally, a particle is simulated in the center of the spectrum-image (10x10 pixels) adding up three peaks at 1, 3 and 5 eV. Each peak has a FWHM of 0.6 eV. The intensity of these peaks is varied in this study. Finally, each pixel of the spectrum-image is multiplied by 60 000 (maximum number of counts in a pixel in the CCD camera) and a Poissonian noise is added.

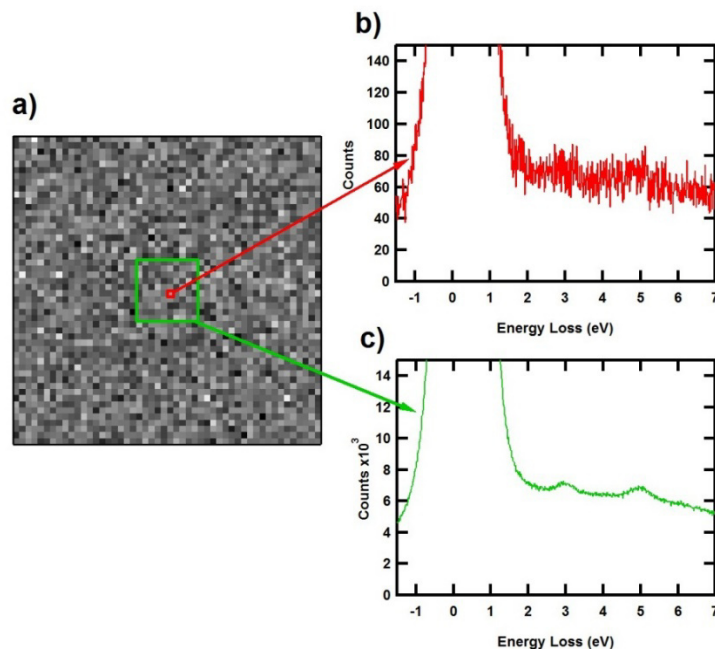


Figure 4.21: (a) Spectrum-image reconstructed (50x50 pixels) with a simulated particle at the center (10x10 pixels) which has three peaks at 1, 3 and 5 eV and same FWHM of 0.6 eV and intensity of 10^{-4} ZLP. (b) Spectrum of an individual pixel of the particle in which the peaks are not so clear. (c) Spectrum coming from the sum of all the pixels of the particle in which the SNR increase and the peaks at 3 and 5 eV are visible but the peak at 1 eV is hidden by the ZLP tail.

In order to carry out the RL deconvolution on a simulated spectrum-image, a spectrum coming from the sum of pixels on the region outside the particle is used as point spread function (PSF). In figure 4.22, EEL spectra coming from the sum of all the pixels of the simulated particle is presented after different number of iterations on the simulated spectrum-image. The intensity of the simulated peaks was varied from 10^{-2} ZLP to $5 \cdot 10^{-5}$ ZLP.

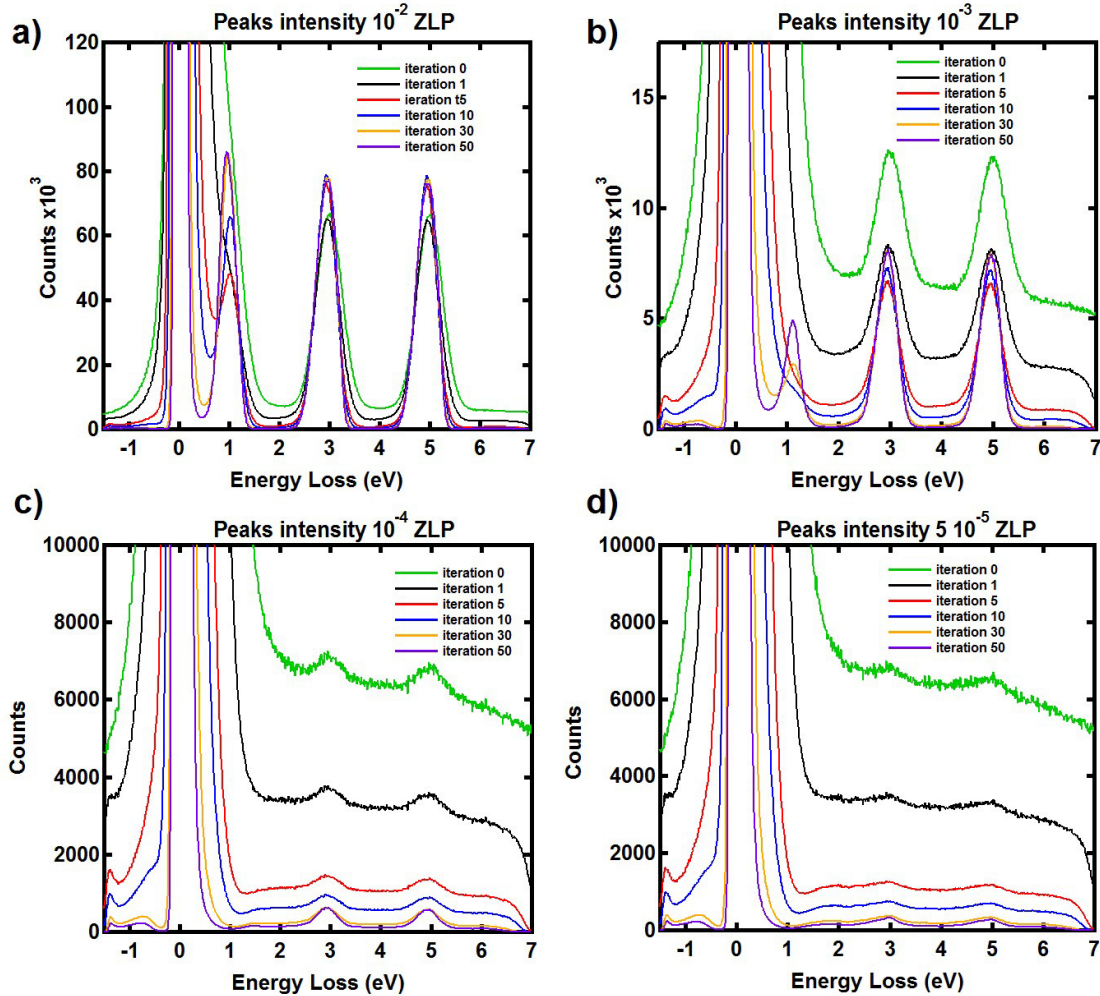


Figure 4.22: EEL spectra coming from the sum of pixels of a simulated particle with three peaks at 1, 3 and 5 eV after applying a RL deconvolution with 1, 5, 10, 30 and 50 iterations on the simulated spectrum-image. The intensity of the peaks was (a) 10^{-2} ZLP. (b) 10^{-3} ZLP. (c) 10^{-4} ZLP and (d) $5 \cdot 10^{-5}$ ZLP. The deconvolution can resolve the peak at 1 eV if the peak intensity is $>10^{-3}$ ZLP. On the other hand, the effect of the deconvolution on the peaks at 3 and 5 eV is not significant.

As observed in figure 4.22, the peak at 1 eV can be resolved after deconvolution if its intensity is $\geq 10^{-3}$ ZLP. This is the case of large nanoparticles where the plasmon peaks are intense (as the case of aluminum nanotriangles in this thesis). On the other hand, the peaks at 3 and 5 eV does not take much advantage of the deconvolution. The only advantage for these peaks is a reduction of noise with the increase of the number of iterations, which is due to the fact that the RL deconvolution is based in a Poisson statistic, but at the expense of apparitions of artifacts that can be misinterpreted.

For all these reasons in the EELS experiments of small silver nanoparticles, where the plasmons have intensities of $\sim 10^{-3}$ ZLP and 10^{-4} ZLP at energies > 2 eV, we decided not

to apply the RL deconvolution. Instead, we performed a fitting method to extract the energy position and subtract the ZLP background. This is described in the following section.

4.10. Fitting noise data and background subtraction

In order to extract the background in a Low-Loss EEL spectrum, different methods exist. Deconvolution [10], [92] and reflected tail [95] techniques have been widely used to remove the Low Loss background. However, the reflected tail technique needs symmetric ZLP and deconvolution can add artifacts as mentioned in previous section. Another methods of fitting have been used such as the spline fit [106] giving good results.

In this section a fitting method is presented that was used to extract the energy position and subtract the ZLP background on the EEL spectrum of small silver nanoparticles. This method is illustrated in figure 4.23 and it is performed as follow:

An EEL spectrum taken on the substrate (covered by silica) is normalized by the ZLP maximum and fitted with 4 Gaussians between 1 to 7 eV (figure 4.23a). The fitting parameters are used to model the ZLP background on a normalized EEL surface signal of a nanoparticle (figure 4.23b). The modeled ZLP background is then subtracted on the EEL surface signal (figure 4.23c). Finally, the surface plasmon peak is fitted with a Gaussian with the least square fitting method using Hyperspy [96] (figure 4.23d).

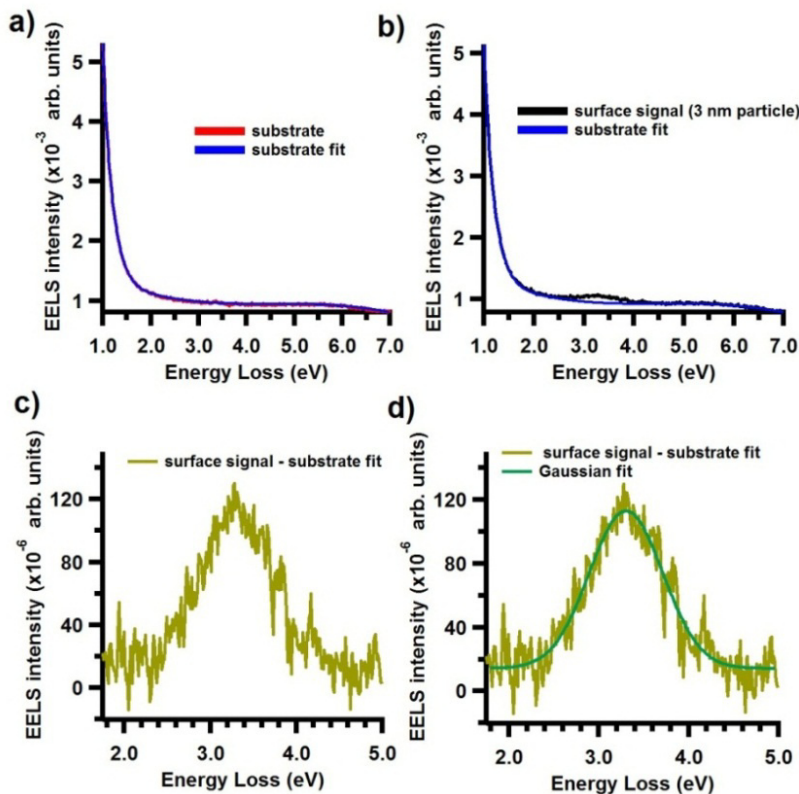


Figure 4.23: Procedure to extract the energy position and FWHM of a weak plasmon peak from a 3 nm silver particle. (a) An EEL spectrum taken on the substrate (covered by silica) is normalized by the ZLP and fitted with 4 Gaussians in the range 1 - 7 eV. (b) The fitting parameters are used to model the ZLP background of a normalized surface signal of a nanoparticle. (c) The modeled ZLP background is then subtracted on the surface plasmon signal. (d) A Gaussian fit is applied with the least square fitting method by using Hyperspy [96].

Due to the weak SNR of the plasmon signal in small nanoparticles it is necessary to know the precision of the fit on a noisy peak. In order to verify the accuracy of a fit, Gaussian peaks are simulated with the same intensity of real data of silver particles. A Poissonian noise is added to the simulated Gaussians peaks in order to model the noise of the real data (see figure 4.24a). All the simulated Gaussian peaks are generated with the same energy position of 3.6 eV and same FWHM of 0.6 eV (green curves in figure 4.24a).

Finally, a Gaussian fit is applied on the simulated Gaussian peaks in order to verify how well the energy position (3.6 eV) and FWHM (0.6 eV) values are reobtained by the fit in presence of noise. Figure 4.24b shows the results of the fitting on simulated Gaussian peaks and shows that the energy positions of the fitting are close to 3.6 eV with a relative error of 0.93 %. The smaller the particle, the lower the accuracy of the fit. On the other hand, the FWHM presents a relative error of 10 %. This means that the estimation of the plasmon energy position has a very good accuracy and it is better than the estimation of the FWHM. The free software Hyperspy [96] was used to do the fitting in this study.

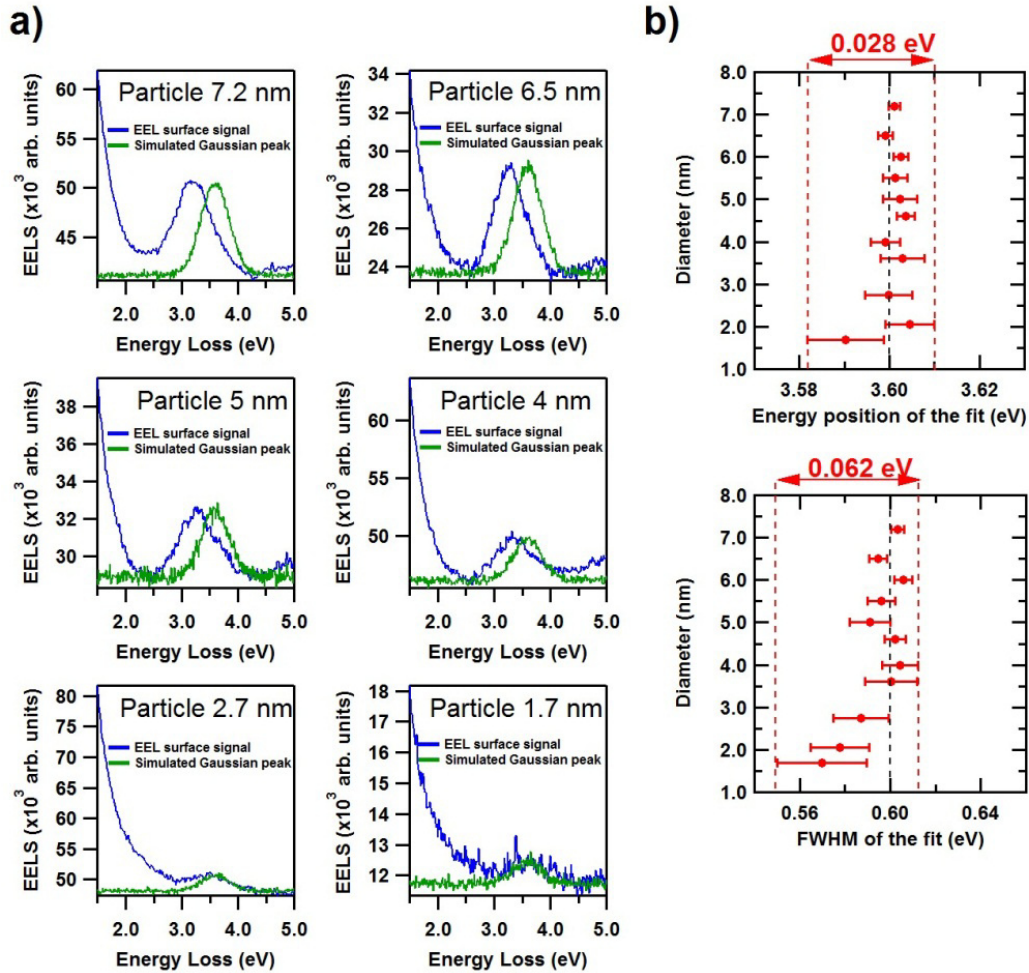


Figure 4.24: (a) Simulated Gaussian peaks (green curves) with the same intensity and comparable noise (Poissonian noise) of real data (real data in blue curves) of silver particles from 7.9 to 1.7 nm diameters. All the simulated Gaussian peaks have energy positions of 3.6 eV and FWHM of 0.6 eV. (b) A Gaussian fit is applied on the simulated Gaussian peaks in order to verify how good the energy position (3.6 eV) and FWHM (0.6 eV) values are reobtained by the fit in presence of noise.

4.11. Conclusion

Throughout this chapter the aberrations in the EEL spectrometer and the sources of noise on the CCD camera were described. We found a good optimization of the EEL spectrometer together with a good parameters acquisition which enabled the reduction of the ZLP width and the increase the dynamic range, the increase of signal-to-noise ratio and the signal-to-background. It was found that in particles smaller than 5 nm that the electron dose can affect drastically the particle morphology and special care has to be taken into account. The effect of the electron dose and the way to avoid it were described. All the optimization procedures applied in EELS experiments for small particles enabled the detection of plasmon signals in particles as small as 1.7 nm. A fitting method with several Gaussians was employed in order to remove the ZLP tail and to extract the plasmon energy positions in noisy data with an accuracy of 0.93 % relative error.

Chapter 5: Optical and EELS results in silver clusters

5.1. Introduction

The size-dependent plasmonic resonances in metallic nanoparticles, smaller than 10 nm, have been investigated and discussed since several decades. However, the existing literature is as rich as controversial. The size-dependent spectral shifts of the LSPs in small metal nanoparticles, induced by quantum effects, are reported to the red, to the blue or entirely absent with the decrease of particle size. In the older works, where optical measurements have been performed on a set of nanoparticles, there exists an inhomogeneous line broadening which makes difficult to bring out the quantum effects. The observed effect is an average of the contribution of all the particles. In this case a narrow size distribution of particles is needed. In order to overcome this problem, STEM-EELS technique has been used since several decades to study individual particles. STEM-EELS technique can correlate the spectral response with size, shape and environment of the particle. The first attempts in the study of very small individual nanoparticles were carried out in the early works of Batson et al. [107], [108] in supported aluminum spheres, which explored the plasmon resonances in isolated and coupled aluminum spherical nanoparticles in a size range of 10-40 nm in diameter. Achèche et al. [109] detected surface and volume plasmon signals in supported Gallium spherical nanoparticles (8-80 nanometer diameter) with results out of a classical description. Ouyang et al. [110] studied supported silver nanoparticles (4-20 nm) showing a nonmonotonic behavior of surface plasmons as a function of the particle size and suggested microscopic theories. Years later Aizpurua et al. [111] proved theoretically that the results of Ouyang et al. can be deduced from classical theories assuming hemispherical nanoparticles. The instrumental limitation in spatial and energy resolution in STEM-EELS technique at that time imposed problems in the accuracy of the results.

Recently, the size-dependent plasmonic resonance has regained new interest with the improving of the STEM-EELS technique introducing cFEG, monochromators, aberration correctors and faster electronics that have made possible to study particles below 10 nm diameters. Recent STEM-EELS studies [17], [19] found experimentally a strong blue shift of the LSP with decreasing size for silver nanoparticles fabricated by wet chemical methods and deposited onto a substrate (see figure 5.1). These works presented a contradiction with older optical literature [24]–[27] which was not discussed at all in Ref. [17]. Furthermore, the so-called quantum plasmon resonances were interpreted using semiclassical models based on the hard-walled potential well in Ref. [17] and hydrodynamic description of the electron density in Ref. [19]. This interpretation remains, however, highly controversial [22], as several fundamental aspects such as electron spill-out or the influence of the substrate, were not taken into account.

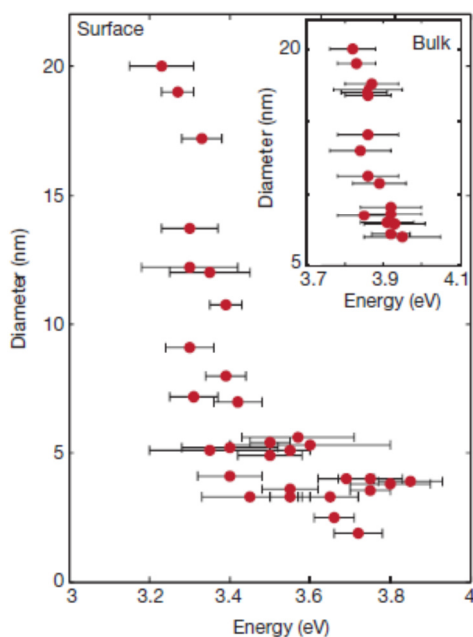


Figure 5.1: Surface and volume plasmon evolution with the size of silver nanoparticles deposited in a carbon substrate. A blue shift on the surface plasmon of around 0.5 eV is observed with the decrease of particle size (taken from Scholl et al. [17]).

Haberland [22] discussed the controversy between EELS results of Scholl et al. [17] and older works in optical experiments, see figure 5.2. The blue shift of the supported silver particles in EELS experiment has a higher slope than the case of optical experiments. However, compare supported clusters with free and gas rare-gas matrix isolated clusters is not simple. It is possible to compare free and rare-gas matrix isolated clusters if one is careful, but in supported particles the substrate could have a more complicated influence than just shifting the peaks by a constant value. Another problem in the comparison between experiments is the fact that the particles in Scholl et al. are fabricated by chemical method and the influence of residual ligands in the surface plasmons is complex.

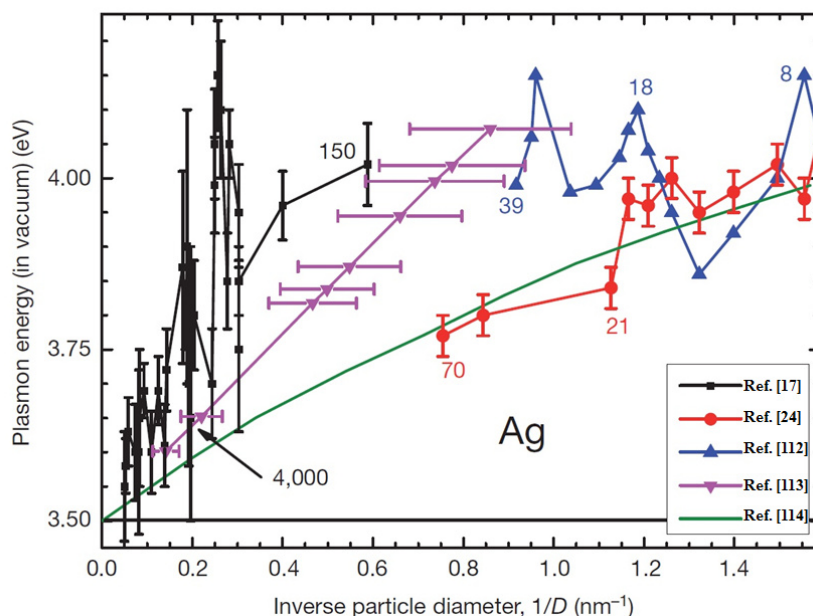


Figure 5.2: Surface plasmon energy of silver nanoparticles as a function of the inverse diameter. EELS experiment corresponds to the black dots [17], the optical experiments are presented in red dots [24], blue dots [112], violet dots [113] and classical/quantal calculations in green line [114]. The data has been scaled to obtain the resonance energies in vacuum. The graph was taken from [22].

The case of physically prepared, embedded, sub-10 nm silver nanoparticles has also been studied by STEM-EELS technique as presented in the work of Raza et al. [28], see figure 5.3. In this case a constant value of the dipolar surface plasmon was observed from 40 down to <10 nm particle diameter (see figure 5.3a). This constant value agrees with optical experiments in physical prepared embedded silver nanoparticles reporting absent of energy shift [26], [27]. However, an abrupt blue shift (~ 0.9 eV) of the dipolar surface plasmon is observed when passing to sizes smaller than 10 nm diameter. This result is in disagreement with respect to optical works in embedded particles. Moreover, as clearly seen on figure 5.3b, this abrupt shift could not be fitted by the hydrodynamical theory used by the authors.

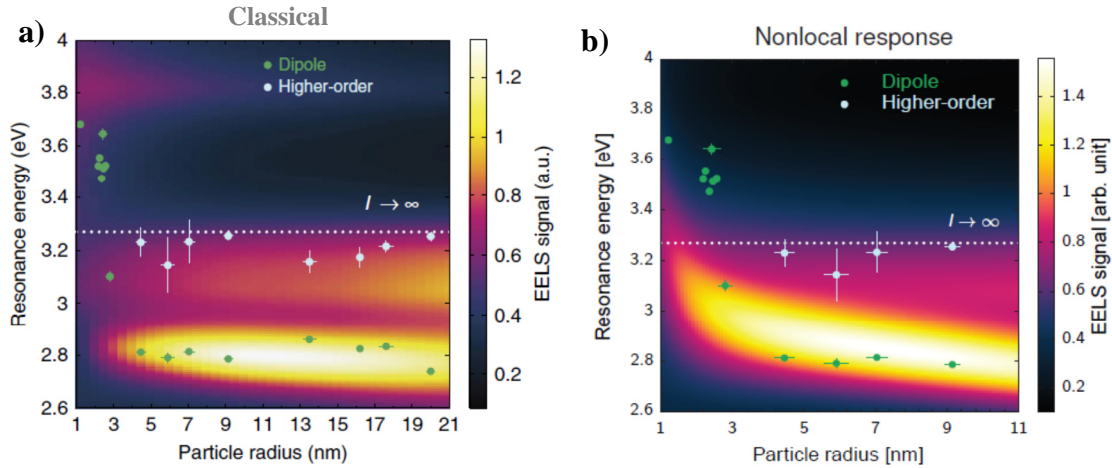


Figure 5.3: Dipolar surface plasmon energy (green dots) and multipolar plasmon resonances (white dots) as a function of the size of embedded silver nanoparticles. The matrix is Si_3N_4 . Points are experimental data, and the underlying intensity plot is (a) Classical simulations. (b) Nonlocal simulations. Data taken from Ref. [28].

Here, we report how complementary experiments on physically prepared, mass-selected, small silver nanoparticles embedded in silica can yield inconsistent results on the same system: while optical absorption shows no size-effect in the range between only a few atoms and ~ 10 nm, a clear spectral shift is observed in single-particle EEL spectroscopy. Our quantitative interpretation, based on a mixed classical/quantal model, resolves the apparent contradictions, not only within our experimental data, but also in the literature. Our comprehensive model describes how the local environment is the crucial parameter controlling the manifestation or absence of size effects.

5.2. Optical absorption results of silver nanoparticles

Optical absorption spectroscopy was performed on ensembles of silica-embedded, physically prepared silver nanoparticles (sample preparation described in section 3.4). The size of the clusters was extended down to less than 1 nm in which the quantum size effects are expected [81], [115]. As figure 5.4 shows, the samples display a strong absorption band (surface plasmon resonance) centered at 2.95 eV, practically independent of the cluster size. For clusters below 100 atoms, an additional peak at 3.75 eV is visible which can be attributed to atoms from cluster fragmentation upon deposition. A comparable signal has been identified as the envelope of the atomic doublet $5sS_{1/2} - 5pP_{1/2}$ and $5sS_{1/2} - 5pP_{3/2}$ at 3.665 and 3.780 eV, respectively [116].

By combining these results with earlier ones [25], [26] (see figure 5.5) we can conclude that in the whole range between 1 and 5 nm diameter (corresponding to a range from ~20 to ~3600 atoms) no significant shift of the optical absorption peak for silica embedded silver nanoparticles occurs. This absence of size effects is consistent with earlier results on larger particles in different glassy matrices [25], [27], [28], [117] but in stark contrast with the observed shift of ≥ 0.3 eV for gas phase and supported nanoparticles [17], [19], [22], [24], [113], [114], [118], [119].

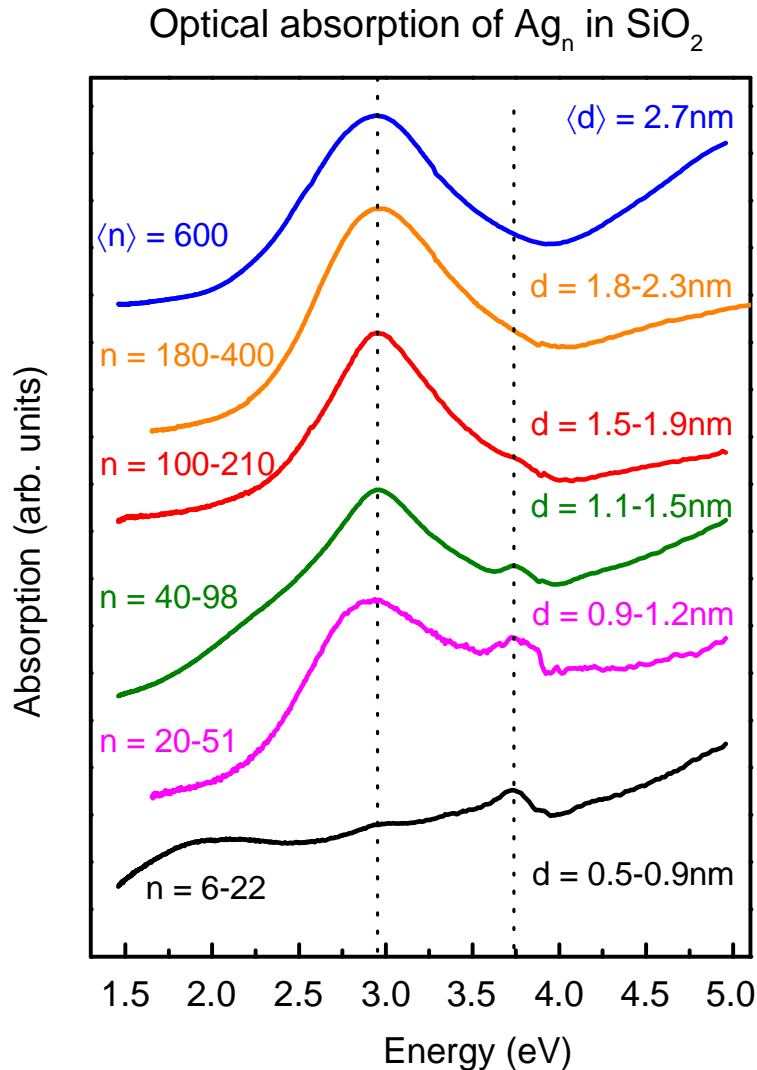


Figure 5.4: Optical absorption spectra for silver nanoparticles of varying size embedded in silica matrix. The blue curve is for a non-mass-selected ensemble centered on a diameter $\langle d \rangle = 2.7$ nm, the other curves are for mass-selected distributions. The minimal and maximal number of atoms per particle transmitted through the mass spectrometer and the corresponding diameters are indicated. The broad signal around 2 eV for the smallest size is an artefact due to imperfect correction of Fabry-Pérot interferences within the silica matrix. The band at 2.95 eV corresponds to the surface plasmon resonance. The atomic peak at 3.75 eV for small sizes is attributed to fragmentation upon deposition.

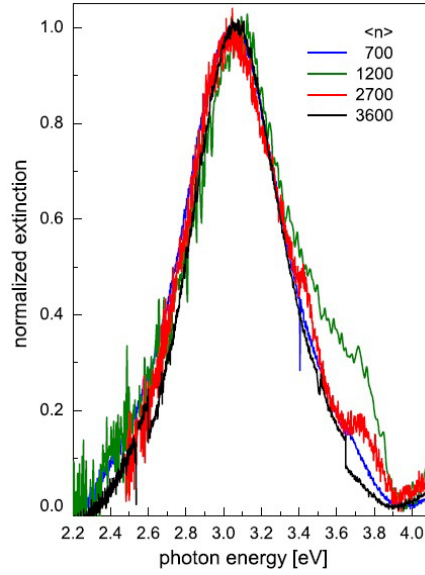


Figure 5.5: Absorption spectra for different silver cluster sizes co-deposited with silica matrix. All samples show comparable plasmonic absorption signals at the same energy position. Graph taken from [26].

5.2.1. Optical absorption results and classical/quantal calculations

In this section classical/quantal calculations are performed in free and embedded silver clusters and the calculations are compared with free silver clusters from literature and with embedded silver clusters from literature and this work. As described in section 2.5 the classical/quantal model takes into account quantum effects such as the electron spill-out, the surface layer of ineffective ion-core polarizability (d), the non-locality of the optical response and the local environment around the particle by a porosity layer (d_m) in the particle/matrix interface.

Figure 5.6 shows the calculation results for free Ag_N clusters, for $d = 0$ (black squares), $d = 3.5 a_0$ (red squares) and $d = 1.89 a_0$ (blue squares). For each d -value the size-evolution of the LSP maximum follows an average $1/R$ scaling law. Actually, all finite size- and surface-induced effects, either of quantum or of classical nature, are expected to follow such a generic scaling law ($1/R$), which reflects the surface to volume ratio [118], [120]. The three sets of data clearly converge towards the classical asymptotic value 3.41 eV ($1/R \rightarrow 0$). This value is the classical LSP energy (quasistatic limit). The convergence towards this asymptotic value proves the accuracy of our TDLDA calculations. For small sizes the large scatter of the results on both sides of the mean $1/R$ scaling law is, on the one hand, due to increasing importance of the atomic structure at decreasing size, neglected in our jellium approximation and, on the other hand, caused by the procedure used for setting the LSP maxima, as pointed out in section 2.5.4. For $d = 0$ a red-shift trend with decreasing size is obtained. This reproduces the red shift tendency of alkali metals Ref. [57], where the electron spill-out is not compensated. Very slight and a noticeable blue-shift trends are obtained for $d = 1.89 a_0$ and $d = 3.5 a_0$, respectively. As it is observed, the calculations with $d = 3.5 a_0$ match very well with literature of free silver clusters. This value will be used throughout this thesis work. This value has also been used in previous works [27], [78], [79].

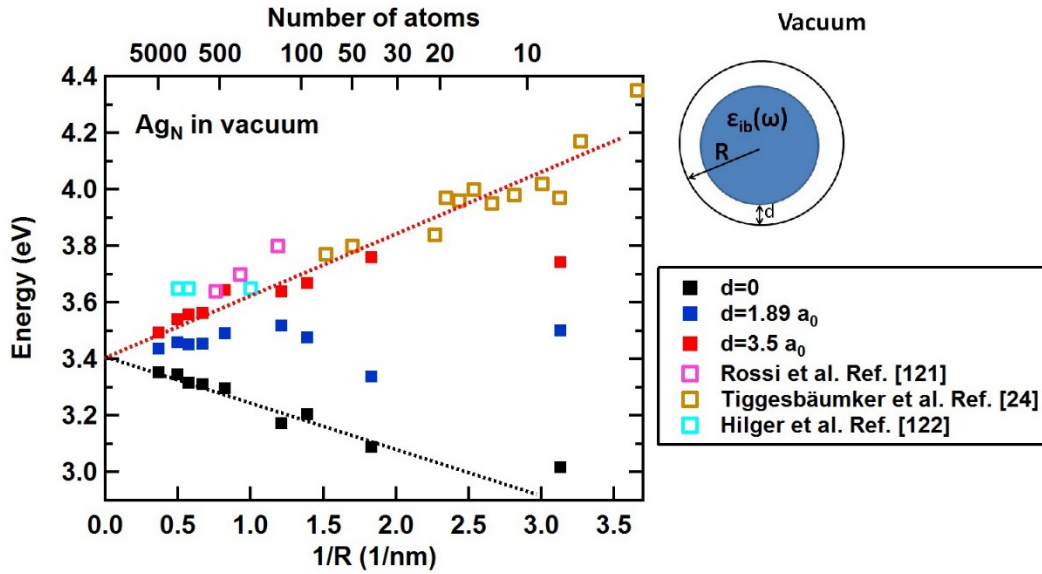


Figure 5.6: Size evolution of the LSP maxima for free silver clusters. d is the thickness of the inner shell of vanishing d -electron polarizability in bohr ($a_0=0.529 \text{ \AA}$). The convergence at $1/R = 0$ indicates the value of the classical prediction. The pink open squares are theoretical TD-DFT results [121], the other open squares represent experimental values taken from Ref. [24] and [122], respectively. Dashed lines are guides to the eye. The insert at the right shows the concentric geometry used for the calculations.

Now we will perform classical/quantal calculations for the case of embedded silver clusters. In previous works the classical/quantal model has been used to explain the optical absorption experiments in embedded silver nanoparticles in alumina matrix [27]. Figure 5.7a shows the optical absorption experiments on silver nanoparticles embedded in alumina matrix from Ref. [27]. The surface plasmon has a constant energy position for all the particle sizes. The classical/quantal calculations reproduced very well the absent of shift, see figure 5.7b.

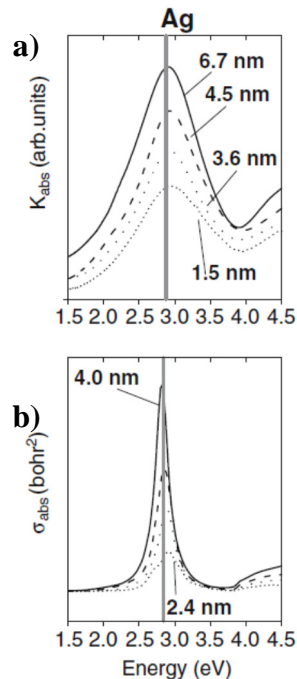


Figure 5.7: Size evolution of the surface plasmon of silver nanoparticles embedded in alumina matrix. (a) Experimental absorption spectra. (b) Calculated absorption spectra obtained by the classical/quantal model of chapter 2, section 2.5. The diameters of the particles are indicated in the graphs. Data taken from Ref. [27].

Figure 5.8 displays the classical/quantal calculation results for silica-embedded Ag_N clusters, for a layer of ineffective ion-core polarizability $d = 3.5 a_0$, for various thicknesses of the porosity layer simulated by a vacuum shell (the color code is indicated in the figure). The results for the parameter set $d = d_m = 0$ are also shown (black circles). For each parameter set (d, d_m) the size-evolution of the LSP maximum follows an average $1/R$ scaling converging towards the classical asymptotic value 3.03 eV ($1/R \rightarrow 0$). This figure shows a good agreement of calculations with optical experiments of silver nanoparticles embedded in silica considering a porosity layer $d_m \sim 0$. Keeping in mind that the d -value is a phenomenological parameter, figure 5.8 suggests nevertheless that the local porosity d_m over the particle surfaces is very weak. One can note that the optical measured LSP frequency in this work, 2.95 eV, is slightly lower than the model prediction 3.03 eV. A tiny underestimation of the effective mass (see the figure 7 in Ref. [123]), as well as that of the $T = 300$ K Wigner-Seitz radius r_s , could explain this slight discrepancy.

Figure 5.8 also provides reasonable semi-quantitative explanations of our experimental findings, in particular those regarding the size trend and electron dose-evolution of the LSP maxima in the single particle EEL spectra where a change of local porosity layer is created by the electron beam as will be discussed later in section 5.3.3.

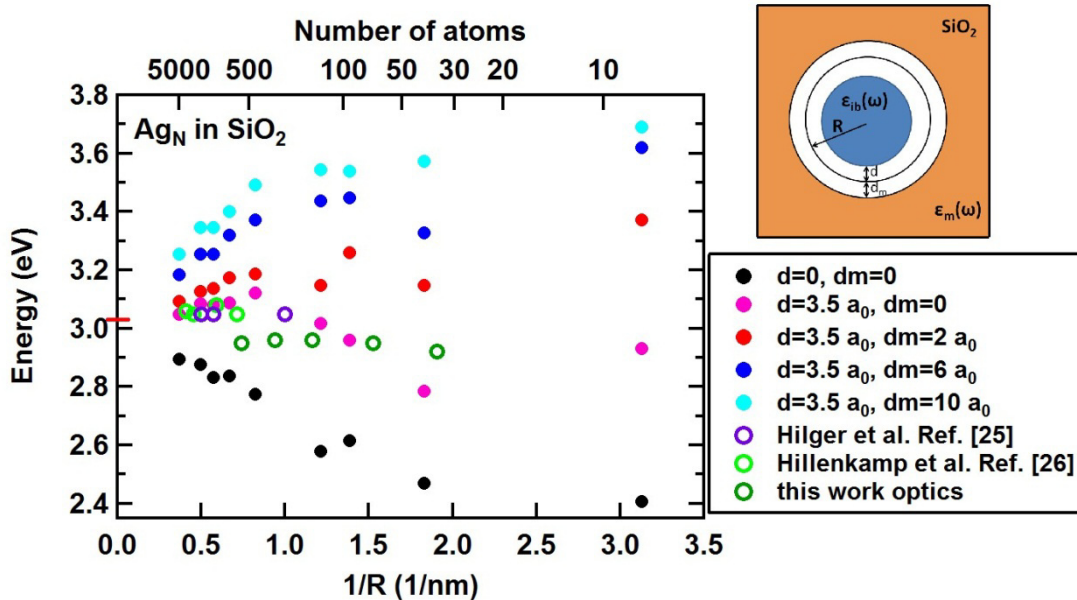


Figure 5.8: Size evolution of the LSP maxima for silica-embedded silver clusters. d is the thickness of the inner shell of vanishing d -electron polarizability. d_m is the thickness of the outer surface shell of vanishing matrix polarizability simulating the local porosity. The red stick at $1/R = 0$ indicates the value for the classical prediction. The open circles represent experimental values taken from [25] and [26] and the optical results of this work. The insert at the right shows the concentric geometry used for the calculations.

Figures 5.6, 5.7 and 5.8 suggest that the classical/quantal model describes very well free and embedded silver particles. Figure 5.9 presents experimental results of free and silica embedded silver clusters together with classical/quantal calculations for free and silica embedded particles. The calculations of free particles with $d = 0$ are also presented to take in mind that the model can also describe the red shift tendency of alkali metal clusters where the electron spill-out is not compensated. This figure proves that the classical/quantal model used in this thesis is quite general to reproduce the tendency of

free and embedded silver clusters.

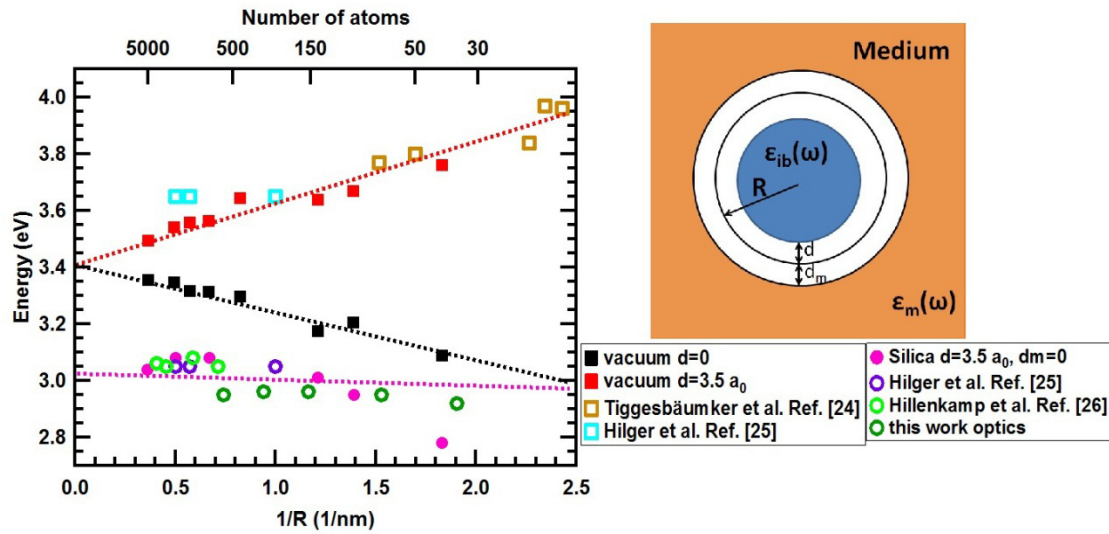


Figure 5.9: Size-dependent shift of the LSP energy of Ag nanoparticles in different environments. The solid squares are the calculated responses for particles in vacuum without (black) and with (red) the layer of reduced polarizability d , compared to experimental values (open squares). The solid pink circles show the theoretical values for silica-embedded Ag particles with the same layer of reduced polarization ($d=3.5 a_0$) and a perfect interface ($d_m = 0$). Open circles depict experimental values from Refs.[24]–[26] and this work. Dashed lines are guides to the eye. The insert at the right shows the concentric geometry used for the calculations.

5.3. EELS results of silver nanoparticles

Single-particle STEM-EELS experiments were performed over a large size range of silver nanoparticles on samples fabricated under identical conditions as those for optical spectroscopy (see section 3.4 for details). The only difference is the thickness of the silica matrix (30-100 nm for STEM-EELS experiments against $1 \mu\text{m}$ thickness for optical experiments).

5.3.1. Surface signal

From a spectrum-image (described in chapter 3) it is possible to extract EEL signal from different regions of the nanoparticle. Figure 5.10 shows typical example HAADF images of 6.5 and 2.0 nm Ag nanoparticles embedded in silica and the corresponding EEL spectra extracted from the particle surface (area between the blue circles). Clearly visible are the strong surface plasmon peak (we remember that the dipolar mode dominate the signal as presented in section 2.4.3). A blue shift is observed between both spectra and with respect to optical spectroscopy results ($\sim 2.95 \text{ eV}$) shown in figure 5.4.

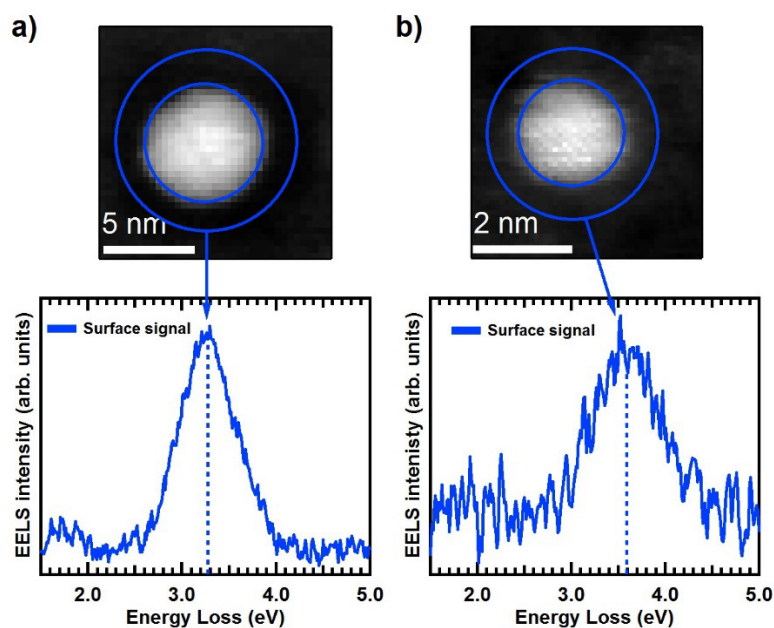


Figure 5.10: *STEM-HAADF image of silica embedded silver nanoparticles of (a) a 6.5 nm and (b) a 2.0 nm and their EEL spectra associated to the surface (region between the blue circles). The spectra were obtained by subtraction of the ZLP tail as presented in section 4.10.*

5.3.2. Electron dose study

A closer study of the EELS data reveals a complex situation. The majority of nanoparticles do not display a plasmon signal at the beginning of an EELS experiment. They are surrounded by a diffuse layer (see figure 5.11a and 5.12a) which can be attributed to silver oxide [124]. We note that once the samples for STEM-EELS are prepared by our collaborators they are sealed in TEM grid containers in a glove box under argon atmosphere and sent to the laboratory in Orsay for STEM-EELS measurements. When the samples arrive they are stored in a desiccator under vacuum. The samples are baked at 100 °C in vacuum before inserting in the microscope as described in 4.7.3. However, the samples for STEM-EELS are much thinner than samples for optical absorption measurements, thus diffusion of ambient oxygen to the clusters is highly efficient on the time scale of hours [26].

Upon continuous electron irradiation, this diffuse layer disappears due to knock-on collisions. In these inelastic collisions, momentum is transferred from the swift electron to a single atom which can then, depending on the momentum transferred, be displaced from its initial position. As the atomic velocity resulting from momentum transfer is higher for light atoms, these are preferentially removed from the sample. Initially (at least partially) oxidized silver nanoparticles do not display a plasmon signal [26], [124] and only after beam-induced reduction does the surface plasmon peak appear and rise with integral electron dose. Under continuing electron illumination of individual particles, the surface plasmon peak also blue-shifts, as shown in figures 5.11b and 5.11d. Even at lowest reasonable dose this electron beam effect on the sample is unavoidable. Note that this spectral shift is related to a different radiation damage than radiolysis, where chemical bonds are broken [125].

The blue shift can be explained by the change of local environment around the particle as it will be verified later by classical/quantal calculations.

As it is observed in figure 5.11, the surface plasmon peak arrives to higher energies in the smallest particles. This is related to the fact that the LSP energy in the smallest particles is more sensitive to the change of environment, as it will be shown later.

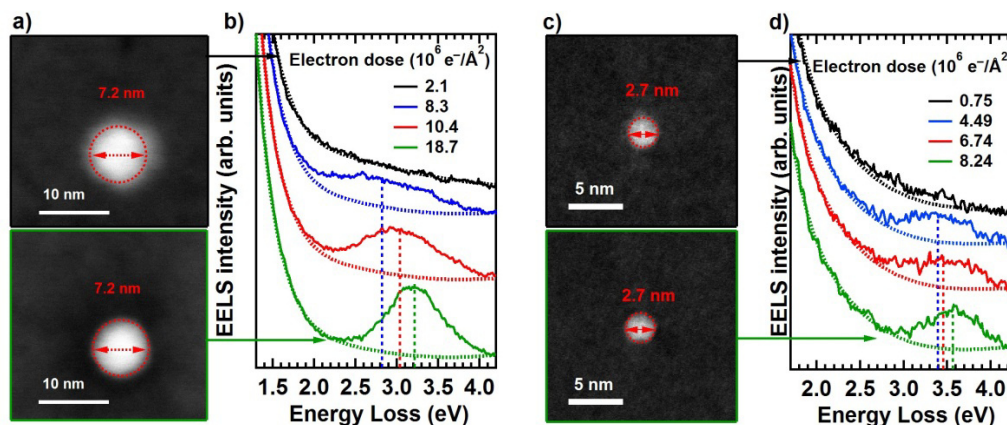


Figure 5.11: (a) STEM-HAADF images of a 7.2 nm silver nanoparticle embedded in silica at low and high electron dose. A diffuse layer related to silver oxide is visible at low electron dose and disappears at higher electron dose. The diameter of the nanoparticle remains the same. (b) Surface plasmon evolution of the 7.2 nm silver nanoparticle with the increase of electron dose. (c) STEM-HAADF images of a 2.7 nm silver nanoparticle diameter embedded in silica at low and high electron doses. The diameter of the nanoparticle remains the same. (d) Surface plasmon evolution of the 2.7 nm silver nanoparticle with the increase of the electron dose. The plots show genuine EELS data (Only a ZLP alignment and a sum of pixels around the particle were applied). The curves have been shifted along the y-axis for clarity. The contributions of the ZLP tail and other background contributions to the EEL spectra are shown as dashed lines.

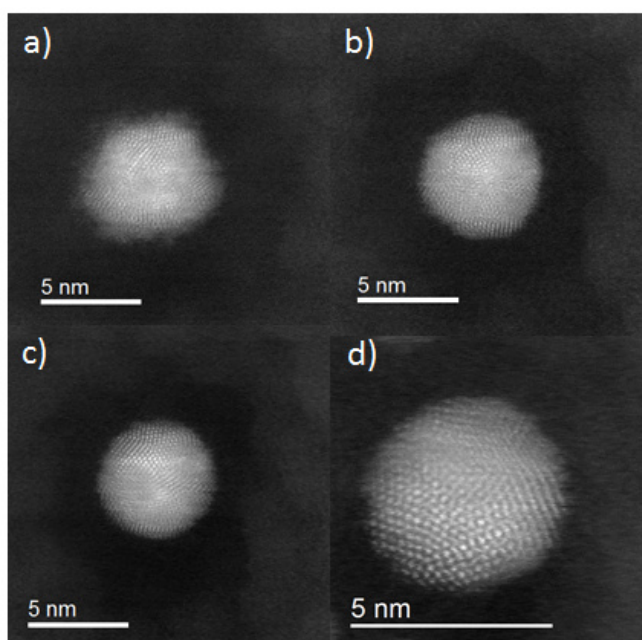


Figure 5.12: High resolution STEM-HAADF images of a silver particle of ~ 5 nm diameter embedded in silica at different irradiation doses. From low to high irradiation doses it is observed: (a) an oxide layer (diffuse layer) at the particle surface. (b) Cleaned interface by the electron irradiation. (c) and (d) show icosahedral structures [126] (the “anti-wedge” or “bow-tie structure” followed by the “cauliflower”), i.e. the particle rotates under the beam.

If the irradiation continues until reaching high electron doses, the surface plasmon blue shift stops and reaches a saturation limit (figure 5.13b). Note that in the smallest particles the electron dose used was lower in order to avoid particle damage. This is the reason why in some of the smallest particles the LSP blue shift saturation is not always reached (figure 5.13d).

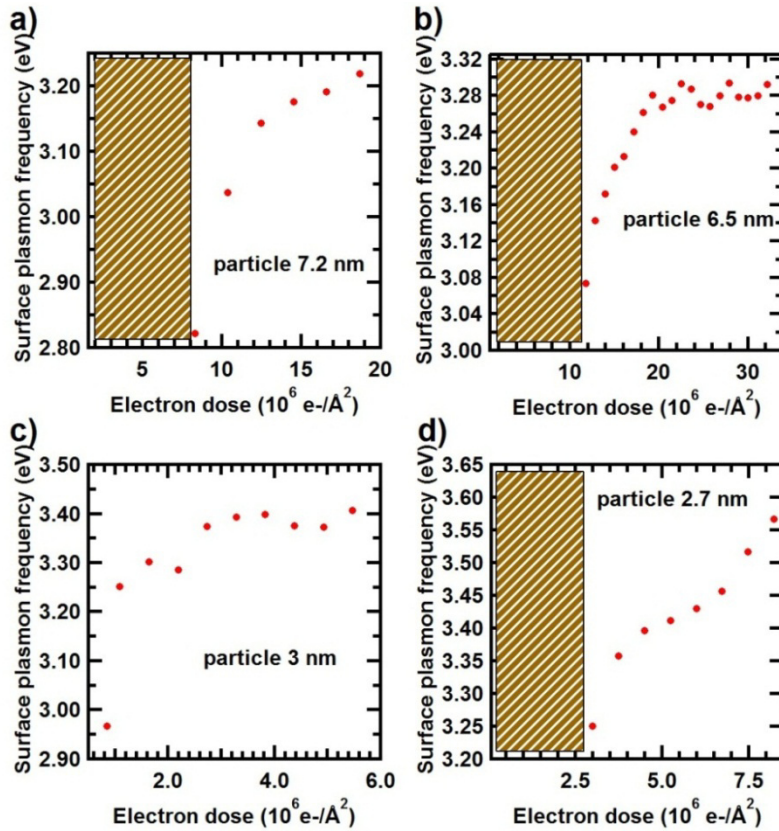


Figure 5.13: Examples of blue shift with electron dose of nanoparticle diameters of (a) 7.2 nm. (b) 6.5 nm. (c) 3 nm. (d) 2.7 nm. At the beginning of the EELS experiments (low electron dose) some of the particles do not show signal due to oxidation. The dashed areas correspond to electron dose regions where EEL spectra have been acquired but no plasmon could reliably be detected out of the noise. At high electron dose the surface plasmon blue shift stop and arrives to a saturation limit as observed in b. To avoid particle damage, the small particles are not exposed to high electron dose and therefore the saturation of the blue shift is not always observed.

The obtained values for the dose-dependent peak position as a function of size are depicted in figure 5.14. The positions of the peaks are obtained by the fitting method presented in section 4.10. The central and right vertical lines depict the classical (size-independent) values of silica-embedded and free silver nanoparticles in the quasistatic limit and calculated using the values of Ref. [127]. The left-most vertical line has been obtained for the classical quasistatic limit of core@shell Ag@Ag_xO nanoparticles at 75% oxidation ratio (see appendix F for details of this calculation).

The data for large diameters scatter around the classical value of 3 eV, but for smaller sizes shifted values of up to ~3.6 eV exceeding even the classical limit in vacuum. The EELS data of this thesis is consistently red-shifted with respect to EELS experiments of Refs. [17], [19] (see figure 5.15), which is explained by the homogeneous high-index environment of the silica matrix.

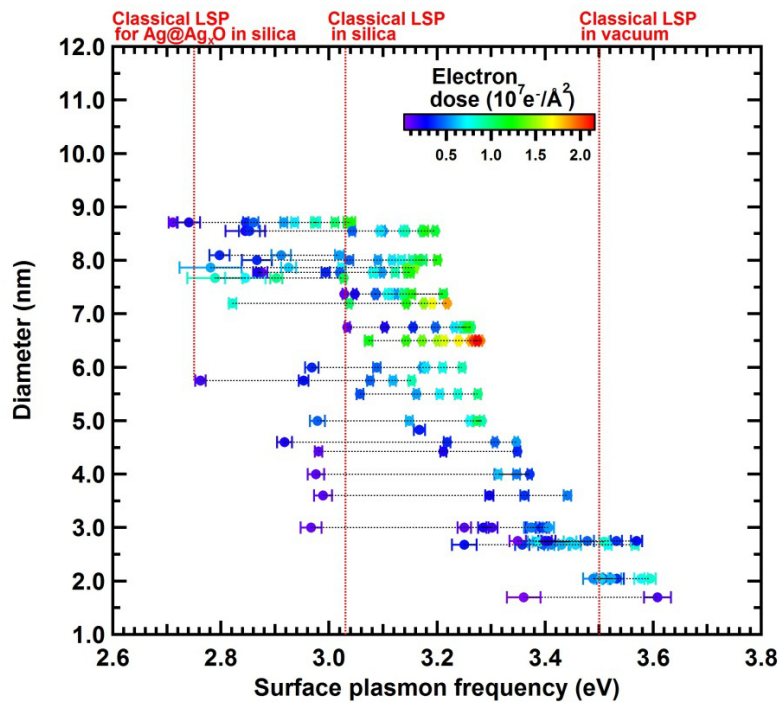


Figure 5.14: Evolution of the surface plasmon peak position of silica-embedded silver nanoparticles as a function of electron dose, indicated in color code. The interaction with the high-energy electron modifies the nanoparticle environment and the plasmon blue shifts to higher energies. The plasmon energy values for each nanoparticle are connected by a black dotted line. The central and right vertical lines depict the classical (size-independent) values for the plasmon of silica-embedded and free silver nanoparticles in the classical quasistatic limit and calculated using the values of Ref. [127]. The left-most vertical line has been obtained for the plasmon in the classical quasistatic limit of core@shell Ag@Ag_xO nanoparticles at 75% oxidation ratio.

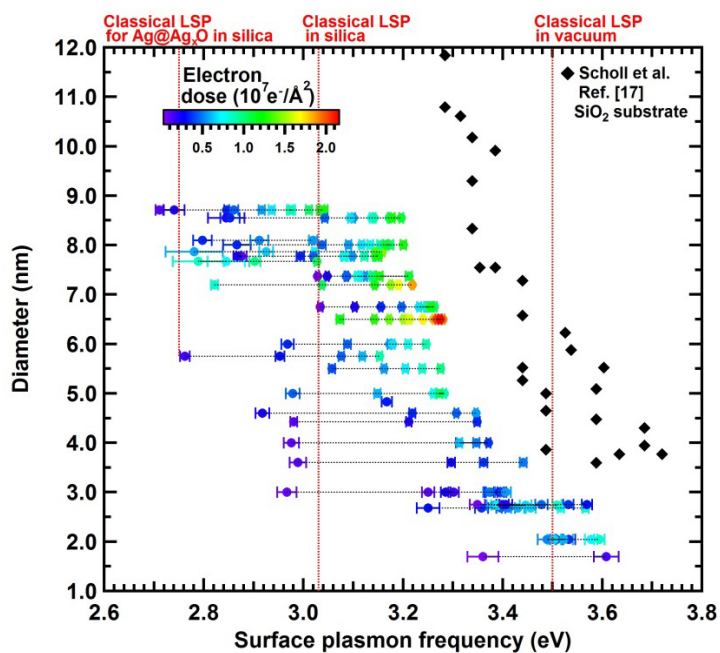


Figure 5.15: EELS results of figure 5.14 compared with data from the supporting information of Ref. [17]. In the reference, the silver nanoparticles were chemically prepared and deposited on a SiO₂ substrate.

5.3.3. STEM-EELS results and classical/quantal calculations

Previous works on composite films involving noble metal clusters embedded in alumina have shown that the matrix porosity, especially in the close vicinity of the metal particles, has a strong impact on the optical properties [27], [78]. An additional and noticeable blue-shift of the LSP frequency, relative to the prediction obtained in using bulk alumina refractive index, was clearly evidenced. More especially, the *local* porosity at the metal/matrix interface (surface roughness, contact defects, different chemical nature of the constituents, etc...) that results in a lowering of the local effective matrix polarizability, has a very strong influence. As we can see in figures 5.11, and 5.12, the EELS experiments suggest that, due to damage induced by the electron beam, a steady removal of matter occurs during the irradiation, creating a porous silica layer around the particle of very low refractive index. As in previous works a vacuum shell of thickness d_m is introduced in the classical/quantal model in order to mimic phenomenologically the spherically-averaged local porosity.

Figure 5.16 displays the classical/quantal absorption spectra calculations of a silica embedded silver nanoparticle with the increase of local porosity (d_m).

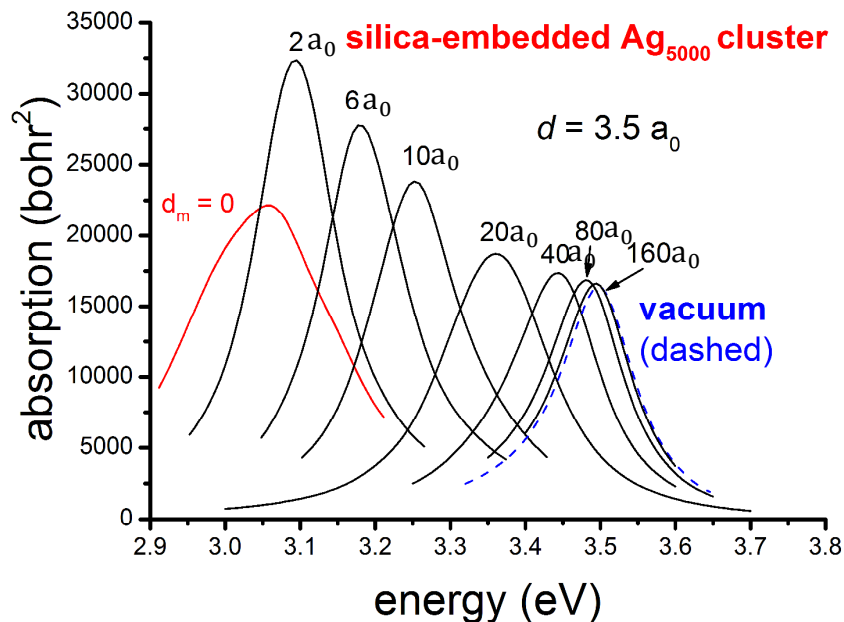


Figure 5.16: Evolution of the absorption spectra of silica-embedded Ag_{5000} (5000 atoms) cluster for increasing value of the thickness d_m (in bohr) of the vacuum-shell simulating the local matrix porosity. The thickness of the inner shell of vanishing d -electron polarizability is set to $d = 3.5 a_0$. The blue dashed spectrum corresponds to free Ag_{5000} cluster.

In samples fabricated for EELS experiments (low thickness of silica matrix), the oxygen diffusion and thus surface oxidation of the silver particles is faster than in the samples fabricated for optics and it prevents the LSP band to be observed at the beginning of the electron irradiation. Under irradiation subsequent and progressive removal of light elements around the particles steadily enlarges the thickness of the porous silica shell, yielding a concomitant blue-shift of the LSP frequency, all the larger that the particle size is smaller, as presented in figure 5.14. In order to estimate the vacuum shell thickness that is required in our modelling for ensuring a blue-shift consistent with the

EELS experiments, calculations in an extended d_m -range have been carried out for the largest investigated size in the calculations $N = 5000$ ($2R \approx 5.5$ nm). In figure 5.17 the experimental LSP blue shift with electron dose of a 6.5 nm particle and the calculated LSP evolution with increasing porosity layer of a 5.5 nm particle are presented. The experimental EELS results show a fast increase of energy and then a slower convergence to an asymptotic value. The asymptotic value is not the vacuum value due to the fact that the matrix is not completely removed and, even removing the entire matrix, the particle will be supported on the substrate. At high electron dose, the HAADF images (see images in figure 5.17a) show a porosity layer of ~ 1 nm around the particle.

The calculation results show the initially very fast and then slower convergence of the absorption spectrum and LSP maximum towards that of a free Ag_{5000} cluster. A thickness of about $10 a_0$ (≈ 0.5 nm) is found sufficient for explaining the blue-shift observed at high electron dose of the experimental EELS result. This small effective value is indeed quite reasonable. We note that due to calculation time, the same particle size as in experiment was not calculated.

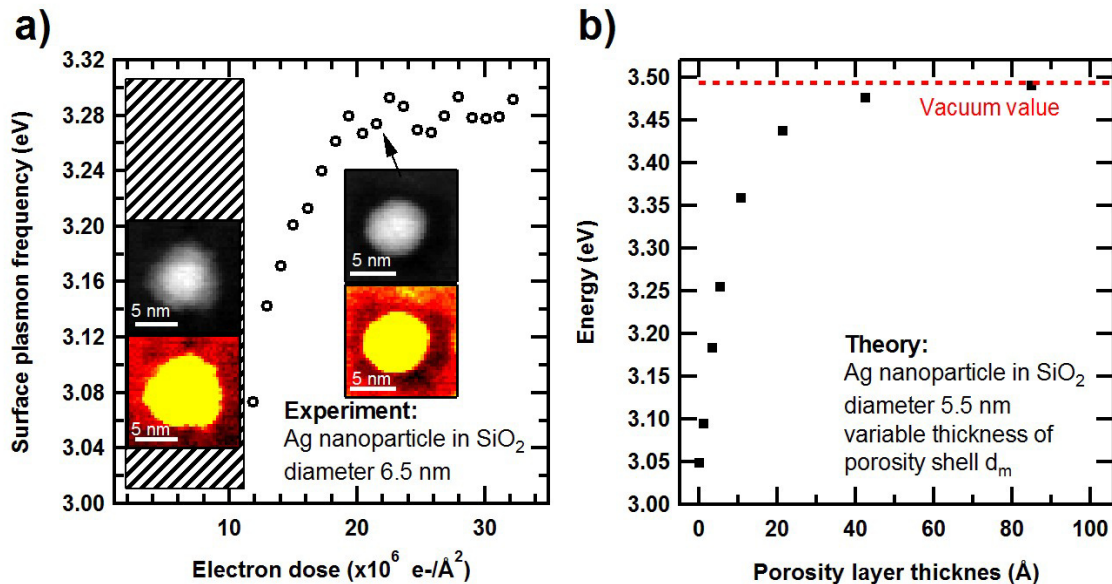


Figure 5.17: (a) Experimental shift of the LSP as a function of electron dose for a 6.5 nm particle. After a minimal electron dose necessary for plasmonic activation (oxide removal), the peak blue-shifts by ~ 200 meV. The thickness of the initial oxide layer estimated by HAADF image was ~ 1 nm. Images of the particle are inserted in the graph to observe the modification of the surface interface with the electron dose (the images are also saturated to highlight the modification of the environment). The dashed area corresponds to electron dose regions where EEL spectra have been acquired but no plasmon could reliably be detected out of the noise. (b) Calculated LSP shift as a function of vacuum layer thickness d_m for a particle of 5.5 nm. A value of $d_m \approx 5$ Å results in a ~ 200 meV shift.

5.4. Comparison of EELS, Optical, and classical/quantal calculation results

Now we can compare the EELS and optical results of this work together with the semi-quantal calculations (see figure 5.18). The EELS data at high dose (like the saturated

value in figure 5.17a) for different nanoparticles is well described by the classical/quantal calculations with a local porosity of $d_m=10 a_0$ ($\approx 5 \text{ \AA}$). On the other hand, the optical absorption measurements (green open circles) match very well with classical/quantal calculations using a $d_m=0$ (perfect coating). In the EELS data for largest particles, the LSP is close to the optical absorption experiments due to the fact that the LSP shift is not so large. However, in the smallest particles, the LSP shifts to higher energies with respect to the optical data due to the fact that the LSP is more sensitive to change of local environment. Then we can conclude that the apparently contradiction between EELS and optical data is the result of the modification of the local environment (increase of matrix porosity layer) by the electron beam irradiation.

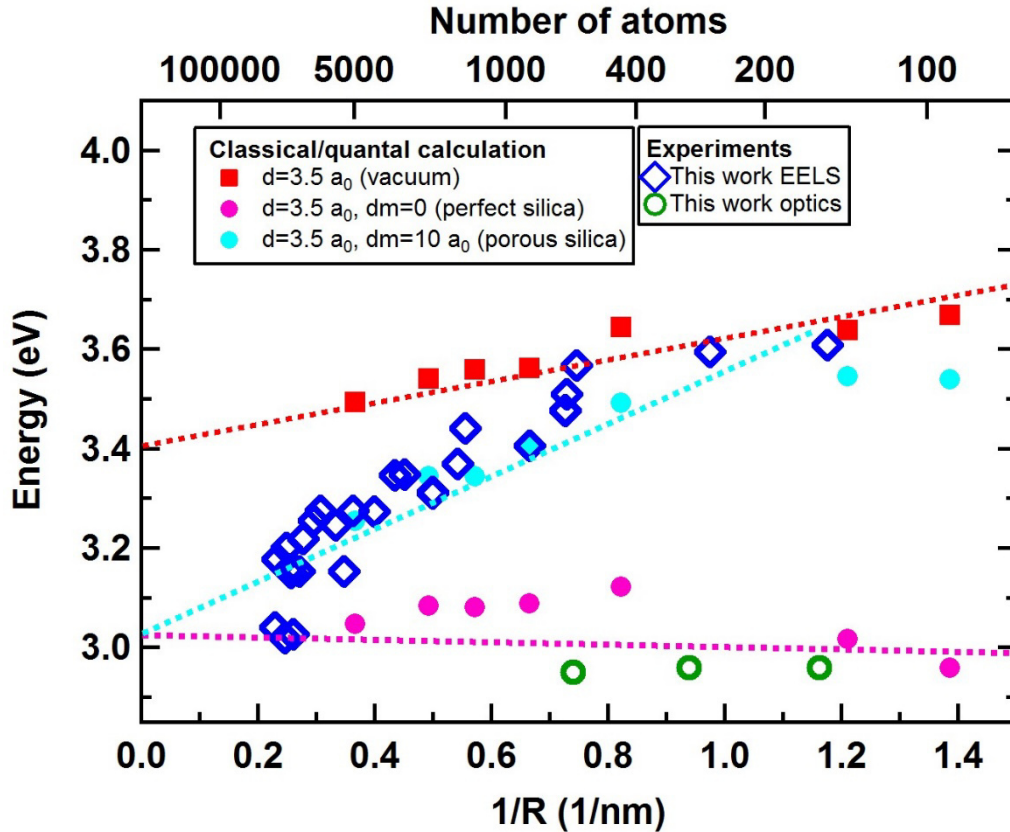


Figure 5.18: Size dependence of the LSP energy in EELS experiments at high dose (like the saturated value in figure 5.17a), as dark blue open diamonds. For comparison are shown the classical/quantal calculation values for free (red squares) and for silica-embedded particles with either a perfect interface ($d_m = 0$, pink circles) or a porous interface layer (mimicked through a vacuum layer of $d_m = 10 a_0$ ($\approx 5 \text{ \AA}$), light blue squares). Also shown are some of the data from optical spectroscopy of this work as open green circles. Dashed lines are guides to the eye.

5.5. Conclusion

In this chapter STEM-EELS and optical experiments results were presented for embedded silver nanoparticles prepared by the same conditions. In the STEM-EELS experiments, the electron beam modified the local environment of the particle and a blue shift of the LSP was observed. Consequently, a LSP blue shift in STEM-EELS experiments seemed in contradiction with optical experiments which did not present any LSP shift. A classical/quantal model which takes into account quantum effects and the environment was employed and allowed to explain how the apparently contradiction between both techniques is the result of the trade-off of quantum effects which can be balanced by the local environment porosity. Up to now EELS technique had suffered from polemics in the quantum regime due to the discrepancy with optical measurements in old literature. Additionally, the EELS, optical and classical/quantal calculation results were compared with older literature solving the contradictions found in literature.

Chapter 6: Volume plasmon

6.1. Introduction

A plasmon wave (quantum of electron density oscillation) can exist inside metals, semiconductors, insulators and liquids [128]. Figure 6.1 illustrates the idea of a plasmon wave inside a solid considering an electron excitation. The atoms of the solid have a size noted a . Each atom presents an electron cloud displacement noted $\xi(x, t)$. The excitation creates a wave of electron density fluctuations propagated through the arrays of atoms. This wave has a wavelength λ which is larger than the distance between atoms. This is a longitudinal wave.

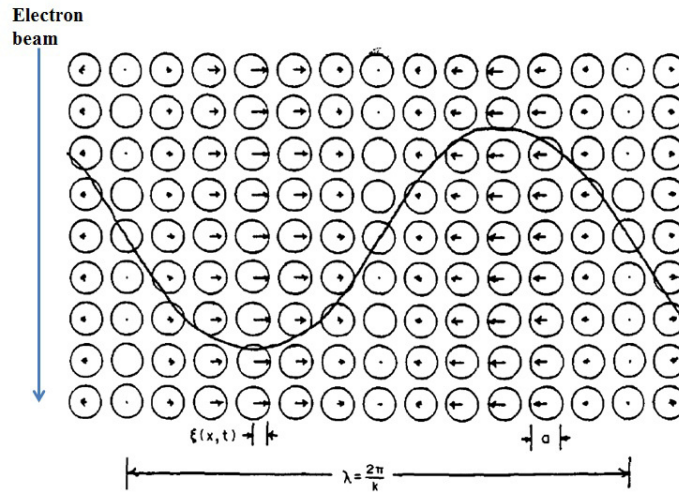


Figure 6.1: Scheme of a plasmon wave created inside a solid induced by an electron excitation. The atoms of the solid are represented by circles. Each atom has a size noted a and the displacement of the electron density in each atom is noted $\xi(x, t)$. The plasmon wave propagates through the array of atoms and has a wavelength λ . Adapted from Ref. [128].

In the case of metals, the conduction electrons are delocalized and not attached to an atom as was treated in section 2.3. If the interaction between electrons is neglected, the plasmon inside the metal (volume plasmon) is defined by the equation 2.3.5 ($\omega_p = \sqrt{ne^2/\epsilon_0 m_e}$), where n is the electron density, e the elementary charge, ϵ_0 the vacuum permittivity and m_e is the effective mass of an electron.

If the Coulomb interaction between electrons is considered, a more complex mechanical treatment is needed, such as the RPA (Random Phase Approximation). The RPA predicts the dispersion of the volume plasmon with the transferred momentum q [129], see figure 6.2. When the dispersion of the volume plasmon enters in the electron-hole continuum (shaded area in figure 6.2), the plasmon decays into an electron-hole pair (Landau damping, discussed in section 2.5.4).

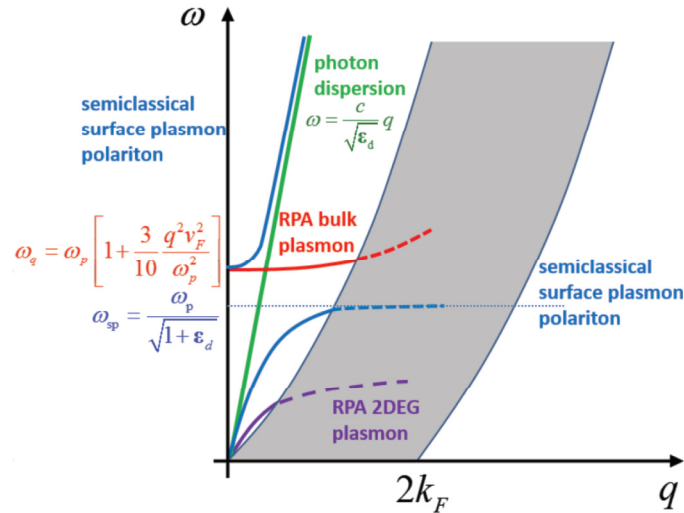


Figure 6.2: Dispersion curves of the RPA volume (bulk) plasmon resonance (red line) and the surface plasmon polaritons (blue lines). The shaded area marks the electron-hole continuum. When the volume plasmon resonance enters in this area, the plasmon decays into electron-hole pairs which is called Landau damping [129], discussed in section 2.5.4. Image taken from Ref. [129].

6.2. Volume plasmon in sub-10 nm metal nanoparticles in literature

The volume plasmon in metals has been studied by electron excitation since the 30s with the works of Rudberg [130], Rudberg and Slater [131] and Ruthemann [132]. Nowadays, the volume plasmon is very well known in large nanoparticles and is routinely detected by STEM-EELS technique.

In recent EELS literature, the volume plasmon has been studied in sub-10 nm metallic nanoparticles. In the case of silver, Scholl et al. [17] reported volume plasmons in particles as small as 5 nm in diameter, see figure 6.3a. According to Scholl et al., below 5 nm diameter, the surface/volume ratio is high and the volume plasmon is diminished considerably. Additionally, the Begrenzung effect (discussed in section 2.4.3) could contribute to the disappearance of the volume plasmon. Another uncertainty comes from the fact that the surface plasmon shifts towards high energies which are close to the volume plasmon energy and it is not easy to clearly separate both signals. They report a blue shift on the volume plasmon with the decrease of particle size which is interpreted by a quantum model.

Hobbs et al. [133] studied volume plasmons in aluminum nanodisks with sizes below 10 nm diameter. A blue shift is reported on the volume plasmon with the decrease of particle size (figure 6.3b). Moreover, the intensity of the volume plasmon as a function of the size is studied. An extrapolation on the data predicts a volume plasmon intensity equal to zero for a particle of 1.6 nm diameter.

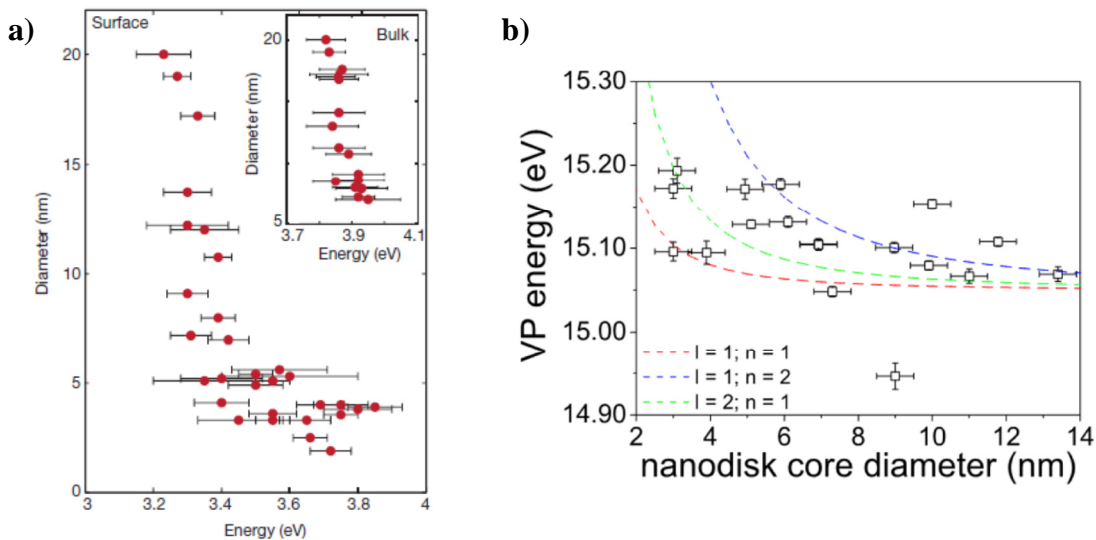


Figure 6.3: *EELS volume plasmon studies in sub-10 nm metallic nanoparticles. (a) Silver nanoparticles deposited directly in a substrate from Ref. [17]. (b) Aluminum disk nanoparticles deposited on a substrate from Ref. [133]. A blue shift of the volume plasmon energy with the decrease of size is observed in both cases.*

To the best of our knowledge, volume plasmons have not been reported in silver nanoparticles smaller than 5 nm diameter. In this part of the thesis, I am trying to explore the region of sizes below 5 nm.

6.3. Volume plasmon results

From a spectrum-image (described in section 3.3.4), the EEL spectra can be extracted from different regions in a particle. HAADF image of a ~9 nm diameter silver nanoparticle embedded in silica is presented in figure 6.4 together with the EEL spectra associated to different regions of the particle. This particle presented a high level of signal and it was possible to do deconvolution without introducing artifacts.

As can be seen, exciting the particle far from the surface (red region), the surface plasmon signal is weak. In a region close to the surface (purple region), the surface plasmon is intense with a well-defined energy position at 3.17 eV. In the blue region between the surface and part of the interior of the particle, the surface plasmon resonance becomes larger. The black region corresponds to the center of the particle and in this region the volume plasmon is observed close to ~4 eV together with the contribution of the surface.

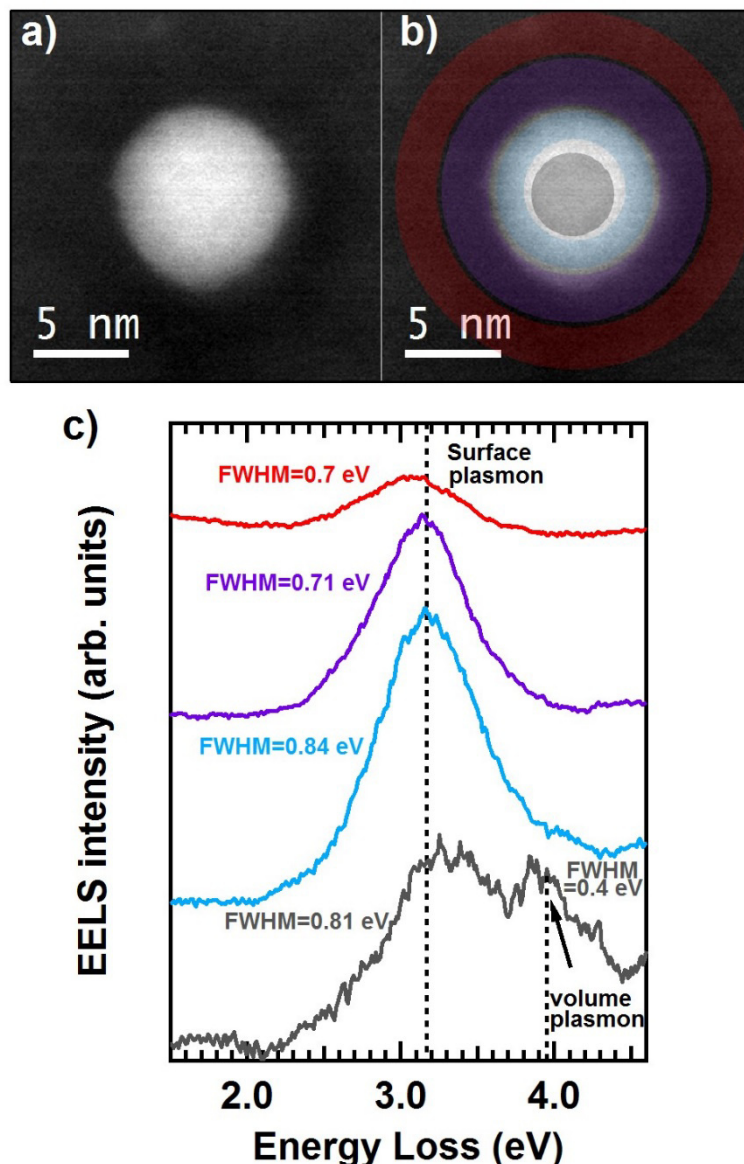


Figure 6.4: (a) HAADF image of a silver nanoparticle of ~ 9 nm diameter embedded in silica matrix. (b) Same HAADF image of a with colored regions where EEL spectra were collected and summed. (c) Deconvoluted EEL spectra coming from the colored regions marked in b. Depending on the location of the electron beam, the surface and volume plasmons can be selectively observed.

6.3.1. Electron dose evolution

In a detailed observation, the appearance of the volume signal depends on the electron dose. Figure 6.5 shows signals coming from the surface and the volume of a 7.2 nm silver nanoparticle in silica at different electron doses. The surface signal corresponds to EEL spectra summed at the surface. The surface plasmon appears and blue shifts with the increase of electron dose as was described previously in section 5.3.2. The appearance of the surface signal is related to the surface oxidation removal. On the other hand, the volume signal (EEL spectra summed in the center of the particle) appears with the increase of electron dose but it is not clear an energy shift with the increase of electron dose. The apparition of the volume signal with the increase of electron dose

seems to be related to the surface oxidation removal, which is strange and unexpected for a volume signal. However, it is possible that in small particles the oxidation extends to the core. This means that the core of the particle could be oxidized and with the increase of electron dose the core oxidation is removed and the volume signal appears.

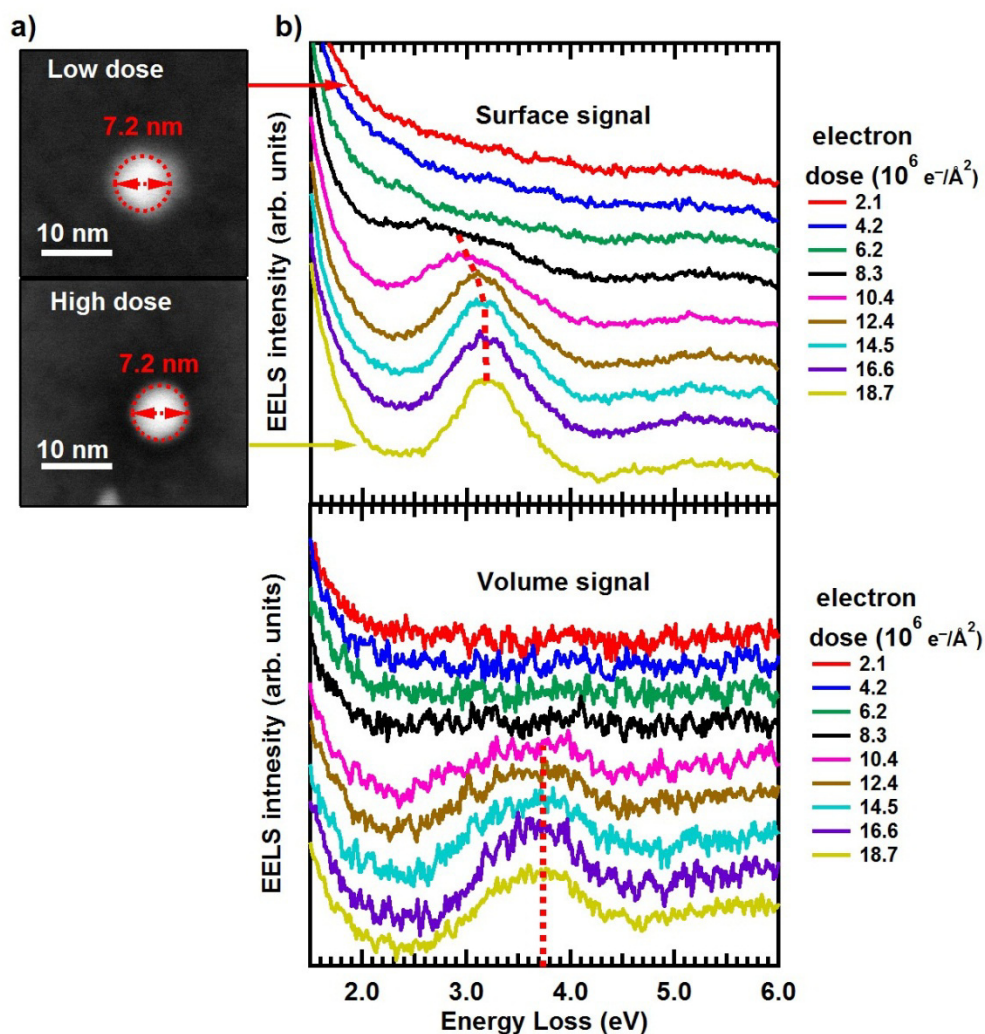


Figure 6.5: (a) HAADF images of a silica embedded silver nanoparticle of 7.2 nm at low and high electron dose. Visible is the removal of the oxidation layer. (b) Signals extracted from the surface and volume of the nanoparticle. The surface signal corresponds to the surface plasmon and it appears and blue shift with the increase of electron dose. On the other hand, the volume signal appears with the increase of electron dose but does not exhibit a clear energy shift.

Another important observation of figure 6.5b is that we do not distinguish two peaks from the volume of the particle as presented previously in figure 6.4 for a larger particle. In a detailed observation of figure 6.5b, the width of the volume signal is larger than the width of the surface plasmon signal. This is maybe due to the contribution from the surface on the volume signal which cannot be distinguished.

Due to the fact that the volume signal does not shift with electron dose, our study will not consider the electron dose dependence on the volume plasmon energy. However, the intensity of the volume plasmon can be affected by the electron dose.

6.3.2. Size evolution

In figure 6.6 it is presented the surface and volume signals of silica embedded silver nanoparticles of different sizes at high electron doses. We can observe that in the largest particles, the volume signal is broad due to the contribution from the surface plasmon. However, in the smallest nanoparticles the volume signal is narrower.

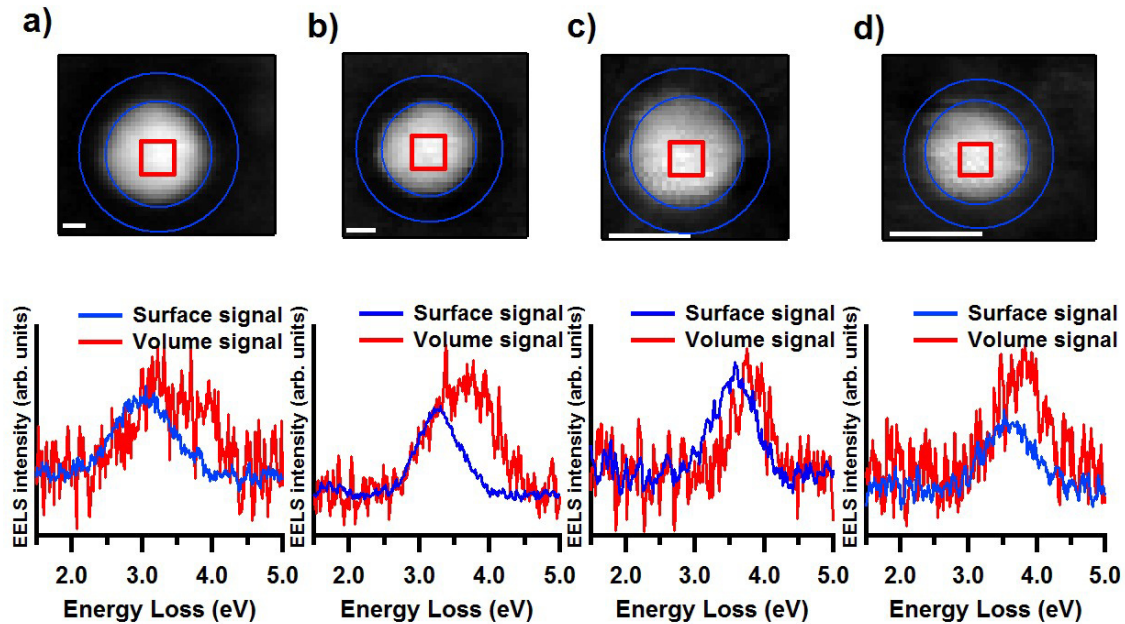


Figure 6.6: Examples of extracted surface and volume signals from large to small silver nanoparticles embedded in silica. (a) 7.9 nm particle. (b) 6.5 nm particle. (c) 2.7 nm particle. (d) 2 nm particle. Scale bar = 2 nm. The red area in the HAADF images has fewer pixels than the blue area and this explains why the volume signals are noisier than surface signals. The background of the spectra was subtracted.

We can extract the volume plasmon energy position by the fitting procedure explained in section 4.10 but using two Gaussians to fit the volume signal: One Gaussian for the surface plasmon contribution and the other one for the volume plasmon. The energy positions and FWHM of the surface plasmons were fixed in the fitting procedure since the parameters were already calculated by the fitting procedure as presented in section 5.3.2. Because the volume signal does not shift with electron dose, we used the EEL spectra coming from the volume at the highest electron doses.

The volume plasmon energy data will be plotted inside the surface plasmon-electron dose evolution of section 5.3.2 for comparison. The surface plasmon-dose evolution study is replotted in figure 6.7 in order to remind it.

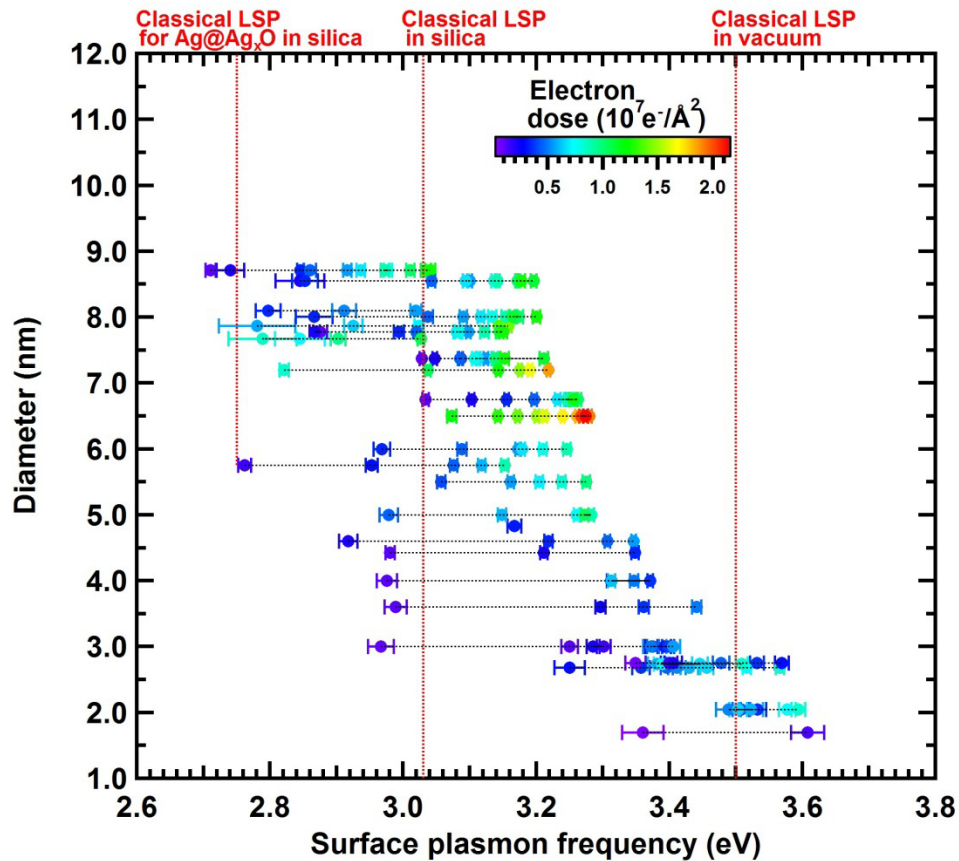


Figure 6.7: Evolution of the surface plasmon peak position of silica-embedded silver nanoparticles as a function of electron dose, indicated in color code. The interaction with the high-energy electron modifies the nanoparticle environment and the plasmon blue shifts to higher energies. The plasmon energy values for each nanoparticle are connected by a black dotted line. The central and right vertical lines depict the classical (size-independent) values for the plasmon of silica-embedded and free silver nanoparticles in the classical quasistatic limit and calculated using the values of Ref. [127]. The left-most vertical line has been obtained for the plasmon in the classical quasistatic limit of core@shell Ag@Ag_xO nanoparticles at 75% oxidation ratio.

Figure 6.8 shows the volume plasmon energy for different silver particles embedded in silica matrix inside the graph of figure 6.7.

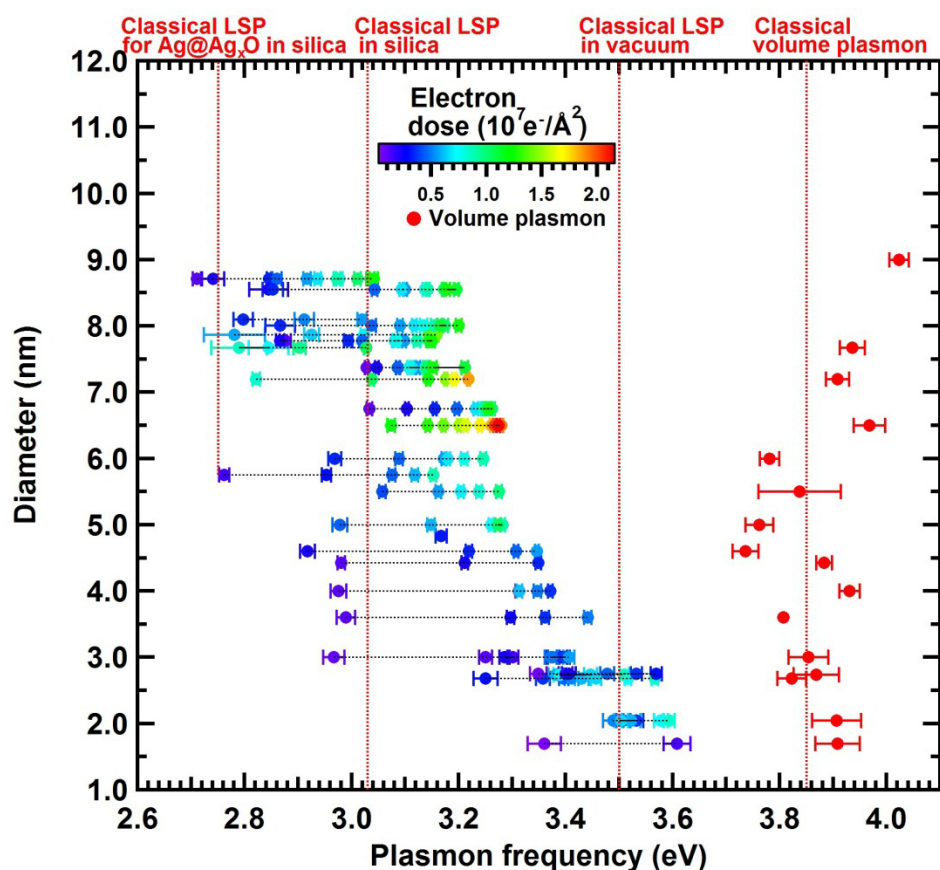


Figure 6.8: Surface plasmon evolution with electron dose (in color code) as presented in figure 6.7 together with the volume plasmon energy data. The volume plasmon data scatter around the classical volume plasmon (3.85 eV).

In figure 6.8, the classical volume plasmon is fixed to 3.85 eV (value reported in Ref. [17] for a silver particle of 20 nm diameter) and plotted as a vertical dashed red line. The volume plasmon data scatter around 3.85 eV. The values below 3.85 eV are maybe due to the fact that the contribution from the surface is not very well subtracted from the volume signal in the fitting. Another problem is the high noise in the volume signal, as discussed in figure 6.6, which could have a high impact in the fitting

The study of the area of the volume plasmon peak with the size of the nanoparticles is presented in figure 6.9. In a first observation (red dots) there is not a clear correlation peak area-size. However, if we consider the data with similar electron doses, the area of the volume plasmon increases with the increase of particle size as expected for a volume plasmon (black crosses).

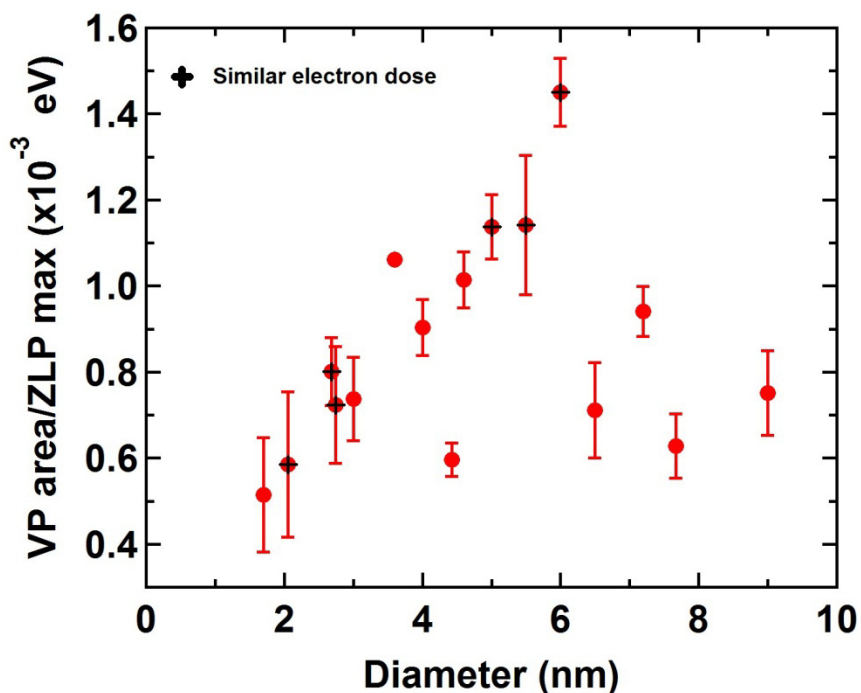


Figure 6.9: Area under the volume plasmon (VP) peak divided by the maximum of the ZLP. The black crosses correspond to the points of similar electron doses. An increase in VP area with the particle size is observed in the points of similar electron doses (black crosses).

6.4. Conclusion

In this chapter we described the volume plasmon excitation by an electron beam. The volume plasmon signal was detected in silver particles smaller than 5 nm which had never been reported previously in the literature. The smallest particle in which we detected the volume plasmon was 1.7 nm in diameter.

The appearance of the volume plasmon depends on the electron dose, which may be related to the oxidation of the particle's core. On the other hand, the volume signal energy position is dose-independent. The size evolution of the volume plasmon energy scattered around 3.85 eV, which is close to the classical volume plasmon energy for large silver nanoparticles in EELS experiments. A deeper study on the volume plasmon of sub-5 nm silver nanoparticles is needed.

Chapter 7: Surface plasmons in triangular nanocavities

7.1. Introduction

The study of plasmon resonances in nanostructures has been widely studied by SNOM and EELS/Cathodoluminescence techniques. The spatial and spectral resolutions offered by these techniques have achieved to resolve a rich variety of plasmon modes in such structures. Recently, a detailed analysis of surface plasmons in flat structures [33] proposed to classify surface plasmon modes into two families. The first one corresponds to the so-called edge modes, which are localized at the periphery of two-dimensional nanoobjects. These edge modes are well-known in the literature and have been reported for several geometries. [10], [33], [38], [134], [135]. On the other hand, the second group of modes corresponds to the so-called pseudoradial breathing modes (RBMs) or simply breathing modes, which are localized inside the two-dimensional nanoobjects, see figure 7.1. Such modes present a charge oscillation as breathing-like and have been reported experimentally for silver nanodisks [33], [38], silver nanosquares [135], and silver nanotriangles [10], [34]–[36]. Moreover, although a large number of studies have been performed on 2D plasmonic objects, only the plasmonics disks [33], [38] received a comprehensive description. In nanodisks the edge modes have been related to plasmon modes on the edge of an infinite border and the RBMs are related to an infinite slab (see figure 7.2). In contrast, the widely studied case of triangular prisms could not be comprehensively described, each study leading only to a partial understanding of the mode structure (Nelayah et al. [10], [36], Keast et al. [34], Hao et al. [35], Kumar et al. [39], Fung et al. [40], Pabitra et al. [41], and Koh et al. [42]).

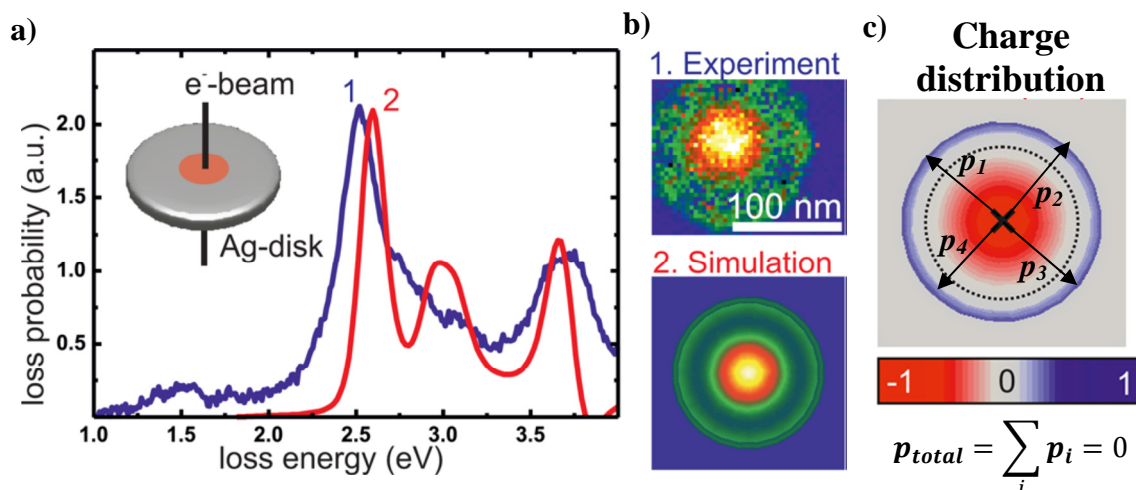


Figure 7.1: Electron beam excitation in the center of a flat nanodisk. (a) Experimental and simulated EEL spectra. (b) Experimental and simulated EELS maps at the resonance energies 1 and 2 respectively. (c) Charge distribution of the plasmon resonance. The charge distribution is concentrated in the center and border of the disk. The charge oscillation is breathing-like and have a zero net dipole moment. Image adapted from Ref. [38].

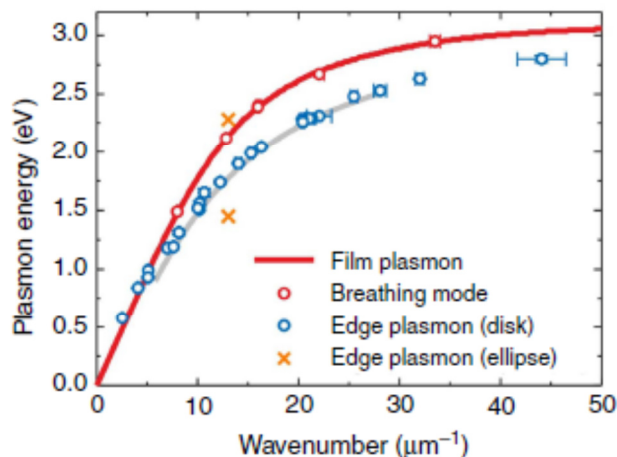


Figure 7.2: Dispersion relation of edge and pseudoradial breathing modes in a flat nanodisk compared to the plasmon modes on the edge of a film (grey line) and Surface Plasmon Polaritons in a silver thin film (red line), respectively. Taken from Ref. [33].

In this chapter we report on high-resolution imaging and spectroscopy of plasmon modes sustained by aluminum nanotriangles using electron energy loss spectroscopy (EELS) performed in a scanning transmission electron microscope (STEM). Through spectral and spatial mapping, we unveil the edge modes concentrated along the boundaries of the nanotriangle and the pseudoradial breathing modes (RBMs) concentrated inside the nanotriangle cavity. We present the indexing of all these modes based on one- and two-dimensional Fabry–Pérot cavity models.

In analogy to the relation between disk edge modes and film edge modes [33], [38] we prove experimentally that nanotriangle edge modes are similar to plasmon modes of linear nanoantennas having the same length as the edge of the triangle. The dispersion relation of triangle edge modes and nanoantenna modes was found identical. On the other hand, the dispersion relation of the triangle RBMs follows that of Surface Plasmon Polaritons (specifically SRSPs) [36] in thin films, as in the case of disk RBMs [33], [38]. Additionally EELS-GDM simulations [32] were performed in order to interpret the results.

7.2. Sample preparation and methods

Aluminum equilateral nanotriangles were fabricated by our collaborators in the Université de Technologie de Troyes (Jérôme Martin and Davy Gérard) by electron beam lithography and lift-off process on a STEM-EELS compatible substrate (30 nm thick Si_3N_4 membrane). The triangle side length varies from 125 to 700 nm, while the thickness of all structures was fixed to 40 nm.

The STEM-EELS measurements were carried out using the UltraSTEM200 microscope of NION company. Throughout this study, we used a 100 kV acceleration voltage and with a typical probe current of 20 pA. Spectrum images (associated with the HAADF images) were acquired with typical 100x100 pixels. After ZLP alignment, the Richardson-Lucy deconvolution [97] (performed with the free software Hyperspy [96]) was used to resolve plasmonic resonances at low energies close to the ZLP. With typically 50 iterations the deconvolution yields a ~ 0.15 eV of ZLP FWHM. An automatic multipeak-fitting procedure (as described in section 3.3.5) with several Gaussian functions was used to generate intensity maps.

7.3. STEM-EELS results of Al nanotriangles

Figure 7.3a presents typical deconvoluted EEL spectra summed on different regions on the same aluminum nanotriangle with a 604 nm side length. The upper inset contains the HAADF image with three boxes in which the EEL spectra were summed. Figure 7.3a reveals distinct and well-defined electron energy loss peaks with maxima between 1 and 4 eV. These features correspond to the multipolar plasmonic resonances sustained by the Al nanotriangles. The resonances obtained at the edges of the triangle (curves blue and red in Figure 7.3a) are in good agreement with even and odd multipolar plasmonic resonances reported previously in Al nanoantennas [136] (see figure 7.4). The spectrum coming from the central part of the nanotriangle (green box) presents a background that comes from the tail of a broad peak centered at 7 eV, which corresponds to the asymptotic limit of SRSPP on aluminum thin film. In Figure 7.3b, the spatial symmetry of the modes is further analyzed by mapping the intensity of the Gaussian functions used in the multi-peak fitting procedure as described in section 3.3.5. This has been reproduced on all nanotriangles of different sizes investigated in this study. These intensity maps are directly linked to the projection onto the electron beam trajectory of the electromagnetic local density of states (zLDOS) [15]. A closer look at the intensity distribution maps evidences two kinds of modes: edge modes located at the edge of the nanotriangle and the pseudo-RBMs located inside the triangular cavity and confined by the triangle boundaries.

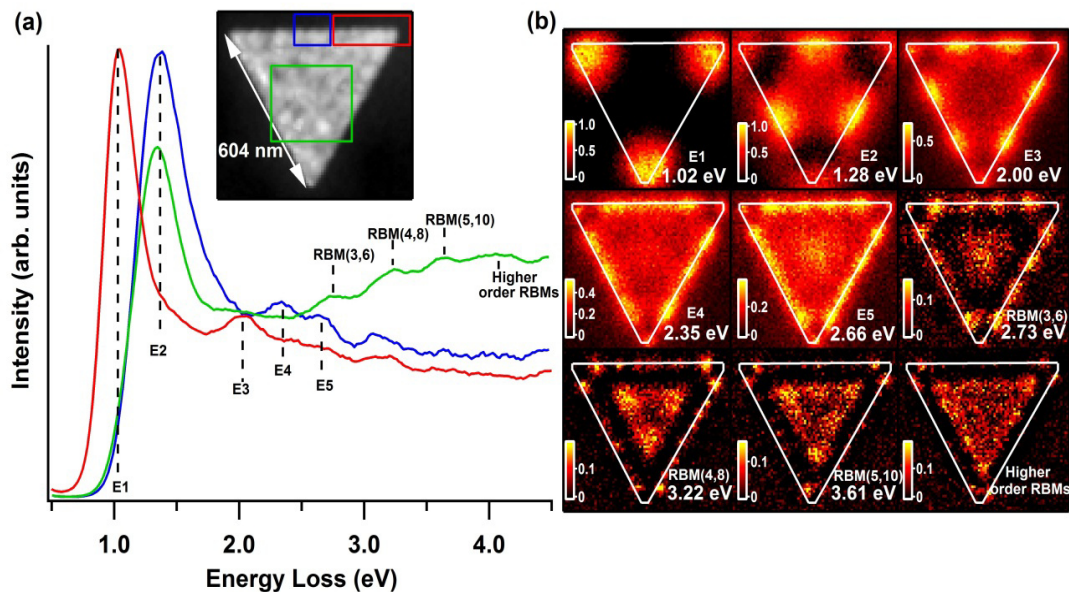


Figure 7.3: (a) Deconvoluted EEL spectra acquired at different locations (color boxes in the HAADF image of the inset) on a single Al nanotriangle with 604 nm side length. The labels *E* and *RBM* stand for the edge and pseudoradial breathing modes observed in the nanotriangle. (b) EELS fitted intensity maps of the plasmon resonances sustained by the Al nanotriangle at the energy of the resonances evidenced in a.

The comparison of edge modes in nanotriangles and nanoantenna modes are presented in figure 7.4. It is clear the tight relation between both plasmon modes. We will see later in section 7.6 that the dispersion relations of both kinds of modes are identical.

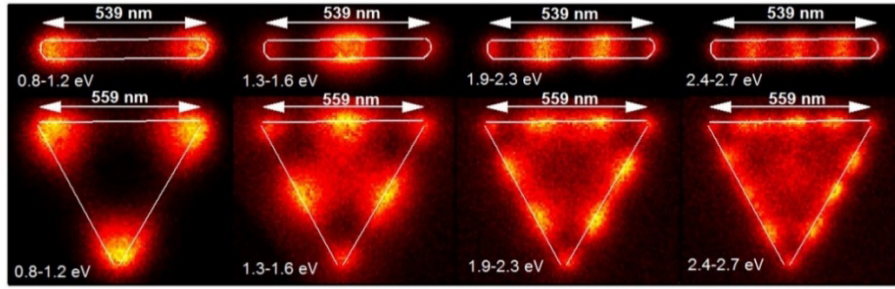


Figure 7.4: Filtered maps of an Al nanoantenna of 539 nm length (same nanoantennas used in Ref. [136]) and an Al nanotriangle of 559 nm side length. It is clear the similarity between nanoantenna modes and nanotriangle edge modes.

To obtain the dispersion of the edge modes and RBMs, we studied Al nanotriangles with side lengths varying from 125 to 700 nm and same thickness of 40 nm. The EEL spectra measured at the nanotriangles edges and nanotriangles centers are shown in figure 7.5a and b, respectively. For both kinds of modes, a monotonous shift of the plasmon modes peaks toward higher energies when the nanotriangle size decreases is evidenced. The different edge modes and RBMs are labeled and their evolution (or energy shift) is highlighted by the red dashed curves, unveiling their dispersion behavior. These results show the tunable properties of the edge modes in the visible-infrared region and the RBMs in the UV region by varying triangle size. Note that an additional peak around 1.5 eV is visible in the smaller nanotriangle of figure 7.5a. This feature is associated with interband transitions (*ib*) in aluminum (between occupied p-levels to unoccupied s-levels). It has been observed that *ib* in aluminum can strongly couple with surface plasmons, resulting in convoluted features [136], [137]. We observe qualitatively in figure 7.5a a slight increase of the line width of mode E1 when it is centered close to the *ib* energy.

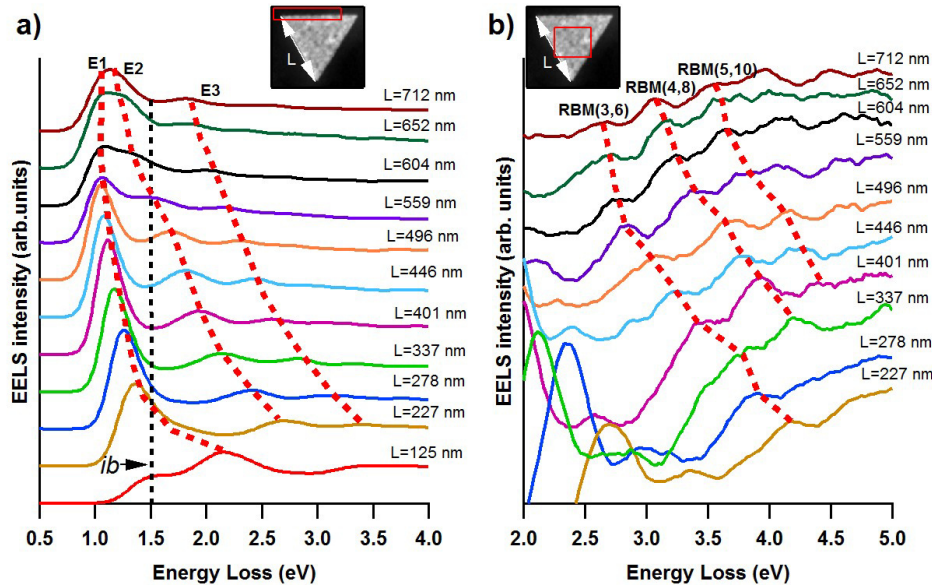


Figure 7.5: Dispersion of the plasmonic edge modes and pseudo-RBMs with varying triangle side lengths. (a) EEL spectra measured on the edge of nanotriangles of different edge lengths. The dashed red lines follow the spectral position of different edge modes and the black dashed line corresponds to the position of interband transitions in aluminum. (b) EEL spectra taken on the center of triangles for different length sizes. The dashed red lines follow the spectral position of different RBMs.

7.4. Fabry-Pérot analytical models

Before discussing the behavior of edge modes and RBMs as a function of the size of the nanotriangles, we need to introduce a robust indexing scheme. For this we will use a one-dimensional Fabry-Pérot cavity to model the edge modes and a two dimensional Fabry-Pérot cavity to model the RBMs. These models were developed with the collaboration of Arnaud Arbouet from the Université de Toulouse, France.

7.4.1. One-dimensional cavity

For the edge modes, we adopt an indexing based on a one-dimensional Fabry-Pérot model. This approach was already used to describe nanoantenna modes [12], [138] and film edge modes [33]. Intensity maps of edge modes can be interpreted as arising from a constructive interference in a one-dimensional Fabry-Pérot cavity.

The constructive interference is obtained whenever half the wavelength of the localized surface plasmon (LSP) wave fits into the triangle edge length. This condition yields the following relation between the LSP wavenumbers (k_n) for the edge modes [12]

$$k_n L = n\pi - \phi \quad (7.4.1)$$

Where n is an integer, L is the triangle edge length and ϕ is the phase shift upon reflection at the boundaries of the cavity. In the following, the different edge mode orders are labeled E_n (E_1, E_2, E_3, \dots). It is worth noting that edge modes only depend on L . In that sense, triangle edge modes behave just like multipolar modes in linear nanoantennas (see figure 7.4) and do not depend on the general symmetry of the nanoparticle. We will prove experimentally later that the dispersion relation of edge modes in nanotriangles is identical to the dispersion relation of nanoantenna modes, provided L stands for the length of the nanoantenna or the edge length of the triangle. This validates the use of equation 7.4.1 in nanotriangle edge modes.

To obtain the phase shift and the wavenumbers of edge modes experimentally, we used the one-dimensional Fabry-Pérot cavity with length L (figure 7.6) and considering an incident plasmon wave that is reflected at the boundary of cavity with a phase shift ϕ .

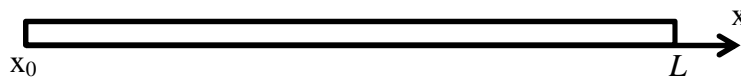


Figure 7.6: Fabry-Pérot linear cavity of size length L .

The incident and reflected surface plasmons can be written as planes waves, i.e. $E_i = Ae^{ik(x-x_0)}$ and $E_r = |r|Ae^{ik(2L-x)}e^{i\phi}$, respectively. We assume that the reflective factor $|r|$ is equal to 1. The wavenumber k is related to the phase shift ϕ by the equation 7.4.1. Summing the incident and reflected waves

$$E_{total} = Ae^{ik(x-x_0)} + Ae^{ik(2L-(x-x_0))}e^{i\phi} \quad (7.4.2)$$

$$E_{total}^2 = A^2[\cos(k(x - x_0)) + \cos(2kL - k(x - x_0) + \phi)]^2 + A^2[\sin(k(x - x_0)) + \sin(2kL - k(x - x_0) + \phi)]^2 \quad (7.4.3)$$

By fitting the experimental maps profiles of the edge modes with the E_{total}^2 expression, it is possible to obtain the phase shift and the wavenumbers of edge modes. One example is shown in figure 7.7 for the analysis of the mode E4 of a nanotriangle.

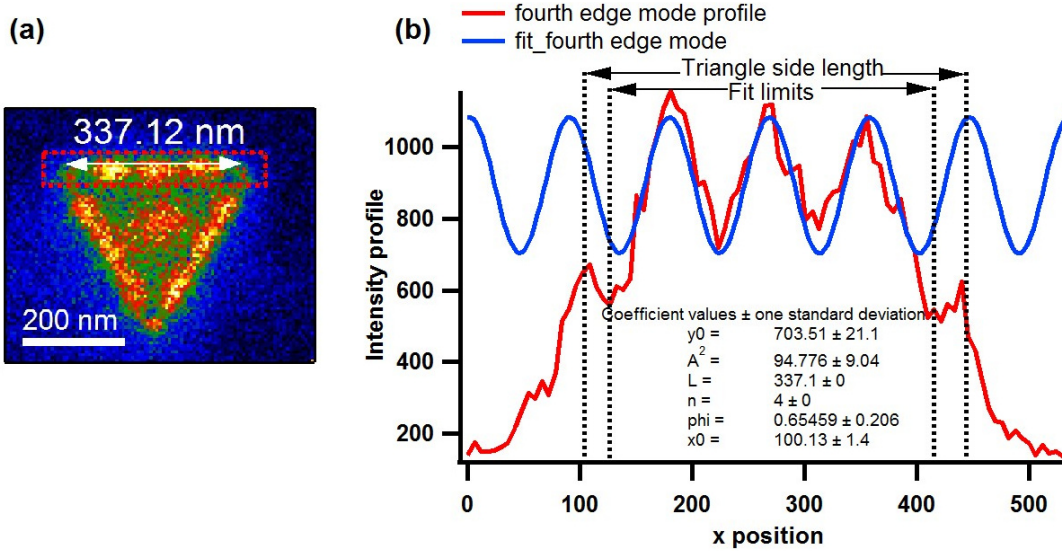


Figure 7.7: (a) Experimental map of the fourth edge mode in a 337 nm nanotriangle side length. (b) Profile extracted from the experimental map (dashed red box in a) and fitted with E_{total}^2 . We set the limits of the fit to avoid the antinode bunching effect [12], [136] (presented at the boundary of the cavity).

We note that the fit in figure 7.7b does not take into account the signal at the vertices of the triangle. This is due to antinode bunching effect which corresponds to a different separation between antinodes at the extremes of the triangle side length. This has been reported in aluminum and silver nanoantennas but its origin is not well understood [12], [136]. Figure 7.8 shows an aluminum nanoantenna where antinode distances in the extremes are different with respect to the antinode distances in the middle. For this reason, the calculation of the wavenumber of the first edge mode in nanotriangles has not been done.

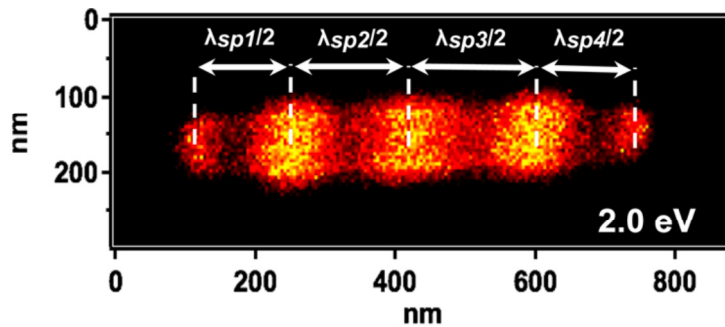


Figure 7.8: Example of the distances between antinodes from an EELS map in an aluminum nanoantenna (from Ref. [136]). The distance between antinodes is not the same, being shorter the antinode distances in the extremes of the nanoantenna. This is the antinode bunching effect [12], [136].

Figure 7.9 shows the phase shift of the edge modes in Al nanotriangles with different side lengths. We have observed that the phase shift of the edge modes has a tendency to decrease with increasing the mode order from around 0.45π to 0.15π . This decrease in phase shift has also been reported in silver nanorods [12]. It means that higher order edge modes are more confined at the edge of the triangle.

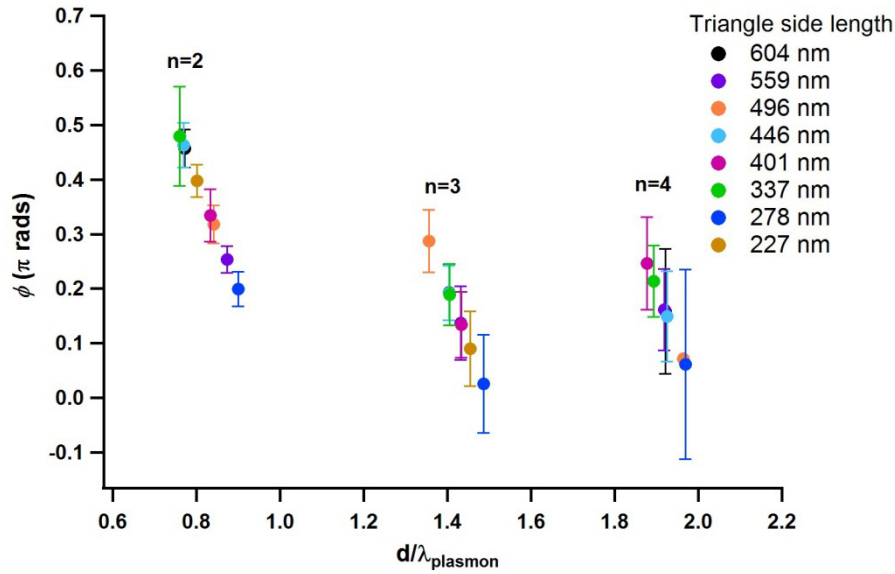


Figure 7.9: Phase shift of the edge modes in Al nanotriangles with different side lengths. Low order modes present a higher phase shift. The phase shift is decreasing when the order of the mode is increasing. The edge mode of order 1 is not taken into account due to the antinode bunching effect [12], [136] at the extremes of the triangle side length.

7.4.2. 2D-triangular cavity

As detailed in the following, the RBMs detected in the aluminum nanotriangles arise from the constructive interference of Short Range Surface Plasmon Polaritons (SRSPPs) propagating on the surface of the metallic particle and bouncing off its boundaries. The existence of these modes shows that the SRSPPs damping either intrinsic or due to scattering at the boundaries into the far-field is sufficiently small in our lithographed structures. Waves confined in two-dimensional structures is a generic problem and the two-dimensional Helmholtz or Schrödinger equations have been solved analytically for a long time for different boundary conditions and in different contexts (acoustics, optical modes in resonators, quantum billiards...). Interestingly, the equilateral triangle is one of the very few cases for which analytical expressions can be given. The energy eigenstates of a particle of mass M inside an infinite quantum well with an equilateral triangular cross-section have been solved analytically [139], [140]. The eigenenergies are

$$E_{lm} = \frac{1}{2ML^2} \left(\frac{h}{2\pi} \right)^2 \left(\frac{4\pi}{3} \right)^2 (l^2 + m^2 - lm) = E_0(l^2 + m^2 - lm) \quad (7.4.4)$$

Where L is the side length of the equilateral triangle. The associated quantized wavenumbers are

$$k_{lm} = \left(\frac{4\pi}{3}\right) \sqrt{l^2 + m^2 - lm} \quad (7.4.5)$$

Figure 7.10 shows the probability density $|\psi(r)|^2$ associated with the first three eigenmodes of a particle enclosed in an infinite quantum well of triangular shape. The similarity between the spatial distribution of these eigenmodes and the electromagnetic eigenmodes detected at high energy in our EELS experiments is striking and is a direct consequence of the similarity between the Schrödinger and Helmholtz partial differential equations. However, in the case of a particle enclosed in an infinite quantum well, the probability density vanishes on the boundaries of the cavity (Dirichlet conditions).

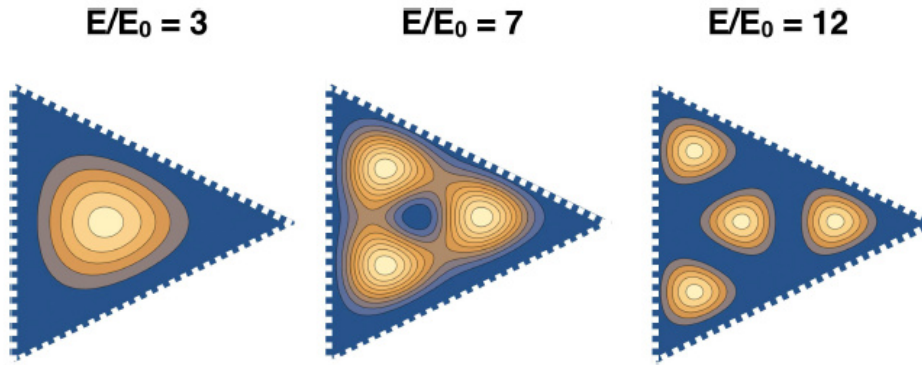


Figure 7.10: Probability density $|\psi(r)|^2$ of the first three eigenmodes of a particle enclosed in an infinite quantum well with a triangular shape obtained from an analytical resolution of Schrödinger equation.

In the case of an electromagnetic surface wave confined within a triangular nanostructure, i.e the present situation, we do not have sufficient information about the reflection coefficient and its dependence on the incidence angle to easily solve this problem. Furthermore, it is interesting to see how the phase shift experienced by the SRSP wave upon reflection on the nanotriangle boundaries impacts the spatial distribution of the plasmon eigenmodes. Therefore, in the following, we adopt the approach initiated by Chang *et al.* and Wysin *et al.* to describe micro-sized dielectric cavities with applications on micro lasers and resonators [141], [142]. In his paper, G. Wysin investigates the electromagnetic modes of equilateral triangle resonators using a set of 6 plane waves matched to each other by Fresnel factors and producing exterior evanescent waves. His model provides estimates of the eigenmodes wave functions, frequencies and lifetimes. We summarize in the following the main lines of their approach, more technical details can be found in Wysin's original paper [142]. Following Chang and Wysin, we consider the sequential reflections of a surface electromagnetic wave off the edges of a triangular cavity. We assume that the SRSP excited in the nanotriangles are confined at the surface of the particles and are reflected following Snell's law sequentially on the different edges. We assume that the reflected SRSP wave acquires a phase-shift which does not depend on the incident angle. In the following, we consider an equilateral triangle resonator of refractive index n_{al} enclosed in a medium of refractive index n_{env} . In the 250-600 nm range, n_{al} is between 0.12 and 1.12. In our case, the ratio of the refractive indexes of resonator and embedding medium is therefore $n_{tr}/n_{env} \sim 0.1-0.5$. Contrary to the case of semiconductor microstructures

embedded in air, the confinement is therefore not caused by total internal reflection but it is due to the confinement of the SRSPs at the surfaces of the aluminum nanoprisms. To understand the formation of confined short range surface plasmon polariton (SRSP) modes, it is instructive to consider the propagation of a wave inside the triangular cavity. We assume that a wave denoted W_1 is outgoing from the bottom edge of a triangular cavity (see figure 7.11) and makes an angle α with the (OX) axis. Considering the laws of reflection and the geometry of the cavity, one can see that upon successive reflections on the edges of the triangle, this wave will generate reflected waves W_i making an angle θ_i with the (OX) axis as listed in Table 7.1 and sketched on figure 7.11. Whereas the order of successive reflections may not follow the present numbering for particular situations, it is important to note that **in all cases**, the final situation can be described by a superposition of these six waves.

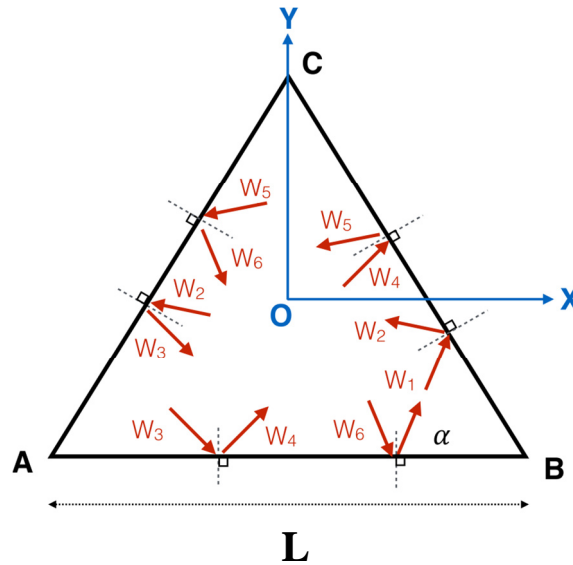


Figure 7.11: Sketch of a triangular metallic particle into which SRSPs are confined.

It can be seen in table 7.1 that in the general case, a minimum of two roundtrips inside the cavity is required for the wave to recover its initial propagation direction. Indeed, after only one round trip in the cavity, the propagation direction of the SRSP wave is different from the original unless $\alpha = \pi/3$. SRSP being p-polarized electromagnetic waves, they have both an electric field component normal to the surface of the metallic particle, i.e along (OZ), and one in the plane of the triangle. These two components are, however, not independent and therefore in the following we focus only on the (OZ) component.

SRSP wave	Edge	Incidence angle	Angle with (OX)
W_1	AB	θ_1	α
W_2	BC	θ_2	$4\pi/3 - \alpha$
W_3	CA	θ_3	$4\pi/3 + \alpha$
W_4	AB	θ_4	$2\pi/3 - \alpha$
W_5	BC	θ_5	$2\pi/3 + \alpha$
W_6	CA	θ_6	$-\alpha$

Table 7.1: Labeling of the 6 different SRSP waves created inside the triangular particle. The angle with the (OX) is presented for each wave.

The electric field inside the triangular cavity can be written as the sum of the contributions from the different propagating waves discussed above

$$\mathbf{E}_{SRSPP,z}(\mathbf{r}) = \sum_i \mathbf{E}_{SRSPP,i,z} e^{i\mathbf{k}_i \cdot \mathbf{r}} \quad (7.4.6)$$

The wavevectors \mathbf{k}_i corresponding to these waves are a function of the magnitude k and initial angle with the (OX) axis α .

The analytical model [142] provides the wavenumbers of the SRSPP eigenmodes formed in a triangular Fabry–Pérot cavity

$$k_{lm}L = \frac{2\pi}{3} \left[(m-l)^2 + 3 \left(\frac{m+l}{3} - \frac{2\phi}{\pi} \right)^2 \right]^{1/2} \quad (7.4.7)$$

Where l and m are integers, L is the side length of the triangle, and ϕ is the phase shift upon reflection at the edges of the triangle. The integers l and m are used to label the RBMs (RBM_{lm}). At each reflection on the nanotriangle edges, we assume that the reflected SRSPP waves experience a phase shift independent of the energy and incidence angle

$$r_{SRSPP} = e^{-i\phi} = \frac{E_{SRSPP,6,z} e^{-ik_6 y \frac{L}{2\sqrt{3}}}}{E_{SRSPP,1,z} e^{-ik_1 y \frac{L}{2\sqrt{3}}}} \quad (7.4.8)$$

It can be shown that these relations can be simultaneously satisfied only for specific initial angles α . These angles and the associated wave vectors for the six waves of equation 7.4.6 can be computed for different values of the reflection phase shift ϕ . From their knowledge, the coefficients $E_{SRSPP,i,z}$ and the complete electric field $\mathbf{E}_{SRSPP,z}(\mathbf{r})$ can be calculated. We compute, for a given phase shift ϕ , the wavenumbers and incidence angle of the different nanotriangle eigenmodes. The spatial distribution of the electric field is then computed from equation 7.4.6. The best match between experimental EELS maps and spatial distribution of the eigenmodes predicted by this analytical model has been obtained with the following integers $\text{RBM}(3,6)$, $\text{RBM}(4,8)$, and $\text{RBM}(5,10)$ for a phase-shift $\phi = 0.45\pi$ (see table 7.2). This value was obtained by systematically varying the phase-shift and comparing the experimental and theoretical spatial distributions. The fact that the phase shift is different from zero reveals that the reflection of the SRSPP could be affected by charge accumulation at the boundaries or by field extension into the vacuum [12]. We found that the phase shift is constant independently of the RBM order. This behavior differs from the case of edge modes where the phase shift decreases with the increase of mode order (see figure 7.9).

Altogether, these results clearly show that the patterns observed inside the triangular aluminum nanotriangles can be ascribed to “breathing-like” Surface Plasmon modes arising from constructive interference of SRSPPs which propagate at the surface of the particle and are sequentially reflected on their edges. The analytical model predicts RBMs that we do not observe experimentally. The Table 7.2 lists the first 11 eigenmodes obtained by the triangular analytical model. We present for each eigenmode the quantum numbers (l,m) , the wavenumber multiplied by the edge length of the triangle (kL), the incident angle (α), the value of the integral of their contribution to the

Electromagnetic Local Density of States (zLDOS) calculated within the triangle limits, the real and imaginary part of the electric field and finally the zLDOS distribution maps. As we can observe only the eigenmodes exhibiting the highest zLDOS have the symmetry of the modes observed experimentally.

l	m	kL	Angle(α)	zLDOS	Real(E)	Im(E)	zLDOS
1	2	2.12	9.82	0.27			
2	4	5.78	43	0.93			
4	5	7.9	74.6	0.3			
3	6	9.87	50.1	1.59			
5	7	12	69.6	0.34			
4	8	14	53	1.35			
7	8	15	82	0.63			
6	9	16.14	67	0.41			
5	10	18.2	54.85	1.42			
8	10	18.97	77	0.67			
7	11	20.3	65.64	0.37			

Table 7.2: First 11 triangle eigenmodes obtained by the triangular analytical model. The columns are: the quantum numbers (l,m), the wavenumber multiplied by the edge length of the triangle (kL), the angle of incidence (α), the value of the integral of the electromagnetic local density of state (zLDOS) calculated in the triangle limits, the real and imaginary part of the electric field and the zLDOS distribution maps.

In Ref. [143], a similar two-dimensional model has been used to describe modes in large triangular cavities. In this case, the modes were completely different (surface plasmon polaritons at the surface of an infinite silver plane) and confined by silver reflector blocks separated by micrometric distances. The phase shift upon reflection was $\sim\pi$, revealing radically different boundary conditions (Dirichlet condition).

7.5. EELS Green Dyadic Method (GDM-Simulations)

To go beyond analytical descriptions of the edge and RBMs, we have performed extensive electro-dynamical simulations using the EELS-GDM method. The simulations were performed by Arnaud Arbouet from the Université de Toulouse, France. A detailed description of EELS-GDM can be found in the Ref. [32]. Briefly, the technique allows the description of the interaction of fast electrons with complex nanostructures and is based on the Green Dyadic Method [144]. This method is able to simulate large structures taking into account the substrate with a reasonable time of calculation. This is the reason why we used this method over BEM or FDTD simulation methods.

Electron energy losses and cathodoluminescence of nano-objects of arbitrary morphologies embedded in complex dielectric media, spectra and maps for both penetrating and non-penetrating electron trajectories can be obtained from the computation of a generalized field propagator. The contribution from the substrate is taken into account by adding the corresponding field-susceptibility to the field susceptibility of vacuum [145].

Throughout this study, we have considered 100 kV electrons impinging on aluminum nanotriangles deposited on a Si_3N_4 substrate ($n=1.98$). The dielectric constant of aluminum has been taken from Rakic *et al.* [53]. The aluminum nanotriangles have been discretized on a hc lattice with typically 8000 dipoles. The contribution from the substrate has been taken into account in the non-retarded approximation using the image dipole approximation. Figure 7.12 shows two EELS maps computed for different positions of a 100 kV electron beam travelling through or in the vicinity of a 700 nm triangle at two different energies. The spatial distribution of the loss probability reveals the excitation of two different edge modes. More than 100 such EELS maps have been computed and automatically processed using a Python script. The data processing consisted in extracting profiles of the electron energy loss probability on one edge of the triangle and along a line crossing the triangle to yield respectively the edge modes and the RBMs. Figure 7.12 shows such EELS profiles computed on one edge of the triangle revealing the excitation of two different edge modes. From these profiles, the position-energy maps that will be shown in figure 7.14 have been reconstructed.

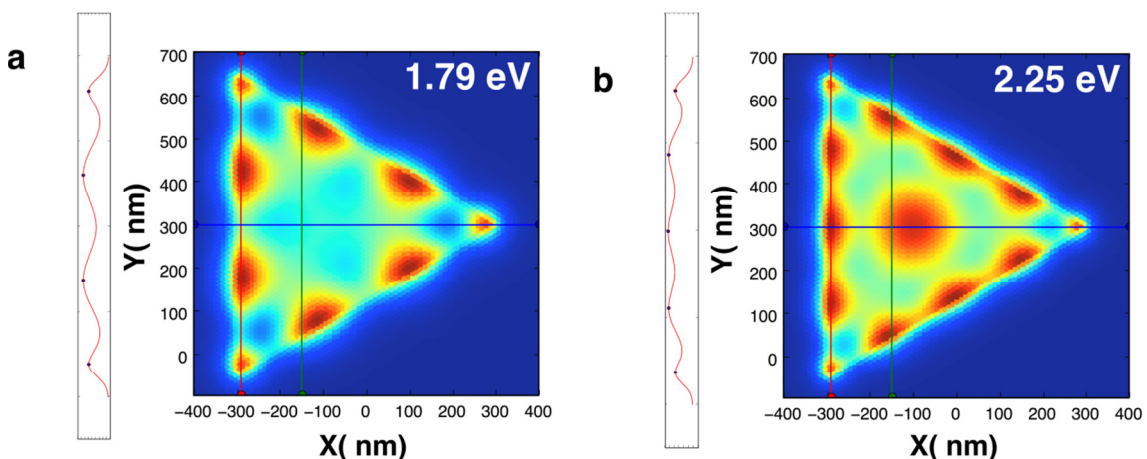


Figure 7.12: EELS-GDM simulation performed on a 700 nm aluminum triangle deposited on a Si_3N_4 substrate. An EELS map and the EELS profile along one edge are shown at two different energy losses. The incident electrons have energy of 100 kV.

7.5.1. Comparison of simulations with EELS results and analytical model

The experimental EELS and analytical maps are compared with extensive electrodynamical simulations using the EELS- Green Dyadic Method (EELS-GDM) [32] (figure 7.13). As it can be observed, the experimental, analytical model and GDM simulated maps match very well for the RBMs inside the triangle. However, on the edge of the triangle we do not observe the same number of lobes. This is expected for the 2D analytical model which does not take into account the edge modes at all, as they are separately simulated as 1D cavity modes, as presented before. In the experimental and GDM simulated maps the number of visible lobes on the edges is different, which is likely due to an energy inversion of some modes in the simulations as we will discuss in figure 7.14.

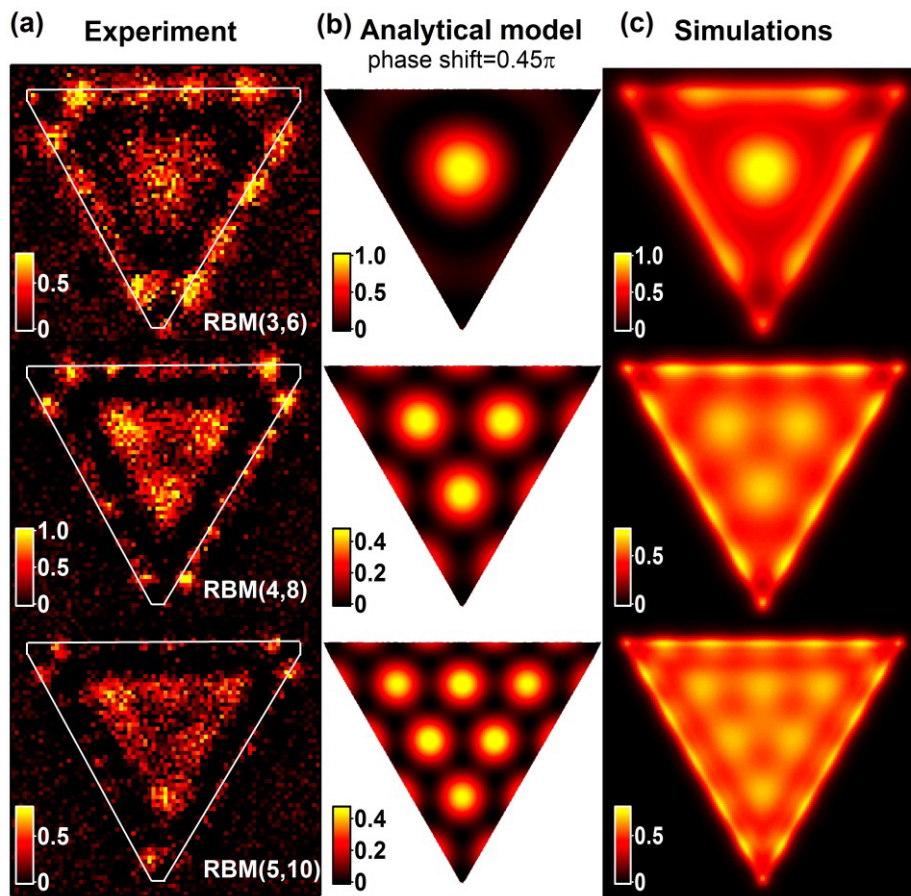


Figure 7.13: (a) Experimental maps of the RBMs of an aluminum nanotriangle of 604 nm side length. (b) Analytical model maps obtained with a phase shift of 0.45π showing the good agreement with experimental maps. (c) EELS-GDM simulations maps computed at the energy of the RBMs.

Figure 7.14 shows the experimental and simulated energy dispersion along the horizontal axis placed at two vertical positions on an Al nanotriangle of 700 nm side length. The energy dispersions were obtained in the following way: spectra across the height of the red rectangles in figure 7.14a,d were integrated, and their intensity as a function of the energy and position along the horizontal axis was plotted in figure 7.14b,e. Figure 7.14c,f presents the corresponding simulated energy dispersion. As it can be observed by comparing figure 7.14b and c, the edge modes are very well

reproduced by the simulations showing a pattern very close to that of the experiments. However, the simulated energy spacing is larger than the experimental one. This relatively larger energy spacing is expected at energies smaller than 1 eV due to the limitation of the deconvolution process to separate peaks. This is reflected in the overlap of E1 and E2 for increased triangle side lengths (figure 7.5a). The experimental RBMs dispersion is also very well reproduced by simulations (figure 7.14f) along a horizontal line close to the center of the triangle. However, again the energy spacing is higher in simulations than in experiments. Differences between the dielectric data taken into account in the simulations and the real ones partly explain this discrepancy. In particular, the refractive index of the Si_3N_4 substrate may have been slightly underestimated in the UV-blue spectral range. Setting aside the difference in energy spacing, the only discrepancy with the simulations is an inversion in energy of the first RBM (RBM(3,6)) with the fourth edge mode (E4). However, this mismatch could be explained due to the native oxide shell of aluminum which is not taken into account in simulations. It could also be due to the shape of the triangle edge used in the computation.

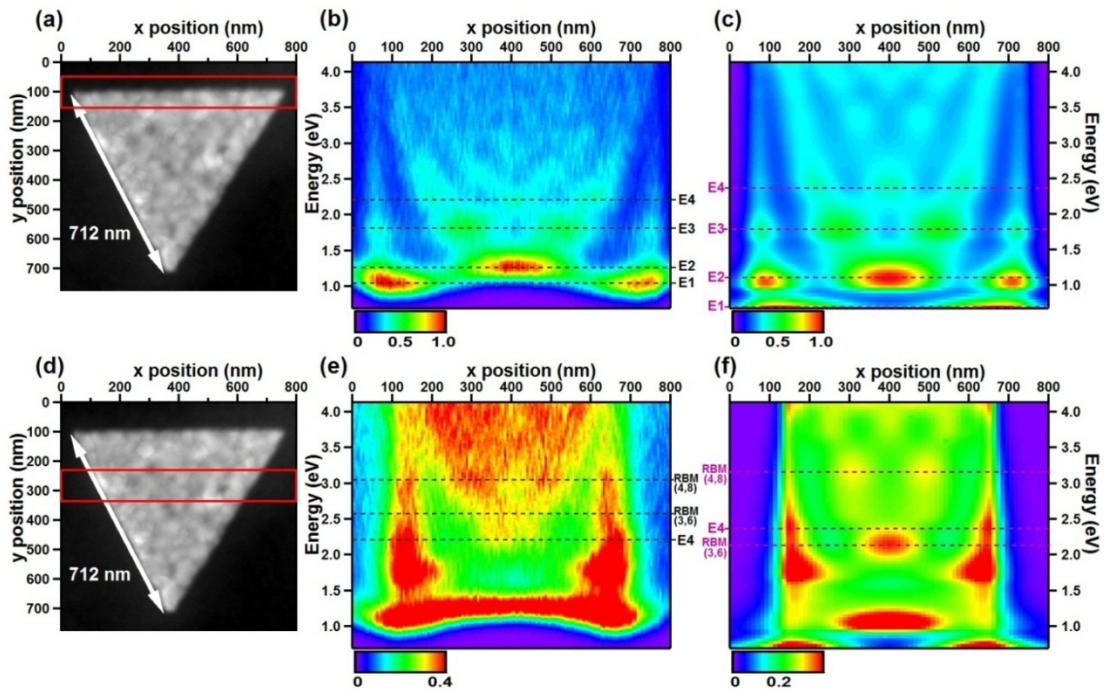


Figure 7.14: (a) HAADF images of an Al nanotriangle of around 700 nm side length. The red box indicates the region studied to obtain the dispersion of edge modes along x axis. (b) Energy dispersion along the x axis marked by the red box in a. (c) EELS-GDM dispersion simulation of a triangle of 700 nm side length along the edge of the triangle. (d) Same HAADF image as in a. The red box is placed close to the center of the triangle in order to obtain the dispersion of RBMs. (e) Energy dispersion along the x axis marked by the red box in d. Intensity has been saturated in order for the faint features at high energy to be visible. (f) EELS-GDM dispersion simulation of a triangle of 700 nm side length along a horizontal line close to the center of the triangle. The energy ranking change for RBM(3,6) and E4 between experiment and simulation is made explicit.

7.6. Dispersion relations

To further understand the nature of edge modes and RBMs, we studied the dispersion relation (E vs k) for both kinds of modes. By using equation 7.4.1 and 7.4.7, it is possible to get a robust and sound definition of the wavenumbers of the edge modes and the RBMs. The edge mode of order 1 is not taken into account due to antinode bunching effect [12], [136] at the extremes of the triangle side length as mentioned in section 7.4.1. To complement this study, we have also measured Al nanoantenna dispersion relation with the same analysis used for edge modes in nanotriangles using equation 7.4.1. Figure 7.15 shows the dispersion relation of both the edge modes in Al nanotriangles and the Al nanoantenna modes. Both dispersion relations match very well.

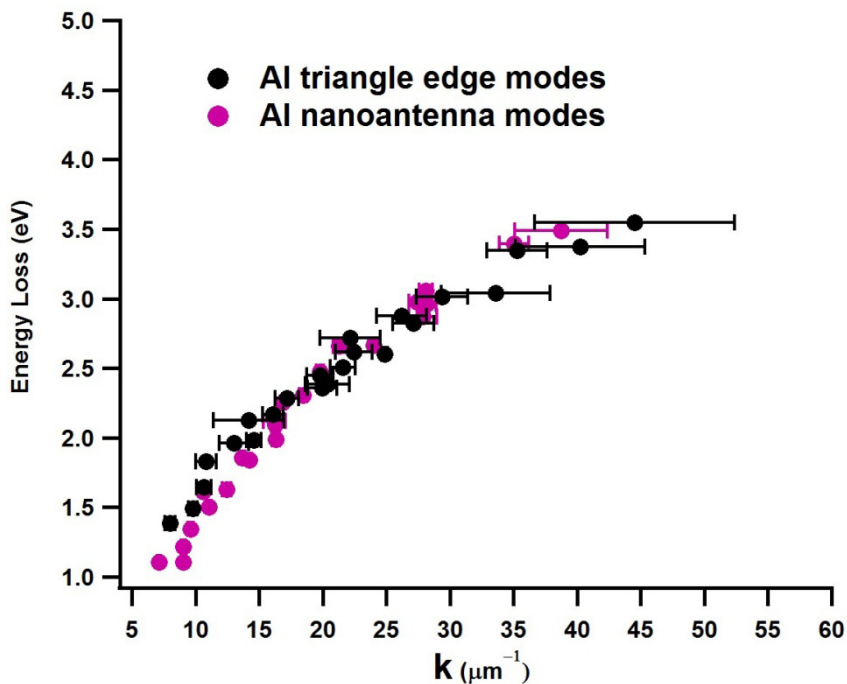


Figure 7.15: Experimental dispersion relation of Al nanotriangle edge modes (black dots) and Al nanoantenna modes (purple dots). To obtain the experimental wavenumbers of Al nanoantenna modes we used the same method described for edge modes in Al nanotriangles in section 7.4.1.

Figure 7.16 shows the dispersion relation (E vs k) for edge modes and RBMs in Al nanotriangles. These two kinds of modes present different dispersion relations, highlighting their different natures. The RBMs can be compared with the analytical dispersion relation of SRSPs in an Al thin film (40 nm thickness) on a Si_3N_4 substrate (30 nm thickness) immersed in vacuum (blue curve) [56]. A similar agreement between the dispersion relation of RBMs and a thin film has been reported in the literature in silver nanodisks [33], [38]. The difference in energy of the dispersion relation of RBMs and edge modes is due to the fact that RBMs come from the interference of Short Range Surface Plasmon Polaritons and therefore they follow the relation dispersion of a thin film. However, edge modes are scaled to the case of nanoantenna modes.

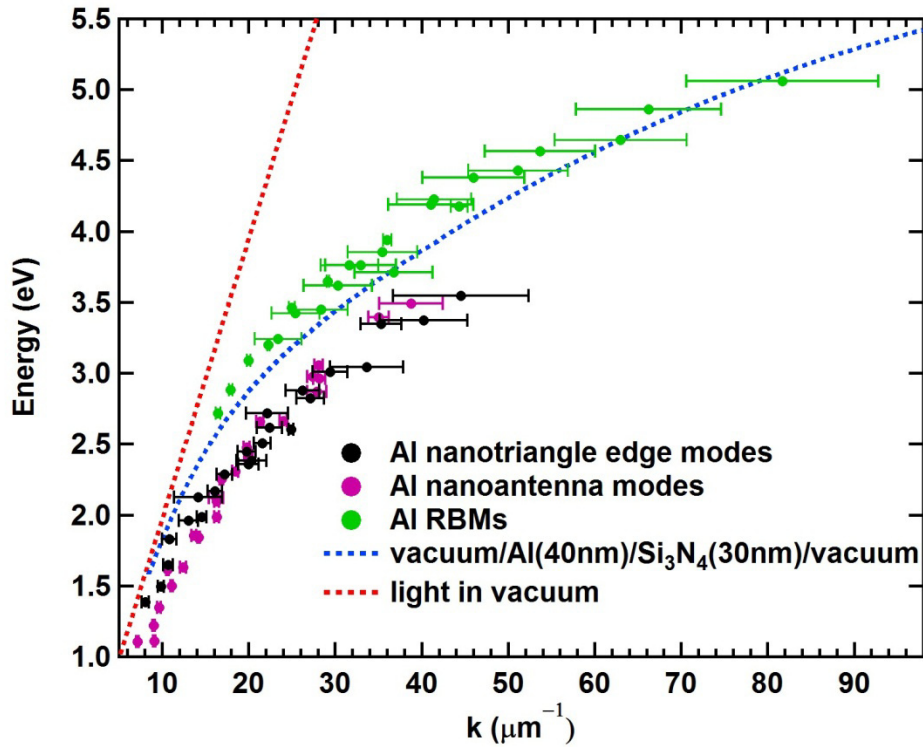


Figure 7.16: Dispersion relation of the edge modes and pseudo-RBMs of Al nanotriangles. The dashed blue curve is the analytical dispersion relation of SRSPs of an Al thin film (40 nm thickness) on a Si_3N_4 substrate (30 nm thickness) immersed in vacuum. We observe that Al edge nanotriangles modes and Al nanoantenna modes match very well. An analogous match is observed between RBMs and the analytical dispersion relation of SRSPs in an Al thin film.

7.7. Conclusion

In summary, we used STEM-EELS to characterize plasmonic resonances supported by Al nanotriangles. Two kinds of modes have been observed, the edge modes and the pseudo-RBMs. Studying different triangles sizes (from 125 to 700 nm side length and same thickness of 40 nm) we found tunable plasmon resonances from IR to UV range. Edge modes are more tunable in the IR-visible range and the RBMs in the UV range. The symmetry of these modes and their energy dispersion have been theoretically verified by rigorous EELS-GDM simulations. One dimensional and two-dimensional Fabry-Pérot analytical models enabled us to label the edge modes and RBMs and to study the phase shift upon reflection. The RBMs phase shift is found independent from the order mode, exhibiting a value of $\sim 0.45\pi$. Finally, the wavenumbers extracted from the linear and triangular resonator models were used to plot the dispersion relation (E vs k) of edge modes and RBMs. The different behavior in the dispersion relation of both modes reveals their distinct nature. It has been proven experimentally that edge modes in Al nanotriangles can be related to Al nanoantenna modes. On the other hand, the RBMs have been related to the dispersion relation of an Al thin film (SRSPs dispersion relation). We not only described the symmetry of these modes but went into details in the phase shift upon reflection of the plasmon waves.

Chapter 8:

Conclusions and perspectives

8.1. General conclusions

Throughout this thesis I explored the high ability of STEM-EELS technique as a local source of radiation. The combination of high spatial and spectral resolution of STEM-EELS has enabled the local exploration of plasmonic properties in metallic nanostructures. The plasmon resonance excitations were also described by optical absorption spectroscopy. A direct link between optical and EELS techniques was shown in a classical regime and with the collaborators this link was extended to a quantum regime.

Two main problems were studied in this thesis. The first one corresponded to the size evolution of surface plasmons in silver cluster of sizes below 10 nm where quantum effects are expected. As secondary subject I studied the classification of plasmon modes in triangular nanoparticles in the classical regime.

The silver clusters samples were studied by STEM-EELS and optical absorption techniques. The silver clusters were fabricated by physical methods (by M. Hillenkamp and N. Troc) and encapsulated in silica matrix. The samples fabricated for STEM-EELS and optical absorption characterizations were prepared under the same conditions. Due to the fact that it is not possible to observe the ensemble of particles during optical absorption experiments, the samples for this characterization were size selected with a narrow size distribution. I optimized the EELS spectrometer and acquisition parameters in order to detect very weak plasmon signals and at the same time to avoid electron beam damage on the small particles. This optimization was obtained after meticulous tests using a homemade EELS detection system with a high dynamic range. This thesis is a first step towards a systematic EELS acquisition optimization in order to detect weak plasmon signals and to prove the feasibility to do EELS experiments in particles as small as 1.7 nm. This was one of the most important result in my thesis work.

Working with our collaborators (J. Lermé), we proved theoretically a direct relation between EELS and optical extinction (or absorption extinction) in a quantum regime for spherical systems. Despite the theoretical link between both techniques, we found experimentally in a first observation, a discrepancy in the experimental results from both techniques. While the optical absorption experiments presented no energy plasmon shift, the STEM-EELS results presented a blue shift tendency with the decrease of particles size. In a more detailed observation, we realized that most of the particles did not show plasmon signal at the beginning of the STEM-EELS experiments and with the continuous increase of electron dose the plasmon signal appeared and blue shifted.

The absence of plasmon signal at the beginning of STEM-EELS experiments was related to an oxidation layer around the particles which maybe come from the diffusion of oxygen through the thin matrix layer of STEM-EELS samples. With the increase of electron dose, the oxide layer is removed by knock-on collisions and the plasmon signal appears. From STEM-HAADF images we observed that the plasmon blue shift was correlated with a modification of the local environment of the particle. Because the light atoms can be more easily removed than heaviest atoms, the oxygen and silica are removed at the particle/matrix interface by the electron irradiation. This damage on the interface (which is unintentional but unavoidable) creates a local porosity around the

particle.

In order to interpret our results, we used a classical/quantal model which takes into account all the relevant effects in a quantum regime such as electron spill-out, ineffective ion-core polarizability, non-locality and a local porosity at the particle/matrix interface. The energy shift of the plasmon resonance was found to be governed by a trade-off of quantum effects. We found by calculations that the increase of local porosity on silver embedded particles promotes a blue shift on the plasmon resonance and which is higher in the smallest particles. The increase of local porosity layer by calculations matched very well with the EELS experiments and, on the other hand, the calculations without porosity layer matched well with the optical results. Therefore, the apparent discrepancy between EELS and optical absorption measurements was understood. Additionally, the EELS, optical absorption and classical/quantal calculation results were compared with older optical literature of silver embedded particles solving the contradictions found in literature.

As a final message we can say that a great care has to be taken in the interpretation of experimental STEM-EELS results in order to separate intrinsic from irradiation induced size effects. Additionally, we found a signal coming from the volume of particles as small as 1.7 nm. A volume plasmon has never been reported in literature in sub-5 nm silver nanoparticles and, therefore, the interpretation of this signal remains to be understood.

The second type of samples studied in this thesis consisted in equilateral aluminum nanotriangles prepared by electron lithography (by J. Martin and D. Gérard) and characterized by STEM-EELS technique. Two kinds of modes were spatially and spectrally revealed: the edge modes and the pseudo-RBMs (radial breathing modes). The edge modes were concentrated in the periphery of the nanotriangles and the pseudo-RBMs inside the nanotriangles. The plasmon modes showed a tuning property by changing the nanotriangle edge length. The symmetry and wavenumbers of the edge modes were described by a one-dimensional (1D) Fabry-Pérot cavity and the dispersion relation of edge modes was found to be similar to the dispersion relation of nanoantenna modes. On the other hand, the pseudo-RBMs were described by a triangular Fabry-Pérot cavity and the dispersion relation of RBMs was found at higher energies with respect to edge modes. This different behavior in the relation dispersions revealed the different nature of both kinds of modes. While the edge modes are related to nanoantenna modes, the pseudo-RBMs are related to the dispersion relation of SRSPs in a supported thin film. The 1D and triangular Fabry-Pérot models enabled a complete indexing schema of both kinds of modes. Additionally, the edge and pseudo-RBMs symmetries as well as their energy dispersions have been theoretically verified by rigorous EELS-GDM simulations (by A. Arbouet).

8.2. Perspectives

The follow-up experiment of my work must involve the transition from a plasmon resonance to discrete molecular/atomic transitions. The question of how many atoms are necessary to have a plasmon signal is still open. However, to do this kind of study very weak signals must be detected. During my thesis, I made several attempts to go below 2 nm particles but the low signal-to-noise and the ZLP tail background limit the observation of weak plasmon signals (see figure 8.1).

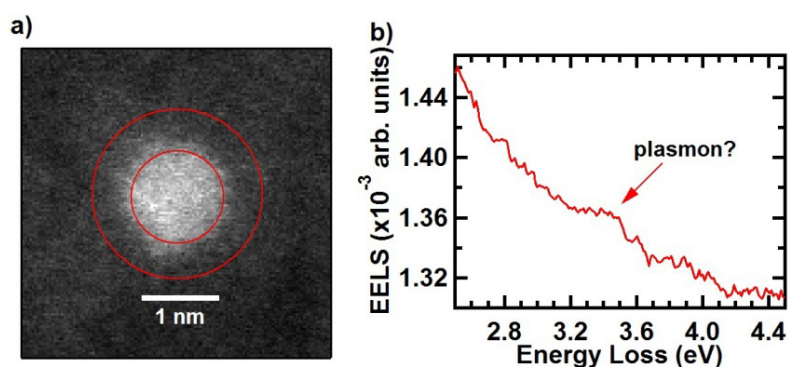


Figure 8.1: (a) HAADF image of a silver nanoparticle of 1.2 nm (~50 atoms) diameter. (b) EEL signal extracted from the surface of the silver nanoparticle.

A new microscope STEM-EELS system of Nion Company (Chromatem microscope) just arrived at the Laboratory at the beginning of this year. This microscope has high voltage stability and a monochromator that leads to an improvement of the energy resolution down to 10 meV (FWHM of the ZLP). The resolution improvement reduces the influence of the ZLP tail on the plasmon signal and consequently the increase of the signal-to-background ratio. This microscope can operate at low acceleration voltage (30 kV) which increases the EELS probability and reduce the particle damage. A direct electron detection system will be installed in the EELS spectrometer which increases the signal-to-noise ratio. All these characteristics will extend the study of plasmon responses in particles below 2 nm. Additionally, a cold sample holder will be installed in order to do studies at temperatures of liquid Nitrogen or liquid Helium. It is expected that discrete atomic/molecular transitions in very small clusters dominate over the plasmon signal at low temperatures.

Studies in gold clusters will be also done with the new microscope. Due to the low energy of the plasmon signal in gold nanoparticles a monochromator is required.

8.2.1. Chromatem preliminary result in a gold nanoparticle

Figure 8.2 displays the comparison of the ZLP in a carbon substrate taken using the UltraSTEM200 and the Chromatem microscopes. The improvement of energy resolution is evident. At the same time the ZLP tail intensity is reduced up to $\sim 10^{-4}$ ZLP maximum. With these improvements a plasmon signal in gold nanoparticles was possible to detect. Figure 8.3 presents preliminary results in a gold nanoparticle with the new Chromatem microscope. It is clearly observed the surface and bulk plasmon signals.

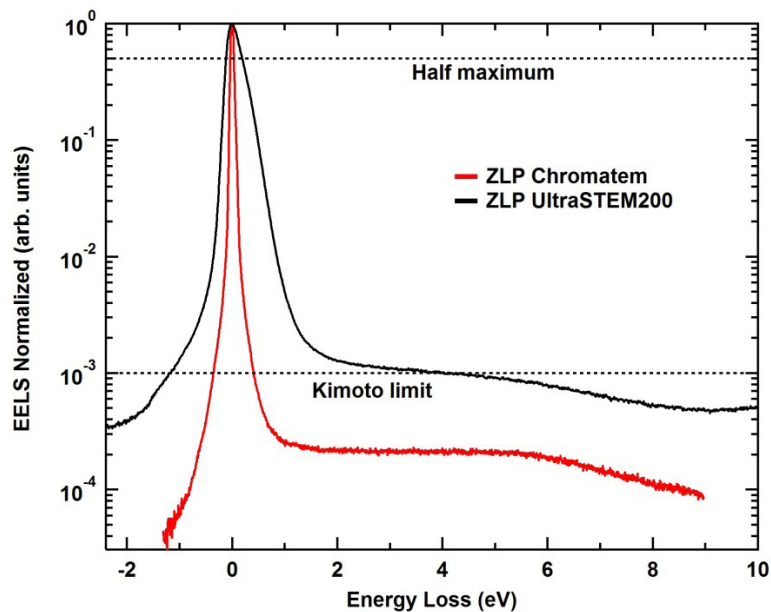


Figure 8.2: Improvement of the energy resolution (decrease of FWHM of the ZLP) in the new Chromatem microscope. The resolution passes from 0.27 eV to 0.070 eV and at the same time the ZLP tail intensity decreases below 10^{-3} ZLP (Kimoto limit) at energies ≥ 0.5 eV in the Chromatem microscope. The difference in intensity of the ZLP tails could be related to the scintillator. Both spectra were taken on carbon substrate.

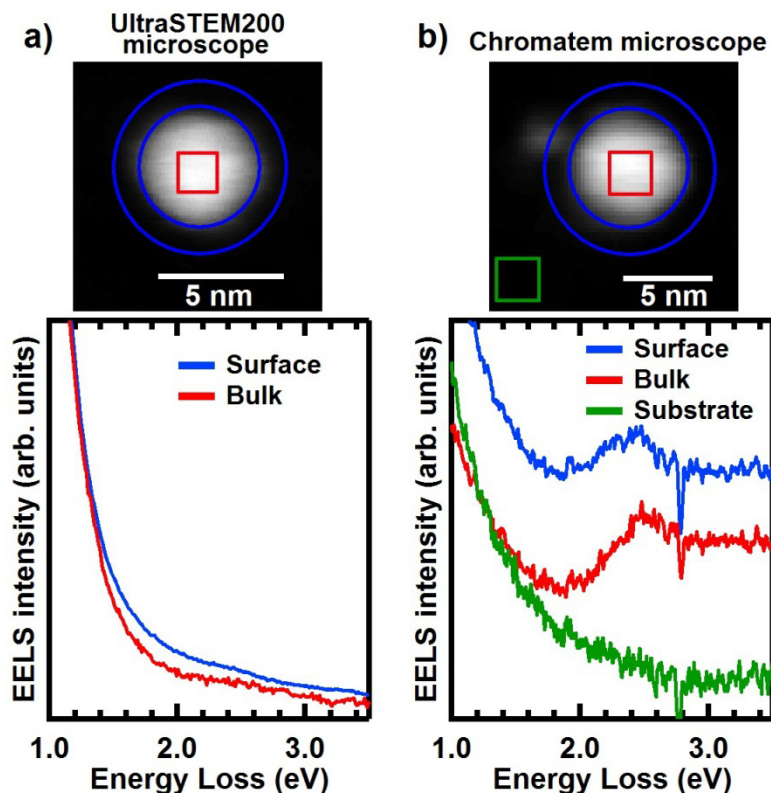


Figure 8.3: (a) HAADF image of a gold particle of ~ 5 nm and the EEL signals extracted from the surface and the volume using the UltraSTEM200 microscope. There is no evidence of plasmon signals. (b) HAADF image of a gold particle of ~ 5.6 nm and the EEL signals extracted from the surface, the volume and the substrate using the Chromatem microscope. The spectra from Chromatem microscope are genuine EELS data with any post-data treatment. The gold particles are deposited on carbon substrate.

Appendices

A. EELS probability of a sphere embedded in an absorbing medium

Here we describe the excitation of LSPs in a sphere embedded in an absorbing medium. We consider an electron excitation in a non-retarded approximation. We will apply the same procedure used in section 2.4.3 except for the assumption of an absorbing medium. For facility, through this appendix, we remember all the steps used to calculate the EELS probability.

An electron passing near a sphere can induce an electric field which reacts back on the electron. We consider a sphere of radius R embedded in an absorbing medium and a point electron moving at a constant velocity $\mathbf{v} = v \hat{\mathbf{z}}$ along the trajectory $\mathbf{r}_e(t) = (x_0, 0, z(t))$, where x_0 is the impact parameter and $z = vt$. In order to facilitate calculations, we will work in a spherical system with the center placed in the center of the sphere.

The coordinates of the electron will be expressed in the referential of the sphere. In this spherical system $r_e = (x_0^2 + z^2)^{1/2}$ and $\cos(\theta_e) = z/r_e = vt/r_e$. The potential of the electron at a position \mathbf{r} where $r_e > r$ is [62], [63]

$$V_e(\mathbf{r}, t) = -\frac{e}{4\pi\epsilon_0\epsilon_m|\mathbf{r} - \mathbf{r}_e|} \quad (\text{A.1})$$

Applying the Fourier transform we obtain

$$V_e(\mathbf{r}, \omega) = \sum_{L=0}^{\infty} \sum_{M=0}^L \frac{a_{LM}^e r^L}{\epsilon_m} P_{LM}(\cos(\theta)) \cos(M\varphi) \quad (\text{A.2})$$

Being $a_{LM}^e = -\frac{e}{4\pi\epsilon_0} N_{LM} I_{LM}$, where N_{LM} and I_{LM} are defined as

$$N_{LM} = \frac{(2 - \delta_{0M})(L - M)!}{(L + M)!} \quad (\text{A.3})$$

And

$$I_{LM}(\omega, x_0) = \int_{-\infty}^{\infty} dt r_e^{-(L+1)} P_{LM}(\cos(\theta_e)) e^{i\omega t} = \frac{2i^{L-M} |\omega/v|^L K_M(|\omega x_0/v|) (\omega/|\omega|)^{L-M}}{v(L-M)!} \quad (\text{A.4})$$

P_{LM} are the associated Legendre polynomials. δ_{0M} is unity if $m=0$ and is zero otherwise. K_M is the modified Bessel function of second kind.

The induced potential inside and outside the particle is obtained by solving the Laplace equation $\nabla^2 V_{ind} = 0$ with the boundary conditions at the interfaces and the continuity of the total potential and the normal component of the displacement electric field. Outside the particle the induced potential is

$$V_{ind,out}(\mathbf{r}, \omega) = -\sum_{L=1}^{\infty} \sum_{M=0}^L \alpha_{LM}^e \frac{R^{2L+1}}{r^{L+1}} P_{LM}(\cos(\theta)) \cos(M\varphi) \frac{L(\varepsilon - \varepsilon_m)}{\varepsilon_m(L\varepsilon + (L+1)\varepsilon_m)} \quad (\text{A.5})$$

The term $L = 0$ does not contribute to the induced potential. Writing $V_e(\mathbf{r}, \omega)$ and $V_{ind,out}(\mathbf{r}, \omega)$ in the form

$$V_i(\mathbf{r}, \omega) = \sum_{L=1}^{\infty} \sum_{M=0}^L r^L P_{LM}(\cos(\theta)) \cos(M\varphi) v_{i,LM} \quad (\text{A.6})$$

with $i = e$ or ind, out one can define the multipolar polarizability of order (L, M) as

$$\alpha_{LM}(\omega) = -4\pi\varepsilon_0\varepsilon_m R^{2L+1} \left. \frac{v_{ind,out,LM}}{v_{e,LM}} \right|_{r=R} \quad (\text{A.7})$$

We assume a sphere filled by a relative permittivity $\varepsilon(\omega)$ and embedded in an absorbing medium of relative permittivity $\varepsilon_m(\omega)$. From equation A.7 the multipolar polarizability is

$$\alpha_{LM}(\omega) = 4\pi\varepsilon_0\varepsilon_m R^{2L+1} \frac{L(\varepsilon - \varepsilon_m)}{L\varepsilon + (L+1)\varepsilon_m} \quad (\text{A.8})$$

We note that in the classical limit the multipolar polarizability only depend on L and we can simplify the notation to $\alpha_L(\omega)$.

The energy loss by a fast electron passing near a sample with constant velocity \mathbf{v} along a straight line $\mathbf{r}_e(t)$ can be related to the force exerted by the induced electric field \mathbf{E}_{ind} acting back on the electron [15]

$$\Delta E = e \int_{-\infty}^{\infty} dt \mathbf{v} \cdot \mathbf{E}_{ind}(\mathbf{r}_e(t), t) \quad (\text{A.9})$$

The energy loss can be expressed in term of the electron energy loss probability per unit of frequency $\Gamma(\omega)$ by the equation $\Delta E = \int_0^{\infty} \hbar\omega d\omega \Gamma(\omega)$ [15]. Using $\mathbf{E}_{ind} = -\nabla V_{ind,out}$ we can write

$$\Gamma(\omega) = -\frac{e}{\pi\hbar\omega} \int_{-\infty}^{\infty} dt \text{Re}\{\mathbf{v} \cdot \nabla V_{ind,out}(\mathbf{r}_e, \omega) e^{-i\omega t}\} \quad (\text{A.10})$$

Solving the product $\mathbf{v} \cdot \nabla V_{ind,out}(\mathbf{r}, \omega)$ evaluated at $\mathbf{r} = \mathbf{r}_e$ and introducing it in equation A.10 we get

$$\Gamma(\omega) = \frac{e^2}{\pi^2 \hbar v^2 \varepsilon_0} \sum_{L=1}^{\infty} \sum_{M=0}^L M_{LM} \left[K_M \left(\frac{\omega x_0}{v} \right) \right]^2 \left(\frac{\omega}{v} \right)^{2L} R^{2L+1} \text{Im} \left[\frac{L(\varepsilon - \varepsilon_m)}{\varepsilon_m(L\varepsilon + (L+1)\varepsilon_m)} \right] \quad (\text{A.11})$$

Being K_M the modified Bessel function of second kind and $M_{LM} = (2 - \delta_{0M}) / [(L - M)! (L + M)!]$.

Multiplying by ε_m^* the numerator and denominator that are in the imaginary factor of the

equation A.11 we get

$$\Gamma(\omega) = \frac{e^2 R}{\pi^2 \hbar v^2 \varepsilon_0 |\varepsilon_m|^2} \sum_{L=1}^{\infty} \sum_{M=0}^L M_{LM} \left[K_M \left(\frac{\omega x_0}{v} \right) \right]^2 \left(\frac{\omega}{v} \right)^{2L} R^{2L+1} \text{Im} \left[\varepsilon_m^* \frac{L(\varepsilon - \varepsilon_m)}{(L\varepsilon + (L+1)\varepsilon_m)} \right] \quad (\text{A.12})$$

$$\Gamma(\omega) = \frac{e^2}{4\pi^3 \hbar v^2 \varepsilon_0^2 |\varepsilon_m|^2} \sum_{L=1}^{\infty} \sum_{M=0}^L M_{LM} \left[K_M \left(\frac{\omega x_0}{v} \right) \right]^2 \left(\frac{\omega}{v} \right)^{2L} \text{Im} \left[4\pi \varepsilon_0 \varepsilon_m^* R^{2L+1} \frac{L(\varepsilon - \varepsilon_m)}{(L\varepsilon + (L+1)\varepsilon_m)} \right] \quad (\text{A.13})$$

We observe that the quantity inside the imaginary factor in equation A.13 is almost similar to the multipolar polarizability of equation A.8. The only difference is the complex conjugate of the relative permittivity of the medium. However, in a non-absorbing medium ($\varepsilon_m^* = \varepsilon_m$) and equation A.13 becomes

$$\Gamma(\omega) = \frac{e^2}{4\pi^3 \hbar v^2 (\varepsilon_0 \varepsilon_m)^2} \sum_{L=1}^{\infty} \sum_{M=0}^L M_{LM} \left[K_M \left(\frac{\omega x_0}{v} \right) \right]^2 \left(\frac{\omega}{v} \right)^{2L} \text{Im}[\alpha_L(\omega)] \quad (\text{A.14})$$

Which is the same expression found in section 2.4.3 equation 2.4.38 for a non-absorbing medium.

B. Estimation of the interband transition (*ib*) permittivity

The classical/quantal calculations described in section 2.5, which takes into account quantum effects and the local environment of the particle, have been performed throughout this thesis. The computations have been carried out thanks to a home-written computer code based on the TDLDA formalism.

The relative complex dielectric function $\varepsilon_{ib}(\omega)$ has been carefully extracted from the experimental complex dielectric function ($\varepsilon_{exp}(\omega) = \varepsilon_{ib}(\omega) + \varepsilon_D(\omega) - 1$) of bulk silver [146] by a Kramers-Kronig analysis after subtracting the conduction-electron contribution $\varepsilon_D(\omega)$, parametrized as a Drude-Sommerfeld formula (see Ref. [79] for the details of the procedure). Briefly the imaginary component $\text{Im}[\varepsilon_{ib}(\omega)]$ is first extracted from the imaginary component of the experimental bulk dielectric function which exhibits a steep rising edge at the interband threshold. The real component is then calculated thanks to the Kramers-Kronig relation linking both components. For this extraction the interband threshold $\omega_{ib} = 3.85 \text{ eV}$ has been assumed (extrapolation to zero of the low-energy rising edge of $\text{Im}(\varepsilon_{exp}(\omega))$). The following bulk parameters r_s and m_e (effective optical electron mass) entering the conduction electron contribution (equation 2.3.4) $\varepsilon_D(\omega) = 1 - \omega_p^2 / (\omega(\omega + i\gamma))$, ($\omega_p(\omega) = (3e^2 / 4\pi\varepsilon_0 r_s^3 m_e)^{1/2}$ is the volume plasmon frequency), have been used: $r_s = 3.02 \text{ bohr}$ [147] and $m_e = m$ (free electron mass) [123]. The damping factors γ have been estimated in fitting $\text{Im}[\varepsilon_{exp}(\omega)]$ with $\text{Im}[\varepsilon_D(\omega)]$ in the spectral range below ω_{ib} . It should be emphasized that the interband contribution $\varepsilon_{ib}(\omega)$ which is obtained through this procedure depends only very slightly on the selected Drude-parameters, because above the interband threshold ω_{ib} the largest part of $\text{Im}[\varepsilon_{exp}(\omega)]$ is exhausted by $\text{Im}[\varepsilon_{ib}(\omega)]$. Therefore, the accuracy depends essentially on the reliability of the experimental data.

With regard to the dielectric function $\varepsilon_m(\omega)$ of the transparent embedding matrix, all calculations have been carried out in involving the tabulated bulk-silica data [146]. In the visible spectral range $\varepsilon_m(\omega)$ varies only slightly and is on the order of 2.16 around 3 eV.

C. Two-body Coulomb interaction in presence of a dielectric media

The results of this part are adapted from Ref. [79].

Single spherical interface

We consider two charged particles located at \mathbf{r}_1 and \mathbf{r}_2 in presence of a particle of radius R with relative permittivity ε surrounded by an infinite medium of relative permittivity ε_m . We introduce the quantities $r_> = \max(r_1, r_2)$ and $r_< = \min(r_1, r_2)$. The Coulomb interaction potential $V_c(\mathbf{r}_1, \mathbf{r}_2)$ between the particles is obtained by solving the Poisson equation with the boundary conditions at the interfaces and the continuity of the potential and the normal component of the displacement vector. Then the Coulomb interaction potential $V_c(\mathbf{r}_1, \mathbf{r}_2)$ is then

$$\frac{1}{\varepsilon_m} \sum_L \left[\frac{r_<^L}{r_>^{L+1}} + \frac{R^{2L+1}}{(r_1 r_2)^{L+1}} \frac{L(\varepsilon_m - \varepsilon)}{L\varepsilon + (L+1)\varepsilon_m} \right] P_L(\cos(\alpha))$$

$r_1, r_2 > R$

$$\sum_L \left[\frac{r_<^L}{r_>^{L+1}} \frac{2L+1}{L\varepsilon + (L+1)\varepsilon_m} \right] P_L(\cos(\alpha))$$

$r_1 < R < r_2 \text{ or } r_2 < R < r_1$

$$\frac{1}{\varepsilon} \sum_L \left[\frac{r_<^L}{r_>^{L+1}} + \frac{(r_1 r_2)^L}{R^{2L+1}} \frac{(L+1)(\varepsilon - \varepsilon_m)}{L\varepsilon + (L+1)\varepsilon_m} \right] P_L(\cos(\alpha))$$

$r_1, r_2 < R$

Where P_L are the Legendre polynomials and α is the angle between the vectors \mathbf{r}_1 and \mathbf{r}_2 .

Two nested spherical interfaces

We consider two charged particles located at \mathbf{r}_1 and \mathbf{r}_2 in presence of a coated particle of radius R_1 with relative permittivity ε . The shell around the particle has a radius R_2 . The relative permittivity in the range $[R_1, R_2]$ is ε_{shell} and the infinite surrounding medium has a relative permittivity ε_m .

The Coulomb interaction potential $V_c(\mathbf{r}_1, \mathbf{r}_2)$ between the particles is obtained by solving the Poisson equation with the boundary conditions at the interfaces and the continuity of the potential and the normal component of the displacement vector. The Coulomb interaction potential $V_c(\mathbf{r}_1, \mathbf{r}_2)$ is then

$$\sum_L \left[\frac{A_L}{r_2^{L+1}} + \frac{1}{\varepsilon_m} \frac{r_<^L}{r_>^{L+1}} \right] P_L(\cos(\alpha))$$

$r_1, r_2 > R_2$

$$\sum_L \left[B_L r_2^L + \frac{C_L}{r_2^{L+1}} \right] P_L(\cos(\alpha))$$

$R_1 < r_2 < R_2 < r_1$

$$\sum_L [D_L r_2^L] P_L(\cos(\alpha)) \quad r_2 < R_1 < R_2 < r_1$$

$$\sum_L \left[E_L r_2^L + \frac{F_L}{r_2^{L+1}} + \frac{1}{\varepsilon_{shell}} \frac{r_2^L}{r_2^{L+1}} \right] P_L(\cos(\alpha)) \quad R_1 < r_1, r_2 > R_2$$

$$\sum_L [G_L r_2^L] P_L(\cos(\alpha)) \quad r_2 < R_1 < r_1 < R_2$$

$$\sum_L \left[H_L r_2^L + \frac{1}{\varepsilon} \frac{r_2^L}{r_2^{L+1}} \right] P_L(\cos(\alpha)) \quad r_1, r_2 < R_1$$

With

$$B_L = -(2L + 1)[L\varepsilon + (L + 1)\varepsilon_{shell}] \left(\frac{R_2}{R_1} \right)^{2L+1} \frac{1}{\Delta r_1^{L+1}}$$

$$C_L = L(2L + 1)(\varepsilon - \varepsilon_{shell}) \frac{R_2^{2L+1}}{\Delta r_1^{L+1}}$$

$$A_L = C_L + R_2^{2L+1} \left[B_L - \frac{1}{\varepsilon_m r_1^{L+1}} \right]$$

$$D_L = B_L + \frac{C_L}{R_1^{2L+1}}$$

$$F_L = \frac{L(\varepsilon - \varepsilon_{shell})}{\varepsilon_{shell}} \left\{ (L + 1)(\varepsilon_{shell} - \varepsilon_m) + [L\varepsilon_{shell} + (L + 1)\varepsilon_m] \left(\frac{R_2}{r_1} \right)^{2L+1} \right\} \frac{r_1^L}{\Delta}$$

$$E_L = -\frac{1}{\varepsilon_{shell} r_1^{L+1}} - \frac{[L\varepsilon + (L + 1)\varepsilon_{shell}]}{R_1^{2L+1}} \frac{F_L}{L(\varepsilon - \varepsilon_{shell})}$$

$$G_L = E_L + \frac{F_L}{R_1^{2L+1}} + \frac{1}{\varepsilon_{shell} r_1^{L+1}}$$

$$H_L = \left\{ \left[(L + 1)(\varepsilon_m - \varepsilon_{shell}) - [L\varepsilon_{shell} + (L + 1)\varepsilon_m] \left(\frac{R_2}{R_1} \right)^{2L+1} \right] \frac{(2L + 1)}{\Delta} - \frac{1}{\varepsilon} \right\} \frac{r_1^L}{R_1^{2L+1}}$$

$$\Delta = L(L + 1)(\varepsilon_m - \varepsilon_{shell})(\varepsilon - \varepsilon_{shell}) - [L\varepsilon + (L + 1)\varepsilon_{shell}][L\varepsilon_{shell} + (L + 1)\varepsilon_m] \left(\frac{R_2}{R_1} \right)^{2L+1}$$

D. Electrostatic potential in two nested spherical interfaces

Considering a coated metallic particle of radius R_1 with relative permittivity ε_{ib} (the conduction electrons have been subtracted). The shell around the particle has a radius R_2 . The relative permittivity in the range $[R_1, R_2]$ is ε_{shell} and the infinite surrounding medium has a relative permittivity ε_m (the medium is non-absorbing).

The solution of the classical electrostatic potential $\phi_c(\mathbf{r}, \omega)$ presented in section 2.5.4 is

$$\phi_c(\mathbf{r}) = \left\{ -\frac{9\varepsilon_{shell}\varepsilon_m}{\Delta'} r \right\} \cos(\theta) E_0 \quad r < R_1$$

$$\phi_c(\mathbf{r}) = \left\{ -\frac{3\varepsilon_m(\varepsilon_{ib} + 2\varepsilon_{shell})}{\Delta'} r + \frac{3\varepsilon_m(\varepsilon_{ib} - \varepsilon_{shell}) R_1^3}{\Delta' r^2} \right\} \cos(\theta) E_0 \quad R_1 < r < R_2$$

$$\phi_c(\mathbf{r}) = \left\{ \frac{(\varepsilon_{ib} + 2\varepsilon_{shell})(\varepsilon_{shell} - \varepsilon_m) + p(\varepsilon_{ib} - \varepsilon_{shell})(2\varepsilon_{shell} + \varepsilon_m) R_2^3}{\Delta'} - r \right\} \cos(\theta) E_0 \quad r > R_2$$

Where

$$\Delta' = (\varepsilon_{ib} + 2\varepsilon_{shell})(\varepsilon_{shell} + 2\varepsilon_m) - 2p(\varepsilon_{ib} - \varepsilon_{shell})(\varepsilon_m - \varepsilon_{shell})$$

And

$$p = \left(\frac{R_1}{R_2} \right)^3$$

E. ZLP in different substrates and vacuum

EEL spectra containing the ZLP were acquired in different substrates and in vacuum. Figure E.1 shows normalized ZLP in logarithmic scale taken in vacuum (red curve), Si_3N_4 substrate covered by silica matrix (brown curve), carbon substrate covered by silica matrix (green curve) and carbon substrate (blue curve). In the case of vacuum, the ZLP tail is below 10^{-4} ZLP at energies ≥ 6 eV and below 10^{-3} ZLP at energies ≥ 1.5 eV. In the case of Si_3N_4 substrate covered by silica matrix, the ZLP tail is below 10^{-3} ZLP at energies ≥ 2 eV. In the case of carbon substrate covered by silica matrix and carbon substrate, the ZLP tail is close to 10^{-3} ZLP at energies ≥ 2 eV and below 10^{-3} ZLP at energies ≥ 7 eV. This is due to the fact that the carbon presents a peak shoulder at around 6 eV.

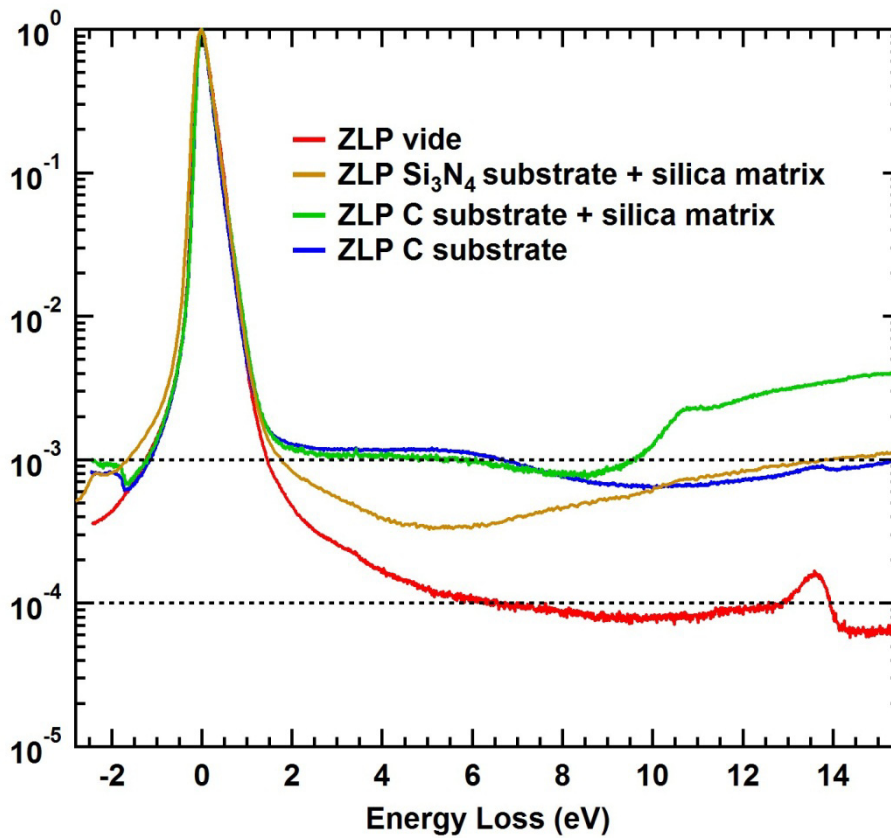


Figure E.1: EEL spectra containing the ZLP acquired in vacuum (red curve), Si_3N_4 substrate covered by silica matrix (brown curve), carbon substrate covered by silica matrix (green curve), and carbon substrate (blue curve). All the data was collected in the USTEM200.

F. Simulation of the plasmonic response of oxidized core-shell Ag/Ag_xO/SiO₂ nanoparticles

These calculations were performed by Emmanuel Cottancin from the Institut Lumière Matière at the Université de Lyon 1, France.

In order to corroborate our interpretation that some of the largest particles investigated by STEM-EELS show initial LSP energies below the expected value of 3 eV (figure 5.14) because of oxidation, we calculated absorption curves within classical Mie theory for concentric core@shell Ag@Ag_xO nano-spheres embedded in a silica matrix [57]. The absorption cross-sections have been calculated in the dipolar approximation for various oxidation ratios (OR), defined as the oxide shell to metal core volume ratio $(R'^3 - R_c^3)/R'^3$ (R_c designates the Ag-core radius, and R' the total radius). For 0% oxidation the pure silver radius is $R = 5$ nm. The calculation of the thickness of the shell for a given level of oxidation by using the lattice parameters of Ag₂O ($a=0.472$ nm [148]) is detailed in Ref. [149]. The increased lattice parameter of the silver oxide results in an increasing total diameter R' upon oxidation. The calculations have been performed with the dielectric function for silver (as used in appendix B) and those deduced from the work of Qiu et al. [150] for oxidized silver (see Ref. [149] for further details). The matrix dielectric function used here is extracted from the tabulated bulk-silica data [151].

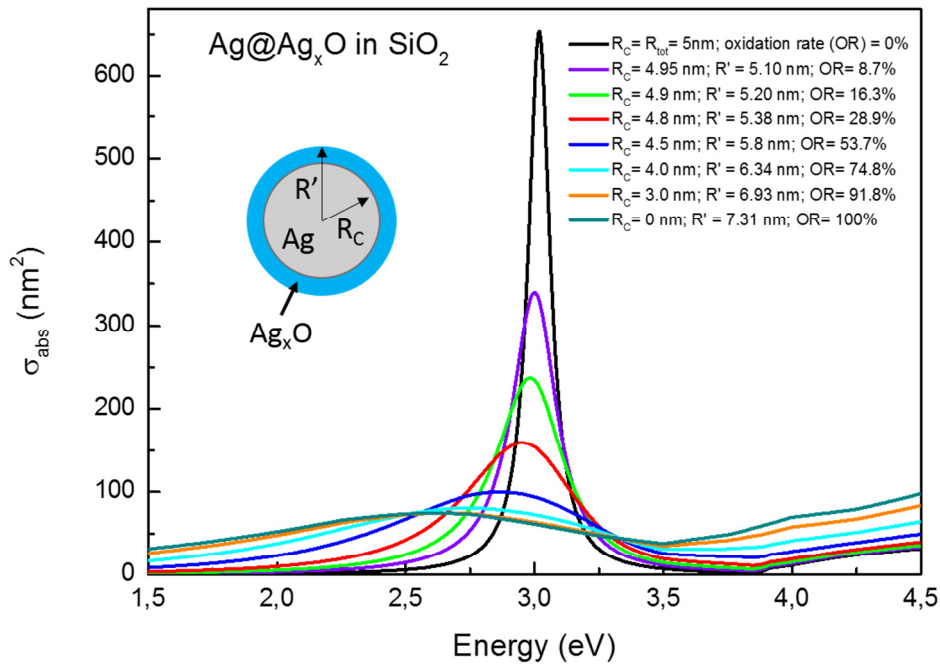


Figure F.1: Calculated absorption cross-sections within the dipolar approximation in a silica-embedded core/shell Ag@Ag_xO spherical geometry for increasing oxidation rates (OR).

The spectral position of the resonance is at 3.03 eV for non-oxidized NPs, as discussed in section 5.2.1. and shifts to <2.7 eV for high oxidation rates. These classical calculations do not depend on the size of the nanoparticles. Only the amplitude of the absorption cross section changes but the oxidation-dependent shift is the same for all the large particles studied. A degree of oxidation of $\sim 75\%$ thus leads to a shift of the LSP of the core/shell particle to ~ 2.75 eV, where the most red-shifted signals were detected.

G. Supplementary STEM-EELS experiments on silver clusters

We have in the meantime performed supplementary experiments on the oxidation of Ag particles in the thin STEM-EELS samples. Several particles were measured and then investigated again after exposure to air for one night. In the first experimental run the usual dependence on electron flux was observed with activation of the signal and blue shift (see figure G.1b). Within the uncertainty the LSP energies were identical after re-exposure to air (see figure G.1c), showing that, at least for this particular sample, several hours are not enough to re-oxidize the particles. The exact diffusion kinetics of oxygen through the silica matrix are, however, beyond the scope of this thesis.

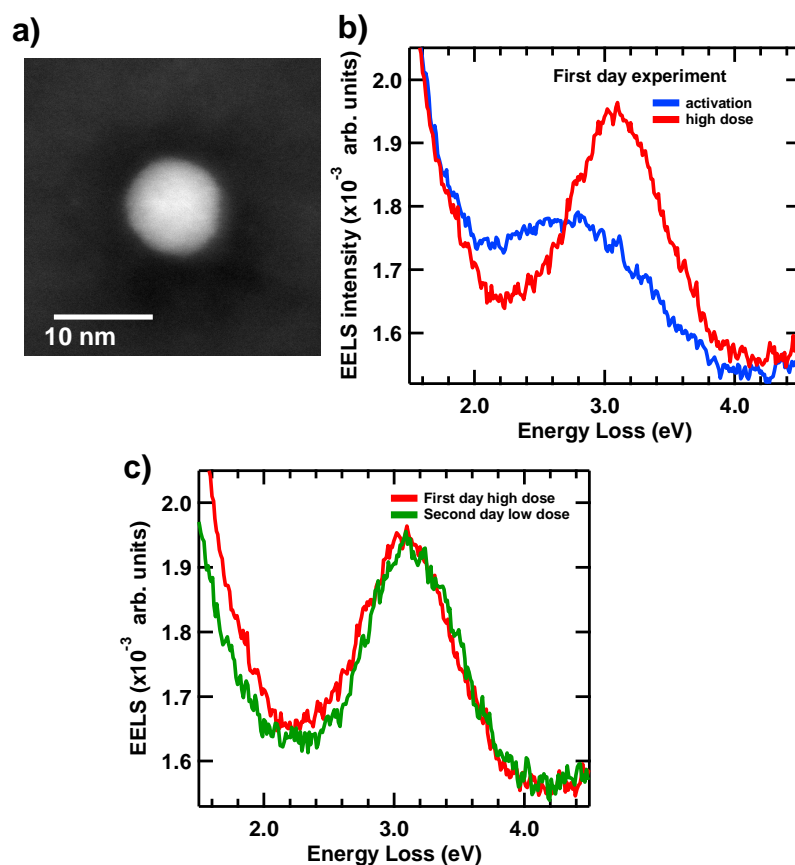


Figure G.1: (a) HAADF image of a silver particle of 9 nm embedded in silica. (b) Surface plasmon signal appears (activation) after removing oxide (blue curve) and it blue shifts to higher energy (red curve) at high electron dose. (c) A second experiment was done after one day of exposition to air. In this second experiment the surface plasmon signal appears at the first acquisition (low electron dose) and its energy is at the same position that the day before (green curve). The linewidth is also the same. All these mean that one night (~12 hours) to air exposition is not enough to re-oxidize the particle.

Bibliography

- [1] K. R. Catchpole and A. Polman, ‘Plasmonic solar cells’, *Opt. Express*, vol. 16, no. 26, pp. 21793–21800, Dec. 2008.
- [2] X. Ren, J. Cheng, S. Zhang, X. Li, T. Rao, L. Huo, J. Hou, and W. C. H. Choy, ‘High Efficiency Organic Solar Cells Achieved by the Simultaneous Plasmon-Optical and Plasmon-Electrical Effects from Plasmonic Asymmetric Modes of Gold Nanostars’, *Small*, vol. 12, no. 37, pp. 5200–5207, 2016.
- [3] R. R. Gutha, S. M. Sadeghi, C. Sharp, and W. J. Wing, ‘Biological sensing using hybridization phase of plasmonic resonances with photonic lattice modes in arrays of gold nanoantennas’, *Nanotechnology*, vol. 28, no. 35, p. 355504, 2017.
- [4] L.-A. Wu, W.-E. Li, D.-Z. Lin, and Y.-F. Chen, ‘Three-Dimensional SERS Substrates Formed with Plasmonic Core-Satellite Nanostructures’, *Sci. Rep.*, vol. 7, no. 1, p. 13066, Oct. 2017.
- [5] C.-W. Chen, Y.-C. Chan, M. Hsiao, and R.-S. Liu, ‘Plasmon-Enhanced Photodynamic Cancer Therapy by Upconversion Nanoparticles Conjugated with Au Nanorods’, *ACS Appl. Mater. Interfaces*, vol. 8, no. 47, pp. 32108–32119, Nov. 2016.
- [6] X. Zhang, X. Li, M. E. Reish, D. Zhang, N. Q. Su, Y. Guitiérrez, F. Moreno, W. Yang, H. O. Everitt, and J. Liu, ‘Plasmon-Enhanced Catalysis: Distinguishing Thermal and Nonthermal Effects’, *Nano Lett.*, vol. 18, no. 3, pp. 1714–1723, Mar. 2018.
- [7] P. Bazylewski, S. Ezugwu, and G. Fanchini, ‘A Review of Three-Dimensional Scanning Near-Field Optical Microscopy (3D-SNOM) and Its Applications in Nanoscale Light Management’, *Appl. Sci.*, vol. 7, no. 10, p. 973, Sep. 2017.
- [8] T. Devkota, M. S. Devadas, A. Brown, J. Talghader, and G. V. Hartland, ‘Spatial modulation spectroscopy imaging of nano-objects of different sizes and shapes’, *Appl. Opt.*, vol. 55, no. 4, pp. 796–801, Feb. 2016.
- [9] A. Crut, P. Maioli, N. D. Fatti, and F. Vallée, ‘Optical absorption and scattering spectroscopies of single nano-objects’, *Chem. Soc. Rev.*, vol. 43, no. 11, pp. 3921–3956, May 2014.
- [10] J. Nelayah, M. Kociak, O. Stéphan, F. J. García de Abajo, M. Tencé, L. Henrard, D. Taverna, I. Pastoriza-Santos, L. M. Liz-Marzán, and C. Colliex, ‘Mapping surface plasmons on a single metallic nanoparticle’, *Nat. Phys.*, vol. 3, no. 5, pp. 348–353, May 2007.
- [11] A. Losquin and M. Kociak, ‘Link between Cathodoluminescence and Electron Energy Loss Spectroscopy and the Radiative and Full Electromagnetic Local Density of States’, *ACS Photonics*, vol. 2, no. 11, pp. 1619–1627, Nov. 2015.
- [12] D. Rossouw, M. Couillard, J. Vickery, E. Kumacheva, and G. A. Botton, ‘Multipolar Plasmonic Resonances in Silver Nanowire Antennas Imaged with a Subnanometer Electron Probe’, *Nano Lett.*, vol. 11, no. 4, pp. 1499–1504, Apr. 2011.
- [13] B. Ögüt, N. Talebi, R. Vogelgesang, W. Sigle, and P. A. van Aken, ‘Toroidal Plasmonic Eigenmodes in Oligomer Nanocavities for the Visible’, *Nano Lett.*, vol. 12, no. 10, pp. 5239–5244, Oct. 2012.
- [14] M. Bosman, E. Ye, S. F. Tan, C. A. Nijhuis, J. K. W. Yang, R. Marty, A. Mlayah, A. Arbouet, C. Girard, and M.-Y. Han, ‘Surface Plasmon Damping Quantified with an Electron Nanoprobe’, *Sci. Rep.*, vol. 3, p. 1312, Feb. 2013.
- [15] F. J. García de Abajo and M. Kociak, ‘Probing the Photonic Local Density of States with Electron Energy Loss Spectroscopy’, *Phys. Rev. Lett.*, vol. 100, no. 10, p. 106804, Mar. 2008.
- [16] A. Hörl, G. Haberfehlner, A. Trügler, F.-P. Schmidt, U. Hohenester, and G. Kothleitner, ‘Tomographic imaging of the photonic environment of plasmonic

- nanoparticles', *Nat. Commun.*, vol. 8, no. 1, p. 37, Jun. 2017.
- [17] J. A. Scholl, A. L. Koh, and J. A. Dionne, 'Quantum plasmon resonances of individual metallic nanoparticles', *Nature*, vol. 483, no. 7390, pp. 421–427, Mar. 2012.
- [18] S. Raza, W. Yan, N. Stenger, M. Wubs, and N. A. Mortensen, 'Blueshift of the surface plasmon resonance in silver nanoparticles: substrate effects', *Opt. Express*, vol. 21, no. 22, pp. 27344–27355, Nov. 2013.
- [19] S. Raza, N. Stenger, S. Kadkhodazadeh, S. V. Fischer, N. Kostesha, A.-P. Jauho, A. Burrows, M. Wubs, and N. A. Mortensen, 'Blueshift of the surface plasmon resonance in silver nanoparticles studied with EELS', *Nanophotonics*, vol. 2, no. 2, pp. 131–138, 2013.
- [20] W. A. de Heer, 'The physics of simple metal clusters: experimental aspects and simple models', *Rev. Mod. Phys.*, vol. 65, no. 3, pp. 611–676, Jul. 1993.
- [21] J. Lermé, H. Baida, C. Bonnet, M. Broyer, E. Cottancin, A. Crut, P. Maioli, N. Del Fatti, F. Vallée, and M. Pellarin, 'Size Dependence of the Surface Plasmon Resonance Damping in Metal Nanospheres', *J. Phys. Chem. Lett.*, vol. 1, no. 19, pp. 2922–2928, Oct. 2010.
- [22] H. Haberland, 'Looking from both sides', *Nature*, vol. 494, no. 7435, pp. E1–E2, Feb. 2013.
- [23] U. Kreibig and M. Vollmer, *Optical Properties of Metal Clusters*. Berlin Heidelberg: Springer-Verlag, 1995.
- [24] J. Tiggesbäumker, L. Köller, K.H. Meiwes-Broer, and A. Liebsch, 'Blue shift of the Mie plasma frequency in Ag clusters and particles', *Phys. Rev. At. Mol. Opt. Phys.*, vol. 48, no. 3, pp. R1749–R1752, Sep. 1993.
- [25] A. Hilger, N. Cüppers, M. Tenfelde, and U. Kreibig, 'Surface and interface effects in the optical properties of silver nanoparticles', *Eur. Phys. J. - At. Mol. Opt. Plasma Phys.*, vol. 10, no. 1, pp. 115–118, Mar. 2000.
- [26] M. Hillenkamp, G. D. Domenicantonio, O. Eugster, and C. Félix, 'Instability of Ag nanoparticles in SiO₂ at ambient conditions', *Nanotechnology*, vol. 18, no. 1, p. 015702, 2007.
- [27] E. Cottancin, G. Celep, J. Lermé, M. Pellarin, J. R. Huntzinger, J. L. Vialle, and M. Broyer, 'Optical Properties of Noble Metal Clusters as a Function of the Size: Comparison between Experiments and a Semi-Quantal Theory', *Theor. Chem. Acc.*, vol. 116, no. 4–5, pp. 514–523, Sep. 2006.
- [28] S. Raza, S. Kadkhodazadeh, T. Christensen, M. Di Vece, M. Wubs, N. A. Mortensen, and N. Stenger, 'Multipole plasmons and their disappearance in few-nanometre silver nanoparticles', *Nat Commun*, vol. 6, Nov. 2015.
- [29] U. Hohenester and A. Trügler, 'MNPBEM – A Matlab toolbox for the simulation of plasmonic nanoparticles', *Comput. Phys. Commun.*, vol. 183, no. 2, pp. 370–381, Feb. 2012.
- [30] N. Geuquet and L. Henrard, 'EELS and optical response of a noble metal nanoparticle in the frame of a discrete dipole approximation', *Ultramicroscopy*, vol. 110, no. 8, pp. 1075–1080, Jul. 2010.
- [31] Y. Cao, A. Manjavacas, N. Large, and P. Nordlander, 'Electron Energy-Loss Spectroscopy Calculation in Finite-Difference Time-Domain Package', *ACS Photonics*, vol. 2, no. 3, pp. 369–375, Mar. 2015.
- [32] A. Arbouet, A. Mlayah, C. Girard, and G. C. des Francs, 'Electron energy losses and cathodoluminescence from complex plasmonic nanostructures: spectra, maps and radiation patterns from a generalized field propagator', *New J. Phys.*, vol. 16, no. 11, p. 113012, 2014.
- [33] F.-P. Schmidt, H. Ditlbacher, U. Hohenester, A. Hohenau, F. Hofer, and J. R.

- Krenn, ‘Universal dispersion of surface plasmons in flat nanostructures’, *Nat. Commun.*, vol. 5, p. 3604, Apr. 2014.
- [34] V. J. Keast, C. J. Walhout, T. Pedersen, N. Shahcheraghi, M. B. Cortie, and D. R. G. Mitchell, ‘Higher Order Plasmonic Modes Excited in Ag Triangular Nanoplates by an Electron Beam’, *Plasmonics*, vol. 11, no. 4, pp. 1081–1086, Aug. 2016.
- [35] E. Hao and G. C. Schatz, ‘Electromagnetic fields around silver nanoparticles and dimers’, *J. Chem. Phys.*, vol. 120, no. 1, pp. 357–366, Dec. 2003.
- [36] J. Nelayah, M. Kociak, O. Stéphan, N. Geuquet, L. Henrard, F. J. García de Abajo, I. Pastoriza-Santos, L. M. Liz-Marzán, and C. Colliex, ‘Two-Dimensional Quasistatic Stationary Short Range Surface Plasmons in Flat Nanoprisms’, *Nano Lett.*, vol. 10, no. 3, pp. 902–907, Mar. 2010.
- [37] E. P. Bellido, A. Manjavacas, Y. Zhang, Y. Cao, P. Nordlander, and G. A. Botton, ‘Electron Energy-Loss Spectroscopy of Multipolar Edge and Cavity Modes in Silver Nanosquares’, *ACS Photonics*, Feb. 2016.
- [38] F.-P. Schmidt, H. Ditlbacher, U. Hohenester, A. Hohenau, F. Hofer, and J. R. Krenn, ‘Dark Plasmonic Breathing Modes in Silver Nanodisks’, *Nano Lett.*, vol. 12, no. 11, pp. 5780–5783, Nov. 2012.
- [39] A. Kumar, K.-H. Fung, J. C. Mabon, E. Chow, and N. X. Fang, ‘Excitation and imaging of resonant optical modes of Au triangular nanoantennas using cathodoluminescence spectroscopy’, *J. Vac. Sci. Technol. B Nanotechnol. Microelectron. Mater. Process. Meas. Phenom.*, vol. 28, no. 6, p. C6C21-C6C25, Nov. 2010.
- [40] K. H. Fung, A. Kumar, and N. X. Fang, ‘Electron-photon scattering mediated by localized plasmons: A quantitative analysis by eigen-response theory’, *Phys. Rev. B*, vol. 89, no. 4, p. 045408, Jan. 2014.
- [41] P. Das, T. K. Chini, and J. Pond, ‘Probing Higher Order Surface Plasmon Modes on Individual Truncated Tetrahedral Gold Nanoparticle Using Cathodoluminescence Imaging and Spectroscopy Combined with FDTD Simulations’, *J. Phys. Chem. C*, vol. 116, no. 29, pp. 15610–15619, Jul. 2012.
- [42] A. L. Koh, A. I. Fernández-Domínguez, D. W. McComb, S. A. Maier, and J. K. W. Yang, ‘High-Resolution Mapping of Electron-Beam-Excited Plasmon Modes in Lithographically Defined Gold Nanostructures’, *Nano Lett.*, vol. 11, no. 3, pp. 1323–1330, Mar. 2011.
- [43] J. Lermé, B. Palpant, E. Cottancin, M. Pellarin, B. Prével, J. L. Vialle, and M. Broyer, ‘Quantum extension of Mie’s theory in the dipolar approximation’, *Phys. Rev. B*, vol. 60, no. 23, pp. 16151–16156, Dec. 1999.
- [44] J. Lermé, ‘Introduction of quantum finite-size effects in the Mie’s theory for a multilayered metal sphere in the dipolar approximation: Application to free and matrix-embedded noble metal clusters’, *Eur. Phys. J. - At. Mol. Opt. Plasma Phys.*, vol. 10, no. 2, pp. 265–277, Apr. 2000.
- [45] D. Barchiesi, ‘Lycurgus Cup: inverse problem using photographs for characterization of matter’, *JOSA A*, vol. 32, no. 8, pp. 1544–1555, Aug. 2015.
- [46] S. Szunerits and R. Boukherroub, ‘*Introduction to Plasmonics: Advances and Applications*’, CRC Press, Mar. 2015.
- [47] J. C. Maxwell, ‘LI. On physical lines of force’, *Lond. Edinb. Dublin Philos. Mag. J. Sci.*, vol. 21, no. 141, pp. 338–348, May 1861.
- [48] G. Mie, ‘Beiträge zur Optik trüber Medien, speziell kolloidaler Metallösungen’, *Ann. Phys.*, vol. 330, no. 3, pp. 377–445, 1908.
- [49] L. Novotny and B. Hecht, ‘*Principles of Nano-Optics*’, Cambridge Core, Sep. 2012.

- [50] F. J. García de Abajo, ‘Nonlocal Effects in the Plasmons of Strongly Interacting Nanoparticles, Dimers, and Waveguides’, *J. Phys. Chem. C*, vol. 112, no. 46, pp. 17983–17987, Nov. 2008.
- [51] N. A. Mortensen, S. Raza, M. Wubs, T. Søndergaard, and S. I. Bozhevolnyi, ‘A generalized non-local optical response theory for plasmonic nanostructures’, *Nat. Commun.*, vol. 5, p. 3809, May 2014.
- [52] W. Yan, M. Wubs, and N. Asger Mortensen, ‘Projected Dipole Model for Quantum Plasmonics’, *Phys. Rev. Lett.*, vol. 115, no. 13, p. 137403, Sep. 2015.
- [53] A. D. Rakić, A. B. Djurišić, J. M. Elazar, and M. L. Majewski, ‘Optical properties of metallic films for vertical-cavity optoelectronic devices’, *Appl. Opt.*, vol. 37, no. 22, pp. 5271–5283, Aug. 1998.
- [54] K. Höflich, U. Gösele, and S. Christiansen, ‘Are Volume Plasmons Excitable by Classical Light?’, *Phys. Rev. Lett.*, vol. 103, no. 8, p. 087404, Aug. 2009.
- [55] M. Li, S. K. Cushing, and N. Wu, ‘Plasmon-enhanced optical sensors: a review’, *Analyst*, vol. 140, no. 2, pp. 386–406, Dec. 2014.
- [56] K. Y. Kim, ‘*Plasmonics - Principles and Applications*’, IntechOpen, Oct. 2012.
- [57] E. Cottancin, M. Broyer, J. Lermé, and M. Pellarin, ‘*Handbook of Nanophysics: Nanoelectronics and Nanophotonics*’, chapter Optical Properties of Metal Clusters and Nanoparticles, CRC Press, Boca Raton, FL, USA, 2011.
- [58] F. J. García de Abajo and A. Howie, ‘Retarded field calculation of electron energy loss in inhomogeneous dielectrics’, *Phys. Rev. B*, vol. 65, no. 11, p. 115418, Mar. 2002.
- [59] F. J. García de Abajo, ‘Optical excitations in electron microscopy’, *Rev. Mod. Phys.*, vol. 82, no. 1, pp. 209–275, Feb. 2010.
- [60] M. Kociak, O. Stéphan, M. G. Walls, M. Tencé, and C. Colliex, ‘Spatially Resolved EELS: The Spectrum-Imaging Technique and Its Applications’, in *Scanning Transmission Electron Microscopy*, Springer, New York, NY, 2011, pp. 163–205.
- [61] J. D. Jackson, ‘*Classical electrodynamics*’, Wiley, New York, 2001.
- [62] T. L. Ferrell, R. J. Warmack, V. E. Anderson, and P. M. Echenique, ‘Analytical calculation of stopping power for isolated small spheres’, *Phys. Rev. B*, vol. 35, no. 14, pp. 7365–7371, May 1987.
- [63] Z. L. Wang, ‘Valence electron excitations and plasmon oscillations in thin films, surfaces, interfaces and small particles’, *Micron*, vol. 27, no. 3, pp. 265–299, Jun. 1996.
- [64] R. H. Ritchie and A. Howie, ‘Inelastic scattering probabilities in scanning transmission electron microscopy’, *Philos. Mag. A*, vol. 58, no. 5, pp. 753–767, Nov. 1988.
- [65] G. Guzzinati, A. Béché, H. Lourenço-Martins, J. Martin, M. Kociak, and J. Verbeeck, ‘Probing the symmetry of the potential of localized surface plasmon resonances with phase-shaped electron beams’, *Nat. Commun.*, vol. 8, p. 14999, Apr. 2017.
- [66] L. Henrard and P. Lambin, ‘Calculation of the energy loss for an electron passing near giant fullerenes’, *J. Phys. B At. Mol. Opt. Phys.*, vol. 29, no. 21, p. 5127, 1996.
- [67] R. Carminati, A. Cazé, D. Cao, F. Peragut, V. Krachmalnicoff, R. Pierrat, and Y. De Wilde, ‘Electromagnetic density of states in complex plasmonic systems’, *Surf. Sci. Rep.*, vol. 70, no. 1, pp. 1–41, Mar. 2015.
- [68] U. Hohenester, H. Ditlbacher, and J. R. Krenn, ‘Electron-Energy-Loss Spectra of Plasmonic Nanoparticles’, *Phys. Rev. Lett.*, vol. 103, no. 10, p. 106801, Aug. 2009.
- [69] V. Bonacic-Koutecky, P. Fantucci, and J. Koutecky, ‘Quantum chemistry of small clusters of elements of groups Ia, Ib, and IIa: fundamental concepts, predictions,

- and interpretation of experiments', *Chem. Rev.*, vol. 91, no. 5, pp. 1035–1108, Jul. 1991.
- [70] B. Anak, M. Bencharif, and F. Rabilloud, 'Time-dependent density functional study of UV-visible absorption spectra of small noble metal clusters (Cu_n , Ag_n , Au_n , $n = 2-9, 20$)', *RSC Adv.*, vol. 4, no. 25, pp. 13001–13011, Mar. 2014.
- [71] F. Rabilloud, 'Description of plasmon-like band in silver clusters: The importance of the long-range Hartree-Fock exchange in time-dependent density-functional theory simulations', *J. Chem. Phys.*, vol. 141, no. 14, p. 144302, Oct. 2014.
- [72] H.-C. Weissker and X. López-Lozano, 'Surface plasmons in quantum-sized noble-metal clusters: TDDFT quantum calculations and the classical picture of charge oscillations', *Phys. Chem. Chem. Phys.*, vol. 17, no. 42, pp. 28379–28386, Oct. 2015.
- [73] G. F. Bertsch, A. Bulgac, D. Tománek, and Y. Wang, 'Collective plasmon excitations in C60 clusters', *Phys. Rev. Lett.*, vol. 67, no. 19, pp. 2690–2693, Nov. 1991.
- [74] A. Bulgac and N. Ju, 'Collective electronic excitations in C60 clusters', *Phys. Rev. B Condens. Matter*, vol. 46, no. 7, pp. 4297–4300, Aug. 1992.
- [75] L. Serra and A. Rubio, 'Core Polarization in the Optical Response of Metal Clusters: Generalized Time-Dependent Density-Functional Theory', *Phys. Rev. Lett.*, vol. 78, no. 8, pp. 1428–1431, Feb. 1997.
- [76] S. Kümmel, P.-G. Reinhard, and M. Brack, 'Structure and optic response of the Na_9^+ and Na_{55}^+ clusters', *Eur. Phys. J. - At. Mol. Opt. Plasma Phys.*, vol. 9, no. 1, pp. 149–152, Dec. 1999.
- [77] W. Ekardt, 'Size-dependent photoabsorption and photoemission of small metal particles', *Phys. Rev. B*, vol. 31, no. 10, pp. 6360–6370, May 1985.
- [78] J. Lermé, B. Palpant, B. Prével, M. Pellarin, M. Treilleux, J. L. Vialle, A. Perez, and M. Broyer, 'Quenching of the Size Effects in Free and Matrix-Embedded Silver Clusters', *Phys. Rev. Lett.*, vol. 80, no. 23, pp. 5105–5108, Jun. 1998.
- [79] J. Lermé, B. Palpant, B. Prével, E. Cottancin, M. Pellarin, M. Treilleux, J.L. Vialle, A. Perez, and M. Broyer, 'Optical properties of gold metal clusters: A time-dependent local-density-approximation investigation', *Eur. Phys. J. - At. Mol. Opt. Plasma Phys.*, vol. 4, no. 1, pp. 95–108, Oct. 1998.
- [80] A. Liebsch, 'Surface-plasmon dispersion and size dependence of Mie resonance: Silver versus simple metals', *Phys. Rev. B*, vol. 48, no. 15, pp. 11317–11328, Oct. 1993.
- [81] S. Fedrigo, W. Harbich, and J. Buttet, 'Collective dipole oscillations in small silver clusters embedded in rare-gas matrices', *Phys. Rev. B*, vol. 47, no. 16, pp. 10706–10715, Apr. 1993.
- [82] V. V. Kresin, 'Collective resonances in silver clusters: Role of d electrons and the polarization-free surface layer', *Phys. Rev. B*, vol. 51, no. 3, pp. 1844–1849, Jan. 1995.
- [83] L. Serra and A. Rubio, 'Optical response of Ag clusters', *Z. Für Phys. AtomsMolecules Clust.*, vol. 40, no. 1, pp. 262–264, Mar. 1997.
- [84] O. Gunnarsson and B. I. Lundqvist, 'Exchange and correlation in atoms, molecules, and solids by the spin-density-functional formalism', *Phys. Rev. B*, vol. 13, no. 10, pp. 4274–4298, May 1976.
- [85] C. Yannouleas and R. A. Broglia, 'Collective and single-particle aspects in the optical response of metal microclusters', *Phys. Rev. At. Mol. Opt. Phys.*, vol. 44, no. 9, pp. 5793–5802, Nov. 1991.
- [86] M. Sardela, Ed., *Practical Materials Characterization*. New York: Springer-Verlag, 2014.
- [87] N. Troc, *Étude des propriétés optiques de nanoparticules d'argent sondées par spectroscopies optique et électronique*. Ph.D. thesis, Lyon, 2016.
- [88] S. J. Pennycook, 'A Scan Through the History of STEM', in *Scanning*

- Transmission Electron Microscopy*, Springer, New York, NY, 2011, pp. 1–90.
- [89] M. Kociak and O. Stéphan, ‘Mapping plasmons at the nanometer scale in an electron microscope’, *Chem. Soc. Rev.*, vol. 43, no. 11, pp. 3865–3883, May 2014.
- [90] O. L. Krivanek, N. Dellby, and A. R. Lupini, ‘Towards sub-Å electron beams’, *Ultramicroscopy*, vol. 78, no. 1, pp. 1–11, Jun. 1999.
- [91] N. Dellby, N. J. Bacon, P. Hrnčirik, M. F. Murfitt, G. S. Skone, Z. S. Szilagy, and O. L. Krivanek, ‘Dedicated STEM for 200 to 40 keV operation’, *Eur. Phys. J. Appl. Phys.*, vol. 54, no. 3, p. 33505, 2011.
- [92] R. F. Egerton, *Electron Energy-Loss Spectroscopy in the Electron Microscope*, 3rd ed. Springer US, 2011.
- [93] O. L. Krivanek, T. C. Lovejoy, N. Dellby, T. Aoki, R. W. Carpenter, P. Rez, E. Soignard, J. Zhu, P. E. Batson, M. J. Lagos, R. F. Egerton, and P. A. Crozier, ‘Vibrational spectroscopy in the electron microscope’, *Nature*, vol. 514, no. 7521, pp. 209–212, Oct. 2014.
- [94] M. J. Lagos, A. Trügler, U. Hohenester, and P. E. Batson, ‘Mapping vibrational surface and bulk modes in a single nanocube’, *Nature*, vol. 543, no. 7646, pp. 529–532, Mar. 2017.
- [95] A. Méndez-Vilas, ‘*Microscopy and imaging science: practical approaches to applied research and education*’, Formatex Research Center, Spain, 2017.
- [96] F. De la Peña, T. Ostasevicius, V. T. Fauske, P. Burdet, P. Jokubauskas, M. Nord, E. Prestat, M. Sarahan, K. E. MacArthur, D. N. Johnstone, J. Taillon, J. Caron, T. Furnival, A. Eljarrat, S. Mazzucco, V. Migunov, T. Aarholt, M. Walls, F. Winkler, B. Martineau, G. Donval, E. R. Hoglund, I. Alxneit, I. Hjorth, L. F. Zagonel, A. Garmannslund, C. Gohlke, I. Iyengar, and H.-W. Chang, ‘HyperSpy 1.3’, *Hyperspy*, May 2017, <https://doi.org/10.5281/zenodo.583693>.
- [97] A. Gloter, A. Douiri, M. Tencé, and C. Colliex, ‘Improving energy resolution of EELS spectra: an alternative to the monochromator solution’, *Ultramicroscopy*, vol. 96, no. 3, pp. 385–400, Sep. 2003.
- [98] E. P. Bellido, D. Rossouw, and G. A. Botton, ‘Toward 10 meV Electron Energy-Loss Spectroscopy Resolution for Plasmonics’, *Microsc. Microanal.*, vol. 20, no. 3, pp. 767–778, Jun. 2014.
- [99] R. E. Smalley, ‘Laser Studies of Metal Cluster Beams’, *Laser Chemistry*, vol. 2, no. 3-4, pp. 167-184, 1983.
- [100] H. Haberland, M. Karrais, M. Mall, and Y. Thurner, ‘Thin films from energetic cluster impact: A feasibility study’, *J. Vac. Sci. Technol. A*, vol. 10, no. 5, pp. 3266–3271, Sep. 1992.
- [101] K. Bromann, C. Félix, H. Brune, W. Harbich, R. Monot, J. Buttet and K. Kern, ‘Controlled Deposition of Size-Selected Silver Nanoclusters’, *Science*, vol. 274, no. 5289, pp. 956–958, Nov. 1996.
- [102] R. H. Fowler, F. R. S, and D. L. Nordheim, ‘Electron emission in intense electric fields’, *Proc R Soc Lond A*, vol. 119, no. 781, pp. 173–181, May 1928.
- [103] S. Lazar, G. A. Botton, and H. W. Zandbergen, ‘Enhancement of resolution in core-loss and low-loss spectroscopy in a monochromated microscope’, *Ultramicroscopy*, vol. 106, no. 11, pp. 1091–1103, Oct. 2006.
- [104] J. A. Hachtel, A. R. Lupini, and J. C. Idrobo, ‘Exploring the capabilities of monochromated electron energy loss spectroscopy in the infrared regime’, *Sci. Rep.*, vol. 8, no. 1, p. 5637, Apr. 2018.
- [105] R. F. Egerton, P. Li, and M. Malac, ‘Radiation damage in the TEM and SEM’, *Micron*, vol. 35, no. 6, pp. 399–409, Aug. 2004.
- [106] B.W. Reed and M. Sarikaya, ‘Background subtraction for low-loss transmission

- electron energy-loss spectroscopy', *Ultramicroscopy*, vol. 93, no. 1, pp. 25–37, 2002.
- [107] P. E. Batson, 'A new surface plasmon resonance in clusters of small aluminum spheres', *Ultramicroscopy*, vol. 9, no. 3, pp. 277–282, Jan. 1982.
- [108] P. E. Batson, 'Surface Plasmon Coupling in Clusters of Small Spheres', *Phys. Rev. Lett.*, vol. 49, no. 13, pp. 936–940, Sep. 1982.
- [109] M. Achèche, C. Colliex, H. Kohl, A. Nourtier, and P. Trebbia, 'Theoretical and experimental study of plasmon excitations in small metallic spheres', *Ultramicroscopy*, vol. 20, no. 1, pp. 99–105, Jan. 1986.
- [110] F. Ouyang, P. E. Batson, and M. Isaacson, 'Quantum size effects in the surface-plasmon excitation of small metallic particles by electron-energy-loss spectroscopy', *Phys. Rev. B*, vol. 46, no. 23, pp. 15421–15425, Dec. 1992.
- [111] J. Aizpurua, A. Rivacoba, and S. P. Apell, 'Electron-energy losses in hemispherical targets', *Phys. Rev. B*, vol. 54, no. 4, pp. 2901–2909, Jul. 1996.
- [112] W. Harbich, S. Fedrigo, and J. Buttet, 'The optical absorption spectra of small Silver clusters (n=8–39) embedded in rare gas matrices', *Z. Für Phys. At. Mol. Clust.*, vol. 26, no. 1, pp. 138–140, Mar. 1993.
- [113] K.-P. Charlé, L. König, S. Nepijko, I. Rabin, and W. Schulze, 'The Surface Plasmon Resonance of Free and Embedded Ag-Clusters in the Size Range $1,5 \text{ nm} < D < 30 \text{ nm}$ ', *Cryst. Res. Technol.*, vol. 33, no. 7–8, pp. 1085–1096, Oct. 1998.
- [114] V. Kasperovich and V. V. Kresin, 'Ultraviolet photoabsorption spectra of silver and gold nanoclusters', *Philos. Mag. B*, vol. 78, no. 4, pp. 385–396, Oct. 1998.
- [115] S. Lecoultre, A. Rydlo, J. Buttet, C. Félix, S. Gilb, and W. Harbich, 'Ultraviolet-visible absorption of small silver clusters in neon: Ag_n (n = 1–9)', *J. Chem. Phys.*, vol. 134, no. 18, p. 184504, May 2011.
- [116] U. Kreibig, 'Small silver particles in photosensitive glass: Their nucleation and growth', *Appl. Phys.*, vol. 10, no. 3, pp. 255–264, Jul. 1976.
- [117] L. Genzel, T. P. Martin, and U. Kreibig, 'Dielectric function and plasma resonances of small metal particles', *Z. Für Phys. B Condens. Matter*, vol. 21, no. 4, pp. 339–346, Dec. 1975.
- [118] N. Nilius, N. Ernst, and H.-J. Freund, 'Photon Emission Spectroscopy of Individual Oxide-Supported Silver Clusters in a Scanning Tunneling Microscope', *Phys. Rev. Lett.*, vol. 84, no. 17, pp. 3994–3997, Apr. 2000.
- [119] T. Lünskens, P. Heister, M. Thämer, C. A. Walenta, A. Kartouzian, and U. Heiz, 'Plasmons in supported size-selected silver nanoclusters', *Phys. Chem. Chem. Phys.*, vol. 17, no. 27, pp. 17541–17544, Jul. 2015.
- [120] M. Brack, 'The physics of simple metal clusters: self-consistent jellium model and semiclassical approaches', *Rev. Mod. Phys.*, vol. 65, no. 3, pp. 677–732, Jul. 1993.
- [121] T. P. Rossi, M. Kuisma, M. J. Puska, R. M. Nieminen, and P. Erhart, 'Kohn–Sham Decomposition in Real-Time Time-Dependent Density-Functional Theory: An Efficient Tool for Analyzing Plasmonic Excitations', *J. Chem. Theory Comput.*, vol. 13, no. 10, pp. 4779–4790, Oct. 2017.
- [122] A. Hilger, M. Tenfelde, and U. Kreibig, 'Silver nanoparticles deposited on dielectric surfaces', *Appl. Phys. B*, vol. 73, no. 4, pp. 361–372, Sep. 2001.
- [123] H. Ehrenreich and H. R. Philipp, 'Optical Properties of Ag and Cu', *Phys. Rev.*, vol. 128, no. 4, pp. 1622–1629, Nov. 1962.
- [124] I. Römer, Z. W. Wang, R. C. Merrifield, R. E. Palmer, and J. Lead, 'High Resolution STEM-EELS Study of Silver Nanoparticles Exposed to Light and Humic Substances', *Environ. Sci. Technol.*, vol. 50, no. 5, pp. 2183–2190, Mar. 2016.
- [125] A. L. Koh, K. Bao, I. Khan, W. E. Smith, G. Kothleitner, P. Nordlander, S. A. Maier, and D. W. McComb, 'Electron Energy-Loss Spectroscopy (EELS) of Surface

- Plasmons in Single Silver Nanoparticles and Dimers: Influence of Beam Damage and Mapping of Dark Modes', *ACS Nano*, vol. 3, no. 10, pp. 3015–3022, Oct. 2009.
- [126] K. Koga and K. Sugawara, 'Population statistics of gold nanoparticle morphologies: direct determination by HREM observations', *Surf. Sci.*, vol. 529, no. 1, pp. 23–35, Apr. 2003.
- [127] P. B. Johnson and R. W. Christy, 'Optical Constants of the Noble Metals', *Phys. Rev. B*, vol. 6, no. 12, pp. 4370–4379, Dec. 1972.
- [128] R. H. Ritchie, R. N. Hamm, J. E. Turner, H. A. Wright, J. C. Ashley, and G. J. Basbas, 'Physical aspects of charged particle track structure', *Int. J. Radiat. Appl. Instrum. Part Nucl. Tracks Radiat. Meas.*, vol. 16, no. 2, pp. 141–155, Jan. 1989.
- [129] H. P. Paudel, A. Safaei, and M. N. Leuenberger, 'Nanoplasmonics in Metallic Nanostructures and Dirac Systems', in *Nanoplasmonics - Fundamentals and Applications*, G. Barbillon, Ed. InTech, 2017.
- [130] E. Rudberg, 'Inelastic Scattering of Electrons from Solids', *Phys. Rev.*, vol. 50, no. 2, pp. 138–150, Jul. 1936.
- [131] E. Rudberg and J. C. Slater, 'Theory of Inelastic Scattering of Electrons from Solids', *Phys. Rev.*, vol. 50, no. 2, pp. 150–158, Jul. 1936.
- [132] G. Ruthemann, 'Diskrete Energieverluste schneller Elektronen in Festkörpern', *Naturwissenschaften*, vol. 29, no. 42–43, pp. 648–648, Oct. 1941.
- [133] R. G. Hobbs, V. R. Manfrinato, Y. Yang, S. A. Goodman, L. Zhang, E. A. Stach, and K. K. Berggren, 'High-Energy Surface and Volume Plasmons in Nanopatterned Sub-10 nm Aluminum Nanostructures', *Nano Lett.*, vol. 16, no. 7, pp. 4149–4157, Jul. 2016.
- [134] L. Gu, W. Sigle, C. T. Koch, B. Ögüt, P. A. van Aken, N. Talebi, R. Vogelgesang, J. Mu, X. Wen, and J. Mao, 'Resonant wedge-plasmon modes in single-crystalline gold nanoplatelets', *Phys. Rev. B*, vol. 83, no. 19, p. 195433, May 2011.
- [135] E. P. Bellido, A. Manjavacas, Y. Zhang, Y. Cao, P. Nordlander, and G. A. Botton, 'Electron Energy-Loss Spectroscopy of Multipolar Edge and Cavity Modes in Silver Nanosquares', *ACS Photonics*, Feb. 2016.
- [136] J. Martin, M. Kociak, Z. Mahfoud, J. Proust, D. Gérard, and J. Plain, 'High-Resolution Imaging and Spectroscopy of Multipolar Plasmonic Resonances in Aluminum Nanoantennas', *Nano Lett.*, vol. 14, no. 10, pp. 5517–5523, Oct. 2014.
- [137] C. Langhammer, M. Schwind, B. Kasemo, and I. Zorić, 'Localized Surface Plasmon Resonances in Aluminum Nanodisks', *Nano Lett.*, vol. 8, no. 5, pp. 1461–1471, May 2008.
- [138] E. S. Barnard, J. S. White, A. Chandran, and M. L. Brongersma, 'Spectral properties of plasmonic resonator antennas', *Opt. Express*, vol. 16, no. 21, pp. 16529–16537, Oct. 2008.
- [139] H. R. Krishnamurthy, H. S. Mani, and H. C. Verma, 'Exact solution of the Schrodinger equation for a particle in a tetrahedral box', *J. Phys. Math. Gen.*, vol. 15, no. 7, p. 2131, 1982.
- [140] M. A. Doncheski and R. W. Robinett, 'Quantum Mechanical Analysis of the Equilateral Triangle Billiard: Periodic Orbit Theory and Wave Packet Revivals', *Ann. Phys.*, vol. 299, no. 2, pp. 208–227, Aug. 2002.
- [141] H. C. Chang, G. Kioseoglou, E. H. Lee, J. Haetty, M. H. Na, Y. Xuan, H. Luo, A. Petrou, and A. N. Cartwright, 'Lasing modes in equilateral-triangular laser cavities', *Phys. Rev. A*, vol. 62, no. 1, p. 013816, Jun. 2000.
- [142] G. M. Wysin, 'Electromagnetic modes in dielectric equilateral triangle resonators', *JOSA B*, vol. 23, no. 8, pp. 1586–1599, Aug. 2006.
- [143] X. Zhu, Y. Zhang, J. Zhang, J. Xu, Y. Ma, Z. Li, and D. Yu, 'Ultrafine and

- Smooth Full Metal Nanostructures for Plasmonics’, *Adv. Mater.*, vol. 22, no. 39, pp. 4345–4349, Oct. 2010.
- [144] O. J. F. Martin, C. Girard, and A. Dereux, ‘Generalized Field Propagator for Electromagnetic Scattering and Light Confinement’, *Phys. Rev. Lett.*, vol. 74, no. 4, pp. 526–529, Jan. 1995.
- [145] C. Girard, ‘Near fields in nanostructures’, *Rep. Prog. Phys.*, vol. 68, no. 8, p. 1883, 2005.
- [146] E. Palik, ‘Handbook of Optical Constants of Solids’, 1st Edition, Academic Press, 1998.
- [147] C. Kittel, ‘*Introduction to Solid State Physics*’, 7th Edition, Wiley, 1996.
- [148] F. X. Bock, T. M. Christensen, S. B. Rivers, L. D. Doucette, and R. J. Lad, ‘Growth and structure of silver and silver oxide thin films on sapphire’, *Thin Solid Films*, vol. 468, no. 1, pp. 57–64, Dec. 2004.
- [149] N. Grillet, D. Manchon, E. Cottancin, F. Bertorelle, C. Bonnet, M. Broyer, J. Lermé, and M. Pellarin, ‘Photo-Oxidation of Individual Silver Nanoparticles: A Real-Time Tracking of Optical and Morphological Changes’, *J. Phys. Chem. C*, vol. 117, no. 5, pp. 2274–2282, Feb. 2013.
- [150] J.-H. Qiu, P. Zhou, X.-Y. Gao, J.-N. Yu, S.-Y. Wang, J. Li, Y.-X. Zheng, Y.-M. Yang, Q.-H. Song, and L.-Y. Chen, ‘Ellipsometric Study of the Optical Properties of Silver Oxide Prepared by Reactive Magnetron Sputtering’, *J. Korean Phys. Soc.*, vol. 46, no. 9, p. 269, Jun. 2005.
- [151] E. D. Palik, ‘Potassium Chloride (KCl)’, in *Handbook of Optical Constants of Solids*, Boston: Academic Press, 1985, pp. 703–718.

Titre: Optique et Structure d'Agrégats Métalliques à l'Echelle Atomique

Mots clés: Nano-agrégats métalliques, Plasmons, Systèmes moléculaires métalliques

Résumé: Il est bien connu que les propriétés optiques des nanoparticules de métaux nobles, en particulier d'or et d'argent, s'écartent fortement de celles de métaux macroscopiques. Pour les tailles comprises entre dix et quelques centaines de nanomètres, elles sont dominées par les plasmons de surface (SP) décrites par des modèles purement classiques. En revanche, les agrégats de quelques dizaines d'atomes se comportent comme des systèmes quantiques, ce qui induit des comportements optiques nouveaux. La structure des nanoparticules et l'environnement diélectrique peuvent affecter les propriétés optiques. Dans cette thèse, j'ai utilisé un microscope électronique à transmission à balayage (STEM) équipé d'un spectromètre à perte d'énergie des électrons (EELS) pour mesurer, en parallèle, les propriétés optiques et structurales de nanoparticules individuelles.

Je présente comment des expériences complémentaires (STEM-EELS et absorption optique) sur de petites nanoparticules d'argent triées en taille et encapsulées dans une matrice de silice donnent au premier abord des résultats incohérents: tandis que, d'une part, l'absorption optique ne montre aucun effet de taille entre quelques atomes et environ 10 nm, un décalage en énergie est observé dans les mesures STEM-EELS. Notre interprétation quantitative, fondée sur un modèle mixte classique/quantique qui prend en compte tous les effets quantiques pertinents, a résolu les apparentes contradictions non seulement dans nos données expérimentales, mais également dans celles de la littérature. Notre modèle décrit comment l'environnement local est le paramètre crucial contrôlant la manifestation ou l'absence d'effets de taille quantique.

En second lieu, je me suis intéressé à la région purement classique à travers des structures lithographiées de quelques centaines de nanomètres. Bien que les cavités plasmoniques triangulaires aient été largement étudiées dans la littérature, une classification en termes de modes de respiration et de bords plasmoniques manquait. Dans cette étude, les résultats expérimentaux de STEM-EELS, des modèles analytiques et des simulations classiques nous ont permis de décrire la nature des différents modes.

Title: Optics and Structure of Metal Clusters at the Atomic Scale

Keywords: Metal nanoclusters, Plasmons, Metal molecular systems

Abstract: It is well known that the optical properties of nanoparticles of noble metals, in particular gold and silver, deviate strongly from those of macroscopic metals. For sizes between ten and a few hundred nanometers, they are dominated by surface plasmons (SPs) described by purely classical models. On the other hand, clusters of a few tens of atoms behave like quantum systems inducing new optical behaviors. The structure of the nanoparticles and the dielectric environment can affect the optical properties. In this thesis I used a scanning transmission electron microscope (STEM) fitted with an electron energy loss spectrometer (EELS) to measure, in parallel, the optical and structural properties of individual nanoparticles. I present how complementary experiments (STEM-EELS and optical absorption) on size-selected small silver nanoparticles embedded in silica yield at first inconsistent results: while optical absorption shows no size-effect in the range between only a few atoms and ~10 nm, a clear spectral shift is observed in STEM-EELS technique. Our quantitative interpretation, based on a mixed classical/quantum model which takes into account all the relevant quantum effects, resolves the apparent contradictions, not only within our experimental data, but also in the literature. Our comprehensive model describes how the local environment is the crucial parameter controlling the manifestation or absence of quantum size effects.

Secondly, I was interested in the purely classical region through lithographed structures of a few hundred nanometers. Although triangular plasmonic cavities have been widely studied in the literature, a classification in terms of plasmonic modes of breathing and edge was missing. In this study, experimental STEM-EELS results, analytical models and classical simulations enabled us to describe the nature of the different modes.

